

**Charging electric vehicles from solar energy
Power converter, charging algorithm and system design**

Chandra Mouli, Gautham Ram

DOI

[10.4233/uuid:dec62be4-d7cb-4345-a8ae-65152c78b80f](https://doi.org/10.4233/uuid:dec62be4-d7cb-4345-a8ae-65152c78b80f)

Publication date

2018

Document Version

Final published version

Citation (APA)

Chandra Mouli, G. R. (2018). *Charging electric vehicles from solar energy: Power converter, charging algorithm and system design*. [Dissertation (TU Delft), Delft University of Technology].
<https://doi.org/10.4233/uuid:dec62be4-d7cb-4345-a8ae-65152c78b80f>

Important note

To cite this publication, please use the final published version (if applicable).
Please check the document version above.

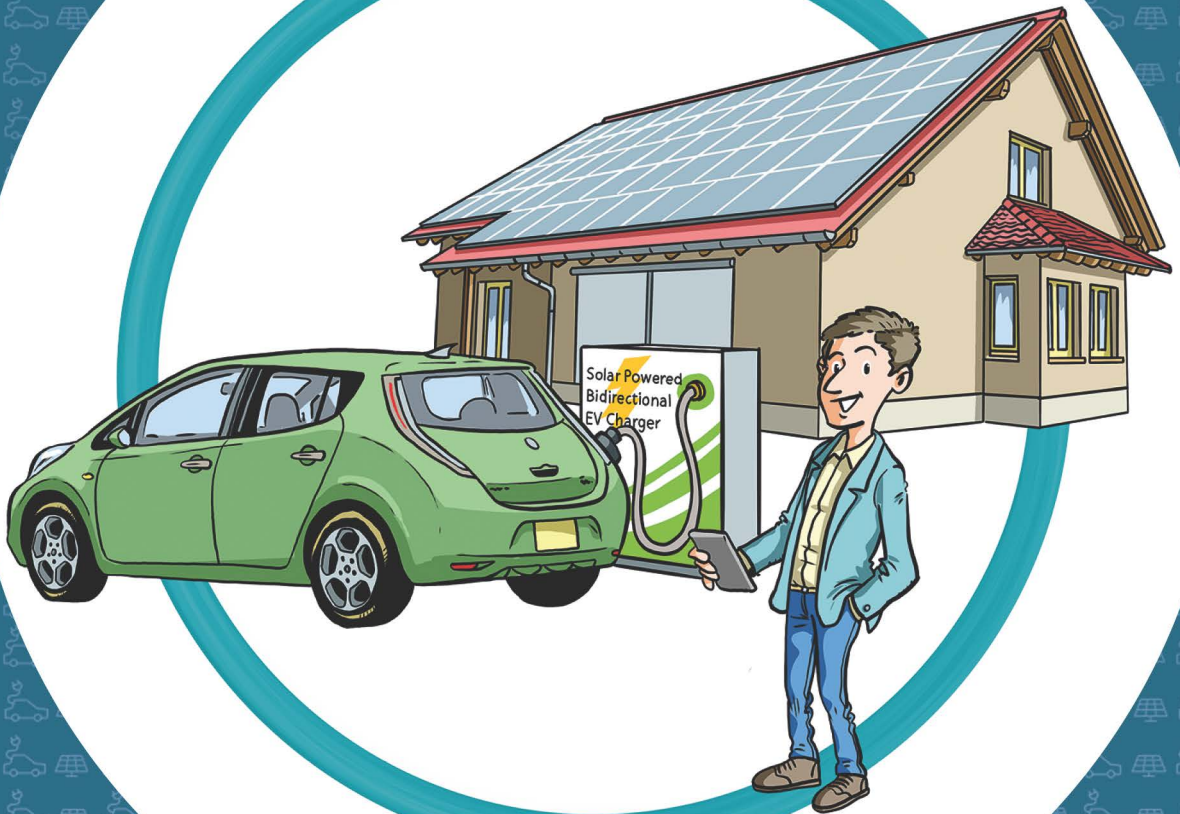
Copyright

Other than for strictly personal use, it is not permitted to download, forward or distribute the text or part of it, without the consent of the author(s) and/or copyright holder(s), unless the work is under an open content license such as Creative Commons.

Takedown policy

Please contact us and provide details if you believe this document breaches copyrights.
We will remove access to the work immediately and investigate your claim.

Charging electric vehicles from solar energy: Power converter, charging algorithm and system design



Gautham Ram Chandra Mouli

**Charging electric vehicles from solar energy:
Power converter, charging algorithm
and system design**

Gautham Ram CHANDRA MOULI

**Charging electric vehicles from solar energy:
Power converter, charging algorithm
and system design**

Dissertation

for the purpose of obtaining the degree of doctor
at the Delft University of Technology
by the authority of the Rector Magnificus, Prof.dr.ir. T.H.J.J. van der Hagen,
chair of the Board for Doctorates
to be defended publicly on
Monday 26 March 2018 at 12:30 o'clock

by

Gautham Ram CHANDRA MOULI

Master of Science in Electrical Engineering,
Delft University of Technology, the Netherlands
born in Chennai, India

This dissertation has been approved by the promotors.

Composition of the doctoral committee:

Rector Magnificus	chairperson
Prof.dr.ir. P. Bauer	Delft University of Technology, promotor
Prof.dr. M. Zeman	Delft University of Technology, promotor

Independent members:

Prof.dr. E. Lomonova	Eindhoven University of Technology
Prof.dr.ir. J. van Mierlo	Vrije Universiteit Brussel
Prof.dr. B. Nahid-Mobarakeh	Université de Lorraine
Prof.dr.ir. A.H.M. Smets	Delft University of Technology
Prof.ir. P.T.M. Vaessen	Delft University of Technology



This research was funded by the Dutch Government under ‘Topsector Energie – TKI Urban Energy’ via the project *EV supported PV smart grid*

ISBN : 978-94-6186-901-2

Printed by Ipskamp Printing (<https://www.proefschriften.net>)

Cover designed by Frank ten Hengel and Gautham Ram Chandra Mouli

Cover pictures by Erwin Suvaal (www.cviiontwerp.nl), Frank ten Hengel and Roland van Roijen

An electronic copy of the thesis can be downloaded from www.library.tudelft.nl



G.R. Chandra Mouli, 2018

Except for the cover, this work is licensed under a Creative Commons Attribution–NonCommercial–ShareAlike 4.0 International License. To view a copy of this license, visit <http://creativecommons.org/licenses/by-nc-sa/4.0/>.

Dedicated with love to my late Ananda patti and Chundu thatha,

*It is our collective and individual responsibility... to preserve and tend to
the environment in which we all live*

--Dalai Lama

Summary

Electric vehicles (EV) are considered to be the future mode of transportation, and 500 million EVs are expected to be on the road in 2030. The key drivers for EVs are their high efficiency and zero tail-pipe emissions. However, EVs are only sustainable if the electricity used to charge them comes from renewable sources and not from fossil fuel-based power plants. It is here that the solar charging of EV has gained interest in recent times, as it provides a clean and sustainable method to charge EVs. The goal of this thesis is to “Develop a highly efficient, V2G-enabled smart charging system for electric vehicles at workplaces, that is powered by solar energy”. The thesis is composed of three main elements – system design, power converter and smart charging algorithms.

System design

The system design of the solar EV charging station investigates the best design for the photovoltaic (PV) system in order to meet the EV charging demands. The design is focused on the Netherlands and considers the diurnal and seasonal solar variations based on data from the Dutch Meteorological Institute. In spite of the lower solar insolation in the Netherlands, an average of 30kWh/day is generated by a 10kW_p PV system. This is sufficient for driving 55,000km/year using a Nissan Leaf EV. There is up to five times difference in energy yield between summer and winter, a phenomenon which cannot be overcome by using a solar tracker. Due to the lower insolation, the PV converter rating can be undersized by 30% with respect to the PV array, resulting in only 3.2% loss of energy.

Simple charging schemes such as Gaussian EV charging are proposed that help match the EV charging to the PV generation and reduce the dependency on the grid. The use of a local storage was found to help in managing the diurnal solar variations but had a negligible effect in overcoming seasonal solar variation. Finally, different ways to connect a single EV-PV charger to several EVs at the workplace are proposed. The main benefit is that it enables the sharing of the charging infrastructure, thereby reducing the cost and space occupied by EV charging systems in the parking lot.

Power converter

Currently, solar EV charging stations use the 50Hz alternating current (AC) grid to exchange power from PV to EV. However, this is not efficient and cost-effective for two reasons. First, EV and PV are fundamentally direct current (DC) in nature, so conversion to AC leads to unnecessary conversion steps and losses. Secondly, two separate DC-AC inverters are required, one for EV and PV, increasing the cost and size of the power electronics.

A suitable solution is hence to use a single integrated converter that charges the EV from PV on DC and requires only a single, common inverter for both EV and PV. In this thesis, a 10kW three-port converter with an internal DC-link is developed that can charge the EV from both the PV and the AC grid. The charger is bidirectional

and can implement vehicle to grid (V2G) where the EV can feed power back to the AC grid. The converter can realize four power flows: $PV \rightarrow EV$, $EV \rightarrow \text{Grid}$, $\text{Grid} \rightarrow EV$ and $PV \rightarrow \text{Grid}$. A comparison of topologies based on power density, efficiency, controllability and component count has shown that the suitable topology for the PV, EV, and grid port are: interleaved boost converter, interleaved bidirectional flyback converter and two-level voltage source inverter, respectively. Interleaving, silicon carbide (SiC) MOSFETs, SiC Schottky diodes and powdered alloy inductors are used in the converter to achieve both high power density and high efficiency. The EV charger is modularly designed and several 10kW power modules can be operated in parallel to scale up to higher powers of up to 100kW easily.

Smart charging algorithms

Smart charging refers to the technique of controlling the magnitude and direction of the EV charging power for different applications. Currently, smart charging algorithms focus on one or few objectives at a time, resulting in small reduction in net costs and numerous charging profiles for the same EV. In this thesis, new charging algorithms are proposed that integrate several applications together for charging the EV. This results in the benefit of each application adding up, thereby reducing the net costs significantly when compared to earlier algorithms. The charging algorithms use mixed integer linear programming to control the EV charging based on: PV forecast, EV user preferences, multiplexing of EVs, V2G demand, energy prices, regulation prices and distribution network constraints. For two specific case studies simulated for Netherlands and Texas, the proposed algorithms reduced the net costs in the range of 32% to 651% when compared to uncontrolled and average rate charging, respectively.

EV-PV charging station

Thus, the EV-PV charging station uses the developed power converter and charging algorithms to directly charge an electric vehicle using solar energy and feed EV power back to the grid. Solar charging of EVs results in net zero CO₂ emissions, lower fuel cost, tax benefits and less dependence on PV feed-in tariffs when compared to gasoline cars or grid charged EVs. Charging on DC reduces the conversion steps and the associated loss when compared to charging on AC. The use of proposed smart charging algorithms reduces the net costs of the EV charging from PV and defers the cost of distribution network upgrades.

The developed EV-PV converter has a much higher peak (95.2% for $PV \rightarrow EV$, 95.4% for $\text{Grid} \rightarrow EV$, 96.4% for $PV \rightarrow \text{Grid}$) and partial-load efficiency than existing solutions. In spite of its bidirectional power flow capability, the power density of the converter is 396W/l, which is three times that of existing solutions based on Si IGBT technology and AC power exchange. The charger is compatible with the CHAdeMO and CCS EV standard; and the corresponding standards for EMI and grid integration. Successfully tests have been carried out with a CHAdeMO compatible Nissan Leaf EV by charging it from PV panels and feeding power back to the grid via V2G.

Samenvatting

Elektrische voertuigen worden gezien als de toekomst van het transport. Naar verwachting zullen er 500 miljoen elektrische voertuigen op de weg zijn in 2030. Voordelen van elektrische voertuigen zijn de grote efficiëntie en de afwezigheid van uitlaatgassen. Elektrische voertuigen zijn echter alleen duurzaam als de elektriciteit die gebruikt wordt om ze op te laden uit duurzame bronnen komt en niet uit fossiele brandstoffen. Recentelijk is er interesse gekomen in het opladen van elektrische voertuigen door middel van zonnepanelen. Het doel van dit proefschrift is om “Een hoog efficiënt V2G-enabled smart oplaadstation voor elektrische voertuigen gevoed door zonnepanelen” te ontwikkelen. Dit proefschrift bestaat uit drie onderdelen: Systeemontwerp, Power converter en Slimme laadalgoritmen.

Systeemontwerp

Het systeemontwerp onderzoekt het beste ontwerp voor het PV-systeem om aan de energievraag van het elektrische voertuig te voldoen. Het ontwerp richt zich op Nederland en houdt rekening met de zonnevariatie gedurende de dag en de verschillende seizoenen, gebaseerd op data van het KNMI. Ondanks het lage aantal zonne-uren in Nederland wordt er door een 10 kW PV-systeem gemiddeld 30 kWh per dag opgewekt. Dit is genoeg om een Nissan Leaf 55.000 km per jaar te laten rijden. Er is een verschil tussen de energieopbrengst in de zomer en de winter van een factor vijf, een fenomeen wat niet overwonnen kan worden door een solar tracker te gebruiken. Door het lage aantal zonne-uren kan de PV-converter ondermaats worden ontworpen, grofweg 30% ten opzichte van de PV-panelen, met maar een 3.2% verlies van energie.

Eenvoudige oplaadconcepten zoals Gaussian charging worden voorgesteld om het opladen van het voertuig minder afhankelijk te maken van de PV-opbrengst. Het gebruik van lokale opslag bleek nuttig i.v.m. de zonnevariatie gedurende de dag, maar had een verwaarloosbaar effect op de seizoensvariaties. Tenslotte worden er verschillende manieren voorgesteld om een enkele PV-oplader aan te sluiten op meerdere voertuigen. Het belangrijkste voordeel is dat dit de werkplek in staat stelt om de oplaadinfrastructuur te delen, waardoor de kosten en het formaat gereduceerd worden.

Power converter

Momenteel gebruiken oplaadstations het 50Hz-wisselspanningsnetwerk om vermogen uit te wisselen tussen de PV en het voertuig. Dit is echter niet efficiënt en kosteneffectief, om twee redenen. Ten eerste zijn het voertuig en de PV fundamenteel gelijkspannig van aard, dus omzetten naar wisselspanning leidt tot onnodige omzettingstappen en verliezen. Ten tweede zijn er twee aparte DC-AC-omvormers nodig, een voor het voertuig en een voor de PV, waardoor de kosten en het formaat toenemen.

Een meer voor de hand liggende oplossing is dan ook om één omvormer te gebruiken, die het voertuig vanaf de PV via een DC-link kan opladen en tevens een verbinding met het AC-grid heeft. In deze thesis wordt een 10kW-omvormer met een interne DC-link en met drie terminals ontworpen, die het voertuig zowel vanuit de PV als uit het AC-grid kan laden. De lader is bi-directioneel en biedt tevens de mogelijkheid tot Vehicle2Grid (V2G), waarbij de energie vanuit het voertuig naar het AC-grid overgebracht kan worden. De omvormer heeft de mogelijkheid voor vier verschillende energiestromen: $PV \rightarrow EV$, $EV \rightarrow AC$ Grid, AC Grid $\rightarrow EV$ en $PV \rightarrow AC$ Grid. De keuze voor een toepasbare topologie, waarbij met name is gekeken naar vermogensdichtheid, efficiëntie, regelbaarheid en aantal componenten, heeft geleid tot de volgende verscheidenheid: een interleaved-boost voor de PV, een interleaved bidirectional flyback voor het elektrische voertuig en een two-level spanningsbron-inverter. Om een hoge vermogensdichtheid en efficiëntie te behalen, werd gebruikgemaakt van interleaving, Silicon Carbide (SiC) MOSFETs, SiC Schottky diodes en magnetica op basis van poedervormige legering. De omvormer is modulair opgebouwd, waardoor het mogelijk is om meerdere 10kW-modules parallel te laten werken om zo het vermogen op te schalen tot 100kW.

Slimme laadalgoritmen

Slim laden refereert aan technieken die toepassing vinden in de regeling van de grootte en richting van het voertuig voor verschillende applicaties. De huidige slimme laadalgoritmen focussen gelijktijdig op één of meerdere criteria, met als gevolg een kostenreductie en een verscheidenheid aan laadprofielen voor eenzelfde type voertuig. In deze thesis worden nieuwe laadalgoritmen voorgesteld welke een verscheidenheid aan toepassingen voor het laden van voertuigen toestaan, waardoor de nettokosten significant kunnen dalen in vergelijking met eerdere algoritmen. Het laadalgoritme in de regeling van het voertuig gebruikt Gemengd Integer Lineair Programmeren om het laden aan te sturen, gebaseerd op: weervoorspellingen, gebruikersvoorkeuren, multiplexing van voertuigen, Vehicle2Grid-connectie, energieprijzen, prijsregulatie en de begrenzingen van het distributienet. Er zijn twee specifieke gebruikersstudies nagebootst, één voor Nederland en de andere voor Texas. Hierin heeft het toegepaste algoritme tot een besparing van 32% tot 651% in de nettokosten geleid, in vergelijking met een gemiddeld ongeregeld laadproces.

EV-PV laad station

In een PV-laadstation is de ontwikkelde omvormer met de laadalgoritmen toegepast, voor het direct laden van een elektrisch voertuig met zonne-energie en het uitwisselen van vermogen vanuit het voertuig naar het AC-grid. Het laden van het voertuig met zonne-energie resulteerde in een zero-CO₂-emissie, lagere brandstofkosten, belastingvoordeel en minder afhankelijkheid van PV terugleververgoeding in vergelijking met benzineauto's of met via het net gevoede elektrische voertuigen. Het laden via een DC-link reduceert het aantal conversiestappen en de daarmee gepaarde omzettingsverliezen, in vergelijking met een lader die op het AC-grid wordt aangesloten. Door toepassing van het slimme

laad algoritme worden de nettokosten voor het laden van het voertuig vanuit de PV gereduceerd en worden de kosten van de aansluiting op het distributienet verlaagd.

De ontworpen PV-omvormer heeft een hogere piek-efficiëntie (95.2% voor PV→EV, 95.4% voor AC Grid→EV, 96.4% voor PV→AC Grid) en hogere deellast-efficiëntie dan gebruikelijke laders. Ondanks de bi-directionele vermogensrichting, is de vermogensdichtheid van de omvormer 396 Watt per liter, wat ongeveer drie keer zoveel is als bij een gebruikelijke omvormer gebaseerd op Silicium IGBT's. De lader is compatibel met de CHAdeMO en CCS EV standaard en met de corresponderende normen voor EMI en netaansluiting. Testen met de CHAdeMO-compatibele Nissan Leaf EV zijn succesvol uitgevoerd, waarbij het voertuig geladen is vanuit de zonnepanelen en er vermogen aan het AC-net is teruggeleverd via het Vehicle2Grid-principe.

Table of Contents

Summary	vi
Samenvatting	viii
Table of Contents.....	xi
Abbreviations.....	xvi
Nomenclature	xviii
1. Introduction	2
1.1. Motivation for research	2
1.2. Research Goal.....	4
1.2.1. System level design.....	4
1.2.2. Power converter design	5
1.2.3. Smart charging algorithms	7
1.3. Research questions and outline of thesis.....	8
1.4. Research publications	12
1.5. References.....	13
2. Charging of electric vehicles from solar energy: A Review.....	18
2.1. EV charging	19
2.1.1. AC charging of EV.....	19
2.1.2. DC charging of EV	19
2.2. Solar photovoltaic PV systems	21
2.3. Charging EV from PV	22
2.3.1. Sustainability and economics.....	22
2.3.2. EV charging system for PV	22
2.4. System Architecture for the EV-PV System	23
2.4.1. Arch. 1 - Separate converter for PV, EV interlinked on AC.....	23
2.4.2. Arch. 2 - Separate converters for PV, EV interlinked on DC.....	23
2.4.3. Arch. 3 - Multiport converter for PV, EV, grid interlinked on AC	24
2.4.4. Arch. 4 - Multiport converter for PV, EV, grid interlinked on DC.....	25
2.5. EV-PV power flows	26
2.6. Comparison of system architectures	27
2.7. Review of EV-PV Power Converter Topology	29
2.8. Nominal rating and topology for the EV-PV Charger	32
2.8.1. 10kW Nominal rating.....	32
2.8.2. Multi-port converter for the EV-PV Charger	32
2.9. Conclusions	34
2.10. References.....	34
3. System design for Solar EV charging station	40
3.1. Introduction	41
3.2. Literature review and contributions	41

3.3.	PV System Design	42
3.3.1.	Estimation of optimal orientation of PV array in the Netherlands... ..	42
3.3.2.	Power output of optimally oriented PV array in the Netherlands.....	44
3.3.3.	Impact of sun tracking system in increasing in PV energy yield	47
3.3.4.	Oversizing the PV array with respect to PV converter power rating ...	48
3.4.	Smart charging of EV.....	49
3.4.1.	Matching the Smart charging of EV to PV generation	50
3.4.2.	Scenario 1 – EV load for 7 days/week	51
3.4.3.	Scenario 2 – EV load for 5 days/week	52
3.5.	Integrating Local Storage in EV-PV Charger	53
3.6.	Connecting multiple EVs to a single EV-PV charger.....	57
3.6.1.	Mult.1 – Using multiple charging plugs with DC disconnectors	59
3.6.2.	Mult. 2 – Using multiple DC/DC converters on DC link.....	59
3.6.3.	Mult. 3 – Multi-winding high-frequency transformer on DC-link.....	59
3.6.4.	Mult. 4 – Multiple DC/DC converters at output.....	59
3.6.5.	Ranking for charging of multiple EV.....	60
3.7.	Conclusions	60
3.8.	References	61
4.	Topology for three-port EV-PV-Grid converter	66
4.1.	Introduction.....	67
4.1.1.	Power converter types for EV-PV charging	67
4.1.2.	Literature Review and contributions	68
4.1.3.	Contributions	70
4.1.4.	Converter specifications.....	70
4.2.	Design of Converters and Loss Modeling.....	70
4.3.	Comparison framework	75
4.3.1.	Comparison criteria	75
4.3.2.	Topologies considered	77
4.4.	DC Link - PV Port Candidates	77
4.4.1.	Topologies.....	77
4.4.2.	Optimal configuration of topology and comparison	79
4.5.	DC link - EV port candidates.....	81
4.5.1.	Topologies.....	81
4.5.2.	Optimal configuration of topology and comparison	83
4.6.	DC link - grid port candidates	84
4.6.1.	Topologies.....	85
4.6.2.	Optimal configuration of topology and comparison	86
4.7.	Impedance-network based converter.....	87
4.7.1.	Operation of quasi Z-Source Inverter	87
4.7.2.	Design and comparison of topology	87
4.8.	Conclusion.....	89
4.9.	References	90

5.	Development of 10kW bidirectional solar EV charger	96
5.1.	Introduction	97
5.2.	EV-PV power converter	97
5.2.1.	Specifications	97
5.2.2.	Topology	99
5.2.3.	Achieving high efficiency and high power density.....	99
5.2.4.	Contributions	101
5.3.	DC/DC converter for PV.....	101
5.3.1.	Operation of interleaved boost converter.....	101
5.3.2.	Inductor design and losses.....	103
5.3.3.	Sizing of input and output capacitor	105
5.3.4.	Loss Estimation in converter	105
5.4.	DC/AC Grid Inverter	107
5.5.	Isolated bidirectional DC/DC converter for EV.....	107
5.5.1.	Operation of interleaved bidirectional flyback in quasi-resonance ..	108
5.5.2.	Flyback transformer design	110
5.5.3.	Variable frequency QR and DCM operation	111
5.5.4.	Sizing of filter capacitors	111
5.5.5.	IBFC losses and efficiency	112
5.6.	Closed Loop Control.....	116
5.6.1.	PV converter	117
5.6.2.	DC/DC bidirectional EV charger	117
5.6.3.	DC/AC Grid inverter.....	117
5.7.	Experimental setup & verification.....	118
5.7.1.	Modular prototype of EV-PV converter	118
5.7.2.	Experimental waveforms.....	119
5.7.3.	Efficiency of converter	123
5.7.4.	Comparison with conventional design	124
5.8.	Testing with a Nissan Leaf - Charging and V2G	126
5.9.	Datasheet of EV-PV charger	126
5.10.	Conclusions	128
5.11.	References.....	128
6.	Energy management system for smart charging of EVs	132
6.1.	Nomenclature	133
6.1.1.	Optimization input parameters	133
6.1.2.	Optimization variables.....	134
6.2.	Introduction	135
6.2.1.	Immediate, average rate and randomly delayed charging.....	135
6.2.2.	Smart charging.....	136
6.3.	Literature review and overview of contributions	137
6.4.	Preliminaries and Inputs.....	138
6.4.1.	Layout of the EMS.....	138

6.4.2.	Trading energy and reserves in the energy market.....	140
6.4.3.	Receding horizon model predictive control.....	141
6.5.	MILP formulation.....	141
6.5.1.	Acceptance criteria.....	141
6.5.2.	Constraints: EV and user inputs.....	142
6.5.3.	Constraints: EV-PV charger and car park.....	143
6.5.4.	Objective function	145
6.5.5.	Simulation.....	146
6.6.	Simulation study: Netherlands	146
6.6.1.	Simulation parameters	146
6.6.2.	Simulation platform.....	148
6.6.3.	Simulation results	148
6.7.	Simulation study: Texas	151
6.7.1.	Simulation parameters	151
6.7.2.	Simulation platform.....	152
6.7.3.	Simulation results	153
6.7.4.	Case studies.....	155
6.7.5.	Inferences.....	156
6.8.	Implementation aspects	157
6.9.	Conclusions	158
6.10.	References	159
7.	Implementation of Smart charging and V2G	164
7.1.	Introduction.....	165
7.2.	Smart Charging and V2G on AC.....	165
7.2.1.	Smart charging via AC charging	165
7.2.2.	V2G via AC charging.....	166
7.3.	Smart Charging via CHAdeMO	166
7.4.	Smart Charging via CCS/COMBO	168
7.5.	Experimental Verification.....	169
7.5.1.	Smart charging and V2G using CHAdeMO	169
7.5.2.	Smart charging and V2G using CCS/Combo.....	169
7.6.	Conclusions	172
7.7.	References	173
8.	Conclusions.....	176
8.1.	Contributions	176
8.2.	Conclusions	177
8.3.	Future work.....	181
Appendix A: GHG of gasoline, HEV, PHEV and PEV.....		184

Appendix B: Economic and CO₂ Emission Benefits of Solar Charging of EVs	185
B.1. Introduction	185
B.2. Gasoline Vs. electric vehicles	185
B.3. Solar generation in working hours	188
B.4. Charging EV from Rooftop PV or PV carport	190
B.5. Impact of Feed-In Tariffs	192
B.6. Assumptions and limitations of the model	193
B.7. Conclusions	193
B.8. References.....	194
Appendix C: Estimation of ripple and induct. of powdered alloy core inductors...	196
C.1. Introduction	196
C.2. Ripple and inductance roll-off for variable permeability cores.....	199
C.3. Ripple and inductance estimation for boost converter	202
C.4. Conclusion	205
C.5. References.....	206
Appendix D: Datasheet and brochure of 10kW EV-PV charger	207
D.1. Specifications: 10kW Bidirectional EV Charger	207
D.2. Specifications: Add-on solar module	208
D.3. Brochure of EV-PV charger	209
D.4. Concept for future EV-PV charging station	211
A short history of Electric Vehicles	213
List of Publications	216
List of Publications (Related to this thesis)	216
Recognition received.....	217
List of Publications (Collaborative projects)	218
Acknowledgements	219
Curriculum Vitae.....	223

Abbreviations

2LC	Two Level Converter
3LNPC	Three Level Neutral Point Clamped Converter
3LTC	Three Level T-Type Converter
AC	Alternating Current
APX	Amsterdam Power Exchange
AR	Average Rate charging
AWG	American Wire Gauge
BCM	Boundary Conduction Mode
CAN	Controller Area Network communication
CIIBC	Coupled Inductors Interleaved Boost Converter
CCM	Continuous Conduction Mode
CCS	Combined Charging System, also COMBO
CH	Charge mode
CO ₂	Carbon di-oxide
CPO	Charge Point Operator
CP	Control Pilot of EV connector
CSPI	Cooling System Performance Index
DAB	Dual Active Bridge
DC	Direct Current
DCM	Discontinuous Conduction Mode
DF	Dielectric Factor
DOD	Depth of Discharge of battery
DSO	Distribution System Operator
EMC	Electromagnetic compatibility
ERCOT	Electric Reliability Council of Texas
ESR	Equivalent Series Resistance
EV	Electric vehicle
EVSE	Electric Vehicle Supply Equipment
FIT	Feed-in tariff
FBT	Flyback Transformer
GHG	Greenhouse gas
HEV	Hybrid Electric Vehicle
IBC	Interleaved Boost Converter
IBFC	Interleaved Bidirectional Flyback Converter
ICT	Information and Communications Technology
IEC	International Electromechanical Commission
IEEE	Institute of Electrical and Electronics Engineers
IGBT	Insulated Gate Bipolar Transistor
iGSE	Improved Generalized Steinmetz Equation
IPT	Inductive Power Transfer
ISO	Independent System Operator
HFT	High Frequency Transformer
IMM	Immediate (Uncontrolled) charging
KNMI	Koninklijk Nederlands Meteorological Institute

LVS	Low Voltage Switching
MILP	Mixed Integer Linear Programming
MOSFET	Metal Oxide Semiconductor Field Effect Transistor
MPC	Multi-Port converter
MPPT	Maximum Power Point Tracking
MSE	Modified Steinmetz Equation
MZVPWM	2- Medium-1-Zero-Vector Pulse-Width Modulation
NSPWM	Near State Pulse-Width Modulation
OPT	Optimized smart charging
PCB	Printed Circuit Board
PEV	Plug-in battery electric vehicle
PF	Power Factor
PHEV	Plug-in Hybrid Electric Vehicle
PLC	Power Line Carrier communication
PP	Proximity Pilot of EV connector
PSM	Phase Shift Modulation
PV	Photovoltaic
PWM	Pulse Width Modulation
QR	Quasi-resonance
qZSI	quasi Z-Source Inverter
RND	Randomly delayed charging
Si	Silicon
SiC	Silicon Carbide
SAE	Society of Automotive Engineers
SOC	State of Charge of battery
SPWM	Sinusoidal Pulse-Width Modulation
SVPWM	Space Vector Pulse-Width Modulation
TCO	Total Cost of Ownership
THD	Total Harmonic Distortion
TLBC	Three Level Boost Converter
TPC	Three-port power converter
V2G	Vehicle to Grid
V2X	Vehicle to Everything; X= Home (V2H), Load (V2L), Grid (V2G)
VSI/VSC	Voltage Source Inverter/Converter
ZCS	Zero Current Switching
ZSI	Z-Source Inverter
ZVS	Zero Voltage Switching
ZVS-QS	Zero Voltage Switching Quasi Square-Wave
ZVT	Zero Voltage Transition

Nomenclature

Chapter 2

P_{ch}	- Charging power of the EV battery
I_{ev}	- Charging current of the EV battery
V_{ev}	- Voltage of the EV battery
E_{ch}	- Charging energy delivered to the EV battery
t_{ch}	- Charging time of the EV battery
α_{MPC}	- Efficiency of power conversion between PV and EV in MPC (Arch. 3,4)
β_{MPC}	- Efficiency of EV charger in MPC (Arch. 3,4)
γ_{MPC}	- Efficiency of PV converter in MPC (Arch. 3,4)
η_{iMPC}	- Efficiency of inverter present in MPC (Arch. 3)
η_{dcPV}	- Efficiency of DC/DC converter for PV (Arch. 2)
η_{dcEV}	- Efficiency of DC/DC converter for EV (Arch. 2)
η_{iPV}	- Efficiency of DC/AC inverter for PV (Arch. 1)
η_{iEV}	- Efficiency of DC/AC inverter for EV (Arch. 1)
η_i	- Efficiency of the central inverter (Arch. 2,4)

Chapter 3

$SGHI$	- Global horizontal irradiance
$SDHI$	- Diffuse Horizontal Irradiance
$SDNI$	- Direct Normal Irradiance
T_a	- Ambient temperature
A_m	- Azimuth of the module
θ_m	- Tilt angle of the module
S_m	- Solar irradiance on a module
A_s	- Azimuth of the sun
θ_s	- Tilt angle of the sun
P_m	- PV array output power
T_{cell}	- Temperature of the PV cells
A_{pv}	- Area of module
P_r	- Nominal Power
η	- Avg. Panel Efficiency
V_{mpp}	- Rated Voltage
I_{mpp}	- Rated Current
V_{oc}	- Open-Circuit Voltage
I_{sc}	- Short-Circuit Current
T_{NOCT}	- Nominal Operating Cell Temperature
λ	- Power Temp Coefficient
A_{pv}	- Area of module
P_r	- Nominal Power
P_{grid}	- Power fed to or drawn from the grid

P_{ev}	- EV charging power
P_{pv}	- PV generation power
E_{EV}	- Energy delivered by each EV charging profile
E_{fed}^{grid}	- Total energy fed to the grid over one year
E_{draw}^{grid}	- Total energy drawn from the grid over one year
E_{ex}^{grid}	- Total energy exchanged with the grid over one year
R_v	- EV priority
T_v^a, T_v^d	- Arrival and departure time of v^{th} EV respectively
T_v^p	- Parking time of v^{th} EV
B_v^a	- Energy in the battery of the v^{th} EV upon arrival T_v^a
B_v^{max}	- Capacity and maximum possible energy of v^{th} EV
SOC_v^a	- State of charge of the v^{th} EV upon arrival T_v^a
P_b^{max}	- Maximum charging/discharging power of the storage

Chapter 4

P_{nom}	- Nominal power of the converter
V_{ac}	- RMS voltage of AC grid connection
V_{pv}	- PV MPPT Voltage
I_{pv}	- PV MPPT Current
$\Delta I_{pv\%}$	- PV current ripple (peak-peak)
$\Delta V_{pv\%}$	- PV voltage ripple (peak-peak)
V_{ev}	- EV voltage
I_{ev}	- EV current
V_{dc}	- Internal DC-link voltage
f_{sw}	- Switching frequency
P_S	- Total losses in the switch (conduction and switching losses)
$P_{S,con}$	- Conduction losses of the switch
$P_{S,sw}$	- Switching losses of the switch
I_{DS}	- Switch drain-source current
$R_{DS(on)}$	- Switch on-state resistance
V_{DS}	- Switch drain-source voltage
T_j	- Semiconductor device junction temperature
V_{GS}	- Switch gate voltage
R_G	- Switch gate resistance
E_{on}	- Turn-on energy of the switch
E_{off}	- Turn-off energy of the switch
I_D	- Diode current
P_D	- Total losses in the diode (conduction and switching losses)
$P_{D,con}$	- Diode conduction losses
$P_{D,sw}$	- Diode turn-off losses
I_D	- Diode current during ON state
V_R	- Diode reverse voltage in OFF state

U_{D0}	- Diode forward voltage during ON state
R_D	- Diode equivalent series resistance
E_{Dch}	- Energy stored in parasitic junction capacitance of the diode
P_L	- Total inductor/transformer losses
V_L	- Volume of the inductor/transformer
P_{core}	- Core losses of the inductor
P_{cu}	- Winding copper losses of inductor
V_e	- Volume of the inductor/transformer core
P_v	- Core losses of inductor per unit volume
R_L	- Inductor winding resistance
I_L	- Inductor current
F_L	- Inductor design index
$P_{L,max}$	- Highest inductor losses amongst all designs
$V_{L,max}$	- Largest inductor volume amongst all designs
C_{in}	- Input capacitance
P_{caps}	- Losses in the capacitor set
$R_{ESR,set}$	- ESR of the capacitor set
$N_{c,s}, N_{c,p}$	- Number of series and parallel connected capacitors
R_{ESR}	- ESR of the capacitor
D_F	- Dielectric factor of the capacitor
I_{cap}	- Capacitor current
C_r	- Capacitance of individual capacitor in a set
A_{set}	- Area on the PCB occupied by capacitor set
V_{set}	- Volume of the capacitor set
$A_{set,max}$	- Highest capacitor set PCB area amongst all designs
$V_{set,max}$	- Largest capacitor set volume amongst all designs
F_C	- Capacitor design index
V_S	- Volume of the heat sink
$R_{th,Sa}$	- Thermal resistance of the heat sink to the ambient
C_{SPI}	- Cooling System Performance Index
T_S	- Heat sink temperature
T_a	- Ambient temperature
P_t	- Total losses in the semiconductors
W_j	- Weight factor for criteria j
R_{ij}	- Rating of the topology i for the criteria j
$T_{score,i}$	- Total score of the topology i
N_{cri}	- Total number of criteria for comparison of topology
k	- Coupling coefficient of the coupled inductor or transformer
L_{leak}	- Leakage inductance of the transformer

Chapter 5

P_{nom}	- Nominal power of the converter
V_{ac}	- RMS voltage of AC grid connection
I_{ac}	- RMS current of AC grid connection
P_{ac}	- Nominal power of AC grid connection
V_{pv}	- PV MPPT Voltage
I_{pv}	- PV MPPT Current
P_{pv}	- PV nominal power Current
ΔI_{pv}	- PV current ripple (peak-peak); expressed as percentage $\Delta I_{pv}\%$
ΔV_{pv}	- PV voltage ripple (peak-peak)
V_{ev}	- EV voltage
I_{ev}	- EV current
P_{ev}	- EV charging power
V_{dc}, V_{dc}^*	- Internal DC link voltage and its nominal value
f_{sw}	- Switching frequency
N_i	- Number of interleaved stages
D	- Duty cycle of the switch
d_1	- Duty cycle of diode conduction in IBC
ΔI_L	- Inductor ripple current (peak-peak)
T	- Time period of switching frequency
$I_{L(max)}$	- Maximum inductor current
$I_{L(min)}$	- Minimum inductor current
N_{on}	- Maximum number of switches that are simultaneously ON in IBC
A_L	- Permeance of the core
A_c	- Core area
l_e	- Magnetic path length of the core
V_e	- Volume of the core
B_{max}	- Maximum flux density in the core during operation
ΔB	- Peak-peak change in flux density of the core ($B_{pk} = \Delta B/2$)
P_L	- Total inductor/transformer losses
P_{core}	- Core losses of the inductor
P_{cu}	- Winding copper losses of the inductor
P_v	- Core losses of inductor per unit volume
R_L	- Inductor winding resistance
f_{eq}	- Equivalent frequency for modified Steinmetz equation
I_L	- Inductor winding current (RMS)
C_{in}	- Input capacitance
P_S	- Total losses in the switch (conduction and switching losses)
$P_{S,con}$	- Conduction losses of the switch
$P_{S,sw}$	- Switching losses of the switch
I_{DS}	- Switch drain-source current
$R_{DS(on)}$	- Switch on-state resistance
V_{DS}	- Switch drain-source voltage
T_j	- Semiconductor device junction temperature
T_a	- Ambient temperature

V_{GS}	- Switch gate voltage
R_G	- Switch gate resistance
E_{on}	- Turn-on energy of the switch
E_{off}	- Turn-off energy of the switch
I_D	- Diode current
P_D	- Total losses in the diode (conduction and switching losses)
$P_{D,con}$	- Diode conduction losses
$P_{D,sw}$	- Diode turn-off losses
$V_{R,D}$	- Diode reverse voltage in OFF state
U_{D0}	- Diode forward voltage during ON state
R_D	- Diode equivalent series resistance
E_{Dch}	- Energy stored in parasitic junction capacitance of the diode
P_{filter}	- Total losses in input, output and EMI filters
P_{ctrl}	- Power consumed by the control circuit
D_1	- Duty cycle of diode conduction in IBFC
$I_{L1A(pk)}$	- Peak current of the primary winding of flyback inductor
$I_{L3A(pk)}$	- Peak current of the secondary winding of flyback inductor
k	- Coupling coefficient of the flyback transformer winding
M	- Mutual inductance of flyback transformer winding
E_L	- Energy stored in the flyback inductor
V_{trans}	- Transient voltage overshoot on MOSFET due to leakage inductance
T_F	- Half the time period for quasi-resonance
V_{valley}	- Quasi-resonance valley voltage during switch turn on
$C_{ds(net)}$	- Net drain-source capacitance across primary side MOSFET in IBFC
$C_{ds,S}$	- Output capacitance of the MOSFET
C_{DD}	- Parasitic junction capacitance of the diode
C_{xmer}	- Parasitic capacitance of transformer winding
g	- Inductor air gap
$C_{ev(net)}$	- EV side output filter capacitor of IBFC
E_{QR1}	- Turn-on energy due to the discharging of the MOSFET side QR capacitor
E_{QR2}	- Turn-on energy due to the charging of the diode side QR capacitor
E_{Drr}	- Energy lost in diode due to its reverse recovery
E_{Srr}	- Energy lost in switch due to the reverse recovery of the diode
C_{DC}	- DC link capacitance

Chapter 6

t, v, c	- Optimization indices for time, electric vehicle (EV), and charger respectively
$x_v^{e(ar)}$	- 'Average rate' charging power of v^{th} EV (kW)
t_{dly}	- Time delay for randomly delayed charging (h)
C^{ev}	- Charging costs for entire EV fleet (\$)
S^{PV}	- Revenue from sales of PV power (\$)
S^{as}	- Revenue from sales of ancillary services (\$)
T_v^a, T_v^d	- Arrival and departure time of EV respectively (h)

B_v^a	- Energy in the battery of the v^{th} EV upon arrival T_v^a (kWh)
B_v^d	- Energy in the battery of the v^{th} EV at departure T_v^d (kWh)
d_v	- Charging energy demand of v^{th} EV (kWh)
P_c^{EVr}	- Rated power of each EV charger in c^{th} EV-PV power converter (kW)
P_c^{PVR}	- Rated power of photovoltaic array (PV) connected to c^{th} charger (kW _p)
η_c^{conv}	- Rated efficiency of c^{th} EV-PV charger (%)
ΔT	- Time step for the model predictive control (h)
V	- Number of EV in the car park at time t
C	- Number of EV-PV chargers in the car park
C^{PV}	- Cost of obtaining PV energy (\$/kWh)
$y^{PV(fc)}$	- Maximum uncertainty in solar forecast data (%)
P_c^{conv}	- Rated power of the DC/AC inverter (kW)
$B_{t,v}$	- Energy in the battery of v^{th} EV battery at time t (kWh)
$P_t^{PV(fc)}$	- Solar forecast of 1kW _p PV array installed at the workplace or car park (kW)
C_v^p	- Penalty for not meeting EV energy demand by the departure time (\$/kWh)
C^{V2X}	- Battery degradation penalty for participating in V2G services (\$/kWh)
$P_{t,c}^{PV}$	- Power generated by PV connected to the c^{th} charger at time t (kW)
$a_{t,v}^c$	- Binary variable that determines if the v^{th} EV is active at time t (Active =1)
$a_{t,v}^{ch,v2x}$	- Binary variable if the v^{th} EV is in CH or V2G mode at time t (Charge =1)
$a_{t,c}^{d,f}$	- Binary variable if the c^{th} charger is drawing or feeding power (Draw =1)
K_c^{PV}	- PV scaling factor for c^{th} charger
N_c^{conn}	- Maximum number of EVs connected to the c^{th} EV-PV power converter
N_c^{ch}	- Maximum number of EVs that can simultaneously charge from c^{th} charger
$K_{v,c}$	- Binary variable indicating connection of v^{th} EV with c^{th} charger (Connected =1)
C^{opt}	- Net costs for optimized charging of EV from PV (\$, €)
C^{ar}, C^{rnd}, C^{imm}	- Net costs for average rate, randomly delayed, immediate charging (\$, €)
$p_{t,c}^{draw}, p_{t,c}^{feed}$	- Power drawn and fed to car park by c^{th} charger, respectively (kW)
$p_t^{g(imp)}, p_t^{g(exp)}$	- Power imported and exported to grid by EV car park, respectively (kW)
B_v^{min}, B_v^{max}	- Minimum and maximum possible battery energy of v^{th} EV (kWh)
x_v^{ub}, x_v^{lb}	- Maximum charging and discharging power of v^{th} EV, respectively (kW)
$\eta_v^{ch}, \eta_v^{v2x}$	- Efficiency of charging and discharging of the v^{th} EV, respectively (kW)
$x_{t,v}^{e+}, x_{t,v}^{e-}$	- Charging and discharging power of v^{th} EV at time t respectively (kW)
$x_{t,v}^{r(up)}, x_{t,v}^{r(dn)}$	- Reserve power capacity offered to grid for up and down regulation by v^{th} EV at time t (kW)
$p_t^{e(buy)}, p_t^{e(sell)}$	- Market clearing price for buying and selling electricity from the grid, respectively (\$/kWh)
$p_t^{r(up)}, p_t^{r(dn)}$	- Market clearing price for offering reserve capacity for up and down regulation, respectively (\$/kW)
p_t^{DN+}, p_t^{DN-}	- Distribution network capacity for drawing and feeding power to car park, respectively (kW)

Chapter 7

- E_{buff} - Buffer capacity required by CCS for smart charging
- V_{ev} - EV battery voltage
- I_1, I_2 - CCS current setpoint for smart charging
- t_1 - Time taken by the EV to respond to the new current request
- t_2 - Time taken by the EV to change current to the new current setpoint
- I_{set} - EV charging current/Charging current setpoint from EV
- I_{ref} - Charging current set point requested by the charger

1

Introduction

1. Introduction

1.1. Motivation for research

Electric vehicles (EVs) are considered to be the future mode of transportation. The *Paris Declaration on Electro-Mobility and Climate Change and Call to Action*, calls for the global deployment of 100 million electric vehicles by 2030. EVs are much more energy efficient than gasoline/diesel powered vehicles and they do not produce any tailpipe emissions. They have a much simpler drivetrain, are much less noisy and require little maintenance.

However, EVs are only sustainable if the electricity used to charge them comes from renewable sources and not from fossil fuel based power plants [1]–[3]. This is highlighted in Fig.1.1, where the well-to-wheel greenhouse gas emissions (GHG) from a fuel perspective of a conventional gasoline car is compared with those of a hybrid electric vehicle (HEV), plug-in hybrid electric vehicle (PHEV) and plug-in electric vehicle (PEV) for different cases of the fuel mix for electricity generation (Appendix A). It is evident that any form of an electric car, be it an HEV, PHEV or PEV always has lower well-to-wheel emissions from a fuel perspective than a comparable gasoline car. At the same time, the emissions of the electric car are itself dependent on how clean the fuel mix is [1]–[3]. If EVs are charged from a grid that is predominantly powered by fossil fuels like coal or natural gas, the emissions are significant and not zero, contrary to popular belief. On the other hand, if EVs are charged from a grid which is largely powered by renewable energy, then the net emissions are close to zero. The challenge, then, is to power EVs in the future using sustainable sources of energy.

Wind, solar, hydropower, geothermal, biogas or tidal energy are excellent sources of renewable energy to power electric vehicles in the future. Amongst these, the use of solar photovoltaic panels to charge EVs is an attractive option due to several reasons:

1. The cost of solar PV has been continuously falling over the past decades and is less than $1\$/W_p$ [4].
2. PV power has high accessibility to EV users as PV modules can be installed on the roofs and as solar car parks, close to where EVs will be, as shown in Fig.1.2. The PV potential of rooftops or parking places is largely unutilized today, and this can be exploited in the future.
3. There is both reduced energy and power demand on the grid due to EV charging as the charging power is locally generated in a ‘green’ manner through solar panels [5]–[7]. This reduces/delays the need for grid reinforcement.
4. Conventionally, PV systems use a battery to store the solar energy to manage the seasonal and diurnal variations in solar generation. In the case of charging EVs from PV, the EV battery can serve as an energy storage for the PV, and no additional battery will be required [8]–[11].
5. The cost of charging the EV from solar is cheaper than charging it from the grid, and it reduces the impact of low PV feed-in tariffs [12], [13].
6. PV systems have low noise, have no rotating parts and are practically maintenance free.

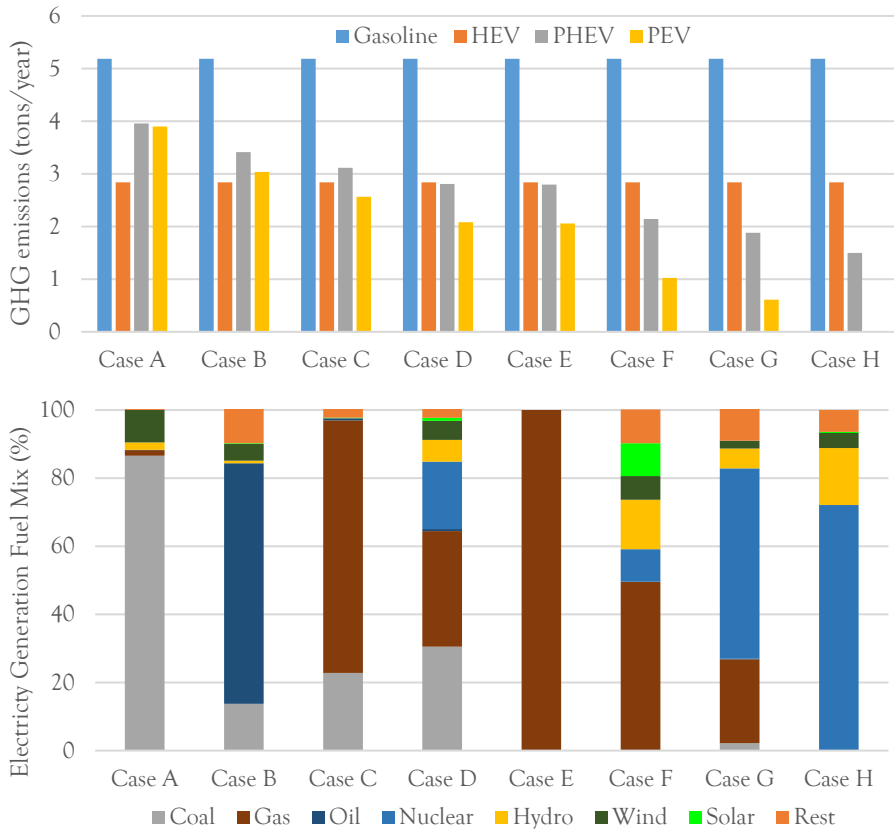


Fig.1.1. The well-to-wheel emissions of EV are dependent on the electricity fuel generation mix. 'Rest' includes generation from biomass, geothermal and other fossil fuels. (Based upon data from the US Department of Energy, Refer to Appendix A)



Fig.1.2. An impression of a solar powered EV charging station at workplace where the EVs are charged from PV installed on rooftop and as solar carport (By M. Leendertse)

Hence, the charging of electric vehicles from PV panels can make EVs truly sustainable and reduce the net cost of the charging infrastructure. This is the vision and motivation for this thesis. A connection to the conventional alternating current (AC) grid is provided in order to feed any excess PV power or draw power for EV charging if PV generation is insufficient. This ensures that neither the PV generation nor EV charging is hindered in the case the other is insufficient/absent.

1.2. Research Goal

The goal of the dissertation is:

“To develop a highly efficient, V2G-enabled smart charging system for electric vehicles at workplaces, that is powered by solar energy.”

The thesis focusses on charging of EVs from PV at workplaces like office buildings and factories. The reason for this focus is three-fold. First, workplaces offer a relatively large area for installation of PV modules as seen in Fig.1.2. The working hours of employees during the day largely matches the hours when the sun is shining. This provides ample time to charge the EV battery from the solar energy. Finally, the 7-9 hour long parking of vehicles at the workplace allows the use of lower charging powers, thus reducing the cost and complexity of the EV chargers needed. The long parking times also make it suitable to implement smart charging which helps in reducing the costs further.

In order to realize such a solar powered EV charging infrastructure, three elements are essential – system-level design, development of a solar EV charger and formulation of smart charging algorithms. These three research elements form the core of this thesis, and the research gaps in them are explained further.

1.2.1. System level design

The aim of the system level design is to design the PV and EV system so as to match the solar generation with the EV charging demand. The challenge, however, is that solar generation is location dependent and characterized by seasonal and diurnal variations. Traditionally, the design of the PV system and EV charging infrastructure have been analyzed as separate topics without considering their vital inter-relations. In this thesis, an integrated system design considering both EV and PV is hence implemented. For the case of Netherlands, it requires the detailed modeling of the meteorological data like solar irradiance and temperature and analyzing the daily commuting requirements of EV users. The effect of PV tracking system and the use of a smaller rated power converter with respect to the PV system rating is studied as well.

Secondly, simple smart charging techniques such as a Gaussian EV charging profile can help the EV charging to closely follow the variable PV generation [14]-[17]. At the same time, a local storage has the potential to manage the solar variations by storing energy during excess generation and provide power when the generation is low [18]-[23]. While the two techniques have been independently shown to help solar charging of EV, they have not been evaluated together. Further, in the case of workplace

charging, EV charging demand is typically for 5days/week on weekdays while the PV generates power on all 7days/week. The crucial impact of this difference between supply and demand, on the system design, has not been investigated earlier. This thesis combines both smart charging and local storage to show how the two influence each other and what impact they have on the 5day/week and 7day/week EV charging load. It further goes to show the positive effect that storage has on diurnal solar variation, while there is a negligent effect on seasonal solar variation.

1.2.2. Power converter design

The power converter design investigates the power converter topology, semiconductor device technology, power density, efficiency, closed-loop control and EV charging standards to enable the solar charging of EVs. In simple words, it is the hardware that facilitates the possibility to charge EVs from PV.

The existing solutions for charging EV using solar energy is to use a DC/AC solar inverter to extract power from a PV array and then use an AC/DC EV charger to charge the EVs [14], [24]-[27]. This is shown in Fig.1.3 where separate power converters are used for PV and EV. The AC grid is hence used as power exchange medium between EV and PV. However, this solution is not efficient and is inflexible due to several reasons:

1. EV and PV are fundamentally direct current (DC) in nature, so exchanging power over AC requires more power conversion and is less efficient than DC power exchange. This is because high power inverters/rectifiers used for EV and PV typically have a two-step power conversion, a DC/DC stage, and a DC/AC stage. With DC power exchange between EV and PV, the DC/AC stage can be avoided.
2. Two DC/AC inverters are needed in the existing solution, one in the PV converter and one in the EV converter, adding to the cost and complexity of the system.
3. Solar inverters and EV chargers are currently designed as separate devices with no common control interface. This makes it challenging to practically implement charging algorithms to control the EV charging based on PV generation.
4. EV batteries can not only be charged from the grid but can also discharge power back to the grid. This phenomenon is called Vehicle-to-grid (V2G), and it requires a bidirectional EV charger (charge and discharge). With V2G, the EV can act as a controllable electrical generator for the grid [28], [29]. This would be even more beneficial if solar energy is stored in the EV during the day and can be extracted from the EV during the night. Currently, commercially available EV chargers are not bidirectional and hence do not offer the V2G technology.
5. Finally, the current generation of power converters are built using traditional silicon semiconductor technology, due to which the switching frequency is limited to <30kHz. The lower switching frequency leads to larger passive components in the converters, thereby increasing the converter volume and decreasing the power density.

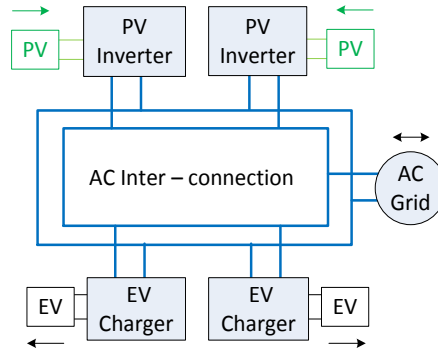


Fig.1.3. Existing solution for solar charging of EV is based on a DC/AC solar inverter to extract PV power and then an AC/DC EV charger is used to charge the EV.

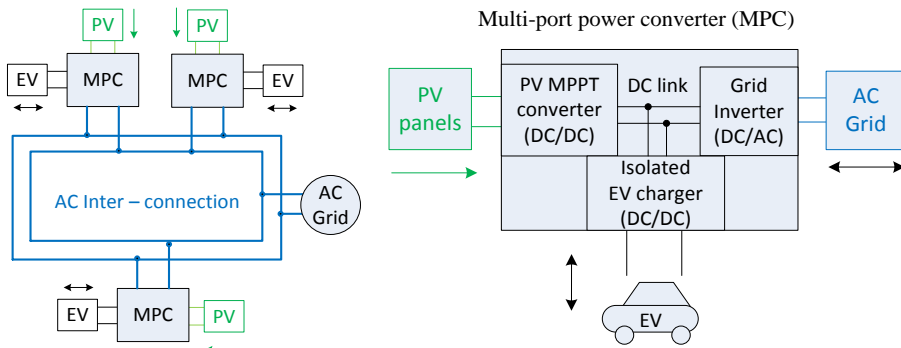


Fig.1.4. A suitable solution would be an integrated multi-port power converter (MPC) capable interconnecting PV and EV on DC and can connect to the AC grid as well.

In order to overcome these drawbacks, a suitable solution would hence be to develop a dedicated multi-port power converter (MPC) that is capable of connecting to PV, EV, and grid, as shown in Fig.1.4. It would be more efficient to connect EV and PV on DC in the integrated converter rather than on AC. Thus, it would enable the DC charging of EV from DC power of PV as shown in Fig.1.5. A single bidirectional DC/AC inverter can be used for both the PV and EV instead of two inverters required in the existing solution, as can be seen in Fig.1.4. Further, the new generation of silicon carbide power semiconductor devices can be used that enable higher switching and thereby higher power density. Such a high power converter would be challenging to design in terms of achieving high efficiency, high power density, bi-directional power flow and stable control. This thesis aims to overcome these challenges to realize such an integrated EV-PV charger. The development of the EV-PV charger was done in collaboration with the industrial partners Power Research Electronics (www.pr-electronics.nl) and Last Mile Solutions (www.lastmilesolutions.com)

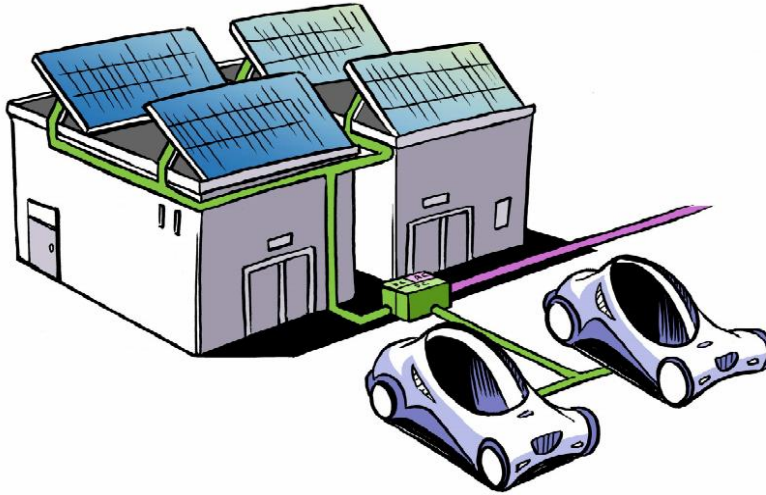


Fig.1.5. PV and EV interconnected on DC (green) and exchange power in AC (pink) with the AC grid only when there is power mismatch.

1.2.3. Smart charging algorithms

Smart charging is a method by which charging of EVs can be intelligently controlled and/or shifted so that one or several useful objectives can be achieved besides obtaining a fully charged EV battery. For example, if it is known from solar forecast data that it is going to be a cloudy morning followed by a sunny afternoon, smart charging can help schedule the EV charging in the afternoon rather than in the morning. Alternatively, the objective can be to reduce the cost of charging based on dynamic energy prices. Several smart charging algorithms for electric vehicles have been proposed that schedule the charging of an EV fleet based on inputs such as EV user preferences, energy prices, the offer of ancillary services or reactive power support [15], [30]–[34]. These algorithms have shown to significantly reduce the charging cost when compared to the uncontrolled charging of EVs.

However, the drawback with the current approach is that each of these parameters like EV user preferences, energy prices or forecast of renewable energy are considered as independent inputs and solved as separate optimization problems. This leads to several different EV charging profiles being obtained as a solution; one charging profile coming as a solution per set of inputs. This is impractical as a single EV cannot be controlled with different charging profiles at the same time. Secondly, the algorithms are not customized for a particular power electronic hardware as mentioned earlier, which makes it difficult to directly implement and use them on EV charging systems. Finally, most charging algorithms are not tested with actual EVs, and their compatibility with the EV charging standards is not verified.

Hence, it is vital to make a single problem formulation that bundles several applications together so that one optimal EV charging profile is obtained to control

the EV. This results in the addition of benefits from each application, making the net benefit large enough to encourage large-scale deployment of smart charging. In this thesis, a new set of smart charging algorithms is developed to optimally use the PV energy and reduce the cost of EV charging. The key feature is that it combines six applications into one formulation: EV user preferences, charging of EV from PV, vehicle-to-grid, energy prices from the market, multiplexing of several EVs to a single charger and offer of regulation services to the independent system operator (ISO). This results in large reduction in net costs, much higher than what has been achieved earlier. Further, the implementation of smart charging and V2G is tested using EVs compatible with CHAdeMO and CCS/Combo which are the two global standards for DC charging of EVs.

1.3. Research questions and outline of thesis

The three research elements above are formulated into seven chapters. The research questions that are answered in each chapter of the thesis can be seen below. Fig.1.6 shows the outline of the thesis and the interrelation between the chapters.

System level design

Chapter 2: Charging electric vehicles from solar energy: A Review

- *What are the advantages and drawbacks of the existing system for charging electric vehicles from photovoltaic systems?*
- *What is the best system architecture for an EV-PV charging system considering efficiency, bidirectionality, and modularity?*

The chapter reviews the current state of the art technology for charging electric vehicles from solar energy to investigate their advantages and drawbacks. Existing EV-PV systems are compared on the basis of system architecture, PV system, isolation, use of storage, bidirectionality and converter topology. Based on this, the system architecture, power rating of the system is chosen, and methods to make it modular are investigated.

Chapter 3: System design of the solar EV charging station

- *How does the EV charging requirements at workplace match with the energy yield of a PV system in the Netherlands?*
- *Can a solar tracking system and/or a local storage help mitigate the difference between PV supply and EV charging demand?*
- *How does the presence of employees in the workplace for 5 days and 7 days a week affect the system design?*
- *How can multiple EVs be connected to a single EV-PV charger for sharing of the charging infrastructure?*
- *What are the economic and CO₂ emission benefits of solar charging of EV at the workplace?*

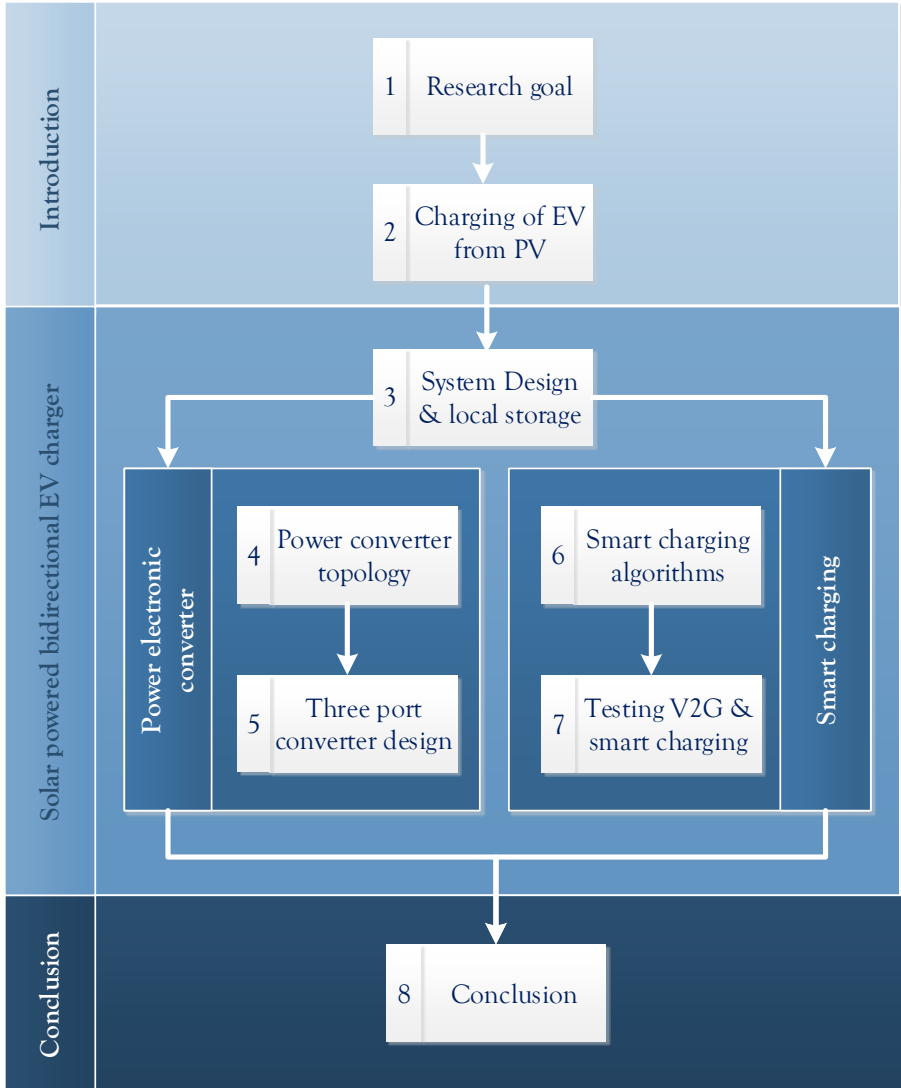


Fig.1.6. Outline of thesis chapters and interrelations

Based on the review presented in chapter 2, chapter 3 examines the optimal system design of the PV system and local storage for charging of electric vehicles at workplaces. The design is done for the Netherlands based on Dutch meteorological data. The EV charging requirements and influence of employees working five or seven days/week on the system design are explored as well. Further, the possible economic and CO₂ emission benefits of using the developed EV-PV charging station is estimated and compared with respect to fossil fuel powered cars and grid charged electric cars.

Power converter design

Chapter 4: Topology for three-port EV-PV-Grid converter

- *How is the power converter design influenced by the requirements of the EV charging and PV system standards?*
- *Which power converter topology is suitable for bidirectional charging of EV?*
- *Which power converter topology will result in high peak and partial load efficiency and high power density when charging EV from PV and grid?*

The chapter compares several system architectures and power converter topologies for the EV-PV charging system using detailed modeling. The use of silicon carbide (SiC) and power alloy inductors is considered in order to increase the converter efficiency and power density. The best topology is chosen based on multiple criteria such as efficiency, the number of components, controllability, power density and efficiency improvements.

Chapter 5: Development of 10kW bidirectional solar EV charger

- *How can SiC devices, interleaving, and power alloy cores be used to achieve high efficiency and power density power conversion?*
- *What is the stable closed loop control required for implementing four power flows: PV →EV, EV →Grid, Grid →EV and PV →Grid?*

Chapter 5 explains how the best topology chosen from chapter 4 is designed in detail and developed as a prototype. With the aim of building a commercial prototype, efficiency, volume and cost are considered in the converter development. Three independent closed loop controls are developed for each of the three ports. The developed prototype is tested both in the lab and using a CHAdeMO compatible Nissan Leaf EV.

Smart charging algorithms

Chapter 6: Energy management system for smart charging of EVs

- *What is the drawback with currently existing smart charging algorithms and how can it be overcome?*
- *How can EV smart charging, based on the solar forecast, energy prices, multiplexing, ancillary services, EV user and V2G, be formulated in a single charging algorithm?*

- *How much does the net cost of EV charging from PV reduce by using charging algorithms that combine solar forecast, energy prices, regulation services and V2G?*

The chapter studies the use of smart EV charging algorithms to reduce the cost of charging EVs using the developed EV-PV converter. Mixed integer linear programming (MILP) is used to formulate an integrated algorithm for smart charging based on the solar forecast, energy prices, multiplexing, ancillary services, EV user and V2G. The reduction in the net cost of the EV-PV system is estimated for the developed algorithm and compared with uncontrolled, average rate, randomly delayed charging and with smart charging based one or few of the applications mentioned above.

Chapter 7: Implementation of smart charging and V2G

- *What are the differences in the implementation of smart charging and V2G between CHAdeMO and CCS/COMBO DC charging standard and which is more suitable?*

This chapter compares the CHAdeMO and CCS/COMBO charging standards in their implementation of smart charging and vehicle to grid and brings out its influence on the charging system design, response time, flexibility in charging from renewable sources and buffer capacity required. Two CHAdeMO and CCS compatible EVs are experimentally tested with the implementation of smart charging and V2G, and the corresponding results are analyzed.

Conclusion and Appendices

Chapter 8: Conclusions

Chapter 8 concludes the key results obtained from the thesis with respect to system-level design, power converter development and use of smart charging algorithms. Recommendations are provided for future research directions.

Appendix A: GHG of gasoline, HEV, PHEV, and PEV

This appendix lists the assumptions for the estimation of GHG emissions for different types cars, based on data from the US Department of Energy.

Appendix B: Economic and CO₂ Emission Benefits of Solar Charging of EVs

This appendix provides the economic, tax and carbon-dioxide emission benefits of using the developed EV-PV charging station to charge electric cars and compared with respect to the use of fossil fuel powered cars and grid-charged electric cars.

Appendix C: Estimation of ripple and inductance of powdered alloy core inductors

This appendix provides the mathematical model for estimation of inductance variation and non-linear currents in powdered alloy inductors that are extensively used for the power converters presented in chapter 5.

Appendix D: Datasheet and brochure of 10kW EV-PV power converter

The appendix provides the datasheet and brochure of the developed 10kW solar powered bidirectional EV charger. It presents results from the collaboration with the Industrial Design faculty of TU Delft where the physical design of the EV-PV charging station was developed considering aesthetics, ergonomics, user comfort and safety.

1.4. Research publications

The list of publications relevant to this thesis and corresponding chapters that are based on it:

Journal publications

1. G. R. Chandra Mouli, P. Bauer, and M. Zeman, "System design for a solar powered electric vehicle charging station for workplaces," *Appl. Energy*, vol. 168, pp. 434-443, 2016 (*Chapter 3*)
2. G.R. Chandra Mouli, J. Schijffelen, P. Bauer, and M. Zeman, "Design and Comparison of a 10kW Interleaved Boost Converter for PV Application Using Si and SiC Devices," *IEEE J. Emerg. Sel. Top. Power Electron.*, vol. 5, issue 2, pp. 610-623, 2016 (*Chapter 5*)
3. D. van der Meer, G. R. Chandra Mouli, G. Morales-Espana, L. Ramirez Elizondo, and P. Bauer, "Energy Management System with PV Power Forecast to Optimally Charge EVs at the Workplace," *IEEE Transactions on Industrial Informatics*, vol. 14, issue 1, pp. 311-320, 2018 (*Chapter 6*)
4. G. R. Chandra Mouli, R. Baldick, M.Kefayati, and P. Bauer, "Integrated PV Charging of EV Fleet Based on Dynamic Prices, V2G and Offer of Reserves", *IEEE Transactions on Smart Grids*, 2017, pp. 1-13 (*Chapter 6*)

Journal publications (Under review at the time of thesis publication)

1. A. Bassa, G. R. Chandra Mouli and P. Bauer, "Evaluation of Topologies for a Solar Powered Bidirectional Electric Vehicle Charger", *IET power electronics*, under review (*Chapter 4*)
2. G. R. Chandra Mouli, J. Schijffelen, M.v.d Heuvel, M.Kardolus, P. Bauer, and M. Zeman, "A 10kW Solar-Powered Bidirectional EV Charger Compatible with Chademo and COMBO", *IEEE Transactions on Power Electronics*, under review (*Chapter 5*)

Conference publications

1. G. R. Chandra Mouli, P. Bauer, and M. Zeman, "Comparison of system architecture and converter topology for a solar powered electric vehicle charging station," in *9th International Conference on Power Electronics and ECCE Asia (ICPE-ECCE Asia)*, 2015, pp. 1908-1915 (*Chapter 2*)

2. G. R. Chandra Mouli, J. Kaptein, P. Bauer, and M. Zeman, "Implementation of dynamic charging and V2G using CHAdeMO and CCS/Combo DC charging standard," in IEEE Transportation Electrification Conference and Expo (ITEC), 2016, pp. 1–6 (*Chapter 7*)
3. G. R. Chandra Mouli, M. Leendertse, V. Prasanth, P. Bauer, S. Silvester, S. van de Geer, and M. Zeman, "Economic and CO₂ Emission Benefits of a Solar Powered Electric Vehicle Charging Station for Workplaces in the Netherlands," in IEEE Transportation Electrification Conference and Expo (ITEC), 2016, pp. 1–7 (*Appendix B*)
4. G. R. Chandra Mouli, J. Schijffelen, P. Bauer, and M. Zeman, "Estimation of ripple and inductance roll off when using powdered iron core inductors," in Power Conversion and Intelligent Motion (PCIM) Europe 2016 (*Appendix C*)
5. G.R. Chandra Mouli, D. van der Meer, P. Bauer, M. Zeman, J. Schijffelen, M. van den Heuvel and M. Kardolus, "Charging Electric Vehicles from Solar Energy: Integrated Converter and Charging Algorithms", Energy Open symposium, 2017

1.5. References

- [1] M. Messagie, F. S. Boureima, T. Coosemans, C. Macharis, and J. Van Mierlo, "A range-based vehicle life cycle assessment incorporating variability in the environmental assessment of different vehicle technologies and fuels," *Energies*, vol. 7, no. 3, pp. 1467–1482, 2014.
- [2] A. Nordelöf, M. Messagie, A. M. Tillman, M. Ljunggren Söderman, and J. Van Mierlo, "Environmental impacts of hybrid, plug-in hybrid, and battery electric vehicles—what can we learn from life cycle assessment?," *International Journal of Life Cycle Assessment*, vol. 19, no. 11, pp. 1866–1890, 2014.
- [3] S. Rangaraju, L. De Vroey, M. Messagie, J. Mertens, and J. Van Mierlo, "Impacts of electricity mix, charging profile, and driving behavior on the emissions performance of battery electric vehicles: A Belgian case study," *Appl. Energy*, vol. 148, pp. 496–505, 2015.
- [4] "Photovoltaic (PV) Pricing Trends: Historical, Recent, and Near-Term Projections," *Natl. Renew. Energy Lab. Lawrence Berkeley Natl. Lab.*, pp. 1–30, 2012.
- [5] P. Denholm, M. Kuss, and R. M. Margolis, "Co-benefits of large scale plug-in hybrid electric vehicle and solar PV deployment," *J. Power Sources*, vol. 236, pp. 350–356, 2013.
- [6] D. P. Birnie, "Solar-to-vehicle (S2V) systems for powering commuters of the future," *J. Power Sources*, vol. 186, no. 2, pp. 539–542, Jan. 2009.
- [7] X. Li, L. A. C. Lopes, and S. S. Williamson, "On the suitability of plug-in hybrid electric vehicle (PHEV) charging infrastructures based on wind and solar energy," in *2009 IEEE Power & Energy Society General Meeting*, 2009, pp. 1–8.
- [8] G. R. Chandra Mouli, P. Bauer, and M. Zeman, "Comparison of system architecture and converter topology for a solar powered electric vehicle charging station," in *2015 9th International Conference on Power Electronics and ECCE Asia (ICPE-ECCE Asia)*, 2015, pp. 1908–1915.
- [9] G. R. Chandra Mouli, P. Bauer, and M. Zeman, "System design for a solar powered electric vehicle charging station for workplaces," *Appl. Energy*, vol. 168, pp. 434–443, Apr. 2016.

- [10] G. Carli and S. S. Williamson, "Technical Considerations on Power Conversion for Electric and Plug-in Hybrid Electric Vehicle Battery Charging in Photovoltaic Installations," *IEEE Trans. Power Electron.*, vol. 28, no. 12, pp. 5784–5792, Dec. 2013.
- [11] P. Goli and W. Shireen, "PV powered smart charging station for PHEVs," *Renew. Energy*, vol. 66, pp. 280–287, Jun. 2014.
- [12] G. R. C. Mouli, M. Leendertse, V. Prasanth, P. Bauer, S. Silvester, S. van de Geer, and M. Zeman, "Economic and CO₂ Emission Benefits of a Solar Powered Electric Vehicle Charging Station for Workplaces in the Netherlands," in *2016 IEEE Transportation Electrification Conference and Expo (ITEC)*, 2016, pp. 1–7.
- [13] P. J. Tulpule, V. Marano, S. Yurkovich, and G. Rizzoni, "Economic and environmental impacts of a PV powered workplace parking garage charging station," *Appl. Energy*, vol. 108, pp. 323–332, Aug. 2013.
- [14] M. Brenna, A. Dolara, F. Foadelli, S. Leva, and M. Longo, "Urban Scale Photovoltaic Charging Stations for Electric Vehicles," *IEEE Trans. Sustain. Energy*, vol. 5, no. 4, pp. 1234–1241, Oct. 2014.
- [15] M. van der Kam and W. van Sark, "Smart charging of electric vehicles with photovoltaic power and vehicle-to-grid technology in a microgrid; a case study," *Appl. Energy*, vol. 152, pp. 20–30, Aug. 2015.
- [16] P. Kadar and A. Varga, "PhotoVoltaic EV charge station," in *2013 IEEE 11th International Symposium on Applied Machine Intelligence and Informatics (SAMII)*, 2013, pp. 57–60.
- [17] P.-E. Dziadek, W. Feucht, A. Mittnacht, H.-G. Kula, and H. Frank, "Eco-friendly application of EVs for home-to-work and home-to-education transports," in *2013 IEEE International Conference on Industrial Technology (ICIT)*, 2013, pp. 705–709.
- [18] N. Kawamura and M. Muta, "Development of solar charging system for plug-in hybrid electric vehicles and electric vehicles," in *2012 International Conference on Renewable Energy Research and Applications (ICRERA)*, 2012, pp. 1–5.
- [19] Y. Gurkaynak and A. Khaligh, "Control and Power Management of a Grid Connected Residential Photovoltaic System with Plug-in Hybrid Electric Vehicle (PHEV) Load," in *2009 Twenty-Fourth Annual IEEE Applied Power Electronics Conference and Exposition*, 2009, pp. 2086–2091.
- [20] Y. Gurkaynak and A. Khaligh, "A novel grid-tied, solar powered residential home with plug-in hybrid electric vehicle (PHEV) loads," in *2009 IEEE Vehicle Power and Propulsion Conference*, 2009, pp. 813–816.
- [21] D. M. Robalino, G. Kumar, L. O. Uzoechi, U. C. Chukwu, and S. M. Mahajan, "Design of a docking station for solar charged electric and fuel cell vehicles," in *2009 International Conference on Clean Electrical Power*, 2009, pp. 655–660.
- [22] M. Tesfaye and C. C. Castello, "Minimization of impact from electric vehicle supply equipment to the electric grid using a dynamically controlled battery bank for peak load shaving," in *2013 IEEE PES Innovative Smart Grid Technologies Conference (ISGT)*, 2013, pp. 1–6.
- [23] S. Mesentean, W. Feucht, H.-G. Kula, and H. Frank, "Smart charging of electric scooters for home to work and home to education transports from grid connected photovoltaic-systems," in *2010 IEEE International Energy Conference*, 2010, pp. 73–78.
- [24] J. G. J. G. Ingersoll and C. A. Perkins, "The 2.1 kW photovoltaic electric vehicle charging station in the city of Santa Monica, California," in *Conference Record of the IEEE Photovoltaic Specialists Conference*, 1996, pp. 1509–1512.
- [25] University of Iowa, *Solar electric vehicle charging station*. University of Iowa.
- [26] Oak Ridge National Laboratory, *Solar-Assisted Electric Vehicle Charging Stations*. 2011.

-
- [27] M. Alonso Abella, M. A. F. ChenloAbella, and F. Chenlo, "Photovoltaic charging station for electrical vehicles," in *Proceedings of 3rd World Conference on Photovoltaic Energy Conversion*, 2003, vol. 3, pp. 2280–2283.
- [28] W. Kempton, V. Udo, K. Huber, K. Komara, and S. Letendre, "A test of vehicle-to-grid (V2G) for energy storage and frequency regulation in the PJM system," pp. 1–32, 2008.
- [29] W. Kempton and J. Tomić, "Vehicle-to-grid power implementation: From stabilizing the grid to supporting large-scale renewable energy," *J. Power Sources*, vol. 144, no. 1, pp. 280–294, 2005.
- [30] T. Ma and O. A. Mohammed, "Optimal Charging of Plug-in Electric Vehicles for a Car-Park Infrastructure," *IEEE Trans. Ind. Appl.*, vol. 50, no. 4, pp. 2323–2330, Jul. 2014.
- [31] T. Ma and O. Mohammed, "Economic analysis of real-time large scale PEVs network power flow control algorithm with the consideration of V2G services," in *2013 IEEE Industry Applications Society Annual Meeting*, 2013, pp. 1–8.
- [32] M. Kefayati and C. Caramanis, "Efficient Energy Delivery Management for PHEVs," in *2010 First IEEE International Conference on Smart Grid Communications*, 2010, pp. 525–530.
- [33] M. Kefayati and R. Baldick, "Energy Delivery Transaction Pricing for flexible electrical loads," in *2011 IEEE International Conference on Smart Grid Communications (SmartGridComm)*, 2011, pp. 363–368.
- [34] Y.-M. Wi, J.-U. Lee, and S.-K. Joo, "Electric vehicle charging method for smart homes/buildings with a photovoltaic system," *IEEE Trans. Consum. Electron.*, vol. 59, no. 2, pp. 323–328, May 2013.

2

Charging electric vehicles from solar energy: A Review

2. Charging electric vehicles from solar energy: A Review

This chapter is based on:

G. R. Chandra Mouli, P. Bauer, and M. Zeman, "Comparison of system architecture and converter topology for a solar powered electric vehicle charging station," *9th International Conference on Power Electronics and ECCE Asia (ICPE-ECCE Asia)*, pp. 1908–1915, 2015

Summary

Electric vehicles (EV) can be charged in a sustainable way by charging them from photovoltaic (PV) panels. In order to build a solar-powered EV charging infrastructure, it is important first to make a literature review of existing EV-PV systems developed by academia and industry. In this chapter, the current state of the art technology for charging electric vehicles from solar energy is reviewed to investigate their advantages and drawbacks. This is used as a first step for making qualitative decisions on the system architecture, power converter topology, implementation of modularity and the EV charging standard that is adopted for this thesis.

Outline

Section 2.1 evaluates the EV charging systems used globally with respect to charging standards, power levels, type, and mode. Section 2.2 gives an overview of the status of PV generation around the world. In section 2.3, the environmental and economic benefits of PV charging of EV are highlighted and the suitable EV charging system for PV is chosen. Subsequently, the different possible system architecture for an EV-PV charger and the power flows are described in section 2.4 and 2.5, respectively. Section 2.6 compares the system architecture qualitatively, and the system architecture for the EV-PV charger is chosen.

A review of power converters that integrate EV and PV is made in section 2.7, and the systems are reviewed based on system architecture, converter topology, isolation and bi-directional power capability for V2G operation. Finally, Section 2.8 elucidates the choice of 10kW nominal rating for the power converter and describes the two types of multiport converters for the EV-PV charger – one based on a high-frequency three-winding transformer and the second based on a central DC-link.

2.1. EV charging

Charging of electric vehicles (EV) can be done today with AC or DC charging [1], [2]. In both methods, the power from the grid is converted from AC to DC and is used to recharge the battery inside the vehicle. The electric vehicle battery is typically a few kWh in the case of an HEV and PHEV and is tens of kWh in the case of PEV. A few examples are HEV: Toyota Prius with 1.3kWh battery; PHEV: BMW i8 PHEV with 7.1kWh battery and PEV: Tesla Model S with 85kWh battery.

The DC charging power P_{ch} is fed in terms of a charging current I_{ev} to charge the batteries with a voltage, V_{ev} :

$$P_{ch} = V_{ev}I_{ev} \quad (1)$$

The energy delivered to the battery E_{ch} over a time period t_{ch}

$$E_{ch} = \int_0^{t_{ch}} P_{ch} dt \quad (2)$$

2.1.1. AC charging of EV

AC charging of EV is done using the onboard AC/DC power converter of the EV using a single phase or three phase AC connection. Currently, there exist three types of AC charging systems used globally [3]–[6] as shown in Fig. 2.1 and Table 2.1:

1. Type1, single phase charger used in the USA (SAE J1772-2009)
2. Type 2 Mennekes, single and three phase charger used in Europe (VDE-AR-E 2623-2-2)
3. Type 3, single phase and three phase charger from the EV plug alliance
4. Tesla dual charger for single phase AC and DC used in the USA

Due to space and weight restrictions on the EV, AC charging is limited to Level 2 charging power levels of up to 43kW (Three-phase 400V, 63A). In the US, the Type 1 plug provides for single-phase charging using three power pins – namely phase (L1), neutral (N) and earth pin (E). The Type 2 plugs used widely in Europe supports three-phase charging using five power pins - three phase pins (L1,L2,L3), neutral (N) and earth pin (E).

The IEC61851-1 standard defines charging mode for AC charging namely Mode 1, Mode 2 and Mode 3. In the case of Mode 1 and mode 2, the charging power is derived from a standard non-dedicated power socket, and mode 2 has an additional in-cable protection device built into it. Mode 3 makes use of a dedicated electric vehicle supply equipment (EVSE) where the EVSE has both control and protection functionality built into it. This is the preferred charging mode for public charging stations and for residential charging at high powers.

2.1.2. DC charging of EV

For high power charging of EV beyond 50kW, DC charging is used. DC charging comes under Mode 4 charging as defined in IEC 61851-1, where a dedicated off-board AC/DC converter supplies DC power directly to the EV's battery. Since off-board



Fig. 2.1. Plug for AC charging- US Type 1 SAE (left), European Type 2 Mennekes (middle) and Tesla plug (right). Image courtesy: Mennekes, Michael Hicks on Wikipedia, insideevs.com



Fig. 2.2. Plug for DC charging - CCS/Combo charger for US (left), European (right) . and CHAdeMO plug (bottom). Image courtesy: SAE, CHAdeMO

chargers are unrestricted by space and weight constraints of onboard chargers, they can go up to Level 3 charging power levels of 350kW, as shown in Table 2.1. Currently, there exist three types of DC charging systems used globally [4]-[7] as shown in Fig. 2.2 and Table 2.1:

1. CCS/COMBO (Combined Charging System, Combo 1 and Combo 2)
2. Type 4 CHAdeMO
3. Tesla dual charger for single phase AC and DC used in USA and Tesla Type 2 plug used for DC charging in Europe

The three systems use three power pins for transferring the power namely - two DC power pins DC+, DC- and one earth pin (E). They differ however in the communication and control protocol used. For example, CHAdeMO uses CAN bus communication and uses a total of 7 pins for control and communication while CCS uses Power Line Carrier communication (PLC) and 2 communication pins. It is important to note that both Type 1 and 2 AC charging and type 4 DC charging via CCS uses the same physical pin for communication and control.

The charging system of Tesla is unique in the respect that it uses the same two power pins for both single phase AC and DC and two communication pins. The Tesla coupler and interface are designed in such a way that the EV can be charged

Table 2.1. AC and DC Charging plugs, power levels in Europe, Japan and USA

Plug	Number of pins (Communication)	Charging level	Voltage, current, Power
Type 1 SAE J1772 USA/Japan	3 power pins - L1,N,E 2 control pins - CP, PP (PWM over CP)	AC Level 1	1 Φ 120V, \leq 16A, 1.9 kW
		AC Level 2	1 Φ 240V, \leq 80A, 19.2kW
Type 2 Mennekes Europe	4 power pins - L1,L2,L3,N,E 2 control pins - CP, PP (PWM over CP)	AC Level 1	1 Φ 230V, \leq 32A, 7.4kW
		AC Level 2	3 Φ 400V, \leq 63A,43kW
Type 4 CHAdEMO	3 power - DC+,DC-,E 7 control pins (CAN comm.)	DC Level 3	200-500V, \leq 400A, 200kW
SAE CCS/ Combo	3 power pins -DC+,DC-,E 2 control pins - CP, PP (PLC over CP, PE)	DC Level 3	200 -1000V \leq 200A, 200kW
Tesla US	3 power pins - DC+,DC-,E (or) L1,N,E 2 control pins - CP, PP	DC Level 2	Model S, 400V, \leq 300A, 120kW

using a Tesla charger (either AC or Supercharger) or using an adapter from a Type 1 SAE J1772 charger or a CHAdEMO charger.

A key benefit of DC charging is that the charger can be made bidirectional for implementing vehicle-to-everything (V2X) [8], [9]. V2X is the general terminology that corresponds to discharging the EV to supply power to a home (V2H), building (V2B), load (V2L) or to a grid (V2G). Through V2X, the EV can be used for several new applications such as a storage for renewable energy, provide ancillary services to the grid like voltage and frequency regulation, or reduce the peak demand on the network. Currently, both CHAdEMO and CCS have communication protocols to facilitate bidirectional charging.

2.2. Solar photovoltaic (PV) systems

Solar photovoltaic (PV) systems have gained immense popularity over the last decade as a means of distributed generation. By the end of 2016, total installed capacity in the world reached 300GW with a record 75GW installed in 2016 alone [10]. This has been mainly driven by two reasons: the efficiency of PV systems has been steadily increasing, and at the same time the cost of PV systems has been drastically reducing over the years. Residential and commercial solar PV costs have more than halved over the last 7 years, and utility-scale solar projects have recently broken records for cheapest electricity ever [11], [12]. This had made solar energy not just an excellent source of clean electricity but an excellent source of cheap electricity as well.

At the same time, solar generation suffers from diurnal and seasonal variations, and this necessitates an energy storage, an expensive component by itself. Second, distribution system operators (DSO) around the world are expected to reduce the feed-in tariffs for solar over the next few years so as to match with wholesale electricity prices. This could drastically affect price economics of solar for grid-in and encourage self-use of solar energy like residential loads and EV charging. As mentioned in chapter 1, the solar generation potential of workplace rooftops and car parks is largely unexploited today. All this of these indicates the great potential of solar PV for charging of EVs [2].

2.3. Charging EV from PV

2.3.1. Sustainability and economics

There are two key benefits of charging electric vehicles from solar PV systems, namely, sustainability and economics. From a well-to-wheel, fuel usage and life cycle assessment perspective, charging electric vehicles from solar energy results in much higher energy efficiency, and much lower net emissions and environmental impact [13]-[15], (Refer to Appendix B). Secondly, due to the falling prices of PV system, solar PV electricity is already cheaper than conventional electricity in many parts of the world. Further, depending on the car segment, the total cost of ownership of an electric car is already lower than a comparable internal combustion engine car [16]. Finally, with the removal of net metering and possible reduction in feed-in tariffs in the future, charging EVs from PV increases PV self-consumption and ensures a return on investment for the PV system. All of these factors make solar charging of EV attractive from an environment, sustainability and cost perspective.

2.3.2. EV charging system for PV

As mentioned earlier, the charging system widely used in Europe for AC charging is based on the Type 2 Mennekes plug. It supports both single and three phase AC charging at Level 2 charging power level [2]. However, in the future, DC charging using CHAdeMO and the Combined Charging Standard (CCS) will be most preferred charging standard for charging EV from PV at the workplace. This is due to the following reasons:

1. Both EV and PV are inherently DC by nature
2. Smart charging of EV is possible, where the EV charging power can be varied with time.
3. DC charging facilitates V2G protocol

Hence, this thesis will concentrate on DC charging of EV. While DC charging is usually of higher power of the order of 50kW, the focus here is on low power DC charging. This is because, as mentioned earlier, cars are parked at the workplace for typically 8h every day. The long parking times means that the same energy can be delivered to the EV at a lower charging power. For example, 80kWh energy can be provided in 8h using the 10kW charger, which allows 666 km distance for a 2016

Nissan Leaf and 522 km distance for a Tesla Model S (Nissan Leaf NEDC¹ range of 200km with 24kWh battery, 2017 Tesla Model S 75D NEDC range of 490km with 75kWh battery). This is more than sufficient for the daily driving requirements for 6 to 10 employees.

2.4. System Architecture for the EV-PV System

To charge the EVs from solar energy, different possible system architectures can be used. In all the cases, the EV-PV charging system integrates the PV array, the electric vehicle supply equipment (EVSE) and the AC grid with the primary motive to charge the EVs directly from the PV power. Two different types of power converters can be used to integrate the PV, EV and the grid:

1. A single multi-port converter (MPC) that integrates the grid, PV, and EV.
2. Separate power converters for the grid, PV, and EV which are interlinked on a common interconnection.

The power converters themselves can be connected to each other either using an AC or DC interconnection. The interconnection between the converters is used to share the PV power amongst different EVs and exchange power between the EV and the grid. Using the two power converter types mentioned above, the system architecture can be of four types based on whether the interlinking bus is AC (1 Φ 230V 50Hz or 3 Φ 400V, 50Hz grid) or DC:

2.4.1. Architecture 1 - Separate converter for PV, EV interlinked on AC

Fig. 2.3(a) shows the schematic of Architecture 1. Separate converters are used for the PV panels and for the EV charging/discharging. The PV converter is a DC/AC inverter that incorporates maximum power point tracking (MPPT), and the EV charger is an AC/DC converter. The existing 50Hz AC grid is the backbone of the architecture, and all the power is passed via the grid. The disadvantage is that the PV power cannot be directly used in DC form to charge the EV. This results in the unnecessary conversion from DC to AC in PV inverter and back from AC to DC in the EV charger.

2.4.2. Architecture 2 - Separate converters for PV, EV interlinked on DC

Fig. 2.3(b) shows the schematic of Architecture 2, which uses a DC interconnection to connect the converters for the PV panels, EV, and the grid. The PV and EV converters are both DC/DC converters that have MPPT control and charge control respectively. The DC interconnection facilitates the direct use of the DC power of PV for DC charging of EV, which results in higher efficiency [17]-[19]. A central inverter connects the DC interconnection with the AC grid. The central inverter is vital for V2G operation and enables the feeding/drawing of the power due to the difference

¹ The New European Driving Cycle (NEDC) is a driving cycle designed to assess the emission levels and fuel economy of passenger vehicles. The US Environmental Protection Agency (EPA) driving cycle and the Worldwide harmonized Light vehicles Test Procedure (WLTP) are also used for the same purpose.

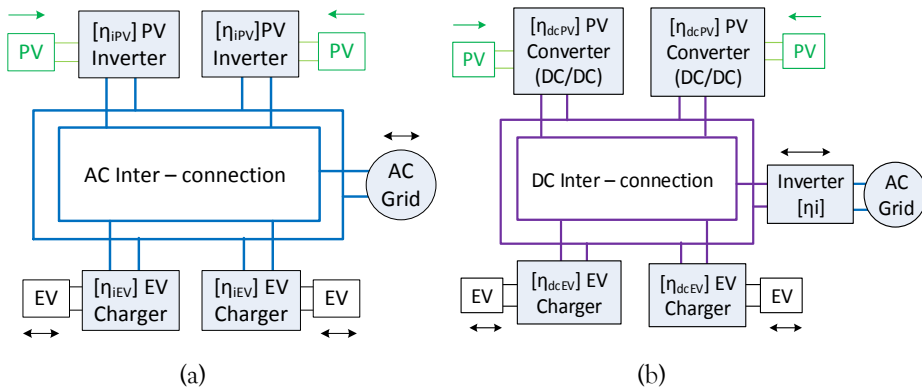


Fig. 2.3. (a) System Architecture 1 and (b) System Architecture 2 for the EV-PV charger

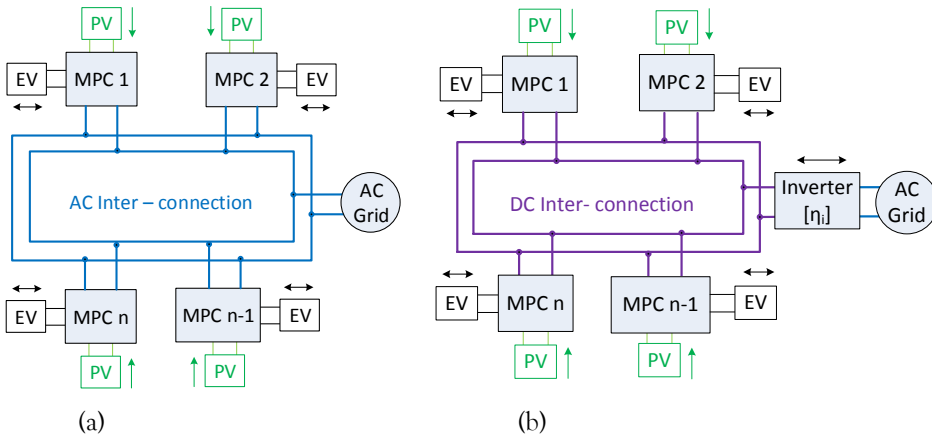


Fig. 2.4. (a) System Architecture 3 and (b) System Architecture 4 for the EV-PV charger using multiport converters

between PV generation and EV charging demand. Depending on the power rating of size of the DC interconnection and the number of sources and loads connected to it, the DC interconnection can be expanded to a DC micro-grid.

The disadvantage of Architecture 2 is that the DC interconnection has to be built separately, instead of making use of the existing AC grid infrastructure. The control and protection of the DC interconnection have to be implemented depending on the size, power handled and power variations that are possible.

2.4.3. Architecture 3 - Multiport converter for PV, EV, grid interlinked on AC

Fig. 2.4(a) shows the schematic of Architecture 3 which uses a multi-port converter (MPC) as shown in Fig. 2.5(a). The multi-port converter connects the converter for the PV array, the EV and the AC grid using a central DC-link. Multiple MPC are connected to each other via the AC grid. Integration of power electronic converters

for PV, EV, and grid into one MPC leads to higher power density, lower component count, cost reduction and ease of control [20], [21]. Control of EV charging from PV can be achieved through the controller of the MPC while in the previous two architecture, communication has to be established between the separate PV and EV converters. The only disadvantage is that the DC PV power from one MPC cannot be used to charge the EV of another MPC without conversion to AC.

2.4.4. Architecture 4 - Multiport converter for PV, EV, grid interlinked on DC

Fig. 2.4(b) shows the schematic of Architecture 4 which is a combination of Architecture 2 and 3. It uses a multi-port converter as shown in Fig. 2.5(b) to integrate the converters for the PV array and EV. Many MPCs are interconnected to each other using a DC interconnection. A high power, central inverter is used to connect to the AC grid. This central inverter is better than using several small inverters embedded within the MPC as in architecture 3. Similar to Architecture 2, the DC interconnection can be expanded to a DC micro-grid depending on the power

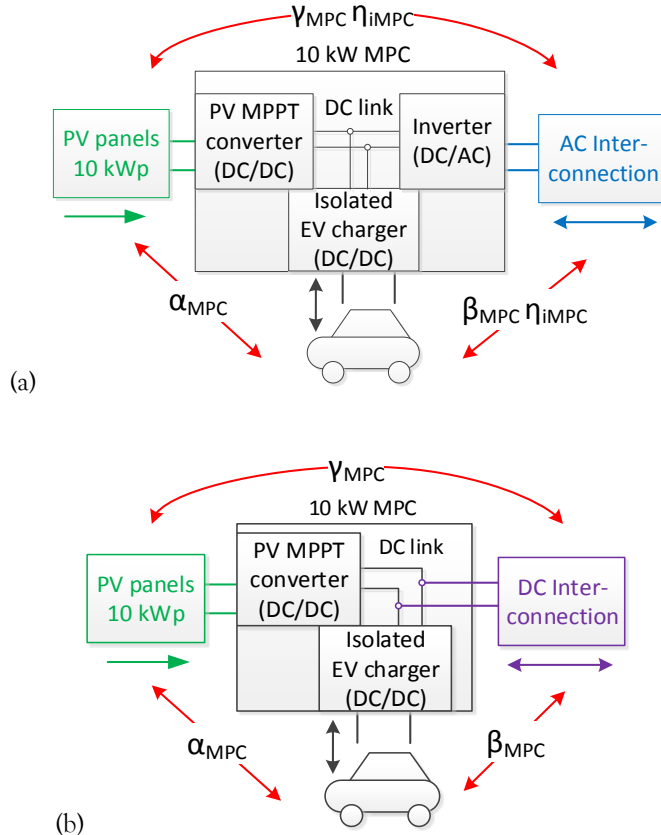


Fig. 2.5. Block diagram of multi-port converter for (a) Architecture 3, (b) Architecture 4. The efficiency variables are explained in section 2.4.

handled and other sources and loads that are connected.

2.5. EV-PV power flows

There are four possible power flows in an EV-PV charging system when using multiport or separate converters, named as *EVPV Mode 1 to 4* as shown in Fig. 2.6 and Table 2.2.

- **EVPV Mode 1** – EVPV Mode 1 is the direct use of PV power for EV charging; which is the main objective of the charging system. Mode 1a is a special case of Mode 1 charging which is applicable for architectures 3 and 4 that uses an MPC. Mode 1a corresponded to the power exchange from the PV panel connected to one EV-PV MPC to the EV connected to another EV-PV MPC. This could occur in the case of a workplace where EVs are not connected to all EV-PV chargers.
- **EVPV Mode 2** – EVPV Mode 2 corresponds to the power flow from the grid to the EV for EV charging. Mode 2 is used when solar generation is insufficient to meet the EV charging requirements.
- **EVPV Mode 3** – EVPV Mode 3 is the power exchange from EV to grid for V2G.
- **EVPV Mode 4** – EVPV Mode 4 is used for feeding the PV power directly to the grid. This mode is enabled under the condition that there is no EV for charging or the EV battery is full.

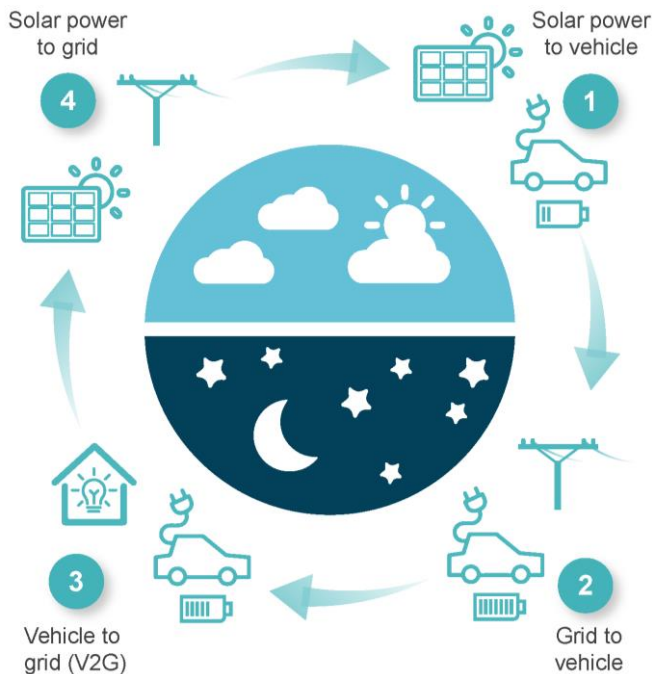


Fig. 2.6. Four possible power flow mode in an EV-PV system: Mode 1: PV→EV, Mode 2: Grid→EV, Mode 3: EV→Grid and Mode 4: PV→Grid

The efficiency of power flows for all the modes for the four system architectures is shown in Table 2.2 and indicated in Fig. 2.3, Fig. 2.4 and Fig. 2.5 where:

α_{MPC} - Efficiency of power conversion between PV and EV in MPC [Arch. 3,4]

β_{MPC} - Efficiency of EV charger in MPC [Arch. 3,4]

γ_{MPC} - Efficiency of PV converter in MPC [Arch. 3,4]

η_{iMPC} - Efficiency of inverter present in MPC [Arch. 3]

η_{dcPV} - Efficiency of DC/DC converter for PV [Arch. 2]

η_{dcEV} - Efficiency of DC/DC converter for EV [Arch. 2]

η_{iPV} - Efficiency of DC/AC inverter for PV [Arch. 1]

η_{iEV} - Efficiency of DC/AC inverter for EV [Arch. 1]

η_i - Efficiency of central inverter [Arch. 2,4]

In comparing the architectures 1 and 2 as per Table 2.2, it can be observed that $\eta_{iPV} < \eta_{dcPV}$ and $\eta_{iEV} < \eta_{dcEV}$ due to lack of power conversion from DC to AC when power flows PV to EV for mode 1. However, η_{iEV} will be approximately the same as $(\eta_{dcEV} \eta_i)$, i.e., $\eta_{iEV} \approx \eta_{dcEV} \eta_i$ for mode 2,3,4 if similar power converter topology is used for the AC EV charger in architecture 1 as compared to the combination of grid inverter and DC EV charger as used in architecture 1. So the gains in efficiency due to direct DC power consumption for architecture 2 are restricted solely to mode 1, with the need to develop and control the DC interconnection.

In contrast, architecture 3 provides the benefit of higher conversion efficiency for mode 1 without the use of a DC interconnection as $\alpha_{MPC} \approx (\eta_{dcPV} \eta_{dcEV})$ and $\alpha_{MPC} > \eta_{iEV} \eta_{iPV}$. This makes architecture 3 more suitable than both 1 and 2. For architecture 3 and 4, $(\gamma_{MPC} \beta_{MPC}) \approx \alpha_{MPC}$. With the advent of future DC (micro) grids [22], architecture 4 will be more attractive than 3 due to improved efficiency of energy exchange between EV and PV of multiple EV-PV chargers in the neighborhood. It must be noted that the ohmic losses in conductors are neglected here in the comparison as the physical location of PV and EV will be the same irrespective of the type of architecture used. What will differ is the location of the converters.

2.6. Comparison of system architectures

Table 2.3 provides a qualitative comparison of the four system architectures. Those marked in red and green indicate the disadvantages and advantages of that architecture respectively. The direct DC charging of EV from PV without the conversion to AC results reduces the number of conversion steps and the associated losses. This is a major advantage of Architecture 2,3,4 over 1. The use of an MPC results in the use of a single inverter for both the EV and PV, either within the MPC (Architecture 3) or for the entire DC interconnection (Architecture 4). The common inverter leads to a lower component count, higher power density, and lower losses when compared to separate converters as in Architecture 1,2.

An added benefit of the MPC is the ease of controlling the individual EV, PV, grid converters within as against controlling separate power converters using a communication infrastructure. Finally, the DC interconnection of Architecture 2 and 4 does not make of the existing AC grid infrastructure. Hence, the construction of a

Table 2.2. Comparison of the conversion stages and efficiency for different EV-PV system architectures

Mode	Power Flow	Arch. 1	Arch. 2	Arch. 3	Arch. 4
1	PV power \rightarrow EV charging	η_{iPV} η_{iEV}	η_{dcPV} η_{dcEV}	α_{MPC}	α_{MPC}
1a	PV power \rightarrow EV charging (Between multiple EV-PV chargers)			$(\gamma_{MPC} \eta_{iMPC})$ $\eta_{iMPC} \beta_{MPC}) =$ $\alpha_{MPC} (\eta_{iMPC})^2$	$\gamma_{MPC} \beta_{MPC}$ $\approx \alpha_{MPC}$
2	Grid power \rightarrow EV charging	η_{iEV}	$\eta_{dcEV} \eta_i$	$\beta_{MPC} \eta_{iMPC}$	$\beta_{MPC} \eta_i$
3	EV power \rightarrow Grid charging	η_{iEV}	$\eta_{dcEV} \eta_i$	$\beta_{MPC} \eta_{iMPC}$	$\beta_{MPC} \eta_i$
4	PV power \rightarrow Grid charging	η_{iPV}	$\eta_{dcPV} \eta_i$	$\gamma_{MPC} \eta_{iMPC}$	$\gamma_{MPC} \eta_i$

Table 2.3. Qualitative comparison of the EV-PV system architectures. This thesis focusses on architecture 3.

	Architecture			
	1	2	3	4
Efficiency gain due to direct connection of DC power of EV and PV (with no AC conversion)	No	Yes	Yes	Yes
Possibility of directly using DC power of PV to charge EV between multiple EV-PV chargers	No	Yes	No	Yes
Higher power density, lower component count and cost reduction due to MPC	No	No	Yes	Yes
Ease of control of EV charging from PV with minimal communication infrastructure	No	No	Yes	Yes
Requires the construction of a DC interconnection along with the necessary protection and control	No	Yes	No	Yes

separate DC interconnection with its control and protection poses as a disadvantage for Architecture 2 and 4.

This thesis will focus on the use of an MPC based on Architecture 3. The main reason behind this choice is that it enables the direct DC charging of EV from PV and requires only a single inverter to the AC grid. Secondly, the use of an AC interconnection for power exchange between the chargers and with the grid makes the MPC usable with the existing AC grid infrastructure available globally. A detailed quantitative comparison of the architectures is, however, beyond the scope of this thesis.

2.7. Review of EV-PV Power Converter Topology

In this section, EV-PV chargers that have been published in earlier works are compared in Table 2.4 based on the system architecture, the power rating of EV and PV, isolation and bidirectional power flow capability of EV charger and power converter topology. To design a highly efficient EV-PV charger, it is vital to have minimum conversion stages between the PV panels and the EV. DC interconnection between PV and EV is one means to achieve this. Secondly, the EV charging standards [3], [4] necessitate isolation in the EV charger so that the EV is isolated from all sources of power for safety reasons. This means that the EV must be isolated from both the PV and the grid. Thirdly, the use of a bidirectional EV charger facilitates the implementation of V2G technology.

Table 2.4. Comparison of topology, system architecture and EV charger design from literature

Paper	System Arch.	[PV, EV] Power (kW)	EV Isolation	Bidirect. EV charging	Power converter topology & design
[23]	1	[2.1, 2.4]	-	-	Standard PV inverter of 93% efficiency used. Standard AC EV charger used.
[24]	1	[1, -]	-	-	EV bike charging with local storage.
[25]	1	[51.5, 3.5]	-	-	Standard AC EV charger and SMA Sunnyboy PV inverters are used.
[26]	1	[5.1, 7]	-	Yes	Modified industrial variable speed drive with a full-bridge topology used as bidirectional converter for EV (V2G possible).
[27]	1	[47, -]	-	-	Standard AC EV charger and PV inverters used.
[28]	1	[13, 2]	-	-	Boost converter for PV charges 70kWh local storage and 1-phase inverter feeds PV power to grid. Standard AC charger used for EV charging.
[29]	1	[8.2, 2]	-	-	Bidirectional DC/DC converter charges local storage from PV, and H-bridge inverter feeds PV power to the grid. Standard AC charger used for EV charging.
[30]	1	[9.2, -]	-	-	Grid connected inverters feed PV power to grid. Standard AC charger used for EV charging.
[31]	1	[3.6, <22]	-	No	PV inverters and standard AC EV chargers used. EV charging powers of 3.7kW, 7kW, 11kW and 22kW are compared and 3.7kW shows the maximum utilization of PV power for EV charging.
[17], [18]	2	[4x1.2, 2x4]	No	No	Direct DC charging of EV from PV. ZVT-PWM buck converter for PV and EV and separate 5kW inverter, an 8kW rectifier for the grid are all interlinked on 210V DC bus. Up to 5% improved efficiency compared to architecture 1.

Paper	System Arch.	[PV, EV] Power (kW)	EV Isolation	Bidirect. EV charging	Power converter topology & design
[32], [33]	2	[100, -]	-	-	Direct DC charging of EV from PV using common DC bus.
[34], [35]	2	[25, 10]	No	Yes	10kW DC/DC converter with zero voltage switching quasi square-wave (ZVS-QSW) switching at 98% efficiency used for EV charging. 575V central DC link interconnects PV and EV converters. The aim is mitigation of solar irradiance intermittency.
[36]	2	[100,430]	No	Yes	Single phase bidirectional DC/DC converters with no isolation are used for PV and EV to connect to a 480V DC grid. AC grid connected voltage source converter (VSC) ensures power balance and stability of the system.
[37]	2	[20,60]	No	Yes	
[38]	2	[65, 160/66]	No	No	DC grid of 350V is used to interface EV, PV, grid, fixed storage, wind and dump load. Bidirectional converter connected to fixed storage ensures power balance and voltage stability of DC-grid.
[39]	2	[-, 3]	Yes	Yes	3kW bidirectional contactless charger for EV. Isolation is inherently present due to the air core transformer used.
[40]	2	[9.8, 10]	No	-	Batteries/EV are directly connected on a common DC-link. Buck converter with MPPT connects PV to DC-link.
[41]	~2	[3.8, 3]	No	No	3.3kW direct DC charging of EV from PV at 70% efficiency. Charge controller charges 48V battery from PV. Boost converter connected to 48V battery is used for EV charging.
[42]	~2	[0.4, -]	No	-	Direct DC charging of EV from PV using boost converter. Bidirectional buck/boost converter controls power flow between EV battery and EV motor.
[43], [44]	3	[3.3, 3.3]	No	Yes	3.3kW direct DC charging of EV from PV. MPC with boost converter for PV, H-bridge inverter for grid and interleaved buck converter for EV interlinked on 380V DC link. 7% to 15% improved efficiency compared to architecture 1.
[45]	3	[5, 10]	Yes	Yes	Symmetrically isolated Z-source converter used for EV charging from PV. Comparison with transformer-less and high-frequency transformer isolated topologies for PV indicates that transformerless topology exhibits the highest efficiency of up to 97%.
[46]	3	[5, 6]	No	Yes	Quasi-Z-source inverter with 680V DC link and 3 Φ grid connection. 96kWh local storage integrated into EV-PV charger. 4 EV chargers can be active simultaneously.

Paper	System Arch.	[PV, EV] Power (kW)	EV Isolation	Bidirect. EV charging	Power converter topology & design
[47]	3	[2, 2]	No	Yes	Quasi-Z-source inverter with 350V DC link and 3 Φ grid connection. Converter designed for battery charging (and not for EV).
[48], [49]	3	[5.5, 4.5]	No	No	MPC made of Boost converter for PV, 1-phase H-bridge inverter for grid and buck converter for EV interlinked on 400V DC link.
[50]	~3	[, 10]	No	Yes	Z-source converter for charging EV from PV. 3 Φ bidirectional inverter connects EV to the grid.
[21]	4	-	No	Yes	Three port converter for PV, battery, and load. The load is isolated. Designed for battery charging application (Not specifically for EV).
[20]	4	-	No	Yes	Four-port converter for PV, battery, wind, and load. The load is isolated. Designed for battery charging application (Not specifically for EV).
[51]	4	-	Yes	Yes	Three port isolated DC-DC-DC converter using a high-frequency AC transformer link.
[19]	1,3	[20, 3]	-	-	Direct charging of EV from PV DC/DC converter at 90% efficiency. No converter for PV; DC-AC-DC charging results in 40% losses.
[52]	~1, 3	[1.9, 3.2]	-	-	MPC with isolation for integrating local storage, PV, and grid. EV charged from AC grid using AC charging stand.
[53]	1, 2	-	Yes	-	Contactless charging of EV from PV. Isolation is inherently provided by the air core transformer of the inductive power transfer (IPT) system.

It can be seen from Table 2.4 that research work in EV-PV chargers have been focused on all four different system architectures. For architecture 1, the use of standard commercially available AC EV chargers and PV inverters is common. Many publically available PV powered EV charging station like [25], [27] are based on this simple architecture. Architecture 4 has been the least explored, most reasonably because of its use of a futuristic DC grid. [20], [21] which use a PV system to charge batteries is indirectly based on the use of architecture 4. The DC load port of the converter in [20], [21] can be connected to a central DC-grid, and an isolated DC converter can be used for the battery charger to enable it for EV charging. Buck and boost converters (with no isolation) are most commonly used topology for the PV converter and EV charger.

An important observation is that the isolation requirements for the EV has been neglected or not addressed in almost all research works except [39], [45], [53]. This means that these designs are not suited for real-world charging applications due to lack of isolation. In the case of [39], [53], the isolation indirectly stems from the use of

an air-core transformer for the contactless charging of the EV. Secondly, only [39], [45], have implemented an EV charger with both isolation and bidirectional operation. It is hence the aim of this thesis to develop a high power EV-PV charger that is both isolated and bidirectional and can enable direct DC charging of EV from PV.

2.8. Nominal rating and topology for the EV-PV Charger

2.8.1. 10kW Nominal rating

A 10kW EV-PV charger will be considered in this thesis that provides both charging and discharging of the EV for up to 10kW. This is in line with the CHAdeMO standard for enabling 10kW V2G from EV. Second, commercial fast chargers of >50kW typically use 10kW modular converters operated in parallel for increasing the power output. Third, since the cars are parked for long durations of 7h-9h at the workplace, fast charging of EV at 50kW or more would be unnecessary. Finally, the semiconductor currents are in the range of 10-35A at around 10kW power at the PV, EV, grid ports. This is close to the upper nominal current limit of mass-produced semiconductor switches, enabling low-cost sourcing of converter components. In the case of the PV system, a 10kW_p array will be required that typically consists of 30 to 50 panels depending on the rating of the panel and occupies a panel area of about 70m^2 . For 10kW power, the EV-PV charger will use a 3ph. 400V, 16A connection that can supply up to 11kVA

2.8.2. Multi-port converter for the EV-PV Charger

There are two possible multi-port converter that can be used for the EV-PV charging based on Architecture 3. These are shown in Fig. 2.7(a)-(b) as MPC A and MPC B. The main difference between the two MPC is whether the PV panels are isolated from the grid or not. They both use a central DC-link within the converter to exchange power between the three ports. The DC link must be rated above the peak voltage of the three-phase grid, i.e., $> 400\sqrt{2}$.

In MPC A in Fig. 2.7(a), a central DC link within the MPC interconnects the converters for EV, PV array and the grid, similar to that shown in Fig. 2.5(a). A non-isolated DC/DC converter is used for the MPPT of the PV array. A high-frequency (>20kHz) isolated DC/DC converter is used for the EV charging. The use of a high-frequency isolation is better than using a 50Hz isolation transformer on the AC grid side, due to the drastic reduction in the transformer size and cost that can be achieved. Due to the lack of isolation for the PV, it is important that the PV leakage currents are within the limits as set by the standards (IEC 61727).

In MPC B shown in Fig. 2.7(b), a three-winding high-frequency transformer is used to integrate the 10kW converters for the EV, PV, and grid [51]. The advantage is that the design provides isolation between all three ports and which prevents the problem of leakage currents. At the same time, the drawback of this MPC is three-fold when compared to MPC A. Firstly, the power flow path from PV to the grid has three conversion stages, $\text{DC} \rightarrow \text{AC} \rightarrow \text{DC} \rightarrow \text{AC}$, which leads to higher losses. Secondly, as

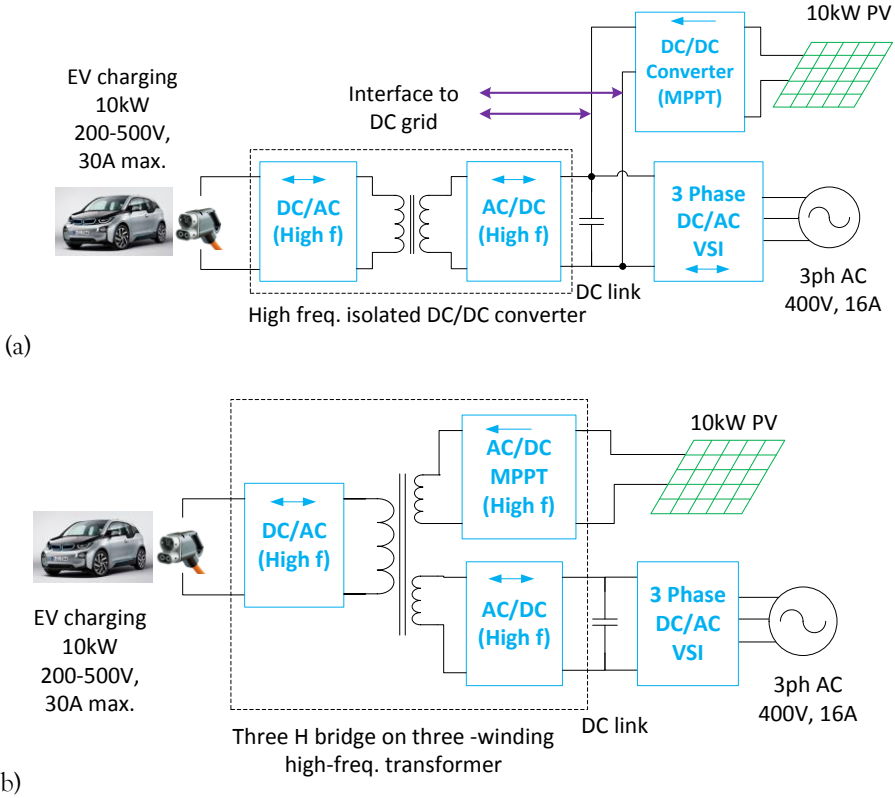


Fig. 2.7. Block diagram of multiport converter (a) MPC A, (b) MPC B based on system architecture 3

per European standards (IEC 61727), isolation is not obligatory in the current flow path from the PV to grid as long as the leakage currents are within the limits. Hence, the presence of isolation leads to additional losses in the transformer. Thirdly, there is a high complexity in the design of the three-winding transformer and converter control, making the design not modular.

In this thesis, MPC A is used for EV-PV converter with a nominal rating of 10kW. As will be explained in Chapter 4 and 5, the use of a two-stage conversion between the PV and grid and the inverter controller can be used to limit the PV leakage currents. Hence, a simple DC/DC non-isolated topology can be used for the PV converter instead of a three-winding transformer based MPC. This makes the converter design simpler, scalable (modular) and reduces the PV conversion losses. In Chapter 4, a detailed quantitative evaluation of topologies for PV, EV and grid converter for MPC A is made considering power components, switching frequency, efficiency and power density.

2.9. Conclusions

DC EV charging in the future will be facilitated through CHAdeMO and Combined charging standard as it enables dynamic charging, fast charging and V2G support. This thesis focuses on DC charging as the EV battery and PV are both fundamentally DC by nature.

Different system architectures and power converter topologies for a solar powered EV charging station are analyzed and compared. Architecture 3 which uses a three-port converter that connects to the EV, PV and grid provides several advantages over the other architecture - direct use of DC power of PV for EV charging, the ease of control and higher power density that is achieved due to the use of an integrated converter and the usage of the existing AC grid for connection of multiple EV-PV chargers. An analysis of published research work in the field of EV-PV charging shows that isolation and bidirectional capability of the EV charger has been neglected by most works. The focus has been mainly on architectures 1 and 2, where separate converters are used for PV and EV. Multi-port converters (MPC) are gaining attention currently and will be the direction of research for future designs of solar powered EV charging station.

In this thesis, 10kW is chosen as the nominal power rating for the converter based on V2G power requirements, modularity and low power requirements at workplaces due to long parking times of car. MPC can have power flow via a central DC-link or via high-frequency transformer AC link. Due to a lower number of conversion stages for power flow from PV→grid and since isolation is not required in Europe between PV and grid, the central DC-link based MPC is preferred.

2.10. References

- [1] M. Yilmaz and P. T. Krein, "Review of Battery Charger Topologies, Charging Power Levels, and Infrastructure for Plug-In Electric and Hybrid Vehicles," *IEEE Trans. Power Electron.*, vol. 28, no. 5, pp. 2151–2169, May 2013.
- [2] P. Bauer, Yi Zhou, J. Doppler, N. Stemberger, and Y. Zhou, "Charging of electric vehicles and impact on the grid," in *Proceedings of 13th International Symposium on Mechatronics, MECHATRONIKA 2010*, 2010, pp. 121–127.
- [3] SAE Standard J1772, "SAE Electric Vehicle and Plug-in Hybrid Electric Vehicle Conductive Charge Coupler," pp. 1–93, 2010.
- [4] "Standard IEC 62196 - Plugs, socket-outlets, vehicle connectors and vehicle inlets - Conductive charging of electric vehicles - Part 1, 2, 3," pp. 1–176, 1–122, 1–71, 2014.
- [5] "Standard IEC 61851 - Electric vehicle conductive charging system - Part 1, 21, 23, 24," pp. 1–287, 1–47, 1–159, 1–63, 2014.
- [6] www.teslamotors.com, "Tesla EV charging and supercharger technology."
- [7] CHAdeMO Association, "Technical specifications of quick charger for the electric vehicle," *CHAdeMO Protoc. Rev. 1.1*, 2010.
- [8] W. Kempton, V. Udo, K. Huber, K. Komara, and S. Letendre, "A test of vehicle-to-grid (V2G) for energy storage and frequency regulation in the PJM system," pp. 1–32, 2008.
- [9] W. Kempton and J. Tomić, "Vehicle-to-grid power implementation: From stabilizing the grid to supporting large-scale renewable energy," *J. Power Sources*, vol. 144, no. 1, pp.

- 280–294, 2005.
- [10] IEA, “A snapshot of global PV markets 2016,” 2016, pp. 2875, 2878.
- [11] R. Fu, D. Chung, T. Lowder, D. Feldman, K. Ardani, and R. Margolis, “NREL U.S. Solar Photovoltaic System Cost Benchmark Q1 2016 Report,” Jan. 2016.
- [12] J. Shankleman and C. Martin, “Solar Could Beat Coal to Become the Cheapest Power on Earth,” *Bloomberg*, 2017. [Online]. Available: <https://www.bloomberg.com/news/articles/2017-01-03/for-cheapest-power-on-earth-look-skyward-as-coal-falls-to-solar>.
- [13] M. Messagie, F. S. Boureima, T. Coosemans, C. Macharis, and J. Van Mierlo, “A range-based vehicle life cycle assessment incorporating variability in the environmental assessment of different vehicle technologies and fuels,” *Energies*, vol. 7, no. 3, pp. 1467–1482, 2014.
- [14] A. Nordelöf, M. Messagie, A. M. Tillman, M. Ljunggren Söderman, and J. Van Mierlo, “Environmental impacts of hybrid, plug-in hybrid, and battery electric vehicles—what can we learn from life cycle assessment?,” *International Journal of Life Cycle Assessment*, vol. 19, no. 11, pp. 1866–1890, 2014.
- [15] S. Rangaraju, L. De Vroey, M. Messagie, J. Mertens, and J. Van Mierlo, “Impacts of electricity mix, charging profile, and driving behavior on the emissions performance of battery electric vehicles: A Belgian case study,” *Appl. Energy*, vol. 148, pp. 496–505, 2015.
- [16] M. Messagie, K. Lebeau, T. Coosemans, C. Macharis, and J. van Mierlo, “Environmental and financial evaluation of passenger vehicle technologies in Belgium,” *Sustain.*, vol. 5, no. 12, pp. 5020–5033, 2013.
- [17] G. Gamboa, C. Hamilton, R. Kerley, S. Elmes, A. Arias, J. Shen, and I. Batarseh, “Control strategy of a multi-port, grid connected, direct-DC PV charging station for plug-in electric vehicles,” in *2010 IEEE Energy Conversion Congress and Exposition*, 2010, pp. 1173–1177.
- [18] C. Hamilton, G. Gamboa, J. Elmes, R. Kerley, A. Arias, M. Pepper, J. Shen, and I. Batarseh, “System architecture of a modular direct-DC PV charging station for plug-in electric vehicles,” in *IECON 2010 - 36th Annual Conference on IEEE Industrial Electronics Society*, 2010, pp. 2516–2520.
- [19] M. Vaidya, E. K. Stefanakos, B. Krakow, H. C. Lamb, T. Arbogast, and T. Smith, “Direct DC-DC electric vehicle charging with a grid connected photovoltaic system,” in *Conference Record of the IEEE Photovoltaic Specialists Conference*, 1996, pp. 1505–1508.
- [20] Z. Qian, O. Abdel-Rahman, C. Hamilton, M. Batarseh, and I. Batarseh, “An integrated four-port converter for compact and efficient hybrid power systems,” in *Proceedings of 2010 IEEE International Symposium on Circuits and Systems*, 2010, pp. 2207–2210.
- [21] Z. Qian, O. Abdel-Rahman, H. Hu, and I. Batarseh, “An integrated three-port inverter for stand-alone PV applications,” in *2010 IEEE Energy Conversion Congress and Exposition*, 2010, pp. 1471–1478.
- [22] L. Mackay, T. G. Hailu, G. R. Chandra Mouli, L. Ramirez-Elizondo, J. A. Ferreira, and P. Bauer, “From DC Nano- and Microgrids Towards the Universal DC Distribution System – A Plea to Think Further Into the Future,” in *2015 IEEE Power & Energy Society General Meeting*, 2015, pp. 1–5.
- [23] J. G. J. G. Ingersoll and C. A. Perkins, “The 2.1 kW photovoltaic electric vehicle charging station in the city of Santa Monica, California,” in *Conference Record of the IEEE Photovoltaic Specialists Conference*, 1996, pp. 1509–1512.
- [24] S. Mesentean, W. Feucht, H.-G. Kula, and H. Frank, “Smart charging of electric scooters for home to work and home to education transports from grid connected photovoltaic-systems,” in *2010 IEEE International Energy Conference*, 2010, pp. 73–78.

- [25] University of Iowa, "Solar electric vehicle charging station."
- [26] I. Cvetkovic, T. Thacker, G. Francis, V. Podosinov, D. Boroyevich, F. Wang, R. Burgos, G. Skutt, and J. Lesko, "Future home uninterruptible renewable energy system with vehicle-to-grid technology," in *2009 IEEE Energy Conversion Congress and Exposition*, 2009, pp. 2675–2681.
- [27] Oak Ridge National Laboratory, *Solar-Assisted Electric Vehicle Charging Stations*. 2011.
- [28] Y. Gurkaynak and A. Khaligh, "Control and Power Management of a Grid Connected Residential Photovoltaic System with Plug-in Hybrid Electric Vehicle (PHEV) Load," in *2009 Twenty-Fourth Annual IEEE Applied Power Electronics Conference and Exposition*, 2009, pp. 2086–2091.
- [29] Y. Gurkaynak and A. Khaligh, "A novel grid-tied, solar powered residential home with plug-in hybrid electric vehicle (PHEV) loads," in *2009 IEEE Vehicle Power and Propulsion Conference*, 2009, pp. 813–816.
- [30] M. Alonso Abella, M. A. F. ChenloAbella, and F. Chenlo, "Photovoltaic charging station for electrical vehicles," in *Proceedings of 3rd World Conference on Photovoltaic Energy Conversion*, 2003, vol. 3, pp. 2280–2283.
- [31] M. Brenna, A. Dolara, F. Foadelli, S. Leva, and M. Longo, "Urban Scale Photovoltaic Charging Stations for Electric Vehicles," *IEEE Trans. Sustain. Energy*, vol. 5, no. 4, pp. 1234–1241, Oct. 2014.
- [32] P. J. Tulpule, V. Marano, S. Yurkovich, and G. Rizzoni, "Economic and environmental impacts of a PV powered workplace parking garage charging station," *Appl. Energy*, vol. 108, pp. 323–332, Aug. 2013.
- [33] P. Tulpule, V. Marano, S. Yurkovich, and G. Rizzoni, "Energy economic analysis of PV based charging station at workplace parking garage," in *IEEE 2011 EnergyTech*, 2011, pp. 1–6.
- [34] J. Traube, F. Lu, and D. Maksimovic, "Electric vehicle DC charger integrated within a photovoltaic power system," in *2012 Twenty-Seventh Annual IEEE Applied Power Electronics Conference and Exposition (APEC)*, 2012, pp. 352–358.
- [35] J. Traube, F. Lu, D. Maksimovic, J. Mossoba, M. Kromer, P. Faill, S. Katz, B. Borowy, S. Nichols, and L. Casey, "Mitigation of Solar Irradiance Intermittency in Photovoltaic Power Systems With Integrated Electric-Vehicle Charging Functionality," *IEEE Trans. Power Electron.*, vol. 28, no. 6, pp. 3058–3067, Jun. 2013.
- [36] M. Tabari and A. Yazdani, "A Mathematical Model for Stability Analysis of A DC Distribution System for Power System Integration of Plug-In Electric Vehicles," *IEEE Trans. Veh. Technol.*, vol. PP, no. 99, pp. 1–1, 2014.
- [37] M. Tabari and A. Yazdani, "Stability of a dc Distribution System for Power System Integration of Plug-In Hybrid Electric Vehicles," *IEEE Trans. Smart Grid*, vol. 5, no. 5, pp. 2564–2573, Sep. 2014.
- [38] B. E. Noriega, R. T. Pinto, and P. Bauer, "Sustainable DC-microgrid control system for electric-vehicle charging stations," in *2013 15th European Conference on Power Electronics and Applications (EPE)*, 2013, pp. 1–10.
- [39] F. Turki, A. Guetif, and C. Sourkounis, "Contactless charging electric vehicles with renewable energy," in *2014 5th International Renewable Energy Congress (IREC)*, 2014, pp. 1–6.
- [40] M. Benaouadj, A. Aboubou, M. Becherif, M. Y. Ayad, and M. Bahri, "Recharging of batteries/supercapacitors hybrid source for electric vehicles application using photovoltaic energy in a stand-alone point," in *2012 First International Conference on Renewable Energies and Vehicular Technology*, 2012, pp. 161–166.
- [41] D. M. Robalino, G. Kumar, L. O. Uzoечи, U. C. Chukwu, and S. M. Mahajan, "Design of a docking station for solar charged electric and fuel cell vehicles," in *2009*

- International Conference on Clean Electrical Power*, 2009, pp. 655–660.
- [42] Z. Li and A. Khaligh, “An integrated parallel synchronous rectifier and bi-directional DC/DC converter system for solar and wind powered hybrid electric vehicle,” in *2009 35th Annual Conference of IEEE Industrial Electronics*, 2009, pp. 3779–3784.
- [43] G.-Y. Choe, J.-S. Kim, and B.-K. Lee, “A Bi-directional battery charger for electric vehicles using photovoltaic PCS systems,” in *2010 IEEE Vehicle Power and Propulsion Conference*, 2010, pp. 1–6.
- [44] D. H. Kim, G. Y. Cheo, and B. K. Lee, “Design and control of an optimized battery charger for an xEV based on photovoltaic power systems,” *J. Electr. Eng. Technol.*, vol. 9, no. 5, pp. 1602–1613, 2014.
- [45] G. Carli and S. S. Williamson, “Technical Considerations on Power Conversion for Electric and Plug-in Hybrid Electric Vehicle Battery Charging in Photovoltaic Installations,” *IEEE Trans. Power Electron.*, vol. 28, no. 12, pp. 5784–5792, Dec. 2013.
- [46] Z. Rasinab and M. F. Rahmana, “Grid-connected quasi-Z-source PV inverter for electric vehicle charging station,” in *2013 International Conference on Renewable Energy Research and Applications (ICRERA)*, 2013, pp. 627–632.
- [47] Z. Rasin, K. Ahsanullah, and M. F. Rahman, “Design and simulation of quasi-Z-source grid-connected PV inverter with bidirectional power flow for battery storage management,” in *IECON 2013 - 39th Annual Conference of the IEEE Industrial Electronics Society*, 2013, pp. 1589–1594.
- [48] P. Goli and W. Shireen, “PV Integrated Smart Charging of PHEVs Based on DC Link Voltage Sensing,” *IEEE Trans. Smart Grid*, vol. 5, no. 3, pp. 1421–1428, May 2014.
- [49] A. Nagarajan and W. Shireen, “Grid connected residential photovoltaic energy systems with Plug-In Hybrid electric Vehicles(PHEV) as energy storage,” in *IEEE PES General Meeting*, 2010, pp. 1–5.
- [50] Lei Shi, Haiping Xu, Dongxu Li, Zuzhi Zhang, and Yuchen Han, “The photovoltaic charging station for electric vehicle to grid application in Smart Grids,” in *2012 IEEE 6th International Conference on Information and Automation for Sustainability*, 2012, pp. 279–284.
- [51] H. Krishnaswami and N. Mohan, “Three-Port Series-Resonant DC–DC Converter to Interface Renewable Energy Sources With Bidirectional Load and Energy Storage Ports,” *IEEE Trans. Power Electron.*, vol. 24, no. 10, pp. 2289–2297, Oct. 2009.
- [52] N. Kawamura and M. Muta, “Development of solar charging system for plug-in hybrid electric vehicles and electric vehicles,” in *2012 International Conference on Renewable Energy Research and Applications (ICRERA)*, 2012, pp. 1–5.
- [53] T.-E. E. Stamati and P. Bauer, “On-road charging of electric vehicles,” in *2013 IEEE Transportation Electrification Conference and Expo (ITEC)*, 2013, pp. 1–8.

3

System design of the solar EV charging station

3. System design of the solar EV charging station

This chapter is based on:

G. R. Chandra Mouli, P. Bauer, and M. Zeman, "System design for a solar powered electric vehicle charging station for workplaces," *Appl. Energy*, vol. 168, pp. 434–443, Apr. 2016

Summary

In the previous chapter, a review of existing systems for charging EV from PV was made, and the system architectures were compared. As a first step, in this chapter, the system-level design for an EV-PV charger is investigated based on a 10kW multi-port power converter. The main components in the system namely EV, PV, grid and an optional local storage are designed and sized for the case of Netherlands. Data from the Dutch Meteorological Institute (KNMI) is used for estimating the PV generation potential. The EV charging requirements and influence of employees working five or seven days/week on the system design is explored. Based on this, the use of a local storage to mitigate the diurnal and seasonal variations in solar is investigated. Finally, different methods to implement modularity to charge multiple EVs from a single EV-PV charger are proposed that can help drastically reduce the cost of the EV charging infrastructure.

Outline

The chapter is divided into five sections. Section 3.2 provides a literature review of existing research works on system design of solar charging systems for EVs. Section 3.3 develops a model to analyze the design and energy yield of 10kW PV array in the Netherlands based on data from KNMI. This is used to determine the optimal orientation of PV panels, relative power converter sizing and to evaluate the seasonal and diurnal variation in solar insolation. In section 3.4, different smart charging strategies for EV are analyzed with an aim to minimize the grid dependency and to maximize the use of solar power. The feasibility of integrating a local storage to the EV-PV charger to make it grid independent is evaluated in section 3.5. The optimal storage size that reduces the grid dependency by 25% is evaluated. Finally, section 3.6 presents different multiplexing methods to connect several EVs to a single EV-PV charger.

3.1. Introduction

This chapter examines the system design for an electric vehicle charging infrastructure using PV panels. The system is designed for use in workplaces to charge electric cars of the employees as they are parked during the day. The motive is to maximize the use of PV energy for EV charging with minimal energy exchange with the grid. The system architecture is based on a three-port converter that connects to the EV, PV and AC grid as in Fig. 3.1.

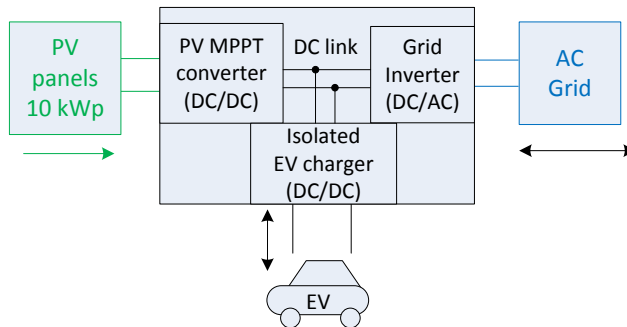


Fig. 3.1. System architecture of the grid-connected 10kW three-port EV-PV charger

3.2. Literature review and contributions

Several earlier works have analyzed the design of an EV charging station based on PV [1]-[10]. The mutual benefit of charging EV from solar energy has been highlighted in [11][12] where the potential to charge EV from solar allows for higher penetration of both technologies. In [13], the negative effects of excess solar generation from PV on a national level has been shown to be mitigated by using it for charging EVs. This is especially applicable for charging at the workplace, as shown in [12]. In [14], [15], for the case of Columbus and Los Angeles, USA, the economic incentive and CO₂ offsets for PV charging have been shown to be greater than charging the EV from the grid.

A major disadvantage of charging EV from PV is the variability in the PV production. Smart charging provides for flexibility of EV charging in order to closely match the PV production. [16] has shown that smart charging combined with V2G has the dual benefit of increasing PV self-consumption and reducing peak demand on the grid. In [17], the EV charging profile is varied with time so that maximum PV utilization occurs. It can be seen that the excess PV energy reduces with higher EV penetration [18], [19]. Alternately, the total number of vehicles that are charging at a constant power can be dynamically varied so that the net charging power follows the PV generation, as seen in [20]. This type of sequential charging shows great benefit than simultaneous EV charging, which is proved in [21] by considering 9000 different cases. A time shift scheduling is used in [22] to manage the charging of e-scooters so that the net charging power follows the PV profile. This method is further improved with the use of weather forecast data [23].

A second method to overcome the PV variation is to use a local storage in the PV powered EV charging station, like in [24]–[28], [19]. The storage is typically charged when there is excess solar energy and is then used to charge the EV when solar generation is insufficient [19]. In [29], three different algorithms for (dis)charging the local storage are compared, and it was shown that a sigmoid function based discharging of the storage and charging during the night and solar excess was the best strategy. Since storage is an expensive component, optimally sizing the storage is vital. This aspect has been neglected by the chapters mentioned above.

Secondly, research works that analyzed the use of smart charging have not considered the use of local storage and vice versa. The two methods are investigated together in this work for a solar powered EV charging station. Thirdly, in case of workplace charging, it is important to distinguish the effects of weekday and weekend EV charging load. This is because rooftop PV installed in the workplace will produce energy even in the weekends even though the EVs of the employees are not present on Saturday-Sunday. This chapter analyses the PV system design and EV charging in a holistic manner considering the above aspects.

The new contributions of the work compared to earlier works are as follows:

1. Determination of the optimal orientation of PV panels for maximizing energy yield in the Netherlands and comparing it with the use of tracking systems
2. The possibility of oversizing the PV array power rating with respect to the power converter size based on metrological conditions of the location.
3. Smart charging of EV using Gaussian charging profile and EV prioritization, which is superior to constant power charging.
4. Determination of grid impact of two different types of workplace/commercial charging scenario considering 5 days/week and 7 days/week EV load by running round-the-year simulation.
5. Optimal sizing of local storage considering both meteorological data and smart charging of EV
6. Proposing various multiplexing strategies by which a single EV charger can be shared amongst multiple EVs for simultaneous and/or sequential charging of EVs

3.3. PV System Design

The 10kW three-port converter connected to the 50Hz AC grid was chosen as the suitable system architecture based on Chapter 2 [5]. Solar power is the primary power source of the grid-connected EV-PV charging system. The solar power is generated using a 10kW_p photovoltaic (PV) array that is located in the workplace. The panels could be located on the building rooftop or installed as a solar carport [1].

3.3.1. Estimation of optimal orientation of PV array in the Netherlands

To evaluate the power and energy generated by a 10kW_p PV array in the Netherlands, an accurate measurement of the weather data is required. For this purpose, the meteorological data from the Dutch Meteorological Institute (KNMI) is used, which has a resolution of 1 minute [30]. Global horizontal irradiance (S^{GHI}),

Diffuse Horizontal Irradiance (S^{DHI}), Direct Normal Irradiance (S^{DNI}) and ambient temperature (T_a) are obtained from KNMI for the years 2011-2013. A 10kW_p PV array was modeled in MATLAB using 30 modules of Sun power E20-327 modules rated at 327W [31], whose specifications are shown in Table 3.1. They are connected in 5 parallel strings having 6 modules in series having a combined installed power of 9810W.

To estimate the solar irradiance on a module (S_m) with a specific azimuth (A_m) and tilt angle (θ_m) as shown in Fig. 3.2, an estimation of the position of the sun throughout the year is required. A solar position calculator is hence built using [32], [33] by which the azimuth (A_s) and altitude (a_s) of the sun throughout the year at the location of the KNMI observatory can be determined. With the sun's position, the irradiance on a panel with specific orientation (A_m, θ_m) can be estimated using the geometric models in [34]–[36] and the Isotropic sky diffused model [34], [37] where S_m^{DNI}, S_m^{DHI} are the components of DNI and DHI which is incident on the panel:

$$S_m^{DNI} = S^{DNI}(\sin\theta_m \cos a_s \cos(A_m - A_s) + \cos\theta_m \sin a_s) \quad (1)$$

$$S_m^{DHI} = S^{DHI} \frac{1 + \cos\theta_m}{2} \quad (2)$$

$$S_m = S_m^{DHI} + S_m^{DNI} \quad (3)$$

In order estimate the output power of a PV array, it is important to consider the ambient temperature, besides the magnitude of incident solar insolation. The PV array is rated for 327W at the STC ambient temperature of 25°. For other ambient temperatures (T_a), the PV array output power (P_m) can be estimated using [38]–[40], where T_{cell} is the temperature of the PV cells:

$$T_{cell} = T_a + \frac{S_m}{800}(T_{NOCT} - 20) \quad (4)$$

$$P_m = \frac{P_r S_m}{1000}[1 - \lambda(T_{cell} - 25)] \quad (5)$$

Using the above equations and meteorological data from KNMI, the output of the 10kW PV array can be estimated. For geographical locations in the northern hemisphere like the Netherlands, the optimal azimuth for the PV panels is $A_m=0^\circ$,

Table 3.1. Parameters of Sun power E20-327 module

Quantity	Value
Area of module (A_{pv})	1.63 m ²
Nominal Power (P_r)	327 W
Avg. Panel Efficiency (η)	20.4%
Rated Voltage (V_{mpp})	54.7 V
Rated Current (I_{mpp})	5.98 A
Open-Circuit Voltage (V_{oc})	64.9 V
Short-Circuit Current (I_{sc})	6.46 A
Nominal Operating Cell Temperature (T_{NOCT})	45 ±2 °C
Power Temp Coefficient (λ)	-0.38% / °C

i.e. facing south. To determine the optimal tilt angle θ_m , the annual energy yield of the 10kW PV system is determined for different tilt angles, as shown in Fig. 3.3.

The maximum annual energy yield is obtained for the years 2011-13 for an optimal tilt of 28° . The corresponding annual energy yield 2011-13 has a mean value of 10,889.8kWh with a standard deviation of 117.23kWh. The corresponding average daily yield for the PV system is 29.8 kWh/day. It must be kept in mind that in practice, it might not be possible to install the PV panels along the optimal orientation due to characteristics of the roof [36]. Further, shading on the panels due to nearby buildings, trees and/or other objects will reduce the yield of the PV system [40]. Since the orientation and shading will vary on a case-to-case basis, the detailed analysis of both is beyond the scope of this research work.

3.3.2. Power output of optimally oriented PV array in the Netherlands

Using an optimally oriented PV array with $A_m=0^\circ$ and $\theta_m=28^\circ$, the power production over one year is estimated using equation (1) to (5) and is shown in Fig. 3.4. and Fig. 3.5.

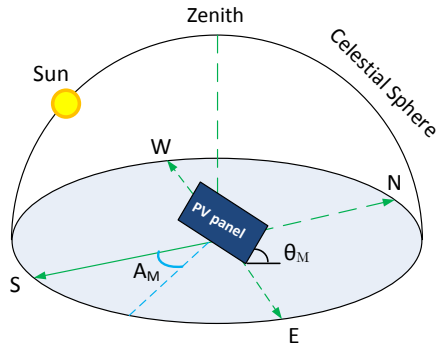


Fig. 3.2. Orientation of the PV panel is defined by azimuth angle A_m (measured from the South) and module tilt angle θ_m (measured from horizontal surface)

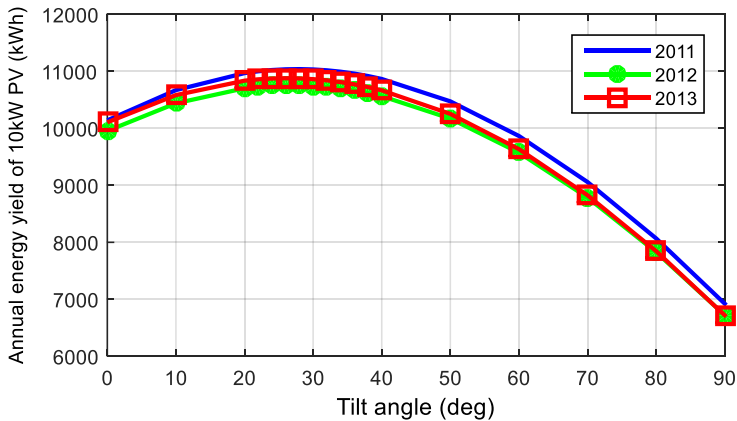


Fig. 3.3. Annual energy yield of 10kW PV system as a function module tilt for years 2011-13. The PV modules were oriented south with azimuth of 0°

In Fig. 3.4., the output power of the 10kW array for every minute can be seen over the year. The seasonal variation in peak output power over one year can be perceived. For example, in 2013, the peak power over 24 hours was as high as 11.9kW in summer and as low as 0.28kW in winter. When the yearly data estimated in Fig. 3.4. is averaged over a 24 hour period for each month; we get the average 24-hour PV profile for different months of 2013 as shown in Fig. 3.5. Two vital observations:

1. PV generation is restricted to only 7-8 hours in the winter months while it is 15 hours in summer
2. Based on a 24h average, the peak power is close to 7kW for July and 2kW for November in Fig. 3.5. So in winter months, there is the double disadvantage of lower sunshine hours and lower peak power as well.

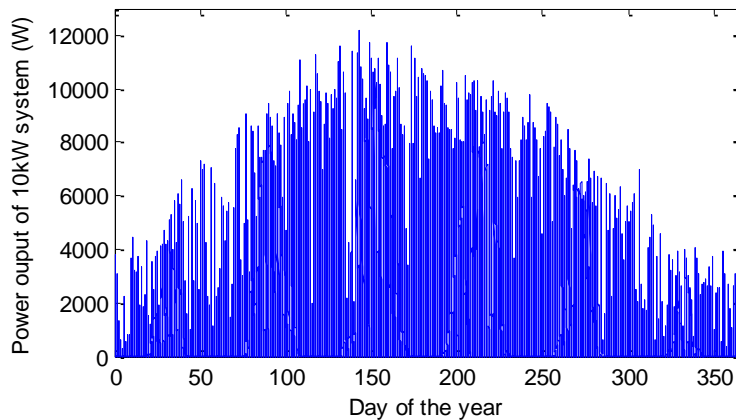


Fig. 3.4. Power output of 10kW PV system as a function of time for 2013. The PV modules were oriented south with a tilt angle of 28° .

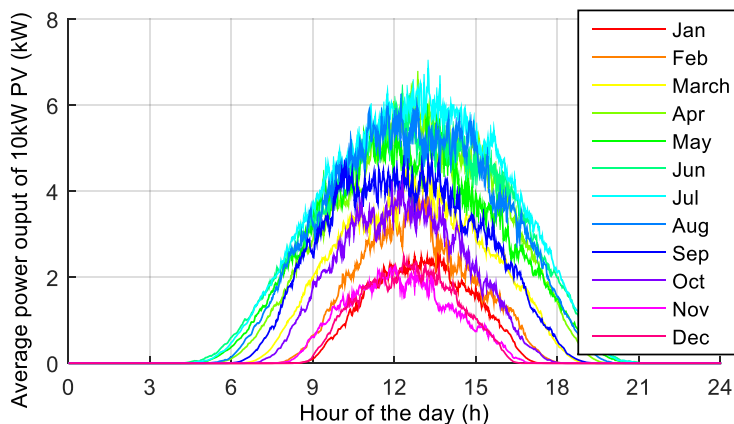


Fig. 3.5. Average power output of 10kW PV system as a function of time of the day for different months of 2013

Fig. 3.6 and Fig. 3.7 show the daily yield of the PV system for each day of the year and as a monthly average for 2013. They clearly show the seasonal variation in PV yield. The actual yield has a variation between 75kWh/day and 1kWh/day for specific days in June and December respectively. With respect to the average daily yield for different months, a difference of up to 5 times can be observed between summer and winter in Fig. 3.7. It can also be observed that even in summer, there are cloudy days with a low daily yield of <10kWh and sunny days in winter with a yield >20kWh.

The daily yield values are compared with the 24kWh battery pack of the 2016 Nissan Leaf EV in Fig. 3.6 and Fig. 3.7. For 54% of the year, the daily yield is greater than 24kWh/day, and for 22% of the year, the yield is greater than 48kWh/day which equals the combined capacity of two Nissan Leafs. Thus, there is a huge difference in energy availability between different days of the year. This seasonal

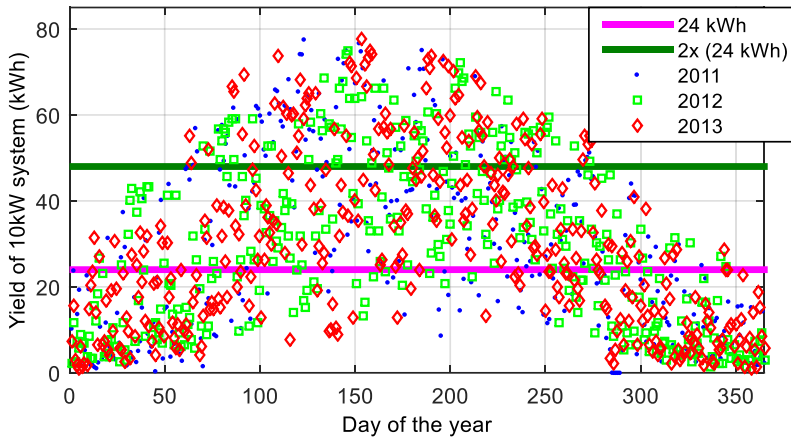


Fig. 3.6. Daily energy yield of 10kW PV system for different days of 2013

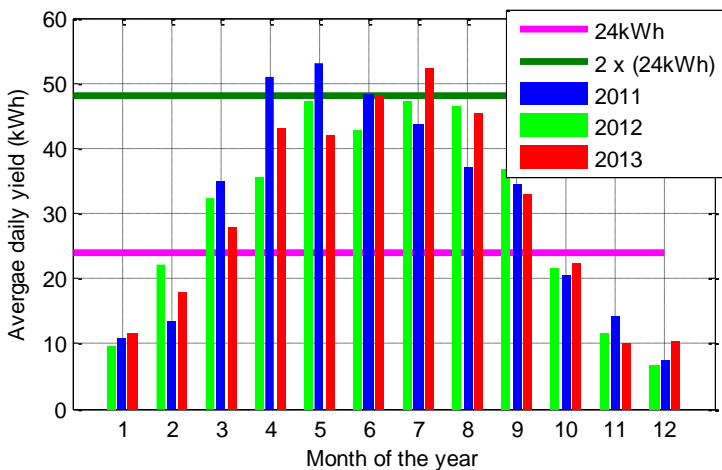


Fig. 3.7. Average daily yield for 10kW PV system for different months of 2013

difference in generation directly necessitates the need for a grid-connected PV system that can ensure reliable power supply to the EV battery throughout the year.

3.3.3. Impact of sun tracking system in increasing in PV energy yield

Since the bottleneck in the PV system design is the low winter yield can be as low as 1kWh/day, the applicability of a sun tracking system to improve winter yield was investigated. The simulations were performed considering the panels to be mounted on a 2-axis tracker ($A_m = A_s$, $\theta_m = 90 - a_s$) and a 1-axis tracker with either tracking of the sun's azimuth ($A_m = A_s$) or the sun's altitude ($\theta_m = 90 - a_s$).

The average daily yield and the annual yield due to use of a tracking system is shown in Fig. 3.8 and Table 3.2 respectively. Compared to fixed orientation of $\theta_m = 28^\circ$, $A_m = 0^\circ$, 17.3% and 13.3% improvement in annual yield are obtained using the 2-axis and 1-axis azimuth tracking system respectively. The 1-axis altitude tracker,

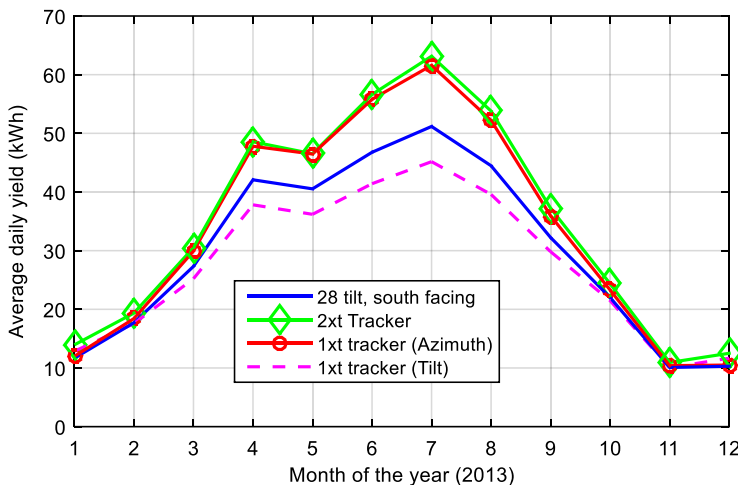


Fig. 3.8. Variation of the average monthly yield for 2013 for fixed orientation and when single/dual axis tracking system is used.

Table 3.2. Annual energy yield of PV system with 28° tilt and 2-axis tracker

	Annual energy yield (kWh)				Gain/Loss in energy yield (%)	Economic gain/loss (€) ^a
	2011	2012	2013	Avg.		
28° tilt	11039.7	10753.5	10876.2	10890	-	-
2 axis tracker	13114	12483	12732	12776	17.3 %	207.5
1 axis tracker (Azimuth)	12573	12116	12329	12339	13.3 %	159.4
1 axis tracker (Tilt)	10255	9946	10022	10074	-7.5 %	-89.7

^a – Based on an industrial electricity price of 0.11€/kWh

however, results in 7.5% reduction in yield. The average gain in yield in the winter months of November to February due to a 2-axis tracker is 1.9kWh/day while in summer the gain is as high as 11.6kWh/day for the month of July.

The concentrated gains in summer make the use of tracking system unattractive in improving the winter PV yield. Further, the tracking system is economically infeasible as the 160€ or 208€ gain in energy cost/year as seen in Table 3.2 cannot offset the 4750€ or 8177€ cost of installing a single or dual axis tracking system respectively (Based on [41], 0.57\$/W and 0.98\$/W is cost for 1-axis and 2-axis tracking system and 1.2\$/1€).

3.3.4. Oversizing the PV array with respect to PV converter power rating

Fig. 3.9 and Table 3.3 show the frequency distribution of the PV output power as a percentage of the daylight time of the year and the corresponding energy distribution. The daylight time corresponds to the total sum of hours in the year when the PV output power is non-zero, which is 4614.5 hours in 2013. While the occurrence of high output power from PV panels is low, the energy delivered by the panels at times of high output power is very high. PV Power >5kW occur only 16% of the daylight time but delivers about 50% of annual PV energy.

Table 3.3. Energy delivered and occurrence of different PV output power

	PV power output (kW)			
	> 2kW	> 5kW	>7kW	> 9 kW
% Daylight time	41.3	16.5	7.7	0.95
% Annual energy	82.7%	48.8%	26%	3.8%

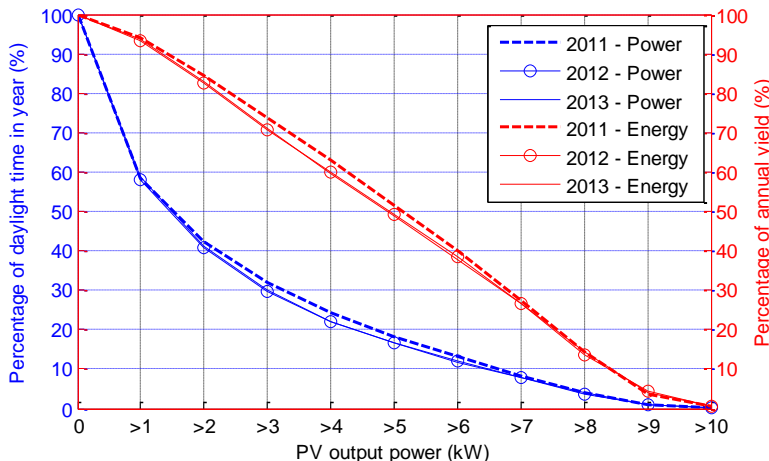


Fig. 3.9. Frequency distribution of output power of PV system shown as a percentage of daylight time (when PV power output is non-zero) and distribution of annual yield shown as a function of output power.

Table 3.4. Reduction in annual PV yield due to oversizing of PV array compared to PV converter

	Inverter size for 10kW PV array			
	2kW	5kW	7kW	9kW
% Energy lost in year	47.5	13.84	3.2	0.16

Similarly, PV power >7kW and >9kW deliver 26% and 3.8% of annual energy respectively as elaborated in Table 3.3. From the table, we can infer that by undersizing the PV power converter by a factor of 0.9 to 9kW, we will lose only 0.16% of the annual energy yield. This is because during times the PV panels can produce >9kW, the inverter will not shut down, it will just produce 9kW. Similarly, using a converter of 7kW or 5kW for the 10kW PV array results in only loss of 3.2% or 13.8% of annual yield as shown in Table 3.4. This observation opens up the opportunity for the PV converter rated power to be undersized compared to the PV array rated power, in a country like the Netherlands.

3.4. Smart charging of EV

Smart charging refers to charging the EV at variable charging power instead of a fixed power. Here, the motive of the smart charging of the EV is to vary the EV charging power to closely follow the PV generation, so that minimum power is fed/drawn from the grid.

The power drawn or fed to the grid can be expressed as given below where P_{PV} , P_{EV} are the PV generation and the EV charging power respectively:

$$P_{grid} = P_{EV} - P_{PV} \quad (6)$$

When $P_{grid} > 0$, power is drawn from the grid while power is fed to the grid when $P_{grid} < 0$. It is assumed that all the EVs arrive at the workplace at 0830hr and are parked till 1700hr, for a total duration of 8.5 hours. 8 different EV charging profiles are compared, and they are shown in Fig. 3.10 along with the average PV generation profile for different months. The charging profiles here are categorized into three types - Gaussian (G1, G2, G3, and G4), fixed (F1, F2) and rectangular profiles (R1, R2) based on the shape of the 24-hour EV power-time curve, as shown in Fig. 3.10 and explained in Table 3.5¹. The fixed and rectangular charging profiles are chosen as they correspond to current EV chargers available in the market that can charge the car with a fixed time in-varying charging power. The Gaussian charging profiles were chosen due to their ability to closely match solar irradiance data [42], [43] and they have their peaks at 1200hr when the sun is at its peak.

The energy delivered by each charging profile E_{EV} can be determined by integrating the power-time curve to obtain the area under the curve:

¹ While fixed EV charging profiles are used in this chapter, smart charging algorithms are developed in chapter 6 by which the EV charging is controlled based on PV forecast, energy prices and network constraints.

$$E_{EV} = \int_{t=0830\text{ h}}^{t=1700\text{ h}} P_{EV}(t)dt \tag{7}$$

All charging profiles deliver 30kWh/day to the EV battery except profile F2 which delivers 85kWh. If a daily commuting distance of 50km/day is considered based on [44], 10kWh/day charging energy is required by a Nissan Leaf (121km range as per EPA driving cycle) assuming 95% charging efficiency. 30kWh/day thus corresponds to the commuting energy needs of three EVs. It also equals the average daily energy yield of the 10kW PV system as per Table 3.2. The three EVs can either be sequentially or simultaneously charged as explained later in section 3.6.

3.4.1. Matching the Smart charging of EV to PV generation

Due to seasonal and diurnal variation in solar generation, there will always be a mismatch between EV demand and PV generation. This difference in power is

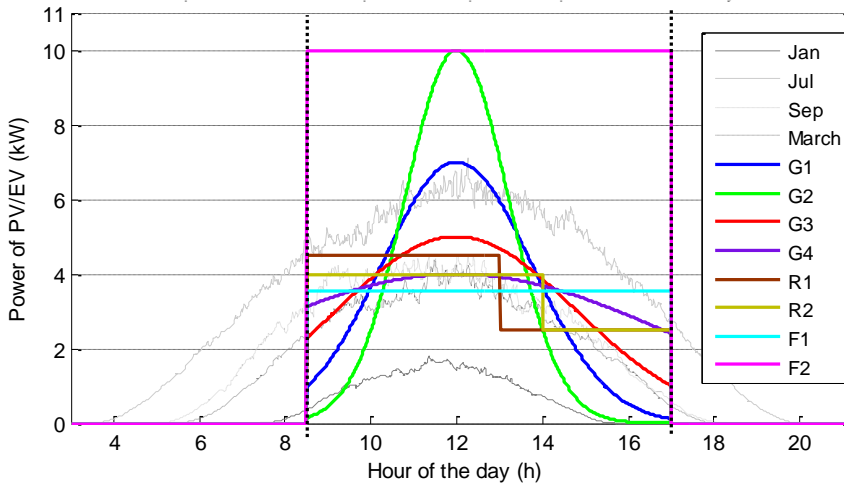


Fig. 3.10. Various EV charging profiles compared with the average daily PV array output for different months of 2013

Table 3.5. Maximum power and energy of the 8 EV charging profiles

EV Charging profile	Max. charging power (kW)	Energy delivered to EV (kWh)
G1 - Gaussian profile	10	30
G2 - Gaussian profile	7	30
G3 - Gaussian profile	5	30
G4 - Gaussian profile	4	30
R1 - Rectangular (4.5kW, 2.44kW)	4.5	30
R2 - Rectangular (4kW, 2.67kW)	4	30
F1 - Constant power (2.58 kW)	2.58	30
F2 - Constant power (10 kW)	10	85

fed/drawn from the grid. The total energy fed to the grid E_{fed}^{grid} and drawn from the grid E_{draw}^{grid} over one year (8760hr) can be estimated as:

$$\text{If } P_{grid}(t) < 0, \quad E_{fed}^{grid} = \int_{t=0}^{t=8760h} P_{grid}(t) dt \quad (8)$$

$$\text{If } P_{grid}(t) > 0, \quad E_{draw}^{grid} = \int_{t=0}^{t=8760h} P_{grid}(t) dt \quad (9)$$

$$E_{ex}^{grid} = E_{draw}^{grid} + |E_{fed}^{grid}| \quad (10)$$

To ensure maximum utilization of PV energy for EV charging, the total energy exchanged with the grid E_{ex}^{grid} must be minimum, assuming there is no PV power curtailment. E_{ex}^{grid} is estimated for two cases - one considering that EV is present on all 7 days of the week and the second considering that EV is present only on weekdays, i.e. 5 days/week. The first case is applicable to places like shopping malls and theaters, while the second for offices, universities, and factories.

3.4.2. Scenario 1 - EV load for 7 days/week

The annual PV yield of the 10kW PV system for 2013 is 10,876kWh while the annual EV demand is 10,950kWh (30 kWh*365 days, assuming the EV to be used all 7 days of the week) for all profiles except F2. Table 3.6 shows the annual energy exchanged with the grid for different charging profiles, ranked in the order of increasing magnitude of grid energy exchange. It can be seen that annual grid energy exchange of G3, G4 is the lowest while the F2 profile results in the maximum energy exchange with the grid.

It can be observed that there exists a minimum energy that is always drawn from the grid irrespective of the charging profile. This is because while the EV demand is constant at 30kWh throughout the year, the PV yield in winter and on cloudy days throughout the year is much less than 30kWh, forcing the system to draw energy from the grid.

Table 3.6. Energy exchanged with grid for 7 days/week EV load

EV Charging profile	Annual energy exchange with grid (kWh)			Rank
	Fed to grid $ E_{fed}^{grid} $	Draw from grid E_{draw}^{grid}	Total E_{ex}^{grid}	
G1	5248	5350	10598	7
G2	4455	4544	8999	6
G3	4113	4213	8326	1
G4	4119	4214	8333	2
R1	4297	4402	8699	5
R2	4180	4282	8462	3
F1	4198	4295	8493	4
F2	1336	21546	22882	8

Further, there is always a minimum surplus energy fed to the grid and this due to two reasons. Firstly, the peak PV array power in summer is more than the peak power of all the load profiles except G2 and F2. Secondly, the sun shines in summer months for over 16 hours (0400hr to 2000hr approx.) which is much more than the 8.5 hours for which the EV is charging. This results in power being fed back to the grid in the early morning and late evening.

EV charging profiles with high peak charging profiles namely G1, G2, and F2 have the lowest rank in Table 3.6. G3, G4, R1, R2 exhibit the better matching with PV and have a peak charging power which is the range of 40% to 50% of the installed watt peak of the PV array. Since lower charging power means lower component ratings in the converter, it can be concluded that profile G4 with a peak EV charging power of 40% of nominal PV power, is most suitable for the Netherlands.

3.4.3. Scenario 2 – EV load for 5 days/week

Simulations from scenario 1 are repeated considering the EV load to be present for only 5 days/week on weekdays and no EV loads for the weekend. Only the charging profiles with rank 1 to 5 are considered here namely G1, G2, G3, F1, and F2. Table 3.7 shows the annual energy exchange with the grid for different charging profiles,

Table 3.7. Energy exchanged with grid for 5 days/week EV load

EV Charging profile	Annual energy exchange with grid (kWh)			Rank
	Fed to grid $ E_{fed}^{grid} $	Draw from grid E_{draw}^{grid}	Total E_{ex}^{grid}	
G3	6053	3024	9077	1
G4	6059	3027	9086	2
R1	6165	3141	9306	5
R2	6094	3067	9161	3
F1	6117	3088	9205	4

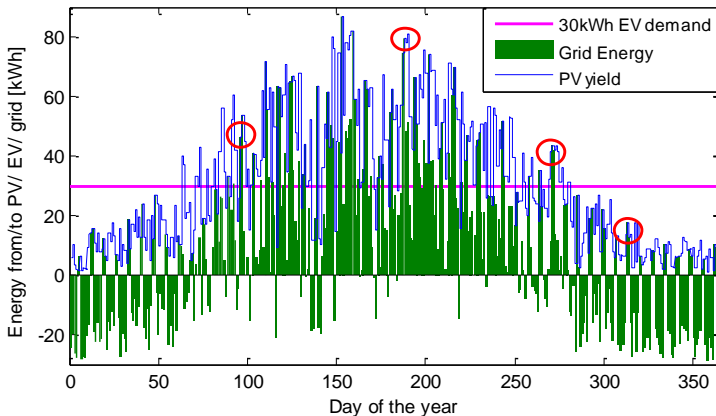


Fig. 3.11. Daily energy yield of PV and energy fed/drawn from grid for 30kWh EV load profile G4 on weekdays.

and it can be seen that the Gaussian profiles G3, G4 exhibit minimum energy exchange. An obvious difference between the values in Table 3.6 and Table 3.7 is that the energy fed to the grid has increased and the energy drawn from the grid has reduced, effectively resulting in the total energy exchanged with the grid to increase.

Fig. 3.11 shows the cumulated daily PV energy yield and energy fed/drawn from the grid for the year 2013 for EV load profile G4. Red circles indicate examples when the PV energy is fully fed to the grid on weekends as there is no EV load. In spite of optimal matching of the EV charging with the PV generation, surplus energy can be observed in summer months being fed to the grid and energy drawn from the grid in the winter months.

3.5. Integrating Local Storage in EV-PV Charger

Due to seasonal and diurnal variation in solar insolation, grid connection becomes pivotal and acts an energy buffer. Besides the grid, a local storage in the form of a battery bank can be used as well. In this section, the possibilities of using a local battery storage to eradicate the grid dependence of the EV-PV charger will be investigated.

At first, a 10kWh lithium-ion battery bank is integrated into the EV-PV charger. The battery is charged and discharged at a maximum C-rate of 1C corresponding to a maximum charging/discharging power of $P_b^{max}=10kW$. The maximum depth of discharge (DOD) is restricted to 80% (between a state of charge (SOC) of 10% to 90%) to ensure a long lifetime of the storage. The efficiency of charging/discharging

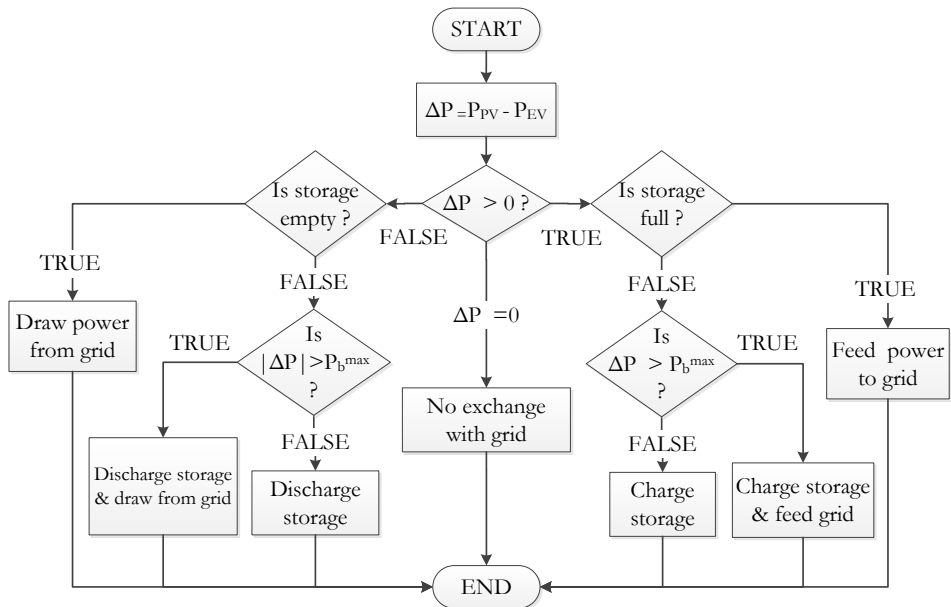


Fig. 3.12. State diagram for operation of EV-PV charger with local storage

of the battery including power converter is assumed to be 93% [45], [46] and the efficiency of power exchange with the grid is considered as 95% [47]. It must be noted that the C-rates, DOD, temperature and control of the charging power can be optimized for the local storage for increasing the efficiency and/or the lifetime of the battery [46], [48]–[50]. This is, however, beyond the scope of this thesis.

Fig. 3.12 shows the state diagram for the operation of the EV-PV charger with local storage. Power is exchanged with the grid only when the storage is full/empty or if the maximum power limit of the storage is reached due to C-rate limitations. If there is a surplus of PV power above the EV demand, it is first used to charge the local storage, while a power deficit is first extracted from the local storage. If the EV demand P_{EV} is more than the maximum charging/discharging power of the storage P_b^{max} due to C-rate limitations, then P_b^{max} is supplied to the EV from the storage and $|P_{EV} - P_b^{max}|$ is drawn from the grid to supply EV. The local storage never feeds/draws power from the grid; it interacts only with EV and PV.

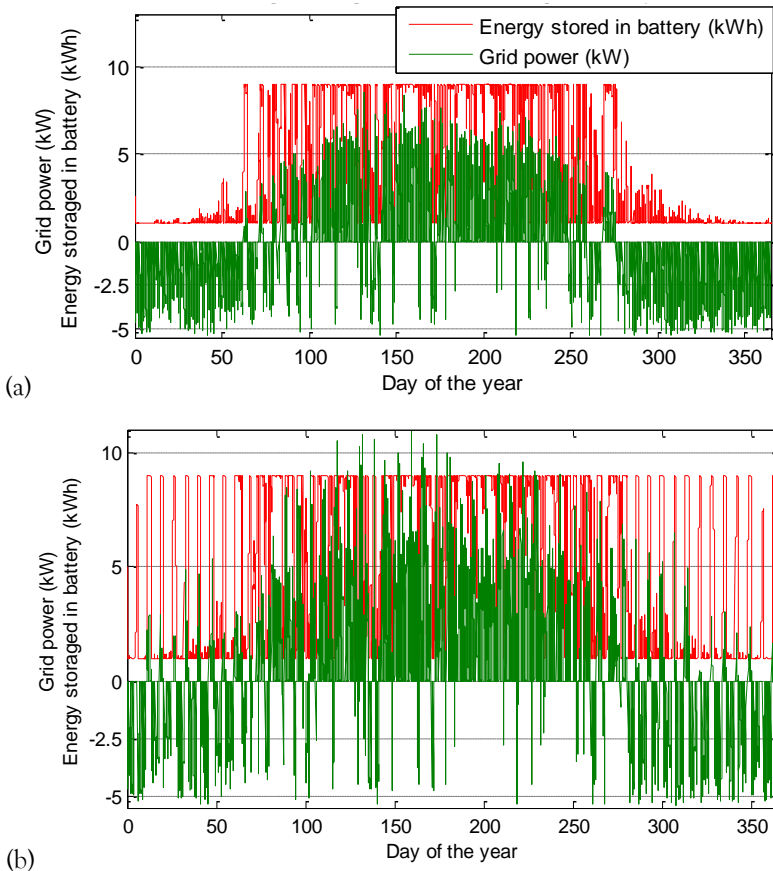


Fig. 3.13. Power exchanged with the grid (kW) and the stored energy in local storage (kWh) for the EV-PV charger for the year 2013 considering EV loads for (a) 7 days/week and (b) only on weekdays i.e. 5 days/week

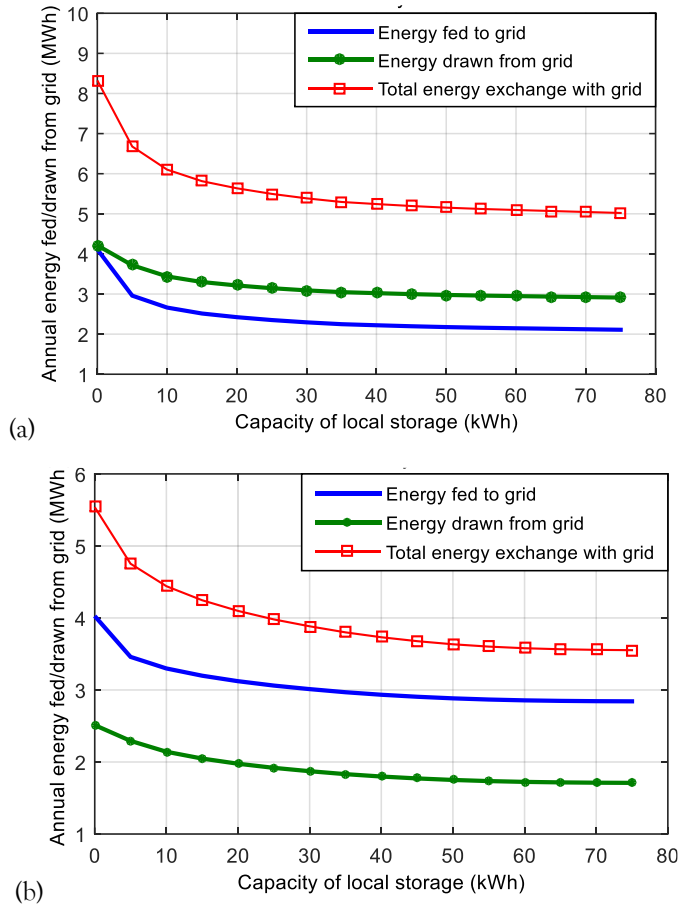


Fig. 3.14. Annual Energy exchanged with the grid for 2013 as a function of storage size, considering EV loads for (a) 7 days/week and (b) only on weekdays for 5 days/week using Gaussian EV profile G4.

Fig. 3.13 shows the power exchanged with the grid and the stored energy in the local battery bank for 2013 (1 min resolution), considering EV loads for both 7 days/week and only on weekdays using profile G4. For 7 days/week load, it can be clearly observed that the battery is eternally empty in the winter months due to lack of excess PV power for charging it. Similarly, the battery is full in the summer months (Day 80 to Day 270) due to high PV generation.

However, the local storage has a positive effect in the case of 5 days/week EV load. As seen in Fig. 3.13(b), the local storage gets periodically charged during the weekends even in winter (days 0 to 50 and days 300 to 365) as there is no EV and this helps supply the EV energy demands on Mondays and Tuesdays. However, for the rest of the week, the storage is depleted of energy in winter and remains full in summer.

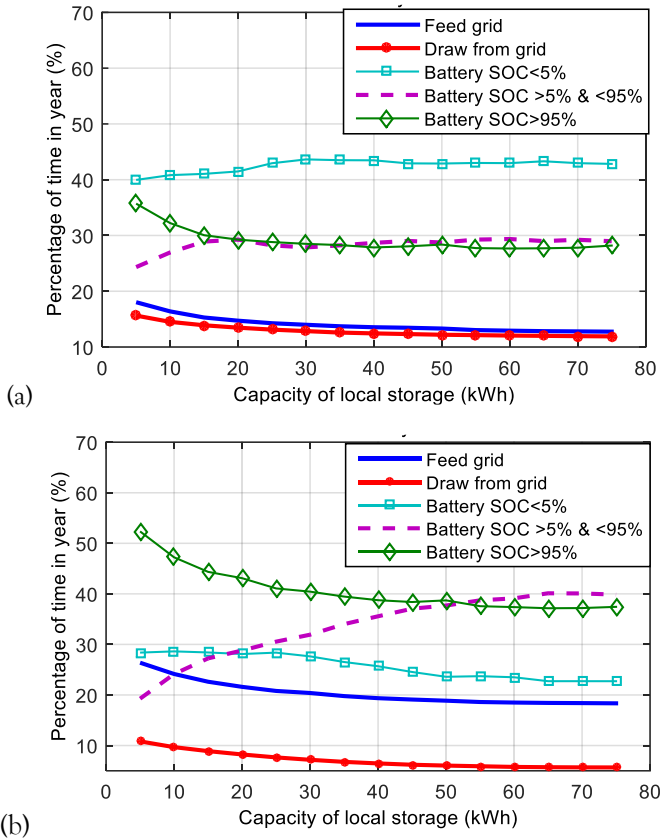


Fig. 3.15. Percentage of time in year when energy is exchanged with grid and battery exhibits specific state of charge for (a) 7 days/week and (b) 5 days/week using Gaussian EV profile G4

Since 10kWh storage is insufficient for making the EV-PV charger grid independent, the storage size was varied from 5kWh to 75kWh to study its impact on the grid energy exchange, as shown in Fig. 3.14 and Fig. 3.15.

It can be observed in Fig. 3.14 that the energy exchanged with the grid reduces with increasing storage size up to a certain point and then saturates henceforth. This means that even with large storage of up to 75kWh, there is still a minimum amount of energy drawn/fed to the grid and it is not possible to make the EV-PV charger grid independent. This is especially true for a country like the Netherlands which shows five times difference in summer and winter sunshine.

Storage SOC remaining > 95% or <5% are both not good for the system as it leaves the battery in an unutilized state; it is either nearly empty or fully charged. Since the battery is used with DOD of 80%, SOC of 95% and 5% are scaled according to the 80% used capacity of the battery. Fig. 3.15 shows that increasing the storage size has minimal impact in improving the utilization of the battery. For a 5-day load profile,

the battery is nearly full or empty (SOC >95% or <5%) for 70% of the time with 30kWh storage and for 65% of the time with 75kWh storage. This proves that with increasing the storage size by 2.5 times, the utilization of the battery is not proportional. Further, the percentage of time in a year for which the EV-PV charger feeds/draws power from the grid does not reduce much with increasing storage size as seen in Fig. 3.15. In case of 5 days/week load, the percentage of time for which energy is fed to the grid is relatively much higher than for 7 days/week load and the percentage of time when energy is drawn from the grid is lower.

From Fig. 3.14, it can be noted that small storage in the range of 5-15kWh exhibits a drastic reduction in grid dependency. This is because 75% of the variation in solar insolation between consecutive days is less than 15kWh. A small storage hence helps in balancing out diurnal and day-day solar variations. For 5 days/week and 7 days/week EV loads, the size of storage to achieve 25% reduction in energy exchanged with the grid is 10kWh. Based on current prices, a 10kWh storage using Li-ion batteries will cost 2000-4000€ [51]. If a smaller storage is preferred, a 5kWh storage can result in 17% and 20% reduction in grid energy exchange for 5 days/week and 7 days/week EV load respectively.

In order to be able to manage the seasonal variation, a few possible solutions are to use a hydrogen-based storage with electrolyzer and fuel cell, use a wind turbine to provide additional generation in winter or use a diesel generator. The investigation of these solutions is beyond the scope of this thesis.

3.6. Connecting multiple EVs to a single EV-PV charger

For the EV-PV charger, the ability to integrate more EVs into one charger will provide for a flexible and modular design. For example, at a workplace, it would be convenient for the EV owner to plug the car for charging in the morning, irrespective of how long the charging would take. With long parking times of 8h at the workplace, having one 10kW charger per car will be unnecessary as charging requirements would be less than $8\text{h} \times 10\text{kW} = 80\text{kWh}$ on a daily basis. Moreover, if a few EV chargers can cater to the charging needs of several EVs, then the cost of the charging infrastructure will be dramatically reduced when compared to using one charger per EV.

Therefore, it would be beneficial to look into methods by which multiple cars can be connected to a single charger in a modular way, referred henceforth as multiplexing. An important consideration based on the review in Chapter 2 is that the EV must be isolated from all power sources including the grid, PV and another EV during charging/V2G operation. In this chapter, four ways to multiplex several EVs to a single charger are proposed based on the multi-port converter of architecture 3 shown in Fig.2.4 (a), Fig.2.5(a) from Chapter 2. They are shown in Fig. 3.16(a)-(d) and are implemented as follows:

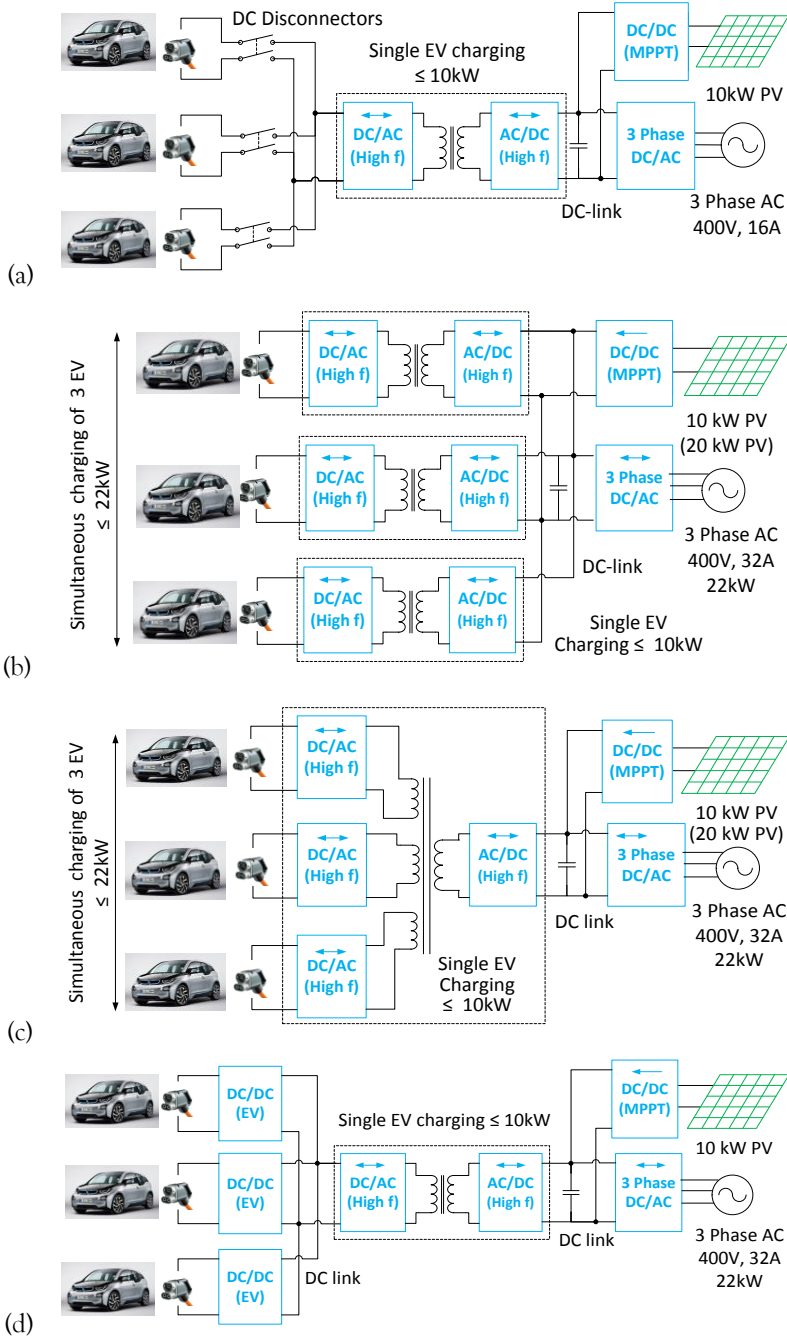


Fig. 3.16. Different ways to connecting a single EV charger to several EVs using MPC based on architecture 3: (a) Multiplexing 1, (b) Multiplexing 2, (c) Multiplexing 3, (d) Multiplexing 4

3.6.1. Multiplexing 1 – Using multiple charging plugs with DC disconnectors

Multiple CHAdeMO and CCS charging ports can be connected to a single EV-PV charger as shown in Fig. 3.16(a). At any point in time, only one of these charging ports is delivering power to the EV while the rest are separated using DC disconnectors. This ensures that the EVs are isolated from each other during charging. To start charging of a new car B while a car A is already charging, can be done by:

1. Reducing the charging power of car A to zero and then stop charging
2. Open DC disconnector of car A and then close the disconnector of car B
3. Initiate the charging of car B

3.6.2. Multiplexing 2 – Using multiple isolated DC/DC converters connected on DC link

Multiple DC/DC converters with isolation can be connected on the DC link of a single EV-PV charger as shown in Fig. 3.16(b). The advantage is more than one EV can be charging/discharging simultaneously as long as they are within the maximum power limit of 10kW. A three-phase grid connection of 32A can facilitate a combined charging of up to 22kW.

3.6.3. Multiplexing 3 – Multi-winding high-frequency transformer on DC-link

A multi-winding high-frequency transformer as mentioned in topology A can be used in the EV-PV charger as shown in Fig. 3.16(c). Each EV can be connected to one of the transformer winding. Similar to strategy 2, the advantage is that multiple EV can be charging or discharging simultaneously. The challenge lies in the design of the multi-winding transformer and its control. While the charging of multiple EV is possible with this strategy, the drawback is that the design is not modular. The transformer and control have to be redesigned based on the number of EV that need to be connected.

3.6.4. Multiplexing 4 – Multiple DC/DC converters at output

Multiple DC/DC converters without isolation can be connected to the DC output of the EV-PV charger as shown in Fig. 3.16(d). This is simpler than strategy 2, which requires multiple isolated DC/DC converters to ensure isolation of EV is from grid and PV. However, the major shortcoming of strategy 4 is the lack of isolation between one EV and another. As long as isolation between the cars is required as per the charging standards [52], [53], this strategy will not be technically feasible for simultaneous charging of EV.

Based on the above examination, it can be observed that strategy 1 is the simplest for integrating multiple EV to a single EV-PV charger. If simultaneous charging of EV is required, strategy 2 should be implemented. As will be seen in Chapter 5, the developed solar EV charger currently has the possibility for multiplexing using Multiplexing 1. In the future, Multiplexing 2 can be implemented if multiple isolated DC/DC converters are used on the central DC-link.

3.6.5. Ranking for charging of multiple EV

The Gaussian load profile G4 can deliver 30kWh energy to the EV. This energy could be distributed amongst multiple EVs if each car requires less than 30kWh of energy. Fig. 3.17 shows an example of the charging of three cars A,B,C with respect to the average irradiance for the month of July 2013.

Multiple cars can be arranged within the charging region and charging can be started according to priority R_v , where B_v^{max} is the capacity of EV battery pack (kWh); T_v^a , T_v^d , T_v^p are the EV arrival, departure and parking time at workplace(hr); SOC_v^a , B_v^a are the state of charge and energy stored in EV at arrival to work:

$$B_v^a = \frac{SOC_v^a}{100} B_v^{max} \tag{11 a}$$

$$T_v^p = T_v^d - T_v^a \tag{11 b}$$

$$R_v = \frac{1000}{B_v T_v^p} \tag{12}$$

The car with the highest priority is charged first. This method will give preference to the EV with low energy and less parking time, to charge first. Thus 30kWh of energy is delivered in total to the three cars, and the excess PV is fed to the grid. If any of the cars require additional energy or if a fourth car D has to be charged, then charging region D is utilized, where the EV is charged partly from PV and partly from the grid.

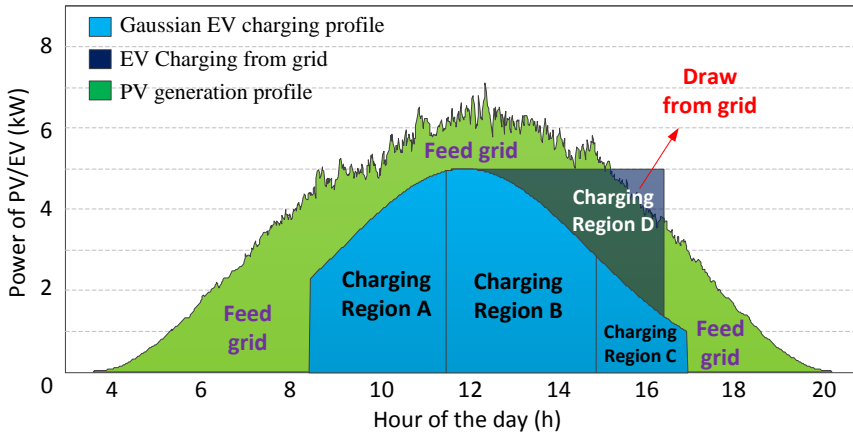


Fig. 3.17. Charging multiple EV using Gaussian charging profile

3.7. Conclusions

Workplace charging of EV from solar energy provides a sustainable gateway for transportation in the future. It provides a direct utilization of the PV power during the day and exploits the solar potential rooftops of buildings. In this chapter, the PV system design and smart charging for a solar energy powered EV charging station for the Netherlands is investigated.

Using data from KNMI, it was seen that the optimal tilt for PV panels in the Netherlands to get maximum yield is 28°. The annual yield of a 10kW PV system using Sunpower modules was 10,890kWh. Using a 2-axis solar tracker increases the yield by 17%, but this gain is concentrated in summer. Solar tracking was thus found to be ineffective in increasing the winter yield, which is the bottleneck of the system. The average daily PV energy production exhibits a difference of five times between summer and winter. This necessitates a grid connection for the EV-PV charger to supply power in winter and to absorb the excess PV power in summer.

Since high-intensity insolation occurs rarely in the Netherlands, the PV power converter can be undersized with respect to the PV array by 30%, resulting in a loss of only 3.2% of the energy. Such a technique provided in this chapter can be used for different metrological conditions in the world for optimally sizing the power converter with respect to the rated power of the PV array.

Smart charging of EV facilitates the variation of EV charging power so as to closely follow the solar generation. Since solar generation exhibits a Gaussian variation with time over a 24h period, Gaussian EV charging profile with a peak at 1200hr and a peak lesser than the installed peak power of the solar panels would be most ideal. The exact value of the Gaussian peak and width are location dependent. EV charging using Gaussian charging profile G3 and G4 with peak power of 5kW and 4kW were found to closely follow the PV generation curve of Netherlands. They delivered 30kWh energy to the EV for both 5 days/week and 7 days/week EV load and resulted in minimum energy exchange with the grid. For charging multiple EV at the workplace, a priority mechanism was proposed that will decide the order of precedence for EV charging, based on stored energy and parking time of EV.

It was proved that a local battery storage does not eliminate the grid dependence of the EV-PV charger in the Netherlands, especially due to seasonal variations in insolation. However small-sized storage in the order of 10kWh helped in mitigating the day-day solar variations and reduced the grid energy exchange by 25%. The storage remains empty in winter for 7 days/week load and gets periodically full in weekends for 5 days/week load. The storage sizing is site-specific and method presented here can be used for different locations to determine the optimal storage size.

Connecting multiple EVs to a single EV-PV charger provides flexibility of charging at the workplace. This can be achieved by using DC disconnectors or several isolated DC/DC converters on the central DC-link to realize a modular design.

3.8. References

- [1] University of Iowa, *Solar electric vehicle charging station*. University of Iowa.
- [2] G.-Y. Choe, J.-S. Kim, and B.-K. Lee, "A Bi-directional battery charger for electric vehicles using photovoltaic PCS systems," in *2010 IEEE Vehicle Power and Propulsion Conference*, 2010, pp. 1–6.
- [3] C. Hamilton, G. Gamboa, J. Elmes, R. Kerley, A. Arias, M. Pepper, J. Shen, and I. Batarseh, "System architecture of a modular direct-DC PV charging station for plug-in

- electric vehicles,” in *IECON 2010 - 36th Annual Conference on IEEE Industrial Electronics Society*, 2010, pp. 2516–2520.
- [4] B. E. Noriega, R. T. Pinto, and P. Bauer, “Sustainable DC-microgrid control system for electric-vehicle charging stations,” in *2013 15th European Conference on Power Electronics and Applications (EPE)*, 2013, pp. 1–10.
- [5] G. R. Chandra Mouli, P. Bauer, and M. Zeman, “Comparison of system architecture and converter topology for a solar powered electric vehicle charging station,” in *2015 9th International Conference on Power Electronics and ECCE Asia (ICPE-ECCE Asia)*, 2015, pp. 1908–1915.
- [6] Oak Ridge National Laboratory, *Solar-Assisted Electric Vehicle Charging Stations*. 2011.
- [7] P. Goli and W. Shireen, “PV powered smart charging station for PHEVs,” *Renew. Energy*, vol. 66, pp. 280–287, Jun. 2014.
- [8] G. Gamboa, C. Hamilton, R. Kerley, S. Elmes, A. Arias, J. Shen, and I. Batarseh, “Control strategy of a multi-port, grid connected, direct-DC PV charging station for plug-in electric vehicles,” in *2010 IEEE Energy Conversion Congress and Exposition*, 2010, pp. 1173–1177.
- [9] F. Fattori, N. Anglani, and G. Muliere, “Combining photovoltaic energy with electric vehicles, smart charging and vehicle-to-grid,” *Sol. Energy*, vol. 110, pp. 438–451, Dec. 2014.
- [10] C. Capasso and O. Veneri, “Experimental study of a DC charging station for full electric and plug in hybrid vehicles,” *Appl. Energy*, vol. 152, pp. 131–142, Aug. 2015.
- [11] P. Denholm, M. Kuss, and R. M. Margolis, “Co-benefits of large scale plug-in hybrid electric vehicle and solar PV deployment,” *J. Power Sources*, vol. 236, pp. 350–356, 2013.
- [12] D. P. Birnie, “Solar-to-vehicle (S2V) systems for powering commuters of the future,” *J. Power Sources*, vol. 186, no. 2, pp. 539–542, Jan. 2009.
- [13] P. Nunes, T. Farias, and M. C. Brito, “Day charging electric vehicles with excess solar electricity for a sustainable energy system,” *Energy*, vol. 80, pp. 263–274, Feb. 2015.
- [14] P. J. Tulpule, V. Marano, S. Yurkovich, and G. Rizzoni, “Economic and environmental impacts of a PV powered workplace parking garage charging station,” *Appl. Energy*, vol. 108, pp. 323–332, Aug. 2013.
- [15] P. Tulpule, V. Marano, S. Yurkovich, and G. Rizzoni, “Energy economic analysis of PV based charging station at workplace parking garage,” in *IEEE 2011 EnergyTech*, 2011, pp. 1–6.
- [16] M. van der Kam and W. van Sark, “Smart charging of electric vehicles with photovoltaic power and vehicle-to-grid technology in a microgrid; a case study,” *Appl. Energy*, vol. 152, pp. 20–30, Aug. 2015.
- [17] P. Nunes, T. Farias, and M. C. Brito, “Enabling solar electricity with electric vehicles smart charging,” *Energy*, vol. 87, pp. 10–20, Jul. 2015.
- [18] S. A. Cutler, B. Schmalberger, and C. Rivers, “An intelligent solar ecosystem with electric vehicles,” in *2012 IEEE International Electric Vehicle Conference*, 2012, pp. 1–7.
- [19] S. Mesentean, W. Feucht, H.-G. Kula, and H. Frank, “Smart charging of electric scooters for home to work and home to education transports from grid connected photovoltaic-systems,” in *2010 IEEE International Energy Conference*, 2010, pp. 73–78.
- [20] P. Kadar and A. Varga, “PhotoVoltaic EV charge station,” in *2013 IEEE 11th International Symposium on Applied Machine Intelligence and Informatics (SAMII)*, 2013, pp. 57–60.
- [21] M. Brenna, A. Dolara, F. Foiadelli, S. Leva, and M. Longo, “Urban Scale Photovoltaic

- Charging Stations for Electric Vehicles,” *IEEE Trans. Sustain. Energy*, vol. 5, no. 4, pp. 1234–1241, Oct. 2014.
- [22] P.-E. Dziadek, W. Feucht, A. Mittnacht, H.-G. Kula, and H. Frank, “Eco-friendly application of EVs for home-to-work and home-to-education transports,” in *2013 IEEE International Conference on Industrial Technology (ICIT)*, 2013, pp. 705–709.
- [23] S. Mesentean, W. Feucht, A. Mittnacht, and H. Frank, “Scheduling Methods for Smart Charging of Electric Bikes from a Grid-Connected Photovoltaic-System,” in *2011 UKSim 5th European Symposium on Computer Modeling and Simulation*, 2011, pp. 299–304.
- [24] N. Kawamura and M. Muta, “Development of solar charging system for plug-in hybrid electric vehicles and electric vehicles,” in *2012 International Conference on Renewable Energy Research and Applications (ICRERA)*, 2012, pp. 1–5.
- [25] Y. Gurkaynak and A. Khaligh, “Control and Power Management of a Grid Connected Residential Photovoltaic System with Plug-in Hybrid Electric Vehicle (PHEV) Load,” in *2009 Twenty-Fourth Annual IEEE Applied Power Electronics Conference and Exposition*, 2009, pp. 2086–2091.
- [26] Y. Gurkaynak and A. Khaligh, “A novel grid-tied, solar powered residential home with plug-in hybrid electric vehicle (PHEV) loads,” in *2009 IEEE Vehicle Power and Propulsion Conference*, 2009, pp. 813–816.
- [27] D. M. Robalino, G. Kumar, L. O. Uzoechi, U. C. Chukwu, and S. M. Mahajan, “Design of a docking station for solar charged electric and fuel cell vehicles,” in *2009 International Conference on Clean Electrical Power*, 2009, pp. 655–660.
- [28] M. Tesfaye and C. C. Castello, “Minimization of impact from electric vehicle supply equipment to the electric grid using a dynamically controlled battery bank for peak load shaving,” in *2013 IEEE PES Innovative Smart Grid Technologies Conference (ISGT)*, 2013, pp. 1–6.
- [29] C. C. Castello, T. J. LaClair, and L. C. Maxey, “Control strategies for electric vehicle (EV) charging using renewables and local storage,” in *2014 IEEE Transportation Electrification Conference and Expo (ITEC)*, 2014, pp. 1–7.
- [30] “CESAR Database, Koninklijk Nederlands Meteorologisch Instituut (KNMI),” <http://www.cesar-database.nl>, 2014.
- [31] “Datasheet - Sun power E20-327 PV module,” 2015.
- [32] “Approximate solar coordinates, The United States Naval Observatory (USNO).” [Online]. Available: <http://aa.usno.navy.mil/faq/docs/SunApprox.php>.
- [33] J. J. Michalsky, “The Astronomical Almanac’s algorithm for approximate solar position (1950–2050),” *Sol. Energy*, vol. 40, no. 3, pp. 227–235, Jan. 1988.
- [34] P. P. G. Loutzenhiser, H. Manz, C. Felsmann, P. A. Strachan, T. Frank, and G. M. Maxwell, “Empirical validation of models to compute solar irradiance on inclined surfaces for building energy simulation,” *Sol. Energy*, vol. 81, no. 2, pp. 254–267, Feb. 2007.
- [35] A. B. Sproul, “Derivation of the solar geometric relationships using vector analysis,” *Renew. Energy*, vol. 32, no. 7, pp. 1187–1205, Jun. 2007.
- [36] V. V. Ashok, C. Onwudinanti, G. R. Chandra Mouli, and P. Bauer, “Matching PV Array Output With Residential and Office Load by Optimization of Array Orientation,” in *PowerTech (POWERTECH), 2015 IEEE Eindhoven*, 2015, pp. 1–6.
- [37] T. M. M. Klucher, “Evaluation of models to predict insolation on tilted surfaces,” *Sol. Energy*, vol. 23, no. 2, pp. 111–114, Jan. 1979.
- [38] E. Skoplaki and J. A. Palyvos, “On the temperature dependence of photovoltaic module electrical performance: A review of efficiency/power correlations,” *Sol. Energy*, vol. 83, no. 5, pp. 614–624, 2009.

- [39] A. Q. Jakhriani, A. K. Othman, A. R. H. Rigitand, and S. R. Samo, "Comparison of solar photovoltaic module temperature models," *World Appl. Sci. J.*, vol. 14, pp. 1–8, 2011.
- [40] O. Isabella, G. G. Nair, A. Tozzi, J. H. Castro Barreto, G. R. Chandra Mouli, F. Lantsheer, S. van Berkel, and M. Zeman, "Comprehensive modelling and sizing of PV systems from location to load," *MRS Proc.*, vol. 1771, pp. 1–7, Apr. 2015.
- [41] E. Drury, A. Lopez, P. Denholm, and R. Margolis, "Relative performance of tracking versus fixed tilt photovoltaic systems in the USA," *Progress in Photovoltaics: Research and Applications*, vol. 22, no. 12, pp. 1302–1315, 2014.
- [42] F. O. Hocaoglu, Ö. N. Gerek, and M. Kurban, "Solar Radiation Data Modeling with a Novel Surface Fitting Approach," in *Neural Information Processing*, vol. 4985, Springer Berlin Heidelberg, 2008, pp. 460–467.
- [43] F. O. Hocaoglu, O. N. Gerek, and M. Kurban, "The effect of model generated solar radiation data usage in hybrid (wind–PV) sizing studies," *Energy Convers. Manag.*, vol. 50, no. 12, pp. 2956–2963, Dec. 2009.
- [44] J. Harikumaran, G. Vereczki, C. Farkas, and P. Bauer, "Comparison of quick charge technologies for electric vehicle introduction in Netherlands," in *IECON Proceedings (Industrial Electronics Conference)*, 2012, pp. 2907–2913.
- [45] "Specifications - Tesla Powerwall (7kWh, 350-450V)," 2015.
- [46] L. Lam and P. Bauer, "Practical Capacity Fading Model for Li-Ion Battery Cells in Electric Vehicles," *IEEE Trans. Power Electron.*, vol. 28, no. 12, pp. 5910–5918, Dec. 2013.
- [47] "Datasheet - SMA SUNNY ISLAND 6.0H / 8.0H," 2015.
- [48] N. Narayan, T. Papakosta, V. Vega-Garita, J. Popovic-Gerber, P. Bauer, and M. Zeman, "A simple methodology for estimating battery lifetimes in Solar Home System design," in *2017 IEEE AFRICON*, 2017, pp. 1195–1201.
- [49] J. Sridhar, G. R. Chandra Mouli, and P. Bauer, "Analysis of load shedding strategies for battery management in PV-based rural off-grids," in *PowerTech (POWERTECH), 2015 IEEE Eindhoven*, pp. 1–6.
- [50] S. B. Peterson, J. Apt, and J. F. Whitacre, "Lithium-ion battery cell degradation resulting from realistic vehicle and vehicle-to-grid utilization," *J. Power Sources*, vol. 195, no. 8, pp. 2385–2392, 2010.
- [51] "Global EV Outlook 2016," *Int. Energy Agency*, pp. 1–51, 2016.
- [52] SAE Standard J1772, "SAE Electric Vehicle and Plug-in Hybrid Electric Vehicle Conductive Charge Coupler," pp. 1–93, 2010.
- [53] "Standard IEC 62196 - Plugs, socket-outlets, vehicle connectors and vehicle inlets - Conductive charging of electric vehicles - Part 1, 2, 3," pp. 1–176, 1–122, 1–71, 2014.

4

Topology for three-port EV-PV-Grid converter

4. Topology for three-port EV-PV-Grid converter

This chapter is based on:

A. Bassa, G. R. Chandra Mouli and P. Bauer, "Evaluation of Topologies for a Solar Powered Bidirectional Electric Vehicle Charger," *IET Power Electronics*, under review.

Summary

In the previous chapters, the review of existing EV-PV system architecture and topology was performed, followed by the system level design of the proposed 10kW EV-PV charger. In chapter 4 and 5, the goal will be to design and build the three-port power electronic converter based on system architecture 3 to integrate EV, PV and the grid. As a first step, in this chapter, the aim is to determine the optimal power converter topology for the 10kW bidirectional charger.

Several topologies are compared using a comparison framework, and the best topology is chosen based on the number of components, converter efficiency, volume, controllability and current ripple. The topologies are optimally designed considering different switching frequency, silicon carbide devices, magnetic cores, current ripple and interleaved operation. The analysis shows that the best topology is a three port converter with a central DC-link with a 3-leg interleaved boost converter for the PV, two-level inverter with sinusoidal modulation for grid and a 4-phase interleaved flyback converter for EV.

Outline

Section 4.1 provides a detailed overview of the two power converter architectures for the EV-PV charger, namely the DC-link based and impedance network based. The corresponding topologies that have been developed in existing literature and the specifications of the EV-PV converter that would be developed in this thesis are presented. Section 4.2 presents the design methodology used to design each of the converter and the loss models used for estimating the converter efficiency and power density. In section 4.3, the comparison framework and weight criteria used for comparison of topologies are explained. Using the DC-link based topologies as a base, section 4.4.4.6 designs and compares different power topologies for the PV, EV and grid port respectively. The impedance network based EV-PV charger is designed in section 4.7 using a quasi Z-source converter. Using the comparison framework from section 4.3, the optimal topology for the three-port EV-PV converter is determined in section 4.8.

4.1. Introduction

A solar powered EV charging system would require the EV, PV and AC grid and a power electronic interface to connect them. The converter must enable the charging of EV from both the solar panels and the AC grid and facilitate bi-directional charging and discharging (V2G) of the EV battery. The bidirectional operation will ensure that the EV can support the grid through V2G and EV battery can be a storage for the PV.

The goal of this chapter is to determine the optimal topology for a three-port power converter (TPC) that integrates EV, PV and the AC grid. Determining the optimal topology is important as it will ensure that the converter has high efficiency, high power density and is of low-cost. The optimal topology is chosen based on the several indices: efficiency, converter volume, the number of components, ripple, controllability and possibility for efficiency improvement.

4.1.1. Power converter types for EV-PV charging

In chapter 2, it was shown why the DC-link based topology is better than using a high-frequency transformer link based topology. This was because isolation is not required between the PV and grid as per the standards as long as the leakage currents are within limits. At the same time, isolation is always required between the EV and the PV, grid. Keeping this in mind, two different converter types are possible for the TPC connecting the EV, PV, and grid:

1. DC-link based:

The first converter type is based on a DC-link (Fig. 4.1.a), which acts as a high voltage energy buffer between the ports. There are three sub-converters with different control algorithms: the PV converter is responsible for maximum power point tracking (MPPT); the EV converter controls the EV (dis)charging power and the inverter is responsible for the power balance with the AC grid. The advantage of this architecture is that it's simple and allows for DC interconnection of EV and PV, thus reducing DC/AC conversion losses. The architecture improves AC/DC inverter utilization, as it can be used during the day for solar production and overnight for EV charging. The design is modular and additional converters can be interfaced on the central DC-link. Further, the DC-link can be connected to a future DC micro-grid. The main disadvantage is that it requires a big DC link capacitor and three different controllers, one for each sub-converter.

2. Impedance-network based:

The second TPC converter type is based on an impedance network converter, like the Z-source converter (Fig. 4.1.b) [1]-[3]. This TPC has an inherent variable voltage DC-link which is connected to an isolated DC-DC converter for the EV charging. The advantage is that it has a lower component count (increased reliability¹) and only two

¹ Reliability of a power converter is affected by several factors such as operating temperature, temperature change, voltage and current stresses on components and several others; and number of components is one of them.

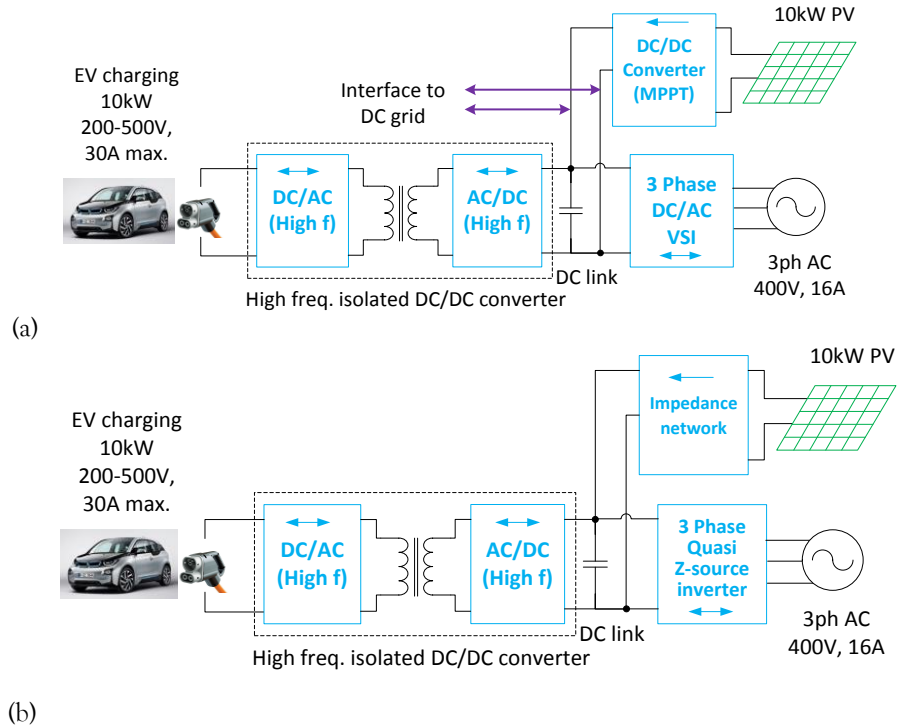


Fig. 4.1. Block diagram of three-port EV-PV converter with (a) DC-link and three sub-converters; (b) Impedance network converter for PV and isolated converter for EV

control algorithms, one per converter. The main disadvantage is the increased control complexity of impedance network converters, and the topology is not intrinsically modular. The variable voltage DC-link poses challenges in the control and design of the isolated EV converter.

4.1.2. Literature Review and contributions

Several topologies and system architecture for PV charging of EVs are reviewed in [4], [5]. It has three main conclusions on the PV charging system for EV: grid-connected systems are more popular than off-grid systems, a TPC with a DC-link is the best system architecture, and that isolation of EV converter was neglected by most works even though it is required by the standards [6]. Four types of EV-PV system architecture are proposed in [4] based on whether an integrated power converter or two separate power converters are used for PV and EV; and if the PV and EV are interconnected on AC or DC.

References [7]-[11] propose the power exchange over AC through the use of a separate PV inverter and AC EV charger (possibly with energy storage). The disadvantage of this approach is that PV and EV are fundamentally DC. So power exchange over AC causes additional losses and needs two inverters instead of one.

Hence an integrated converter with DC-link based power exchange between EV and PV is preferred [12]-[18]. Charging of EV from PV using a 2.4kW Zero Voltage Transition (ZVT) Pulse Width Modulation (PWM) buck converter connected to a 210V DC bus was proposed in [12], [13]. The EV charger is unidirectional with no isolation, and there is high ripple due to the use of buck converter. A 2.4kW prototype with closed-loop control was built that offers EV charging but not V2G. The use of EV charging to mitigate solar intermittency was analyzed in [14], [15]. A 10kW bidirectional DC/DC converter with zero voltage switching quasi square-wave (ZVS-QS) at 98% efficiency is used for EV charging (no isolation). 575V central DC link interconnects PV and EV converters.

A 3kW bidirectional wireless EV charger based on H-bridge inverters and powered from PV is developed in [16]. Up to 90% peak efficiency is reported when using series compensated rectangular coils. A 3.3kW TPC with boost converter for PV, H-bridge inverter for grid and interleaved buck converter for EV (with no isolation) interlinked on 380V DC link is presented in [17], [19]. 7% to 15% improved efficiency compared to AC power exchange is reported. A 5kW TPC made of boost converter for PV, 1-phase H-bridge inverter for grid and buck converter for EV (with no isolation) interlinked on 400V DC link is proposed in [18]. Two DC/DC converters were used for charging an EV from PV via a 48V buffer battery in [20]. The 3.3kW system does not have bidirectional power flow, connection to the grid or isolation for the EV.

In the above studies, the designs are not suited for three-phase high-power applications (>5kW). There is no consideration for the EV charging standards with respect to charging current ripple, isolation and EMI. Similarly, a review of several EV-PV topologies concluded that most designs neglected the EV isolation requirements [4]. Due to its simplicity, the most popular choice for the EV-PV system was to use a separate grid-connected PV inverter and an AC EV charger as opposed to an integrated converter.

In [21], [22], a high-frequency AC-link based on a multi-winding transformer was used for integrating EV, battery storage and renewable energy sources. While the topology provides the benefit of isolation between all ports and is applicable for high powers, it is not useful for EV-PV application because of two reasons. European regulations do not stipulate a need for isolation between the PV and grid. Secondly, PV and EV are DC by nature, so AC-link will lead to unnecessary conversion steps.

In the case of impedance network based topologies, three topologies for EV-PV charging using an isolated DC/DC EV charger are compared in [1] namely, Z-source converter, transformer-less PV inverter and high-frequency isolated PV inverter. The symmetrically isolated 5kW Z-source converter with 10kW EV charger was chosen as the best topology. However, the design procedure cannot be scaled up for higher powers, and the Z-source converter has a high ripple at the PV port preventing maximum power point tracking (MPPT) operation. The quasi-Z-source converter with DC link was used for EV and battery charging in [2], [3]. The topology facilitated bidirectional operation but does not have any isolation for the battery.

4.1.3. Contributions

Based on the above literature review, the contributions of this work compared to earlier works are:

1. There is no existing research that quantitatively compares bidirectional EV-PV converter topologies considering efficiency, power density, component count, controllability and efficiency improvement. This chapter addresses this research gap by comparing nine topologies on the above-listed indices. The topologies considered have isolation for the EV as required by the standards [6], [23] and will enable V2G operation.
2. Each topology is designed considering two switching frequency (50 kHz, 100 kHz), eight silicon carbide (SiC) MOSFETs, thirteen SiC diodes, seventeen inductor core materials of varied core sizes, different modulation techniques and heatsink sizes. This ensures that each topology is itself designed optimally, so there is a fair comparison of topologies. Such detailed design of EV-PV topologies for the sake of comparison has not been done before.
3. Interleaving of converters (one to five stages) is implemented for the appropriate topologies to reduce the ripple at the EV and PV port. This is vital as a high ripple at PV port prevents operation at the PV MPPT point [24], and it reduces the battery lifetime at the EV port [25]. The previous works did not consider the impact of ripple.
4. The chapter focuses on the design of a three-phase, high power converter (10kW) for fast charging EV from solar PV. The existing research in this domain is predominantly on single phase, low power applications (<5kW).

4.1.4. Converter specifications

Table 4.1 and Fig. 4.1 shows the specifications and block diagram of the 10kW EV-PV power converter, respectively. The converter is designed to operate with EV and PV with a wide voltage range, small ripple, high peak and partial load efficiency (>95%) and high power density. The rated power of $P_{nom}=10\text{kW}$ is chosen because EV fast chargers of $\geq 50\text{kW}$ are typically built using modular 10kW power modules. Second, 10kW presents a good balance between PV generation and (Level 2) EV charging requirements [26].

4.2. Design of Converters and Loss Modeling

This section provides a method to optimally design a converter topology to achieve high efficiency and power density considering different design parameters: switching frequency, magnetic core, copper windings, semiconductor devices, capacitor and heat sinks. As shown in Fig. 4.3, this will require several iterations using an accurate loss model of the converter where the design parameters are varied at every cycle. At the end of the iterations, the converter components, volume and efficiency (i.e. losses) of the optimized design are obtained. The loss models presented below are built based on [27]-[29].

Table 4.1. Specifications of EV-PV converter

Parameter	Symbol	Value
Nominal power	P_{nom}	10kW
PV MPPT Voltage	V_{pv}	350-700V
PV MPPT Current	I_{pv}	0 - 30A
PV current ripple (peak-peak)	$\Delta I_{pv\%}$	< 10% of $I_{pv}(\max)$
PV voltage ripple (peak-peak)	$\Delta V_{pv\%}$	< 0.5%
EV voltage	V_{ev}	200-500V
EV current (Bidirectional)	I_{ev}	-30A - +30A
Internal DC-link voltage	V_{dc}	750V (for Arch. 1)
Total Harmonic Distortion		< 5%
AC grid connection		400V, 50Hz AC, 16A

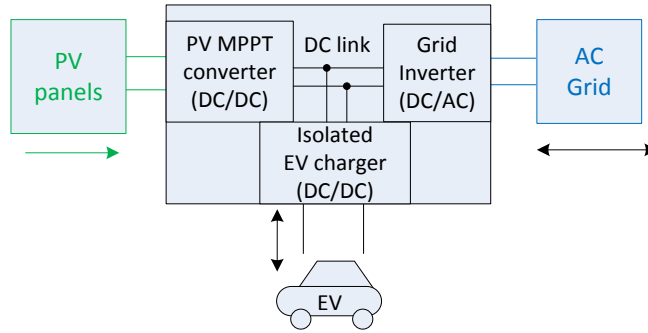


Fig. 4.2. Grid connected bidirectional 10kW three-port EV-PV charger

The switching frequency will determine the size of the passive elements and losses in the semiconductor devices, while the right components can help in reducing the losses. Two different switching frequencies f_{sw} , namely 50 kHz and 100 kHz are considered. A lower and higher frequency are investigated because at a lower switching frequency, a larger inductor is required but the switching losses in the semiconductors are lower. The vice versa occurs at the high frequency of 100 kHz.

1. Semiconductors

SiC MOSFETs and schottky diodes are used in the design instead of silicon devices. This is due to the lower switching/conduction losses and practically zero reverse recovery of the diode. MOSFETs considered are CREE's C3M[0280090D, 0120090D,0065090D] and C2M[0280120D,0160120D, 0080120D, 0040120D, 0025120D]. The chosen CREE Schottky diodes are C3D[04065A, 08065A, 10065A]; C5D50065D and C4D[02120A,05120A, 08120A,10120A, 15120A,20120A,20120D, 30120D, 40120D].

In order to find the optimal switch and diode for each topology, the worst case operating point of the converter in terms of semiconductor losses is considered. The

device which yields the lowest losses at that point is chosen. This method does not prioritize the losses over the entire operating range but minimizes the maximum power dissipation, thereby reducing the heat sink size. 25% margin is used in the device voltage rating to account for transient voltage spikes. The maximum semiconductor junction temperature is set to 100°C at an ambient temperature of ≤ 45°C. This ensures low cabinet/heat-sink/junction temperature for a long lifetime of the converter.

The losses in the SiC MOSFETs P_S consist of conduction losses $P_{S,con}$ and the switching losses $P_{S,sw}$. The losses depend on the drain-source current I_{DS} , on-state resistance $R_{DS(on)}$, drain-source voltage V_{DS} , junction temperature T_j , gate voltage V_{GS} , gate resistance R_G , switching ON and OFF energies E_{on}, E_{off} ; which are calculated for every operating point based on the datasheet.

$$P_S = P_{S,con} + P_{S,sw} \tag{1}$$

$$P_{S,con} = I_{DS,rms}^2 R_{DS(on)}(I_{DS}, T_j, V_{GS}) \tag{2}$$

$$P_{S,sw} = f_{sw} \{ E_{on}(V_{DS}, I_{DS}, T_j, R_G) + E_{off}(V_{DS}, I_{DS}, T_j, R_{GS}) \} \tag{3}$$

For certain soft-switching topologies like zero voltage switching (ZVS), the E_{on}, E_{off} are correspondingly modified based on energy stored in the MOSFET output capacitance C_{oss} . The gate resistance is 2.5Ω and the gate voltage is -5V/20V and -4V/15V for the C2M and C3M series of MOSFET, respectively.

The conduction losses in the schottky diode $P_{D,con}$ can be modeled as a forward voltage $U_{D,0}$ and a series resistor R_D and are obtained from the datasheets. When

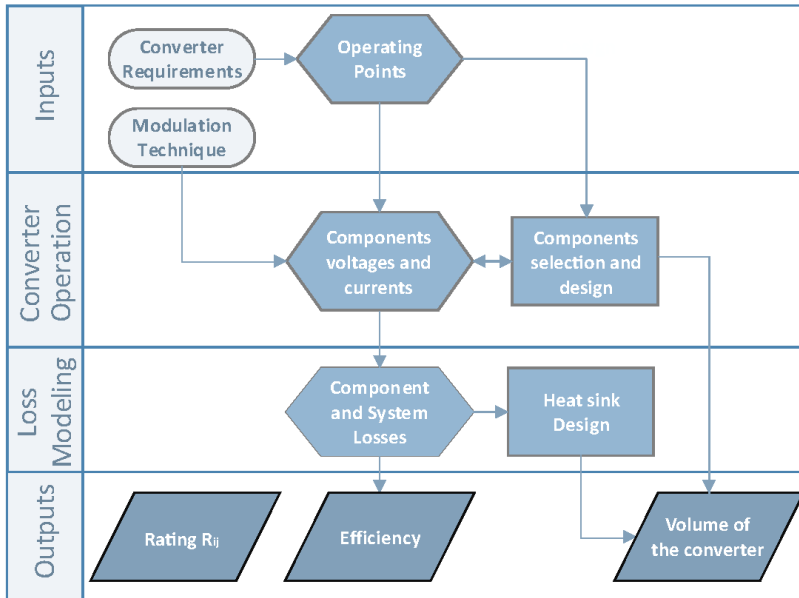


Fig. 4.3. Overview of the methodology used to rate every topology

switching off a schottky diode, there is a loss $P_{D,sw}$ due to the switch-off energy E_{Dch} for charging the junction capacitance. Therefore, the total losses of a diode, P_D is the sum of the conduction losses, $P_{D,con}$ and switch-off losses $P_{D,sw}$, where I_D and V_R are the diode current when ON and reverse voltage when OFF :

$$P_D = P_{D,con} + P_{D,sw} \quad (4)$$

$$P_D = \left\{ I_{D,avg} U_{D0}(\tau_j) + I_{D,rms}^2 R_{D(\tau_j)} \right\} + V_R E_{Dch}(V_R) f_{sw}$$

2. Inductor and HFT design

The aim of the inductor design is to design an inductor that is low on losses and volume, in order to maximize efficiency and power density. Six inductor core size (E16,E25,E32,E42,E55,E65) and four inductor core materials (Magnetics R,P material; FerroxCube 3C92, 3C96) are used. The maximum core size is restricted to E65 to ensure easy Printed Circuit Board (PCB) mounting. The inductor design follows an optimization procedure:

1. For the given topology and specifications, the inductor size and energy storage requirements are estimated. Cores which do not fulfil the requirements are discarded.
2. For the rest of the cores, the minimum and maximum number of turns and the corresponding air gap length are calculated, considering flux saturation limits.
3. The optimal litz wire configuration is determined based on skin and proximity effects, with a maximum current density of $4A/mm^2$ [30]
4. The inductor copper and core losses are calculated for every configuration.
5. The optimal inductor is chosen based on the lowest index F_L that considers both the inductor/HFT losses P_L and total volume V_L as:

$$F_L = \frac{1}{2} \frac{P_L}{P_{L,max}} + \frac{1}{2} \frac{V_L}{V_{L,max}} \quad (5)$$

where $P_{L,max}$, $V_{L,max}$ are the highest losses and largest volume amongst all designs, respectively.

The losses in the inductor, P_L can be estimated from the core (P_{core}) and copper losses (P_{cu}). The core losses depend on the material used, the magnetic flux in the core and the frequency. The Improved Generalized Steinmetz Equation (iGSE) [31] is used to estimate the core losses per unit volume, P_v , based on the Steinmetz-equation parameters (A , a , b) :

$$P_L = P_{core} + P_{cu} = V_e P_v + R_L I_{L(rms)}^2 \quad (6)$$

where R_L is the winding resistance, $I_{L(rms)}$ the RMS inductor current and V_e the volume of the core.

A similar procedure is followed for the losses in the HFT after estimating the flux swing of the core. For the HFT, U cores from four materials (Matglas, MKM nano, Vitroperm, Hitachi Finemet) and 18 sizes (AMCC 4 to AMCC 250) are used. In the case of the LCL toroidal filters (L_{fconv} , L_{fg} , C_f) for the AC grid inverters, 21 powder alloy toroidal cores from Magnetics (KoolM μ 26,60,125; Xflux 26; MPP 14,26;

Amoflux; High flux 26,125) are considered. The LCL filters are designed in such a way so as to limit the Total Harmonic Distortion (THD) to less than 5% and the maximum value of individual harmonics are limited as stipulated in [32]. The filter inductors are sized based on [33]–[35] and the losses estimated using the original Steinmetz equation. The final selection of both the HFT and toroid filter is performed according to (5).

3. Capacitors

Input and output capacitors (C_{in} , C_{out}) are used for filtering the current ripple and to provide a DC voltage. Capacitor design is given importance as the volume occupied can be significant even though the losses are relatively small. Epcos film capacitors of type B32776{-450 to -1100} and B32796{-250 to -40} are used in the design. The capacitor losses, P_{caps} depend on the Equivalent Series Resistance (ESR) R_{ESR} and the series $N_{c,s}$ and paralleled $N_{c,p}$ connection of capacitors to increase the rated voltage and capacitance, respectively:

$$P_{caps} = R_{ESR,set} I_{cap,rms}^2 = \frac{N_{c,s}}{N_{c,p}} \left(R_{ESR} + \frac{D_F}{2\pi f_{eq} C_r} \right) I_{cap,rms}^2 \quad (7)$$

where f_{eq} , $I_{cap,rms}$ are the equivalent frequency and RMS capacitor current, C_r the rated capacitance and D_F the dielectric factor. It is a requirement that the losses do not increase the capacitor temperature beyond 90°C at full load.

The optimum set of capacitors is selected similar to (5), which minimizes the volume and PCB area based on the actual and maximum area (A_{set} , $A_{set,max}$) and volume (V_{set} , $V_{set,max}$) of the capacitor set:

$$F_C = \frac{1}{2} \frac{A_{set}}{A_{set,max}} + \frac{1}{2} \frac{V_{set}}{V_{set,max}} \quad (8)$$

4. Heatsink

The heat sink size is computed from the losses in each semiconductor and the maximum allowed junction temperature. The Cooling System Performance Index (CSPI) method is used to find the heatsink volume [36]:

$$V_S = \frac{1}{R_{th,sa} C_{SPi}} = \frac{1}{(T_S - T_a/P_t) C_{SPi}} \quad (9)$$

where $R_{th,s-a}$ is the thermal resistance of the heat sink to the ambient and V_S , the volume of the heat sink. In this study, a CSPI of $C_{SPi}=10$ has been selected. The necessary $R_{th,sa}$ is obtained via the heat sink temperature T_S , the ambient temperature T_a and the total losses in the semiconductors P_t . Hi-Flow 300P thermal pad with performance of 0.94 °C/W is used. The key is to ensure that the heat sink size is as small as possible in order to increase the power density.

4.3. Comparison framework

4.3.1. Comparison criteria

A comparison framework is used to find the optimal topology for the three-port converter based on a weight factor W_j , as shown in Table 4.2 [37]. The topologies are rated (R_{ij}) from one (worst) to five (best) for each criterion and then the rating is multiplied by the weight factor to give the total score $T_{score,i}$:

$$T_{score,i} = \sum_{j=1}^{N_{cri}} W_j R_{ij} \quad (10)$$

where i refers to the topology, j the criterion and N_{cri} the total numbered of criteria. The converter with the highest score is the best suited for the given requirements and application. The ratings R_{ij} are shown in Table 4.2 for:

1. Number of components- switches, diodes, magnetic elements and capacitors,

A high number of components increases the complexity and cost of the system and reduces the reliability. The weights for different components are shown in Table 4.2. In the case of switches, they have the highest costs and lead to a higher number of gate drive and control circuits; hence a weight of 4. On the other hand, diodes have a weight of 2 as they are uncontrolled elements. The number of magnetic cores adds to the cost, losses and volume of the converter and hence has a weight of 3.

2. Efficiency and volume of converter

Converter efficiency and volume, estimated in the previous section, are the most important criterion and therefore have a weight of 6 and 5, respectively. The European efficiency is used for PV and grid port [38]. Both inverting and rectifying efficiencies are equally considered for grid port. For the EV port, the average efficiency over the entire operating range shown in Table 4.1 is considered. The converter volume is estimated as the sum of the volumes of the heat sink, the inductors/HFT and the capacitors. In general, a converter with higher efficiency has lower losses and has a smaller volume due to a smaller heatsink.

3. Current ripple in EV battery

The EV port topologies are compared based on the EV current ripple magnitude as it significantly affects the battery lifetime [25]. Hence it has a weight of 3.

4. Controllability and efficiency improvement

Controllability addresses the control complexity of a given topology, and it has a weight of 3. The converter efficiency can generally be increased by better modulation techniques, use of snubbers and circuitry to implement Zero Current Switching (ZCS) and/or ZVS. Using a weight of 2, the topologies are rated on how easy it is to implement and how much efficiency improvements can be achieved.

It must be noted that the results of the comparison are dependent on the weight factors that have been given to the various criteria. The weight factors chosen here meet the requirements of this design. Hence, changing the weight factors and the

criterion will result in a different set of topologies being found to be optimal. Secondly, while a brief design of the topologies is presented in this chapter for the sake of comparison, the detailed design and experimental evaluation of the chosen topologies is presented in Chapter 5.

4.3.2. Topologies considered

In the next sections, nine topologies based on the DC-link and impedance network converter are designed based on the procedure in section II and are compared based on the above framework. In the case of DC-link topologies, they are split as candidates for PV, EV and grid port. The PV port candidates considered are the interleaved boost converter, the coupled inductors interleaved boost converter and the three-level boost converter. The EV port candidates considered are the two-phase dual active bridge and the interleaved flyback converter. For the grid port, the topologies considered are the two-level converter, three-level neutral point clamped converter and the three-level t-type converter. Finally, the quasi Z-Source inverter is analyzed for the impedance network based topology.

Table 4.2. Weight and rating scale for comparison framework of topologies

Criterion	j	W _j	Port	0	1	2	3	4	5
Number of switches	1	4	PV	≥6	Linear scale				≤1
			EV	>18					≤8
			Grid	>20					≤6
Number of diodes	2	2	PV	≥6	Linear scale				≤1
			EV	>18					≤2
			Grid	>20					≤6
Number of magnetic core sets	3	3	All	≥6	Linear scale				≤1
Number of capacitors	4	1	All	≥6	Linear scale				≤1
Efficiency η [%]	5	6	PV	η<98.0	Linear scale				η≥99.5
			EV	η<97.25					η≥98.75
			Grid	η<97.5					η≥99.0
			qZSI	η<95.5					η≥98.5
Converter Volume V _c [dm ³]	6	5	PV	V _c >0.6	Linear scale				V _c <0.3
			EV	V _c >1.5					V _c <0.6
			Grid	V _c >0.9					V _c <0.4
			qZSI	V _c >1.5					V _c <0.7
Efficiency improvement	7	2	All	Not possible	Very Difficult	Difficult	Minor challenges	Easy	Very Easy
Controllability	8	3	All	Very difficult	Difficult	Major challenges	Minor challenges	Easy	Very Easy
EV current ripple [A]	9	3	EV	>55	Linear scale				0

It must be noted that several other topologies can be included in the analysis as well. For example, the three-phase dual active bridge can be used for the EV port, where an extra phase is used when compared to the two-phase dual active bridge to substantially lower the filter ratings [39]–[41]. Similarly, isolated resonant topologies can be used for the EV port that use large filters and inductors in the resonant circuit to enable soft switching [42], [43]. Further, coupled inductor quasi Z-source converter can be designed instead of the non-coupled version of the converter which can have a lower ripple, while at the same time increasing the complexity of the control and inductor design [44], [45]. The analysis of these and other possible topologies is beyond the scope of this thesis.

4.4. DC Link - PV Port Candidates

4.4.1. Topologies

Fig. 4.4, Fig. 4.5 and Fig. 4.6 show the three different topologies for the PV port, respectively: the Interleaved Boost Converter (IBC) [28], [46], [47], the Coupled Inductors Interleaved Boost Converter (CIIBC) [48], [49] and the Three-Level Boost Converter (TLBC) [50], [51]. The PV converter must meet specifications in TABLE 4.1 and operate at the MPPT of the PV array.

The IBC is based on paralleling the conventional boost converter, which reduces current and conduction losses in each leg. It has reduced EMI and high efficiency at light load, at the expense of a higher component count. The CIIBC is a modified version of the IBC which reduces the number of inductors by using coupled inductors. This reduces the overall size and improves the regulation of power converters, by improving the current sharing.

Direct and reverse coupling configurations can be used to reduce input ripple or inductor ripple (coupling coefficient, $k=\pm 0.35, \pm 0.5, \pm 0.9$ considered). Lastly, the TLBC offers the advantages of a three-level topology with reduced voltage ratings and double switching frequency at the input current. However, the output current circulates through two diodes, increasing the losses.

4.4.2. Optimal configuration of topology and comparison

The procedure from section II is used to find the optimal configuration for each topology. The configuration with the highest score for the three topologies is shown in Table 4.3: the 3 phases IBC, the 4 phases CIIBC with coupling factor $k=0.9$ and the 2 phases TLBC, all of them switching at 50 kHz. The estimated efficiencies (for $V_{PV} = 500V$) and volume for the three converters are shown in Fig. 4.7.a and Fig. 4.7.b, respectively.

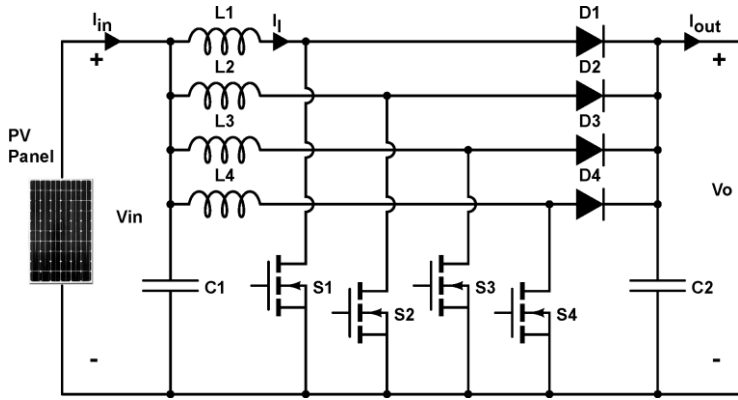


Fig. 4.4. Structure of the four phases interleaved boost converter (IBC)

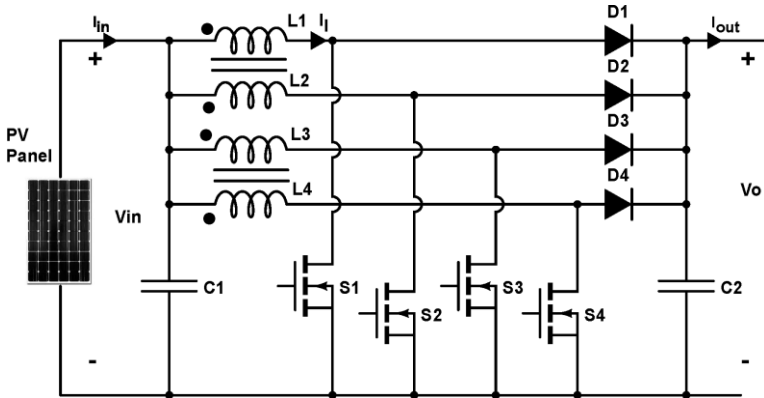


Fig. 4.5. Structure of the four phase coupled inductor interleaved boost converter

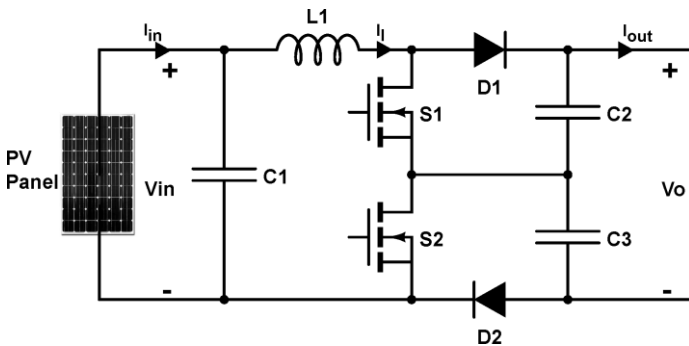


Fig. 4.6. Structure of a one phase three level boost converter (TLBC)

Fig. 4.7.a shows how the highest efficiency of up to 99.5% is reached by the IBC. The steep jumps in the efficiency of CIIBC are due to the inductor coupling and different conduction modes of the converter. The IBC and CIIBC have significantly lower losses over the operating range than the TLBC making the converter more efficient and smaller (due to a smaller heatsink). On the other hand, the CIIBC uses smaller inductors, and less filtering is needed, resulting in a lower converter volume.

The ratings and overall scores in Table 4.3 are estimated based on the comparison framework in section III. From Table 4.3, it can be seen that the 3-phase IBC at 50 kHz frequency has the highest overall score. It is hence the most optimal topology for the PV port.

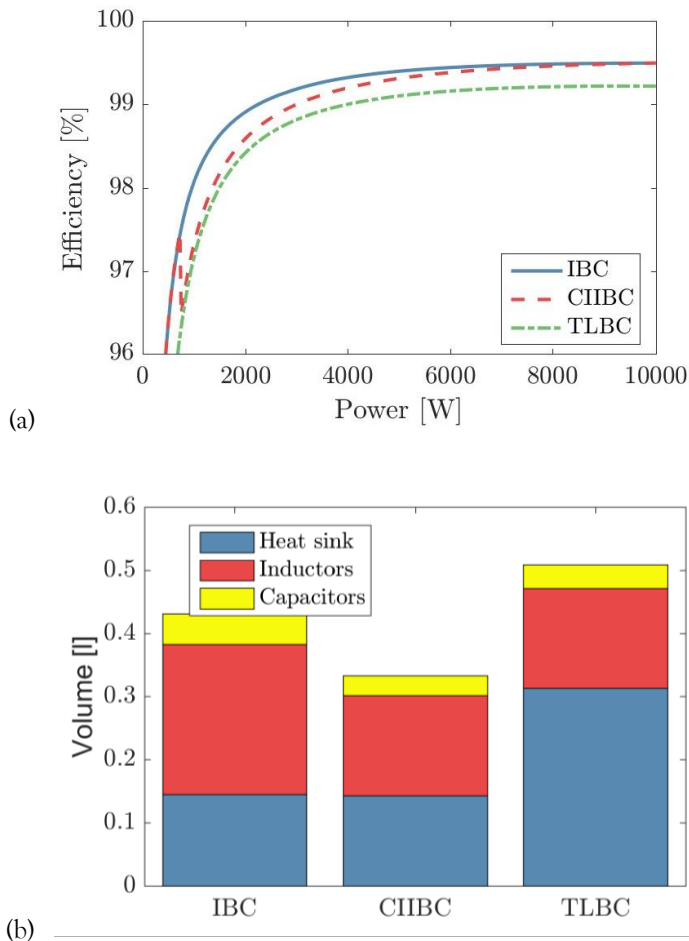


Fig. 4.7. (a) Efficiency of PV port converter candidates for $V_{PV} = 500V$; (b) Volume of the PV port converter candidates: IBC, CIIBC and TLBC

Table 4.3. Optimal design and Score of PV port converters

Optimal Design		IBC 3 ph., 50 kHz		CIIBC (k= -0.9) 4 ph., 50 kHz		TLBC 2 ph., 50 kHz	
MOSFET		C2M0040120D		C2M0080120D		C2M0025120D	
DIODE		C4D20120A		C4D15120A		C4D20120A	
Inductance per phase, Magnetic core, turns, resistance		L1=874 μ H, E65, 3C92, 45 turns, 42m Ω		L1=11.3mH, E65, Magnetics R, 29 turns, 34m Ω		L1=328 μ H, E65, 3C92, 22 turns, 10m Ω	
C_{in}, C_{out} [μ F]		0.688, 8.230		0.510, 2.258		0.511, 4.736	
Criterion	W_j	Value	R_{ij}	Value	R_{ij}	Value	R_{ij}
Switches	4	3	3	4	2	4	2
Diodes	2	3	3	4	2	4	2
Cores	3	3	3	2	4	2	4
Caps.	1	2	4	2	4	3	3
Efficiency [%]	6	99.18	3.93	99.04	3.47	98.77	2.57
Volume [dm ³]	5	0.431	2.82	0.332	4.47	0.509	1.52
Eff. Imp.	2	-	3	-	1	-	2
Control	3	-	4	-	1	-	3
$T_{score} = \sum W_j R_{ij}$		86.68		76.17		63.02	

4.5. DC link - EV port candidates

4.5.1. Topologies

Several DC-DC isolated topologies can be selected for the purpose of charging EV batteries. For this comparison, the Dual Active Bridge (DAB) [29], [52] shown in Fig. 4.8 and the Interleaved Bidirectional Flyback Converter (IBFC) [53], [54] shown in Fig. 4.9, have been selected as possible topologies. Since isolated topologies have lower efficiency than non-isolated topologies, the DAB is operated in ZVS mode, and the IBFC is operated in quasi-resonance (QR), to reduce the switching losses.

The DAB consists of two full bridges connected via an HFT and is operated with phase shift modulation (PSM) [52]. In each phase, a total of eight switches are

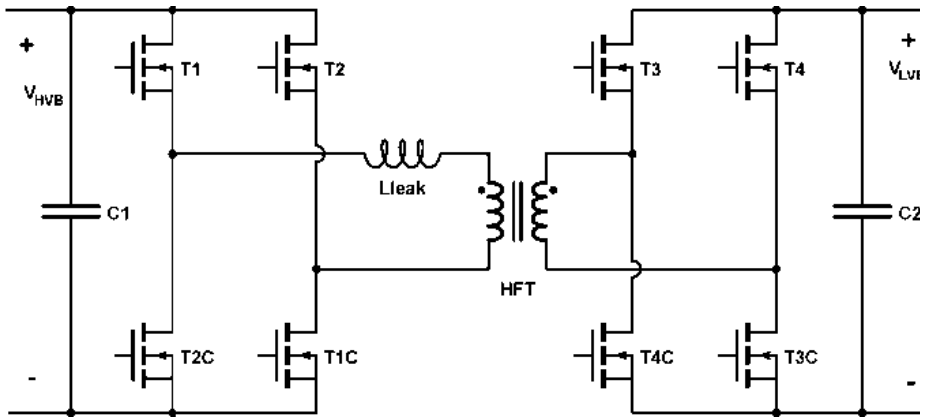


Fig. 4.8. Topology of the Dual Active Bridge (DAB)

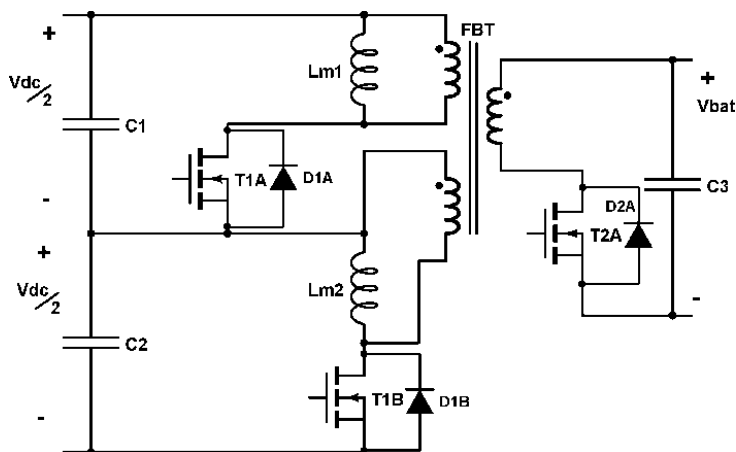


Fig. 4.9. Topology of the Interleaved Bidirectional Flyback Converter (IBFC)

necessary, and an extra external inductance if the transformer’s leakage inductance is not enough. The DAB has inherent isolation, bidirectionality and ZVS possibility. It acts as an ideal current source, and the control is easy to implement. But, it has high current ripple both at the input and the output. In order to increase the range of the ZVS operation of DAB, the leakage inductance L_{leak} and turn ratio n have to be optimally sized.

On the other hand, the IBFC consists of two or more typical flyback converters in parallel, where the secondary diodes are replaced by a switch in order to add bidirectionality. The main advantage is the low number of switches and the lower current ripple if a high number of phases are interleaved. In the topology shown in Fig. 4.9, the flyback transformer has a split primary winding and must have a low leakage inductance to reduce the voltage stress on the switches. QR makes the converter operate with a variable frequency (in this case, 50-200 kHz) and reduces the energy lost due to the output capacitance.

Table 4.4. Review of the analyzed EV port converters.

Optimal Design		DAB (PSM-ZVS) 2 phases, 100 kHz		IBFC (QR) 4 phases, 50-200 kHz	
MOSFET		C2M0080120D primary C2M0025120D second		C2M0040120D	
DIODE		Body diode		C4D15120A primary C4D20120A second.	
Leakage Inductance: magnetic core, turns, resistance, air gap		$L_{leak}=125\mu\text{H}$, E65, 3C92, 36 turns, 41m Ω , 0.35cm air gap		-	
HFT/Inductor (per phase): magnetic core, turns, resistance, air gap		AMCC 50, Vitrop. 500F 40:20 turns, No air gap 17m Ω : 90m Ω		$L_{m1}=L_{m2}=454\mu\text{H}$, E65 core, Magnetics R, 40:20 turns, 48m Ω : 12m Ω 0.12cm air gap	
Input capacitor [μF]		2.32		11.983	
Criterion	W_j	Value	R_{ij}	Value	R_{ij}
Switches	4	16	1	12	3
Diodes	2	0	5	12	1.88
Cores	3	3	3	4	2
Caps.	1	1	5	1	5
Eff. [%]	6	98.03	2.6	98.63	4.6
Vol. [dm ³]	5	1.22	1.56	0.77	4.06
Eff. Impr.	2	-	4	-	2
Control	3	-	3	-	2
Current ripple	3	53.13	0.17	28.21	2.44
Tscore= $\sum W_j R_{ij}$		68.91		91.98	

4.5.2. Optimal configuration of topology and comparison

The design has been performed based on section II, and the best topology configuration is shown in Table 4.4 and Fig. 4.10: the 2 phases DAB at 100 kHz and the 4 phases IBFC in QR. For the DAB and IBFC, the average efficiency for the entire operating range is 98.03 and 98.57; while the average full load efficiency over the voltage range is 97.04 and 98.63, respectively.

Hence the IBFC performs much better than the DAB in spite of the higher switching frequency. In terms of size, the DAB has a bigger volume due to the external inductance and larger heat sink. Finally, the output ripple is much lower for the IBFC by nearly a factor of two. These three factors are reflected in the ratings in Table 4.4, where it is clear that the IBFC with an overall score of 91.98 is better topology than DAB with 68.91 as the score.

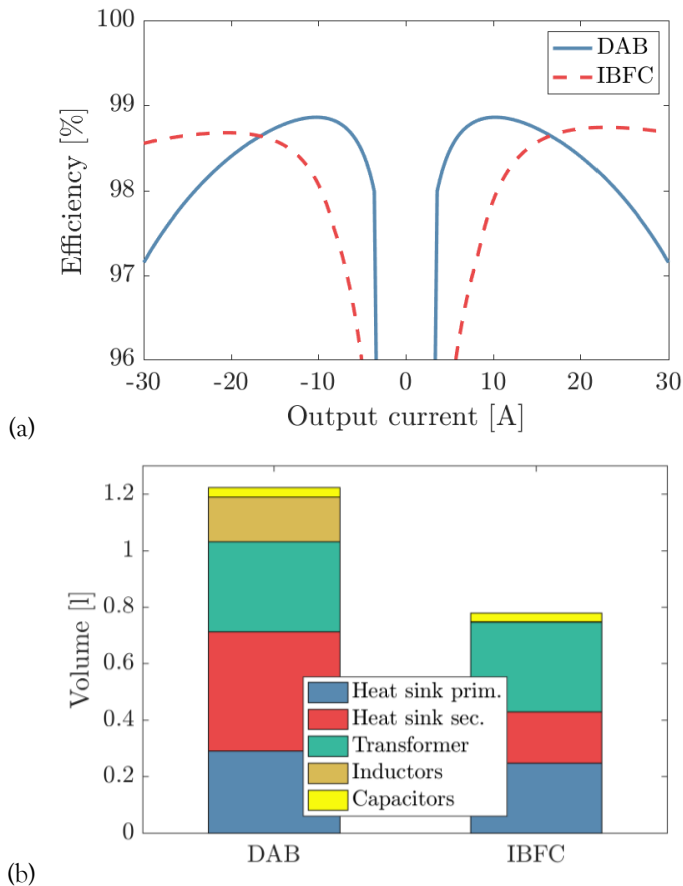


Fig. 4.10. (a) Efficiency for $V_{EV} = 332V$ and (b) Volume of the EV port converter candidates namely the DAB and IBFC

4.6. DC link - grid port candidates

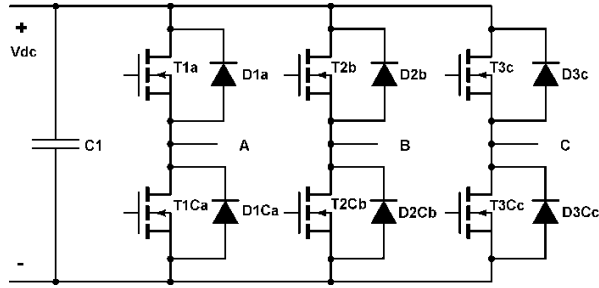


Fig. 4.11. Structure of the Two Level Converter (2LC)

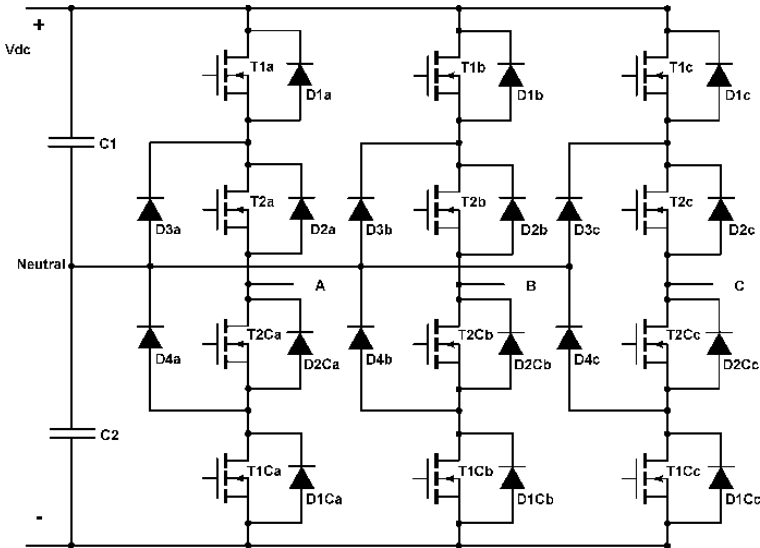


Fig. 4.12. Structure of the Three Level Neutral Point Clamped Converter (3LNPC)

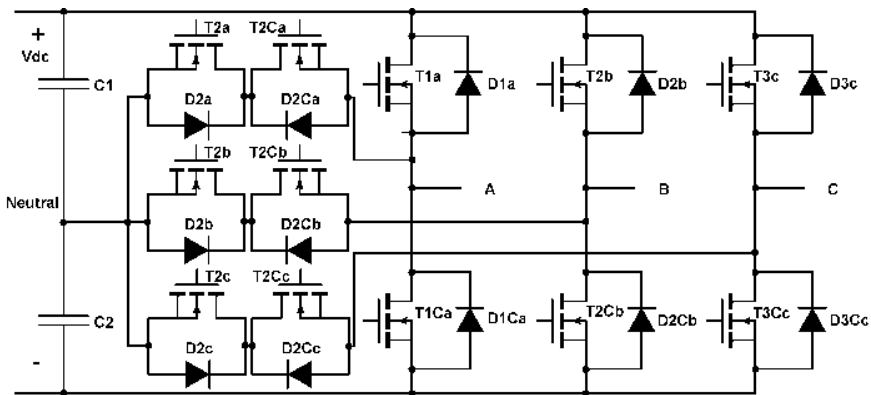


Fig. 4.13. Structure of the Three Level T-Type Converter (3LT2C)

4.6.1. Topologies

The topologies considered for the TPC's grid port converter are: Two Level Converter (2LC) also known as Voltage Source Inverter (VSI) [55] shown in Fig. 4.11, Three Level Neutral Point Clamped Converter (3LNPC) [56] shown in Fig. 4.13 and the Three Level T-Type Converter (3LT2C) [57] shown in Fig. 4.12. Each topology is designed with different modulation techniques: Sinusoidal PWM (SPWM), Space Vector PWM (SVPWM) [58] and Near-State PWM (NSPWM) [59] for the 2LC; and SVPWM and 2-Medium-1-Zero-Vector PWM (MZVPWM) [60] are applied to both the three-level topologies, 3LNPC and 3LT2C.

2LC is the simplest two-level topology and consists of six switches with the corresponding freewheeling diodes in anti-parallel. It is the most used DC-AC topology, due to the low number of components and the simple modulation technique. However, it has a high THD and high switching losses. The three-level topologies clamp the neutral of the DC bus to the output: the 3LNPC clamps using diodes while the 3LT2C relies on MOSFETs with anti-parallel diodes. These topologies have lower output THD and lower output ripple, at the cost of increased components and the modulation complexity. The 3LT2C requires fewer components than the 3LNPC but requires higher voltage ratings.

Table 4.5. Review of the optimal configurations of the analyzed Grid port converters

Optimal Design	2LC, SPWM, 50kHz		3LNPC SVPWM, 50kHz		3LT2C SVPWM, 50kHz		
	Value	R_{ij}	Value	R_{ij}	Value	R_{ij}	
MOSFET	C2M0025120D		C2M0025120D		C2M0025120D		
DIODE, (T-DIODE)	C4D20120A		C5D50065D		C4D20120A, C5D50065D		
LCL filter parameters	$L_{fconv}=480\mu\text{H}$ $L_{fg}=16\mu\text{H}$ $C_f=3.16\mu\text{F}$		$L_{fconv}=214\mu\text{H}$ $L_{fg}=6\mu\text{H}$ $C_f=1.03\mu\text{F}$		$L_{fconv}=214\mu\text{H}$ $L_{fg}=6\mu\text{H}$ $C_f=1.03\mu\text{F}$		
Input capacitor [μF]	40.26		36.39		36.39		
Criterion	W_j	Value	R_{ij}	Value	R_{ij}	Value	R_{ij}
Switches	4	6	5	12	2.86	12	2.86
Diodes	2	6	5	18	0.71	12	2.86
Input Caps.	1	3	3	8	0	8	0
Efficiency [%]	6	98.41	3.03	98.73	4.1	98.63	3.77
Volume [dm^3]	5	0.721	1.79	0.432	4.68	0.411	4.89
Eff. Impr.	2	-	3.5	-	1	-	1
Control	3	-	5	-	3	-	2
$T_{score}=\sum W_j R_{ij}$		82.13		71.86		72.23	

4.6.2. Optimal configuration of topology and comparison

The best topology configuration for grid port and the modulation strategies are shown in Table 4.5: 2LC, with SPWM, 3LNPC with SVPWM and 3LT2C with SVPWM, all operating at 50 kHz. The grid topologies are not compared based on the number of cores and capacitors for the output LCL filter as they all require the same number of cores and capacitors but of different value, volume and losses. The converter losses and volume estimation include that of the LCL filter as well.

Fig. 4.14 shows the efficiency and volume of the grid port topologies. The results indicate a marginally higher efficiency and much lower volume of three-level topologies when compared to the 2LC two-level topology. The larger volume of the 2LC stems from the need for larger LCL filter and a bigger DC input capacitor. But, the 2LC has a higher overall score as it requires a lesser number of switches and diodes and has a simpler control. Hence the 2LC with SPWM is the optimal topology for the grid port.

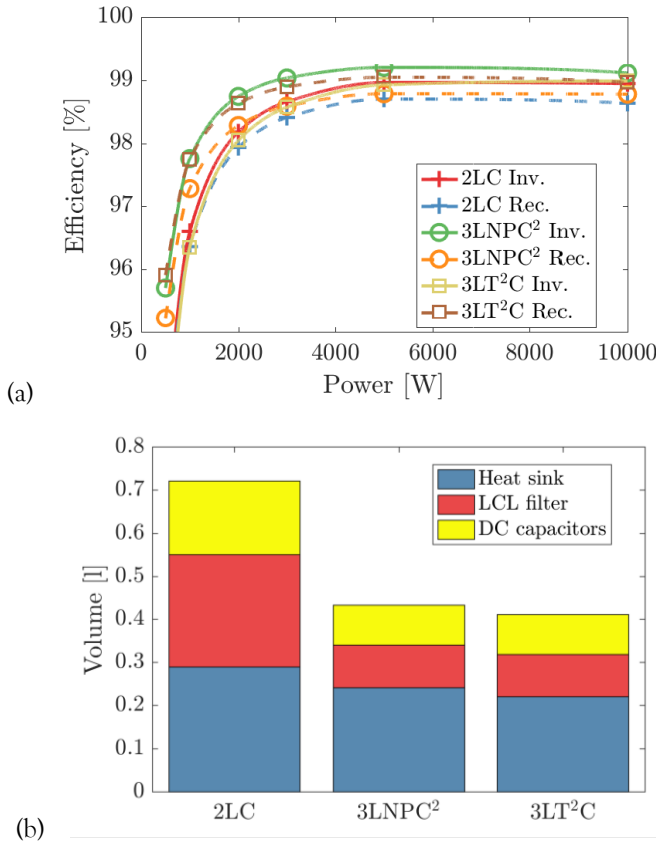


Fig. 4.14. (a) Efficiency of rectifier and inverter mode and (b) Volume of the grid port converter candidates

4.7. Impedance-network based converter

4.7.1. Operation of quasi Z-Source Inverter

The quasi Z-Source Inverter (qZSI) [61] in Fig. 4.15 is a topology derived from the traditional Z-source inverter (ZSI) [62], [63]. It can be used to connect the PV and grid as shown in Fig. 4.1.b. The qZSI inherits all the advantages of the ZSI namely lower component ratings and constant DC current from the source. It can realize buck/boost, inversion and power conditioning in a single stage. The qZSI boosts the input voltage by turning on all the switches in the triple bridge, known as the *shoot-through* state. When the converter is not in the *shoot-through* state, it is controlled like the 2LC, with SVPWM. The voltages across the capacitors are constant in steady state, making the topology suitable for connecting to the EV port topologies. However, this voltage ranges between $\sqrt{2}\sqrt{3}V_{ph} = 563V$ and $777V$, (the inverter voltage when maximum boost is required) increasing the complexity of designing the EV port converter.

4.7.2. Design and comparison of topology

Based on section II, III, the optimal configuration of the qZSI is determined and is shown in Table 4.6. The rating R_{ij} for number of components is estimated separately for the PV and grid part of the qZSI based on Table 4.2 while it's multiplied by two for the other parameters. The low component count of the Z-source converter results in a high rating for the number of switches and diodes. However, the main problem of the qZSI is the need for two big inductors of $L1=L2=1083\mu H$ and four capacitors ($C1,C2,Cz1,Cz2$) for the impedance network if the ripple and current requirements have to be met. Each inductor is composed of eight E65 core (configured in two parallel rows of four series inductors) which makes the converter lossy and bulky. Further, the impedance network diodes have high currents equal to twice the input current and so, three parallel diodes are needed. It must be noted that the core size is limited to E65 to make the design suitable for PCB mounting and manufacturing and the paralleling of diodes is possible as SiC diodes have a positive temp coefficient.

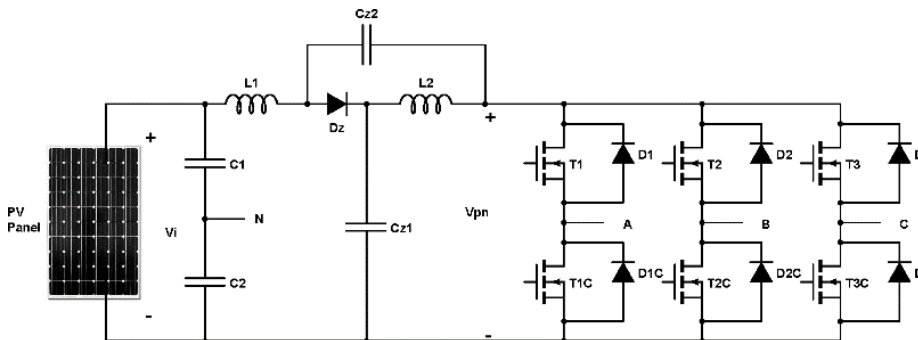


Fig. 4.15. The structure of the quasi Z-Source Inverter

Table 4.6. Review of the quasi Z-Source Inverter

Optimal Design		qZSI, 50kHz	
MOSFET		C2M0025120D	
DIODE (Dz)		C4D20120A, 3 in parallel	
Impedance network Inductance (L1,L2), Capacitance (C1,C2,Cz1,Cz2)		L1=L2=1083.35μH (32 E65 core inductors of 542μH) C1=C2=0.952μF, Cz1=37.7μF, Cz2=37.7μF (C1,C2,Cz1,Cz2 are made of 11 capacitors)	
542μH Inductor: Magnetic core, turns, resistance		3C92, 35 turns, 25mΩ	
LCL filter		$L_{fconv}=214\mu\text{H}$ $L_{fg}=6\mu\text{H}, C_f=1.034$	
Criterion	W_j	Value (PV, Grid)	R_{ij} (PV, Grid)
Switches	4	(0, 6)	(5, 5)
Diodes	2	(3, 6)	(3, 5)
Cores	3	(16,-)	(0, -)
Caps.	1	(11,0)	(0,5)
Efficiency [%]	6*2	97.58	3.47
Volume [dm ³]	5*2	4.37	0
Eff. Impr.	2*2	-	1.5
Control	3*2	-	3
$T_{rating}=\sum W_j R_{ij}$		126.64	

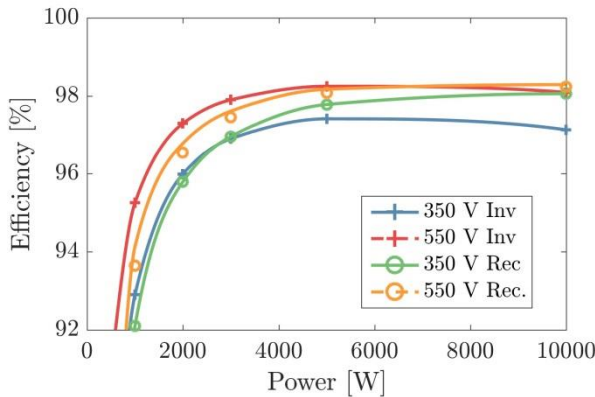


Fig. 4.16. Efficiency of inverter and rectifier mode for $V_{pv} = 230\text{V}$ for the quasi Z-Source Inverter (qZSI)

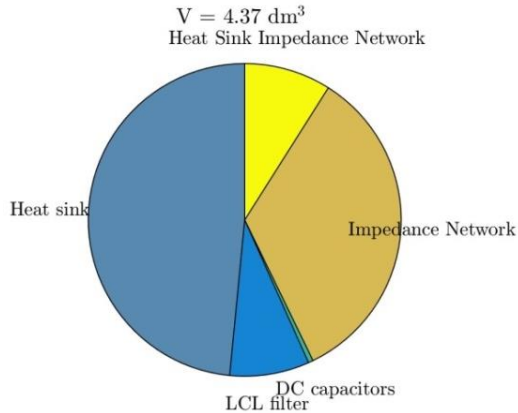


Fig. 4.17. Volume distribution of the quasi Z-Source Inverter (qZSI)

The efficiency of the converter is quite high at 50 kHz as seen in Fig. 4.16. But, most of the losses are concentrated in a small number of semiconductors resulting in a big heat sink. It is for the same reason that the concentrated losses for the 100 kHz design were too high to be dissipated by the heat sinks considered. The large volume of the heat sink and impedance network can be seen in the volume distribution in Fig. 4.17. The final score of the converter in Table 4.6 is 126.64, which is much lower than the combined score of two different PV and grid topologies based on the DC-link converter type. Hence the Z-source is not the preferred topology for the EV-PV converter.

4.8. Conclusion

The chapter presented a detailed design and comparison of topologies to find the optimal topology for a 10kW, grid-connected bidirectional charger for EV that is powered by PV panels. The chapter evaluated nine topologies, namely IBC, CIIBC, TLBC, DAB, IBFC, 2LC, 3LNPC, 3LT2C and the qZSI. The topologies were designed considering two switching frequencies (50 kHz, 100 kHz), eight SiC MOSFETs, thirteen SiC diodes, seventeen core materials of different sizes, varied modulation techniques and a different number of interleaved phases. A multi-criteria framework was then used to quantitatively compare the topologies based on the number of components, efficiency, converter volume, controllability, efficiency improvement and current ripple.

From the evaluation, it was found that impedance based converters were not suitable for high power solar EV charging due to the large impedance network required to handle high currents at low ripple. The DC-link based three port converters are preferred due to direct DC charging of PV from EV. For the PV port, a three-phase interleaved boost converter at 50 kHz was the best topology mainly driven by its high efficiency, easy control and low component count compared to the CIIBC and TLBC. For the EV port, the four-phase interleaved bidirectional flyback converter

was better than the DAB due to its high power density, high partial load efficiency and low current ripple. For the grid port, the two-level converter at 50 kHz with SPWM scored better than the three-level topologies due to lower component count and simpler control while still maintaining a comparable efficiency.

4.9. References

- [1] G. Carli and S. S. Williamson, "Technical Considerations on Power Conversion for Electric and Plug-in Hybrid Electric Vehicle Battery Charging in Photovoltaic Installations," *IEEE Trans. Power Electron.*, vol. 28, no. 12, pp. 5784–5792, Dec. 2013.
- [2] Z. Rasinab and M. F. Rahmana, "Grid-connected quasi-Z-source PV inverter for electricvehicle charging station," in *2013 International Conference on Renewable Energy Research and Applications (ICRERA)*, 2013, pp. 627–632.
- [3] Z. Rasin, K. Ahsanullah, and M. F. Rahman, "Design and simulation of quasi-Z-source grid-connected PV inverter with bidirectional power flow for battery storage management," in *IECON 2013 - 39th Annual Conference of the IEEE Industrial Electronics Society*, 2013, pp. 1589–1594.
- [4] G. R. Chandra Mouli, P. Bauer, and M. Zeman, "Comparison of system architecture and converter topology for a solar powered electric vehicle charging station," in *2015 9th International Conference on Power Electronics and ECCE Asia (ICPE-ECCE Asia)*, 2015, pp. 1908–1915.
- [5] A. R. Bhatti, Z. Salam, M. J. B. A. Aziz, K. P. Yee, and R. H. Ashique, "Electric vehicles charging using photovoltaic: Status and technological review," *Renewable and Sustainable Energy Reviews*, vol. 54, pp. 34–47, 2016.
- [6] "Standard IEC 61851 - Electric vehicle conductive charging system - Part 1, 21, 23, 24," pp. 1–287, 1–47, 1–159, 1–63, 2014.
- [7] University of Iowa, *Solar electric vehicle charging station* . .
- [8] Y. Gurkaynak and A. Khaligh, "Control and Power Management of a Grid Connected Residential Photovoltaic System with Plug-in Hybrid Electric Vehicle (PHEV) Load," in *2009 Twenty-Fourth Annual IEEE Applied Power Electronics Conference and Exposition*, 2009, pp. 2086–2091.
- [9] Y. Gurkaynak and A. Khaligh, "A novel grid-tied, solar powered residential home with plug-in hybrid electric vehicle (PHEV) loads," in *2009 IEEE Vehicle Power and Propulsion Conference*, 2009, pp. 813–816.
- [10] M. Alonso Abella, M. A. F. ChenloAbella, and F. Chenlo, "Photovoltaic charging station for electrical vehicles," in *Proceedings of 3rd World Conference on Photovoltaic Energy Conversion*, 2003, vol. 3, pp. 2280–2283.
- [11] P. J. Tulpule, V. Marano, S. Yurkovich, and G. Rizzoni, "Economic and environmental impacts of a PV powered workplace parking garage charging station," *Appl. Energy*, vol. 108, pp. 323–332, Aug. 2013.
- [12] G. Gamboa, C. Hamilton, R. Kerley, S. Elmes, A. Arias, J. Shen, and I. Batarseh, "Control strategy of a multi-port, grid connected, direct-DC PV charging station for plug-in electric vehicles," in *2010 IEEE Energy Conversion Congress and Exposition*, 2010, pp. 1173–1177.
- [13] C. Hamilton, G. Gamboa, J. Elmes, R. Kerley, A. Arias, M. Pepper, J. Shen, and I. Batarseh, "System architecture of a modular direct-DC PV charging station for plug-in electric vehicles," in *IECON 2010 - 36th Annual Conference on IEEE Industrial Electronics Society*, 2010, pp. 2516–2520.
- [14] J. Traube, F. Lu, D. Maksimovic, J. Mossoba, M. Kromer, P. Faill, S. Katz, B. Borowy, S. Nichols, and L. Casey, "Mitigation of Solar Irradiance Intermittency in Photovoltaic

- Power Systems With Integrated Electric-Vehicle Charging Functionality,” *IEEE Trans. Power Electron.*, vol. 28, no. 6, pp. 3058–3067, Jun. 2013.
- [15] J. Mossoba, M. Kromer, P. Faill, S. Katz, B. Borowy, S. Nichols, L. Casey, D. Maksimovic, and J. Traube, “Analysis of solar irradiance intermittency mitigation using constant DC voltage PV and EV battery storage,” in *2012 IEEE Transportation Electrification Conference and Expo (ITEC)*, 2012, pp. 1–6.
- [16] F. Turki, A. Guetif, and C. Sourkounis, “Contactless charging electric vehicles with renewable energy,” in *2014 5th International Renewable Energy Congress (IREC)*, 2014, pp. 1–6.
- [17] G.-Y. Choe, J.-S. Kim, and B.-K. Lee, “A Bi-directional battery charger for electric vehicles using photovoltaic PCS systems,” in *2010 IEEE Vehicle Power and Propulsion Conference*, 2010, pp. 1–6.
- [18] P. Goli and W. Shireen, “PV powered smart charging station for PHEVs,” *Renew. Energy*, vol. 66, pp. 280–287, Jun. 2014.
- [19] D. H. Kim, G. Y. Cheo, and B. K. Lee, “Design and control of an optimized battery charger for an xEV based on photovoltaic power systems,” *J. Electr. Eng. Technol.*, vol. 9, no. 5, pp. 1602–1613, 2014.
- [20] D. M. Robalino, G. Kumar, L. O. Uzoechi, U. C. Chukwu, and S. M. Mahajan, “Design of a docking station for solar charged electric and fuel cell vehicles,” in *2009 International Conference on Clean Electrical Power*, 2009, pp. 655–660.
- [21] H. Krishnaswami and N. Mohan, “Three-Port Series-Resonant DC–DC Converter to Interface Renewable Energy Sources With Bidirectional Load and Energy Storage Ports,” *IEEE Trans. Power Electron.*, vol. 24, no. 10, pp. 2289–2297, Oct. 2009.
- [22] G. Waltrich, J. L. Duarte, and M. A. M. Hendrix, “Multiport converter for fast charging of electrical vehicle battery: Focus on DC/AC converter,” in *IECON 2011 - 37th Annual Conference of the IEEE Industrial Electronics Society*, 2011, pp. 3626–3633.
- [23] “Standard IEC 62196 - Plugs, socket-outlets, vehicle connectors and vehicle inlets - Conductive charging of electric vehicles - Part 1, 2, 3,” pp. 1–176, 1–122, 1–71, 2014.
- [24] W. Kim, V.-H. Duong, T.-T. Nguyen, and W. Choi, “Analysis of the effects of inverter ripple current on a photovoltaic power system by using an AC impedance model of the solar cell,” *Renew. Energy*, vol. 59, pp. 150–157, 2013.
- [25] K. Uddin, A. D. Moore, A. Barai, and J. Marco, “The effects of high frequency current ripple on electric vehicle battery performance,” *Appl. Energy*, vol. 178, pp. 142–154, Sep. 2016.
- [26] G. R. Chandra Mouli, P. Bauer, and M. Zeman, “System design for a solar powered electric vehicle charging station for workplaces,” *Appl. Energy*, vol. 168, pp. 434–443, Apr. 2016.
- [27] N. Mohan, T. M. Undeland, and W. P. Robbins, *Power Electronics: Converters, Applications, and Design*. John Wiley & Sons, 2007.
- [28] G. R. Chandra Mouli, J. H. Schijffelen, P. Bauer, and M. Zeman, “Design and Comparison of a 10kW Interleaved Boost Converter for PV Application Using Si and SiC Devices,” *IEEE J. Emerg. Sel. Top. Power Electron.*, vol. 5, no. 2, pp. 610–623, Jun. 2017.
- [29] F. Krismer, “Modeling and optimization of bidirectional dual active bridge DC-DC converter topologies,” *PhD thesis, ETH Zurich*, 2010.
- [30] C. R. Sullivan and R. Y. Zhang, “Simplified design method for Litz wire,” in *Conference Proceedings - IEEE Applied Power Electronics Conference and Exposition - APEC*, 2014, pp. 2667–2674.
- [31] K. Venkatachalam, C. R. Sullivan, T. Abdallah, and H. Tacca, “Accurate prediction of

- ferrite core loss with nonsinusoidal waveforms using only steinmetz parameters,” in *Proceedings of the IEEE Workshop on Computers in Power Electronics, COMPEL*, 2002, vol. 2002–Janua, pp. 36–41.
- [32] *519-2014 IEEE Recommended Practice and Requirements for Harmonic Control in Electric Power Systems*. .
- [33] R. Beres, X. Wang, F. Blaabjerg, C. L. Bak, and M. Liserre, “A review of passive filters for grid-connected voltage source converters,” in *Conference Proceedings - IEEE Applied Power Electronics Conference and Exposition - APEC*, 2014, pp. 2208–2215.
- [34] K. Jalili and S. Bernet, “Design of LCL filters of active-front-end two-level voltage-source converters,” *IEEE Trans. Ind. Electron.*, vol. 56, no. 5, pp. 1674–1689, 2009.
- [35] M. Liserre, F. Blaabjerg, and S. Hansen, “Design and control of an LCL-filter-based three-phase active rectifier,” *IEEE Trans. Ind. Appl.*, vol. 41, no. 5, pp. 1281–1291, 2005.
- [36] U. Drogenik, G. Laimer, J. W. Kolar, O. Strategy, and H. Power, “Theoretical Converter Power Density Limits for Forced Convection Cooling,” *Proc. Int. PCIM Eur. 2005 Conf.*, no. 4, pp. 608–619, 2005.
- [37] T. Todorevi, P. Bauer, and J. Ferreira, “Comparison of bidirectional medium-voltage dc-dc converters for energy harvesting using dielectric elastomers,” *PCIM Eur.*, pp. 1–8, 2013.
- [38] H. te Heesen, M. Baron, C. Kurz, and R. Pfatischer, “Definition of the euro efficiency of solar modules,” *25th Eur. Photovolt. Sol. Energy Conf. Exhib.*, pp. 4154–4155, 2010.
- [39] R. W. A. A. De Doncker, D. M. Divan, and M. H. Kheraluwala, “A three-phase soft-switched high-power-density DC/DC converter for high-power applications,” *IEEE Trans. Ind. Appl.*, vol. 27, no. 1, pp. 63–73, 1991.
- [40] S. P. Engel, N. Soltau, H. Stagge, and R. W. De Doncker, “Dynamic and Balanced Control of Three-Phase High-Power Dual-Active Bridge DC–DC Converters in DC-Grid Applications,” *IEEE Trans. Power Electron.*, vol. 28, no. 4, pp. 1880–1889, Apr. 2013.
- [41] H. van Hoek, M. Neubert, and R. W. De Doncker, “Enhanced Modulation Strategy for a Three-Phase Dual Active Bridge—Boosting Efficiency of an Electric Vehicle Converter,” *IEEE Trans. Power Electron.*, vol. 28, no. 12, pp. 5499–5507, Dec. 2013.
- [42] N. H. Kutkut, D. M. Divan, D. W. Novotny, and R. H. Marion, “Design considerations and topology selection for a 120-kW IGBT converter for EV fast charging,” *IEEE Trans. Power Electron.*, vol. 13, no. 1, pp. 169–178, 1998.
- [43] Junjun Deng, Siqi Li, Sideng Hu, C. C. Mi, and Ruiqing Ma, “Design Methodology of LLC Resonant Converters for Electric Vehicle Battery Chargers,” *IEEE Trans. Veh. Technol.*, vol. 63, no. 4, pp. 1581–1592, May 2014.
- [44] Y. P. Siwakoti, F. Z. Peng, F. Blaabjerg, P. C. Loh, and G. E. Town, “Impedance-Source Networks for Electric Power Conversion Part I: A Topological Review,” *IEEE Trans. Power Electron.*, vol. 30, no. 2, pp. 699–716, Feb. 2015.
- [45] W. Qian, F. Z. Peng, and H. Cha, “Trans-Z-Source Inverters,” *IEEE Trans. Power Electron.*, vol. 26, no. 12, pp. 3453–3463, Dec. 2011.
- [46] S. Zhang, “Analysis and minimization of the input current ripple of Interleaved Boost Converter,” in *2012 Twenty-Seventh Annual IEEE Applied Power Electronics Conference and Exposition (APEC)*, 2012, pp. 852–856.
- [47] O. Hegazy, J. Van Mierlo, and P. Lataire, “Analysis, Modeling, and Implementation of a Multidevice Interleaved DC/DC Converter for Fuel Cell Hybrid Electric Vehicles,” *IEEE Trans. Power Electron.*, vol. 27, no. 11, pp. 4445–4458, Nov. 2012.
- [48] B. Ray, H. Kosai, S. McNeal, B. Jordan, and J. Scofield, “A comprehensive multi-mode performance analysis of interleaved boost converters,” in *2010 IEEE Energy Conversion Congress and Exposition*, 2010, pp. 3014–3021.

- [49] H. Kosai, S. McNeal, A. Page, and B. Jordan, "Characterizing the effects of inductor coupling on the performance of an interleaved boost converter," *Proc. Cart. USA*, pp. 237–251, 2009.
- [50] M. T. Zhang, Yimin Jiang, F. C. Lee, and M. M. Jovanovic, "Single-phase three-level boost power factor correction converter," in *Proceedings of 1995 IEEE Applied Power Electronics Conference and Exposition - APEC '95*, pp. 434–439.
- [51] M. Harfman Todorovic, L. Palma, and P. N. Enjeti, "Design of a wide input range DC-DC converter with a robust power control scheme suitable for fuel cell power conversion," *IEEE Trans. Ind. Electron.*, vol. 55, no. 3, pp. 1247–1255, 2008.
- [52] M. H. Kheraluwala, R. W. Gascoigne, D. M. Divan, and E. D. Baumann, "Performance Characterization of a High-Power Dual Active Bridge dc-to-dc Converter," *IEEE Trans. Ind. Appl.*, vol. 28, no. 6, pp. 1294–1301, 1992.
- [53] K. Venkatesan, "Current mode controlled bidirectional flyback converter," *20th Annu. IEEE Power Electron. Spec. Conf.*, vol. 2, pp. 835–842, 1989.
- [54] T. Bhattacharya, V. S. Giri, K. Mathew, and L. Umanand, "Multiphase Bidirectional Flyback Converter Topology for Hybrid Electric Vehicles," *IEEE Trans. Ind. Electron.*, vol. 56, no. 1, pp. 78–84, Jan. 2009.
- [55] A. M. A. Hava, R. J. R. Kerkman, and T. A. T. Lipo, "Simple analytical and graphical methods for carrier-based PWM-VSI drives," *IEEE Trans. Power Electron.*, vol. 14, no. 1, pp. 49–61, 1999.
- [56] A. Nabae, I. Takahashi, and H. Akagi, "A New Neutral-Point-Clamped PWM Inverter," *IEEE Trans. Ind. Appl.*, vol. IA-17, no. 5, pp. 518–523, 1981.
- [57] M. Schweizer and J. Kolar, "Design and implementation of a highly efficient three-level T-type converter for low-voltage applications," *IEEE Trans. Power Electron.*, vol. 28, no. 2, pp. 899–907, 2013.
- [58] T. G. Habetler, F. Profumo, M. Pastorelli, and L. M. Tolbert, "Direct torque control of induction machines using space vector modulation," *Ind. Appl. IEEE Trans.*, vol. 28, no. 5, pp. 1045–1053, 1992.
- [59] E. Ün and A. M. Hava, "A near-state PWM method with reduced switching losses and reduced common-mode voltage for three-phase voltage source inverters," *IEEE Trans. Ind. Appl.*, vol. 45, no. 2, pp. 782–793, 2009.
- [60] M. M. C. Cavalcanti, A. A. M. A. Farias, K. C. K. Oliveira, F. A. S. Neves, and J. L. Afonso, "Eliminating leakage currents in neutral point clamped inverters for photovoltaic systems," *IEEE Trans. Ind. Electron.*, vol. 59, no. 1, pp. 435–443, 2012.
- [61] Y. Li, J. Anderson, F. Peng, and D. Liu, "Quasi-Z-source inverter for photovoltaic power generation systems," *IEEE Appl. Power Electron. Conf. Expo.*, pp. 918–924, 2009.
- [62] F. Z. Peng, "Z-source inverter," in *Conference Record of the 2002 IEEE Industry Applications Conference. 37th IAS Annual Meeting (Cat. No.02CH37344)*, 2002, vol. 2, pp. 775–781.
- [63] O. Ellabban, J. Van Mierlo, and P. Lataire, "A DSP-based dual-loop peak dc-link voltage control strategy of the Z-source inverter," *IEEE Trans. Power Electron.*, vol. 27, no. 9, pp. 4088–4097, 2012.

5

**Development of 10kW
bidirectional solar EV charger**

5. Development of 10kW bidirectional solar EV charger

This chapter is based on:

G. R. Chandra Mouli, J. Schijffelen, P. Bauer, and M. Zeman, "Design and Comparison of a 10kW Interleaved Boost Converter for PV Application Using Si and SiC Devices," *IEEE J. Emerg. Sel. Top. Power Electron.* vol. 5, issue 2, pp. 610-623, 2016

G. R. Chandra Mouli, J. Schijffelen, M.v.d Heuvel, M.Kardolus, P. Bauer, and M. Zeman, "A 10kW Solar-Powered Bidirectional EV Charger Compatible with Chademo and COMBO", *IEEE Transactions on Power Electronics*, under review

Summary

In chapter 4, the optimal topology for the three port converter is determined based on theoretical loss models and a comparative framework. The best topology that was chosen from chapter 4 is designed in detail and developed into a prototype in chapter 5. The goal is to realize a high power density, high-efficiency power converter with closed-loop control and low cost that meets the Chademo and CCS/Combo EV charging standard. The power converter is developed in collaboration with PRE. The high efficiency and power density achieved by the use of silicon carbide (SiC) wide band-gap devices, interleaving and powdered alloy core inductors. A stable closed loop control allows four different power flows: PV→EV, EV→grid, grid→EV and PV→grid. Hence the converter operates as a PV inverter, a bidirectional EV charger and a combination of both. A 10kW prototype has been successfully tested, and its experimental waveforms and measured efficiency are presented. The EV charger is tested with a Nissan Leaf EV by charging and discharging the EV from the grid

Outline

Section 5.2 describes the specifications of the EV-PV power converter, the topology and the design goals for the EV-PV charger. Section 5.3, 5.4, 5.5 provides the detailed design procedure and loss models for the isolated DC/DC converter for the PV, bidirectional DC/AC grid inverter and the DC/DC converter for the EV charging, respectively. Section 5.6 presents the closed loop control for each of the three sub-converters. Section 5.7 describes the experimental prototype developed and the measured waveforms and efficiency of the solar EV charger. The developed charger is compared to a conventional design based on AC power exchange between EV and PV. Finally, section 5.8 describes the charging and V2G of a Nissan Leaf using a CHAdeMO charge controller.

5.1. Introduction

In chapter 4, the optimal topology of the three port bidirectional solar EV charger was determined. In this chapter, the three-port converter is designed in detail along with its closed-loop control and an experimental prototype is developed. The critical aspects of the converter design are achieving high efficiency, high power density, modularity and low cost. In particular, high partial-load efficiency is vital as smart charging is done by controlling the charging power below the rated power. Similarly, high power density ensures that the chargers occupy a small space in the parking lot.

Fig. 5.1 shows the block diagram of the three-port converter with a central DC-link. There are three sub-converters inside: a unidirectional DC/DC converter for the PV, a bidirectional DC/AC inverter to connect to the AC grid and a bidirectional isolated DC/DC converter for EV.

The developed three-port architecture has three advantages. Firstly, since EV and PV are inherently DC in nature, an internal DC-link is used to exchange power between the three sub-converters. Secondly, the grid inverter is inherently bidirectional as it needs to feed PV power to the grid and draw EV charging power from the grid. Hence, by making the isolated DC/DC converter for EV bidirectional as well, V2G operation can be implemented. Thirdly, a single DC/AC inverter is sufficient to connect both PV, EV to the grid. This makes the converter cheaper and smaller. Typically, if an integrated converter is not used, two inverters would be needed, one each for PV and EV.

5.2. EV-PV power converter

5.2.1. Specifications

Table 5.1. shows the specifications of the three-phase, grid-connected EV-PV power converter. The voltage range, isolation and ripple requirements are compatible with the EV charging standards [1], [2]. In order to make the charger commercially usable, the expected lifetime of the power converter must be around 10 years, and efficiency

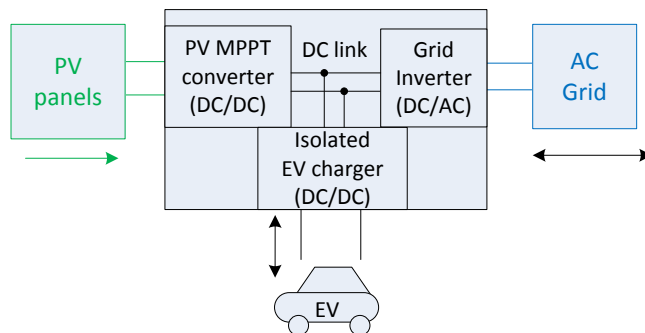


Fig. 5.1. Grid connected bidirectional 10kW three-port EV-PV charger

Table 5.1. Specifications of 10kW EV-PV converter

Parameter	Symbol	
Nominal power of converter	P_{nom}	10 kW
PV MPPT Voltage, Current	V_{pv}, I_{pv}	350-700V, 0-30A
PV current ripple (peak-peak)	$\Delta I_{pv\%}$	< 10% of $I_{pv(max)}$
PV voltage ripple (peak-peak)	ΔV_{pv}	<500mV
EV voltage	V_{ev}	50-500V
EV current	I_{ev}	-30A to +30A
Internal DC-link voltage	V_{dc}^*	750V
EV current ripple (rms)	$\Delta I_{ev(rms)}$	<1Arms @ 10kW
EV voltage ripple (peak-peak)	$\Delta V_{ev(p-p)}$	<500mV
Nominal AC connection	V_{ac}, I_{ac}	400V, 50Hz, 16A
Total Harmonic Distortion		< 5%
Isolation monitoring @ PV		800k Ω
Isolation for EV		4kV (Input-Output)

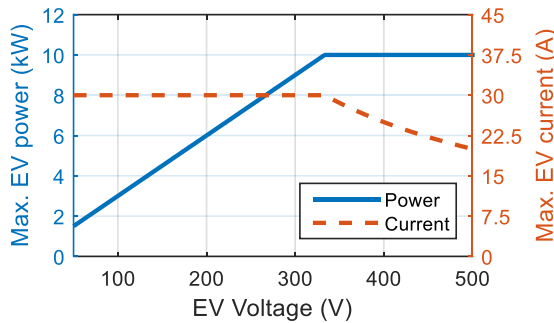


Fig. 5.2. Maximum kW power and current of the EV charger for different battery voltages

of all power conversions between the three port must be above 95%. The internal DC-link voltage is rated at 750V. As the maximum EV current, $I_{ev}=30A$, power curtailment occurs at low EV voltages, as shown in Fig. 5.2. The critical operating point is when EV voltage, $V_{ev}=333.3V$, where both maximum power and maximum current has to be supplied to the EV battery. It must be noted that the specifications here have minor differences from those in chapter 4. For example, the EV voltage range has been expanded to 50-500V because the flyback converter can work well over a wide voltage range. Similarly, the PV ripple has been set to <500mV, which increases the MPPT efficiency.

The power difference between the EV charging demand, P_{ev} , PV power, P_{pv} and the converter losses P_{loss} is met by the grid power P_{ac} . For V2G operation, P_{ev} is negative. The power balance equation is

$$P_{ac} = P_{ev} - P_{pv} + P_{loss} \quad (1)$$

5.2.2. Topology

Fig. 5.3 shows the topology of the three sub-converters in the EV-PV charger: an interleaved boost converter (IBC) for the PV, an interleaved bidirectional flyback converter (IBFC) for the EV and a three-phase voltage source inverter for the AC grid. The neutral of the AC grid is connected to the mid-point of the DC-link. The flyback converter is operated in a quasi-resonant mode to achieve soft switching, while the PV and grid converter are operated with hard switching.

5.2.3. Achieving high efficiency and high power density

The EV-PV power converter has four different power flows: EV→PV, PV→Grid, Grid→EV and EV→Grid. It is hence important to ensure high efficiency for the four power flows, including operations at partial load. Secondly, it is vital that the converter has a high power density and occupies little space when installed near the EV. In order to achieve these two objectives, three techniques are implemented: interleaving, use of silicon carbide devices and powdered alloy core inductors.

Interleaving is used in the both PV and EV DC/DC converters, with the use of three and four interleaved stages, respectively. Interleaving has four advantages:

1. Current through the switches and inductors in each leg is reduced by a factor of $(1/N_i)$, where N_i is the number of interleaved stages. Thus smaller inductors and lower-rated switches can be used.
2. The volume L_{vol} of an inductor is directly proportional to the energy it processes as given by $L_{vol} \propto LI^2$. By interleaving, the total volume $L_{vol(n)}$ of all the interleaving inductors reduces by a factor N_i .
3. Effective frequency as seen at the input is increased by a factor of N_i . This facilitates the operation of each leg at a lower frequency leading to lower switching losses.
4. As the currents in each leg are phase shifted by an angle of $360^\circ/N_i$, the input current ripple is reduced by a factor of $(1/N_i)$ and the voltage ripple by $(1/N_i)^2$.

To achieve high power density, it is important to increase the switching frequency while still maintaining high efficiency. Silicon carbide (SiC) represents a revolution in power semiconductor technology, which can help realize high switching frequency [3], [4]. SiC MOSFETs exhibit very low switching losses while SiC schottky diodes have no reverse recovery and have very low turn-on voltage. SiC MOSFET of >1kV are now commercially available and can replace >1kV Si IGBTs in high power applications. In this chapter, SiC MOSFETs and schottky diodes are used to reduce switching losses and hence achieve higher switching frequency.

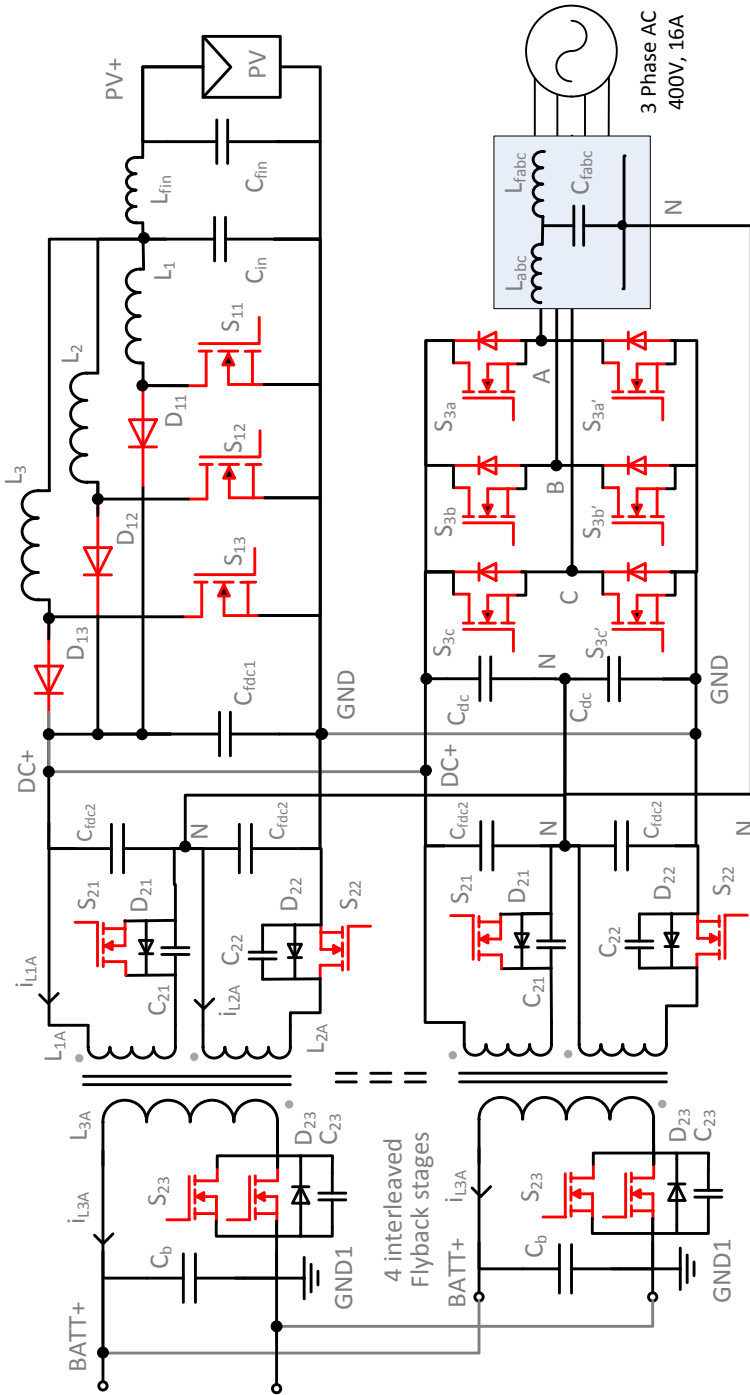


Fig. 5.3. Topology of the three port EV/PV converter with a central DC link

Powdered alloy cores are different from ferrite cores as they have a distributed air gap and much higher saturation flux density (typically 800-1200mT, which is 2 to 3 times higher than that of ferrites with 300-400mT). This means that powdered cores can handle much higher currents without saturation, which is useful for high power applications. The main disadvantages of powdered cores, when compared to ferrites, are their higher core losses, higher cost and inductance variation [Appendix C]. So, if the switching frequency is not too high, they could be excellent replacements for ferrites in higher power density applications. In this work, KoolM μ cores from Magnetics are extensively used in the grid inverter and solar converter [5], [6]. KoolM μ cores are chosen over other powdered cores due to the relatively lower core losses.

5.2.4. Contributions

The contributions of this work compared to earlier works are,

- Developing a 10kW bidirectional, isolated, three-port power converter for direct DC charging of an EV from PV and AC grid. It can be seen from the literature review that such a converter does not currently exist.
- The combined use of SiC devices, high switching frequency, interleaving and KoolM μ inductors has resulted in the developed converter to have much higher partial and peak load efficiency and three times the power density when compared to existing solutions.
- Designing a modular closed-loop control that enables four different power flows using the converter: EV \rightarrow PV, PV \rightarrow Grid, Grid \rightarrow EV and EV \rightarrow Grid (i.e., V2G).
- The converter is designed to be compatible with IEC, CHAdeMO and CCS/Combo DC charging standard with respect to ripple, voltage range and isolation requirements and charge/V2G operation has been tested using a Nissan Leaf EV

5.3. DC/DC converter for PV

The DC/DC PV converter is built using an interleaved boost converter with three interleaved stages as shown in Fig. 5.3 [7]. The detailed design of the converter and its comparison to an IGBT-ferrite based design are shown in [4]. SiC Schottky diodes (CREE C4D15120A), SiC MOSFETs (CREE C2M0080120D) and KoolM μ 40 μ powdered alloy inductors are used in each leg. Each leg operates at a switching frequency, $f_{sw}=47\text{kHz}$.

5.3.1. Operation of interleaved boost converter

Operating waveforms of the IBC are shown in Fig. 5.4. The input PV current is shared equally between the three legs, and the average inductor current is given by $I_{L(avg)} = I_{PV}/3$. When the switch is ON from 0 to (DT) , the current in the inductor rises from $I_{L(min)}$ to $I_{L(max)}$ due to the positive PV voltage. When the switch is OFF, the inductor current decreases and flows through the diode. The voltage ratio of input and output voltage is the same as a normal boost converter for continuous conduction mode (CCM) and discontinuous conduction mode (DCM):

$$\frac{V_{dc}}{V_{PV}} = \frac{d_1 + D}{d_1} \tag{2}$$

where D is the duty cycle of the switches and d_1 is the period when current flows through the diode. In CCM, $d_1 = 1 - D$.

The inductor ripple is vital in designing the PV converter as it directly translates to the input capacitor sizing, inductor size and the efficiency of the MPPT operation.

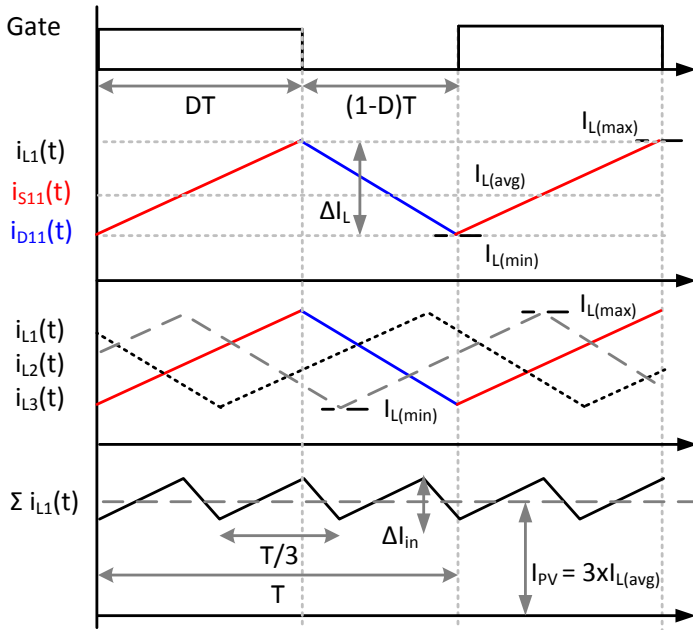


Fig. 5.4. Waveforms of the IBC (top to bottom): Gate signal for S_{11} ; currents through the inductor L_1 , switch S_{11} and diode D_{11} ; phase shifted current through the inductors i_{L1} , i_{L2} , i_{L3} of each interleaved leg; net input current of the three legs in CCM operation

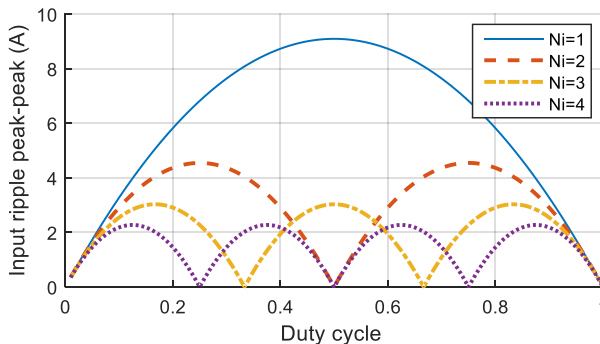


Fig. 5.5. Input ripple ΔI_{PV} as a function of duty cycle, D for different interleaved stages of IBC. $V_{dc}=750V$, $f_{sw}=47kHz$, $L_1=443\mu H$

The peak-to-peak inductor ripple ΔI_L is:

$$\Delta I_L = \frac{V_{PV}D}{f_{sw}L} = \frac{(V_{dc} - V_{PV})d_1}{f_{sw}L} = I_{L(max)} - I_{L(min)} \quad (3)$$

where $I_{L(max)}$, $I_{L(min)}$, are the maximum and minimum inductor current and L the inductance respectively. It can be seen from (3) that, we either need to use a high switching frequency or a large inductor in order to have a low ripple. Both these methods have the drawback of increased switching losses, increased inductor losses and require a larger inductor core and heat sink.

The benefit of interleaving is that the maximum input current ripple ΔI_{pv} is $(1/N_i)$ of the maximum inductor ripple, given by

$$\Delta I_{PV}(D) = \frac{V_{PV}}{f_{sw}L} \left(\frac{N_{on} - N_i D}{1 - D} \right) \frac{1}{N_i} (N_i D - N_{on} + 1) \quad (4)$$

where N_{on} is the maximum number of switches that are simultaneously ON for the given duty cycle.

Fig. 5.5 shows the input ripple as a function of duty cycle for different numbers of interleaved stages. The peak input ripple occurs at $D=(1/2N_i)$, and the input ripple is zero when $D=(1/N_i)$. With three interleaved stages, the input current and voltage ripple reduce by a factor of three and nine, respectively.

5.3.2. Inductor design and losses

For the inductor design, the vital parameter is the maximum input ripple, $\Delta I_{PV(max)}$ when considering all duty cycles. The duty cycle for maximum input ripple can be determined from (4) by setting $d(\Delta I_{in})/dD = 0$ and solving for D , where A_{int} takes odd integral values from 1 to $2N_i$:

$$\Delta I_{PV(max)} = \frac{V_{dc}}{4f_{sw}LN_i} \quad @ D = \frac{A_{int}}{2N_i} \quad (5)$$

For a three-leg IBC, maximum input ripple occurs at odd integral multiples of $D=1/6$ as seen in Fig. 5.5. It must be kept in mind that maximum ripple in inductor $\Delta I_{L(max)}$ always occurs at $D=0.5$ irrespective of N_i . The inductor is sized at the point where the PV feeds maximum current ($I_{pv}=I_{pv(max)}=28.5A$, $V_{pv}=350V$), given by

$$L = \frac{V_{dc}}{4f_{sw}N_i(\Delta I_{PV\%}I_{PV(max)})} \quad (6)$$

Using (6), the required inductance for 47kHz is 443 μ H. The inductor is built using KoolM μ E65 cores as they are suitable for printed circuit board (PCB) mounting and have large core area to reduce the core losses. The parameters of the 40 μ E65 core: permeance $A_L= 230nH/T^2$ at zero DC bias, core area $A_c=540mm^2$, magnetic path length $l_c=147mm$ and core volume $V_c=79400mm^3$. Table 5.2 shows the design of the KoolM μ inductor considering the inductance variation due to soft saturation

Table 5.2. Kool M μ 40 μ Inductor Design and Loss @ 350V, 10kW Input

Inductance (μ H)	L	405	Avg. Inductor current (A)	$I_{L(avg)}$	9.52
Inductance (μ H)	L_{least}	355	Inductor ripple (p-p) (A)	ΔI_L	11.03
Number of turns	N	42	Core Loss (W)	P_{core}	11.75
Winding resistance (m Ω)	R_L	28	Copper loss (W)	P_{cu}	3.77
Peak flux variation (mT)	B_{pk}	78.6	Total inductor loss (W)	P_L	15.53

[Appendix C]. The skin depth for 47kHz is approximately 300 μ m. Hence, litz wire of 1000x0.071mm is used in order to reduce the skin effect.

Equation (7), (8) are used to determine the number of turns, N and the maximum flux density in the core, B_{max} . While 47 turns are required for an inductance of 443 μ H, the bobbin can only accommodate a maximum of 42 turns. Therefore, the inductor is re-designed with 42 turns resulting in an inductor of $L=405\mu$ H at zero current and $L=355\mu$ H at maximum current, due to soft saturation. The smaller inductor will require a larger input capacitor to limit the input voltage ripple.

$$L = A_L N^2 \quad (7)$$

$$B_{max} = \frac{A_L N I_{L(max)}}{A_c} \quad (8)$$

The inductor losses, P_L comprising of the copper losses, P_{cu} and core losses, P_{core} are estimated using the Modified Steinmetz Equation (MSE) [8]. For a boost converter, the equivalent frequency f_{eq} for MSE is

$$P_L = P_{core} + P_{cu} = (A f_{eq}^{a-1} B_{pk}^b) f_{sw} V_e + I_{L(rms)}^2 R_L \quad (9)$$

$$f_{eq} = \frac{2}{\Delta B^2 \pi^2} \int_0^T \left(\frac{dB}{dt} \right)^2 dt = \frac{2}{\pi^2} \left(\frac{D + d_1}{D d_1 T} \right) \quad (10)$$

where ΔB is the peak-peak change in flux density, $B_{pk} = \Delta B/2$ and measured value of $R_L=28m\Omega$. MSE parameters $A=120$, $b=2.09$, $a=1.46$ for the 40 μ KoolM μ core, when P_{core} is in mW/cm³, f_{sw} in kHz, B_{pk} in T and V_e in cm³ [9]. The inductor losses are shown in Table 5.2, where 15.5W is lost per inductor at maximum input power. Since the skin depth at 47kHz is much higher than the litz diameter, the losses due to skin and proximity effect are not considered for the IBC.

The main advantage of the much lower core losses and saturation flux density of KoolM μ is that only a single core set is required per inductor. Using other powdered alloy core inductors will lead to much higher core losses while using ferrites will require two parallel E65 core sets. Secondly, the powder cores exhibit a gradual reduction in inductance under a fault condition, which makes the control of the converter easier and robust. Thirdly, powder cores have a distributed air gap which causes very low copper losses because of the fringing flux.

5.3.3. Sizing of input and output capacitor

When using an IBC, an input capacitor C_{in} is sized to supply the ripple current, ΔI_{PV} :

$$C_{in} = \frac{1}{2} \left(\frac{T}{2N_i} \right) \left(\frac{V_{dc}}{8f_{sw}LN_i} \right) \left(\frac{1}{\Delta V_{PV}} \right) \quad @ D = \frac{A_{int}}{2N_i} \quad (11)$$

Here, an input capacitor of 10 μ F is used which results in a maximum voltage ripple of $\Delta V_{PV}=0.32$ V. A LC filter ($L_{fin}=47\mu$ H, $C_{fin}=10\mu$ F) is used between the input capacitor and PV to further reduce this ripple voltage. A 470nF film capacitor is connected close to the output of each interleaved leg to filter the high frequency output ripple.

5.3.4. Loss Estimation in converter

The IBC operates in CCM and DCM depending on the PV voltage and current. The conduction losses in the diode ($P_{D,con}$, $P_{D,sw}$) and the conduction and switching losses in the MOSFET ($P_{S,con}$, $P_{S,sw}$) are estimated as:

$$P_S = P_{S,con} + P_{S,sw} \quad (12)$$

$$P_{S,con} = I_{DS,rms}^2 R_{DS(on)}(T_j, V_{GS}, I_{DS}) \quad (13)$$

$$P_{S,sw} = f_{sw} (E_{on}(V_{DS}, I_{DS}, R_G, T_j) + E_{off}(V_{DS}, I_{DS}, R_G, T_j)) \quad (14)$$

$$P_D = P_{D,con} + P_{D,sw} = I_{D,avg} U_{D0}(T_j) + I_{D,rms}^2 R_D(T_j) + f_{sw} E_{Dch} \quad (15)$$

$$P_{loss} = 3(P_D + P_S + P_L) + P_{filter} + P_{ctrl} \quad (16)$$

where P_S , P_D are the total switch and diode losses, I_{DS} , I_D are the switch and diode current; $R_{DS(on)}$, R_D are the on-state resistance of the MOSFET and diode; E_{on} , E_{off} are the switch turn-on and turn-off energy; E_{Dch} is loss due to the energy stored in the diode parasitic capacitance; U_{D0} is the on-state voltage of diode. As indicated in the equations above, the switch and diode parameters themselves are a function of the junction temperature T_j , the gate resistance R_G , gate voltage V_{GS} , blocking voltage of the device V_{DS} and the device current I_{DS}/I_D for the specific operating conditions.

P_{filter} is the total losses in the filters namely, the input common mode filter (4m Ω resistance), fuse, input LC filter (11m Ω for L_{fin} , 13m Ω ESR for C_{fin}) and the output capacitor (C_{dc} with $\tan\delta=0.03$). P_{ctrl} is the power consumed in the control and protection circuitry: three 20m Ω shunt resistors added to the MOSFET source for current control; gate drive, power supply and control ICs; and in the extra diode (VS-40EPS) added at the output of the IBC to protect against reverse currents. Reverse recovery losses due to the schottky diode are neglected as they are extremely small in SiC. The turn-on and turn-off gate resistance are 9.4 Ω and 4.7 Ω , respectively and $V_{GS}=20$ V. The ambient and junction temperature are assumed to be 25 $^\circ$ C and 100 $^\circ$ C, respectively.

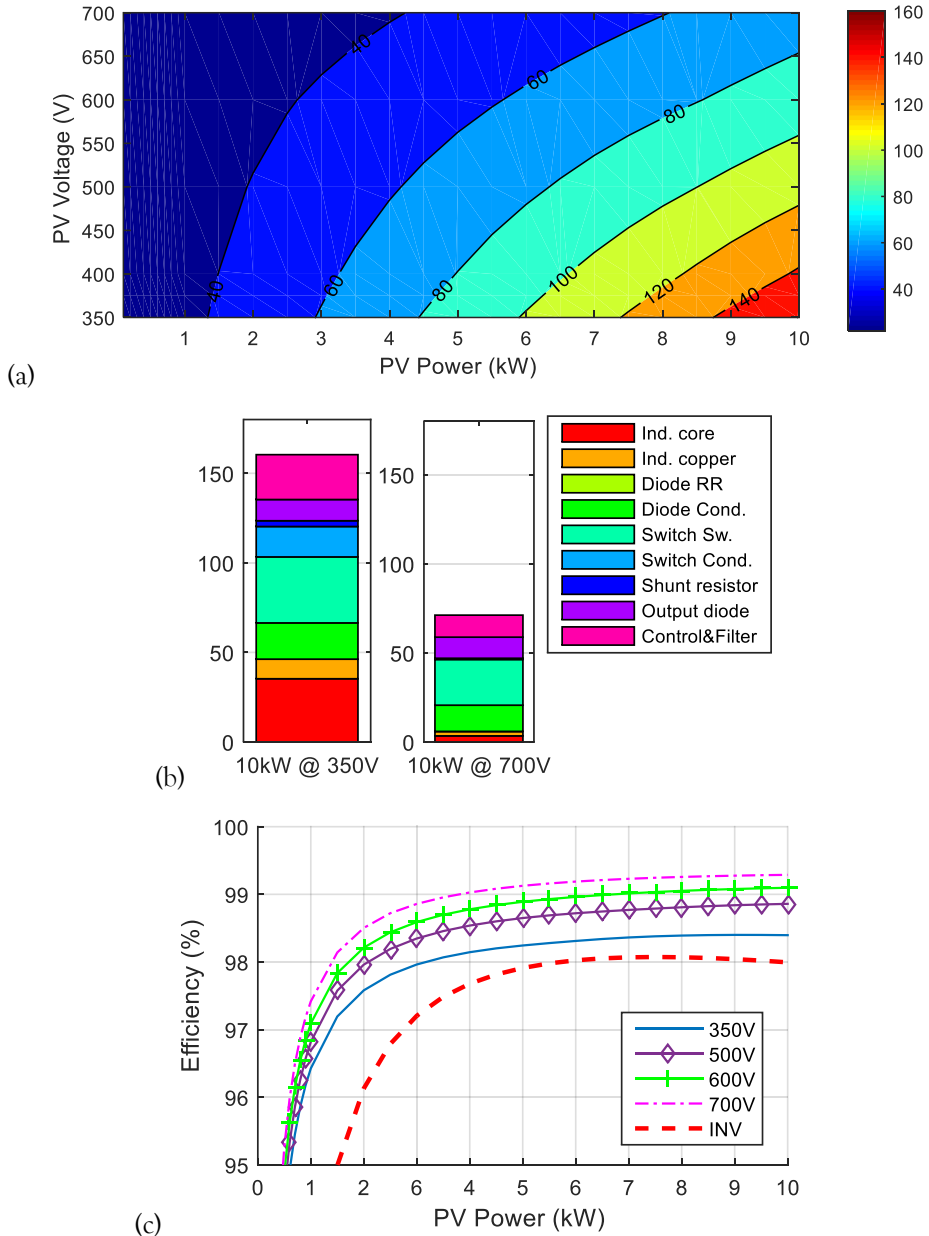


Fig. 5.6. (a) Total losses of the IBC as a function of input PV voltage and power. (b) Split up of losses for 10kW PV input for 350V and 700V PV voltage. (c) Estimated efficiency of IBC as a function of PV power for different voltages

The total converter losses and split up of losses within the converter for different PV voltages and power is shown in Fig. 5.6(a),(b), respectively. The worst case operating point is when $V_{PV}=350\text{V}$, $P_{PV}=10\text{kW}$ with losses of 160.4W. The key observation is the low switching and conduction losses in the MOSFET of 33W and 16W, respectively. On other hand, the three 40 μ powdered core inductors together have a relatively higher loss of 46.5W. The higher losses are the disadvantage of the powdered alloy core with the benefit of needing lesser number core sets with respect to ferrites. It's a trade-off between power density and losses. Fig. 5.6(c) shows the efficiency of the IBC for different PV voltages. The peak efficiency is 99.29% at 10kW,700V PV input.

For comparison, the same converter is designed using ferrite cores and silicon IGBT operating at 19kHz in [4]. The net converter volume was 2.5 times higher, owing to the 3x larger inductors, and bigger heat sinks to dissipate the IGBT switching losses. Thus, the comparison shows that the use of SiC devices and powdered alloy cores can help achieve high power density and high efficiency.

5.4. DC/AC Grid Inverter

The DC/AC stage uses a standard three-phase inverter with three legs and 6 switches and operates from the 750V DC-link [10]–[12]. The converter is operated with sinusoidal PWM with $f_{sw}=47\text{kHz}$. The inverter is designed to both draw and feed current to the grid up to 16A. Since the converter is operated with hard switching, SiC C2M0025120D MOSFETs with a lower $R_{ds(on)}$ are used, along with its body diode. The gate resistances are 15.1 Ω for turn-on, 5.1 Ω for turn-off.

At the inverter input, six 470 μF electrolytic capacitors, connected two in series form the DC-link. Three LCL filter, one per phase are used at the inverter output for filtering out the harmonics as shown in Fig. 5.3 [13], [14]. It's composed of $L_{abc}=236\mu\text{H}$ (E65 40 μ KoolM μ , $N=32$, $R_L=11\text{m}\Omega$); $L_{fabc}=140\mu\text{H}$ (E42 N87, $N=36$, $R_L=21\text{m}\Omega$) and the capacitor $C_{f1}=8\mu\text{F}$. Detailed control using sinusoidal PWM and loss modelling of the three phase inverter are well studied in literature and hence not presented again in this chapter [10]–[14]. The estimated converter efficiency including the losses in the switches, filters and control circuitry (based on section III.D) is shown in Fig. 5.6 (c) with a peak value of 98.05%.

5.5. Isolated bidirectional DC/DC converter for EV

The bidirectional, isolated DC/DC converter for the EV is composed of four interleaved flyback converters (Fig. 5.3). MOSFETs and anti-parallel diodes are used on both sides of the transformer for bidirectional operation. Each 2.5kW flyback module has a three-winding transformer (1:1:1 turns ratio) with two series-connected windings on the DC-link side (primary) and a third winding on the EV battery side (secondary), as shown in Fig. 5.3. For $I_{ev}=30\text{A}$, the corresponding output secondary current in each 2.5kW unit is $I_{ev(m)}=7.5\text{A}$.

The secondary side voltage ranges between 50-500V while the primary voltage is $V_{dc}=750V$. This difference in primary and secondary voltages leads to high secondary side currents (upto 30A). Therefore, two MOSFETs are connected in parallel at the secondary side to reduce the conduction losses. The flyback uses C4D15120A diodes and C2M0080120D MOSFETs with 20Ω turn-on and 10Ω turn-off gate resistance.

5.5.1. Operation of interleaved bidirectional flyback in quasi-resonance

The flyback converter is operated in quasi-resonant (QR) mode for both charging and V2G operation, and this has four main advantages. Firstly, it enables valley switching of the MOSFET which results in reduced turn-on losses due to zero voltage (ZVS) or low voltage switching (LVS). The resonant capacitor (C_{21} , C_{22} , C_{23}) absorbs the turn-off energy, and hence the turn-off losses are nearly zero. Third, the noise at

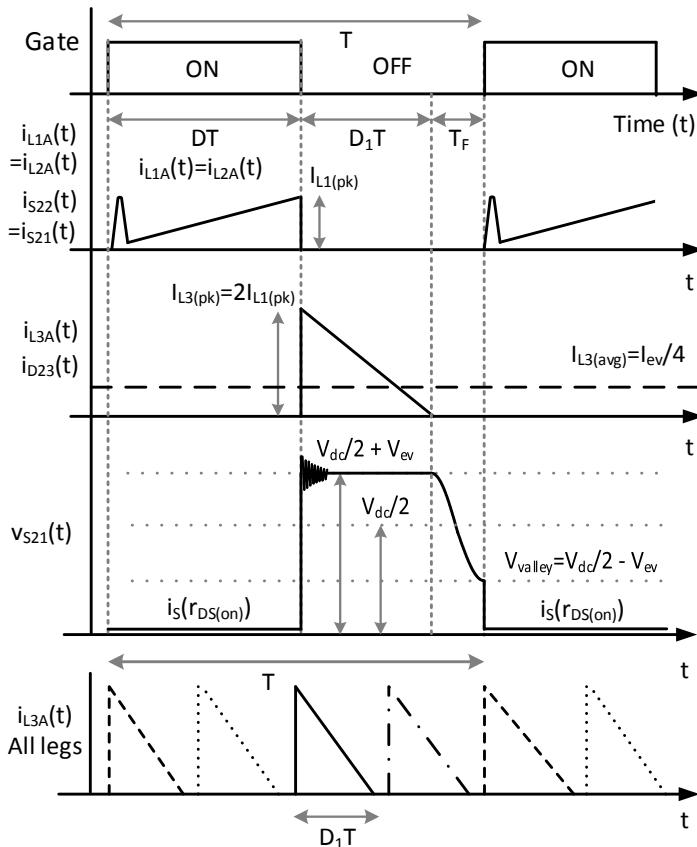


Fig. 5.7. Waveforms for quasi-resonant operation of IBFC (top to bottom): gate signal for switch S_{21} ; current through inductor L_{1A} , L_{2A} and switch S_{21}, S_{22} ; current through inductor L_{3A} and switch S_{23} , drain-source voltage V_{s21} across switch S_{21} ; net output current from all four interleaved IBFC

turn off (dV/dt) is reduced by the resonance capacitor. Finally, the quasi-resonant operation is at the borderline between DCM and CCM and has lower RMS currents than DCM. Fig. 5.7 shows the QR operating waveforms when in charge mode.

0<t<DT: When MOSFETs S_{21} , S_{22} are turned on simultaneously, the currents i_{L1A} , i_{L2A} rise from zero to its peak value $I_{L1A(pk)}$ and energy is stored in the flyback transformer

$$I_{L1A(pk)} = \frac{(V_{dc}/2)D}{(L_{1A} + M)f_{sw}} \quad (17)$$

where $M = k\sqrt{L_{1A}L_{2A}}$ is the mutual inductance, D the duty cycle and f_{sw} the switching frequency.

DT<t<(D+D₁)T: When the switch is turned off, the energy stored in the flyback transformer is delivered to the load. The secondary side diode D_{23} conducts for time interval, D_1/f_{sw} , till the inductor current i_{L3A} goes to zero. Due to the much lower on-state voltage of the SiC shottky diode, the MOSFET body diode does not conduct the load current. The peak current in the secondary inductor, $I_{L3A(pk)} = 2I_{L1A(pk)}$, assuming $k=1$:

$$I_{L3A(pk)} = \frac{V_{ev}D_1}{L_{3A}f_{sw}} = 2I_{L1A(pk)} \quad (18)$$

$$(V_{dc}/2)D = V_{ev}D_1 \quad (19)$$

The power transferred P_{ev} can be related to the peak inductor currents and energy stored in the inductor E_L :

$$E_L = \frac{P_{ev}}{f_{sw}} = 2 \left(\frac{1}{2} L_{1A} I_{L1A(pk)}^2 \right) + M I_{L1A(pk)} I_{L2A(pk)} = \frac{1}{2} L_{3A} I_{L3A(pk)}^2 \quad (20)$$

$$I_{L1A(pk)} = \sqrt{\frac{P_{ev}}{2L_{1A}f_{sw}}} = \frac{1}{2} \frac{(V_{dc}/2)D}{L_{1A}f_{sw}} = \frac{1}{2} \frac{V_{ev}D_1}{L_{3A}f_{sw}} \quad (21)$$

When the secondary diodes are conducting, the voltage across the switch is the sum of the input voltage, $V_{dc}/2$ and the reflected secondary voltage, V_{RO} . Based on Table 5.1. , $V_{RO} = V_{ev}$ and ranges from 50-500V. The maximum MOSFET drain-source voltage $V_{ds(max)}$ is:

$$V_{ds(max)} = \frac{V_{dc}}{2} + V_{RO(max)} + V_{trans} \quad (22)$$

$$V_{ds(max)} = 375 + 500 + V_{trans} \leq 1200V$$

where V_{trans} is the turn-off voltage transient due to leakage inductance of the transformer (Fig. 5.7). Split windings are hence used on the primary side to ensure that $V_{ds(max)} < 1200V$.

(D+D₁)T<t<T: As soon as the diode current reaches zero, the resonant capacitors C_{21} , C_{22} begin to exchange energy with the primary inductors. This causes an LC oscillation on the MOSFET drain-source voltage with a period of $(2T_F)$, as shown in

Fig. 5.7. The MOSFET is hence turned ON at the bottom of the valley when the voltage is at its lowest to reduce the turn-on losses:

$$V_{ds(min)} = V_{valley} = V_{dc}/2 - V_{ev} \quad (23)$$

$$T_F = \pi \sqrt{L_{1A} C_{ds(net)}} \quad (24)$$

$$C_{ds(net)} = C_{21} + C_{ds,S} + C_{DD} + C_{xmer} \quad (25)$$

where $C_{ds(net)}$ is the net drain-source capacitance due to the QR capacitor C_{21} , C_{22} and the parasitic capacitance of the MOSFET $C_{ds,S}$, schottky diode C_{DD} and the transformer windings C_{xmer} . Depending on the difference $(V_{dc}/2 - V_{ev})$, valley switching results in either ZVS or LVS at turn-on. Therefore, the net switching losses are dramatically reduced and can be zero for LVS or ZVS, respectively. This is the primary benefit of the QR operation. The sizing of the resonant capacitor must be such that it is large enough to store the maximum turn-off energy of the MOSFET considering all the operating points.

From the above equations, the duty cycle D and frequency f_{sw} for this flyback can be calculated as:

$$D = \frac{2}{(V_{dc}/2)} \sqrt{\frac{P_{ev} L_{1A} f_{sw}}{2}} \quad (26)$$

$$f_{sw} = \frac{1}{T_F} \left(1 - D - \frac{(V_{dc}/2)}{V_{batt}} D \right) \quad (27)$$

Hence, to increase the EV charging power, a larger duty cycle, a higher inductor peak current and lower switching frequency are required, as shown in Fig. 5.8(a). The operating of the flyback in V2G mode is similar to the charge mode described above. The difference being that in the V2G mode, the two switches S_{23} are turned ON first and the diodes D_{21} and D_{22} conduct during the OFF period of the switch. Since there are four modules operating interleaved, the gate signals are phase shifted by 90° . The net output current is the sum of the four interleaved modules as shown in Fig. 5.7.

Table 5.3 shows the operating regions of the MOSFET for ZVS and LVS for the charge (CH) and V2G modes. V_{ev} ranges from 50-500V and is less than $(V_{dc}/2)=375V$ for majority of the operating range. Hence, the converter operates in ZVS for a large part of V2G mode and in LVS for a large part of charge mode.

5.5.2. Flyback transformer design

The 2.5kW flyback transformer is essentially three coupled inductors on a common magnetic core. Since QR results in variable switching frequency, the limits are set between 30-350 kHz. The required size of the inductor is determined by the maximum power to be handled at the lowest input voltage ($V_{ev}=50V$, $I_{ev(m)}=7.5A$). From equations (17)-(26), the required inductance is can be estimated and it, is $L_{1A}=78.42\mu H$:

$$L_{1A} = \frac{2(V_{dc}/2)^2 D^2}{4P_{ev} f_{sw}} \quad (28)$$

The transformer is built using an Epcos E65 N87 core set [15]. The permeance of the core, A_L varies with the air-gap length, g according to (29) where $K_1=716$ and $K_2=(-0.762)$:

$$g = (A_L/K_1)^{\frac{1}{K_2}} \quad (29)$$

Using (7), (29), the required number of turns $N=18$ when using 2mm spacers on the outer leg and $g=4$ mm. The transformer design is shown in Table 5.4, where L_{1A} , L_{2A} , $L_{3A}=80.06\mu\text{H}$. 200x 0.071mm litz wire is used for the winding. The windings are built in seven parallel-connected layers to reduce the leakage inductance: Layer 1,3,5,7 for the two primary windings and Layer 2,4,6 for the secondary winding.

5.5.3. Variable frequency QR and DCM operation

Fig. 5.8(a) shows the variable frequency QR operation of the IBFC. The switching frequency reduces as the EV charging power increases. The lowest switching frequency of 30kHz is observed when $V_{ev}=50\text{V}$, $I_{ev(m)}=7.5\text{A}$. At very low powers, the maximum switching frequency is restricted to 350kHz and the converter moves to DCM mode with valley skipping. The duty cycle and peak inductor current $I_{L1A(pk)}$, $I_{L3A(pk)}$ increases as the charging power increases, as seen in Fig. 5.8(b) and Fig. 5.8(c), respectively. The maximum secondary inductor current $I_{L3A(pk)}=31.5\text{A}$ occurs at the crucial operating point of $V_{ev}=333\text{V}$, $I_{ev}=30\text{A}$, $I_{ev(m)}=7.5\text{A}$

5.5.4. Sizing of filter capacitors

Fig. 5.7 shows the flyback output current for one 2.5kW stage and the total output current for the 4 interleaved stages. The output ripple reduces by four times due to the interleaved operation. To keep the output voltage ripple within limits, the

Table 5.3. LVS and ZVS operating regions of the 2.5kW Flyback transformer

Situation	CH		V2G	
	Mode	V_{valley}	Mode	V_{valley}
$V_{ev} > V_{dc}/2$	ZVS	0	LVS	$V_{ev} - V_{dc}/2$
$V_{ev} < V_{dc}/2$	LVS	$V_{dc}/2 - V_{ev}$	ZVS	0
$V_{ev} = V_{dc}/2$	ZVS	0	ZVS	0

Table 5.4. 2.5kW Flyback transformer Design

Transformer core, Air gap	A_c, l_c, g	Epcos E65 N87, 4mm net air gap
Turns	N	18:18:18
Parallel layers		2:2:3
Litz wire		200 x 0.071mm litz
Inductance	L_{1A}, L_{2A}, L_{3A}	80.06 μH
Winding resistance	R_L	27.5m Ω , 31.5m Ω , 19m Ω

required output capacitance can be estimated:

$$\Delta V_{ev(p-p)} = \frac{\Delta Q}{C_{ev(net)}} = \frac{I_{ev}(1 - D_1)}{C_{ev(net)}} \left(\frac{T}{4} \right) \quad (30)$$

For each 2.5kW IBFC, capacitance of $C_b=3\mu\text{F}$ is used at the EV output side. The four IBFC stages are then connected in parallel and two $1.5\mu\text{F}$ capacitors, common-mode and differential mode filters are connected to the common output (not shown in Fig. 5.7).

5.5.5. IBFC losses and efficiency

The equations (9)-(10) for the inductor losses and (12)-(15) for the semiconductor losses are used for the loss estimation. The key losses in the IBFC occur in the inductor and semiconductor with minor losses in the capacitors and control circuitry. The estimated losses for one 2.5kW unit can be seen in Fig. 5.9 and Fig. 5.10 for CH and V2G mode EV different powers and voltages. In this design, the resonant capacitor, $C_{21}=C_{22}=C_{23}=470\text{pF}$. Based on the output capacitance of the MOSFET and diode at 400V, the corresponding value of $T_F=1.596\mu\text{s}$.

Flyback transformer losses

For the N87 ferrite core, the Steinmetz parameters are given by $A=47.66$, $b=2.63$, $a=1.4062$ when P_{core} is in kW/m^3 , f_{sw} in kHz, B_{pk} in mT and V_e in m^3 [15]. Due to the same flux density waveforms for both the boost and flyback converter, the same equivalent frequency f_{eq} is applicable for both. A critical aspect of the flyback transformer losses are the AC copper losses P_{cu} due to the high switching frequency between 30-350 kHz. The losses due to skin and proximity effects are estimated based on [16].

Fig. 5.9(a) and Fig. 5.10 (a) shows the estimated losses in the flyback transformer for CH and V2G modes, respectively. Typical for any flyback in QR, the core and copper losses increase with power due to higher flux swing in the core and higher RMS currents respectively. The relatively high copper losses at low powers are due to the skin and proximity effect due to the high switching frequency. There is no difference in flyback transformer losses between CH and V2G mode, as the same power is handled in both cases.

Semiconductor losses

The semiconductor losses are largely dominated by the occurrence of ZVS or LVS, as described in Table 5.3. In case of QR, the turn-off energy is always stored in the quasi-resonant capacitor, and the turn-off losses are nearly zero. For ZVS, the turn-on losses are zero as well. In case of LVS, the turn on-losses are dominated by the energy stored in the QR capacitor on both the primary and secondary side. Hence Eqn. (14) is modified for IBFC for LVS to include the turn-on losses due to the discharging of the MOSFET side QR capacitor E_{QR1} and charging of the diode side QR capacitor E_{QR2} :

$$P_{S,sw} = f_{sw}(E_{on}(V_{DS},I_{DS},R_G,T_j) + E_{off}(V_{DS},I_{DS},R_G,T_j) + E_{CQR1} + E_{QR2}) \quad (31)$$

For CH mode,

$$E_{QR1} + E_{QR2} = \frac{1}{2} C_{ds(net)} (V_{dc}/2 - V_{ev})^2 + \frac{1}{2} C_{ds(net)} \left\{ \left(\frac{V_{dc}}{2} + V_{ev} \right)^2 - (2V_{ev})^2 \right\} \quad (32)$$

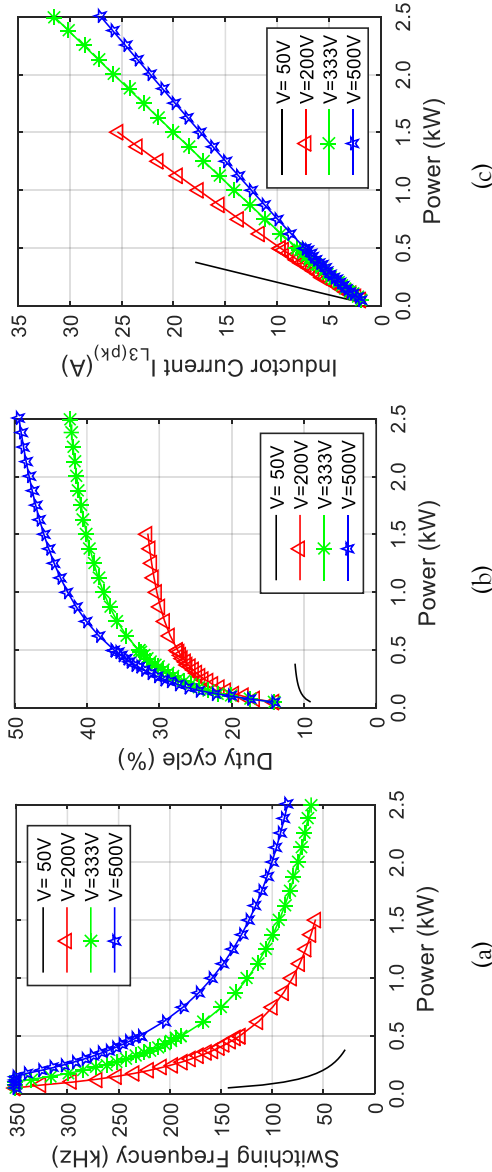


Fig. 5.8. Variation of the (a) Switching frequency, (b) Duty cycle, (c) Peak inductor current $I_{L3(pk)}$ as a function of EV charging power for different EV voltages V_{ev} .

In practice, the leakage inductance causes a significant part of E_{QR2} to be fed to the source/load. Hence, it is assumed here that only 25% of E_{QR2} is lost. Fig. 5.9(b) and Fig. 5.10 (b) shows the total MOSFET and diode losses for CH and V2G mode, where ZVS occurs when $V_{ev} > 375V$ for CH mode and when $V_{ev} < 375V$ for V2G. For both modes, the semiconductor losses increase with increasing power owing to higher RMS currents. However, when LVS occurs, the switching losses dramatically increase at lower powers owing to higher switching frequency, as seen in Fig. 5.8(a), Fig. 5.9(b), Fig. 5.10 (b). Hence, the total semiconductor losses has a U-shape when LVS occurs.

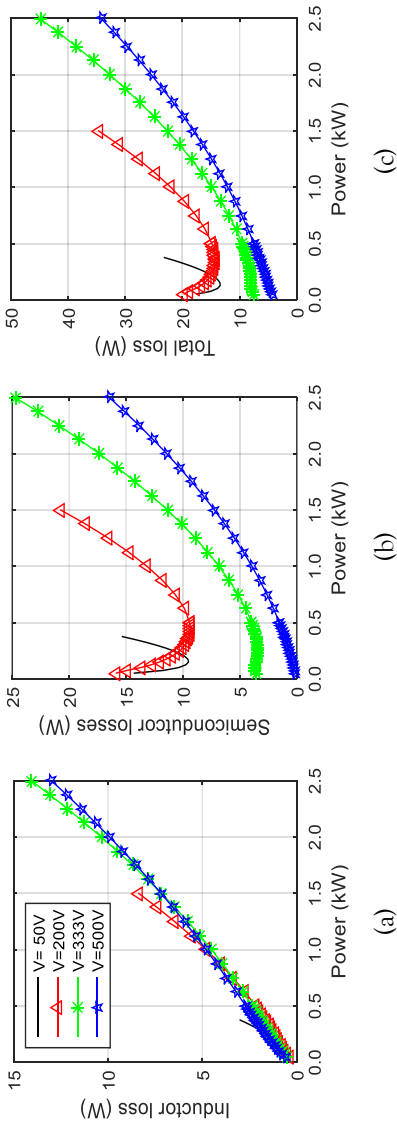


Fig. 5.9. Estimated losses in a 2.5kW IBFC for charge mode for different EV voltages and power: (a) Flyback inductor, (b) Semiconductor (c) Total losses

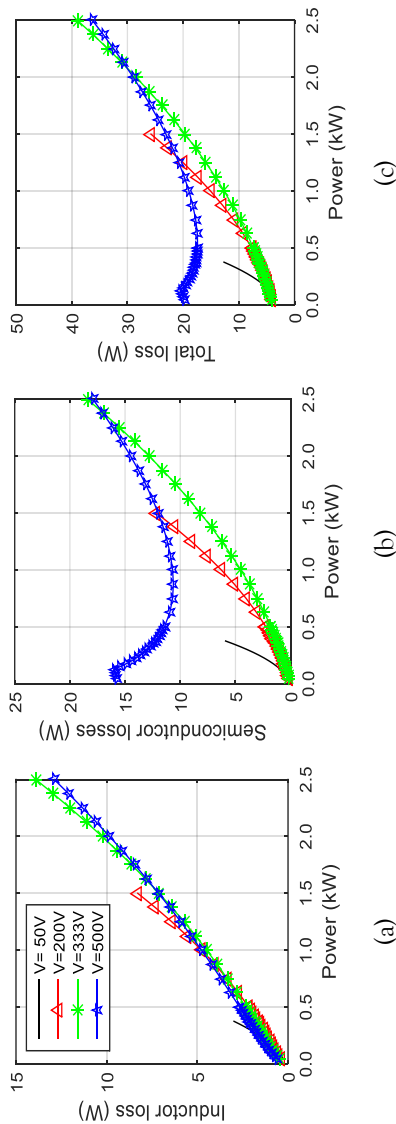


Fig. 5.10. Estimated loss in a 2.5kW IBFC for V2G mode for different EV voltages and power: (a) Flyback inductor, (b) Semiconductor (c) Total losses

Total losses

Fig. 5.9(c) and Fig. 5.10(c) shows the total losses of a 2.5kW IBFC unit including the capacitor and the 2W power of the control circuit. The maximum losses of 44.9 occurs at $V_{ev}=333V$, $P_{ev}=10kW$. The corresponding split-up of losses for CH and V2G modes for the 10kW IBFC is shown in Fig. 5.11(a). The diode conduction losses are high in CH mode, as there is only a single diode at the secondary and not two in parallel, like the MOSFET. The efficiency of the 10kW IBFC is shown in Fig. 5.11(b) and the peak efficiency is 98.8% ($V_{ev}=500V$, CH). The efficiency plot clearly reflects the occurrence of ZVS for CH and V2G mode, as shown in Table 5.3. Commercial EVs typically have voltages in the range of 200-500V, hence the converter has a peak

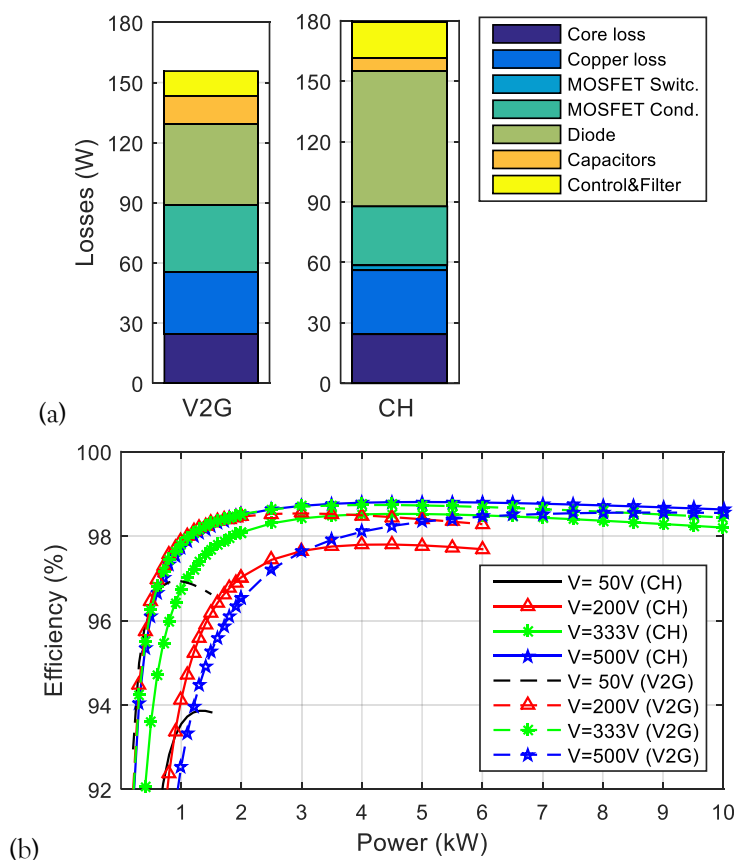


Fig. 5.11. (a) Split up of losses for $V_{ev}=333V$, $P_{ev}=10kW$ power for CH and V2G modes; (b) Efficiency of IBFC for CH and V2G mode for different EV voltages and charging power

efficiency above 97.8% in this voltage range.

5.6. Closed Loop Control

The converter is capable of four different power flows namely EV→PV, PV→Grid, Grid→EV and EV→Grid and this enabled by the closed-loop control. The closed-loop control is modularly organized into three control loops, one for each of the three

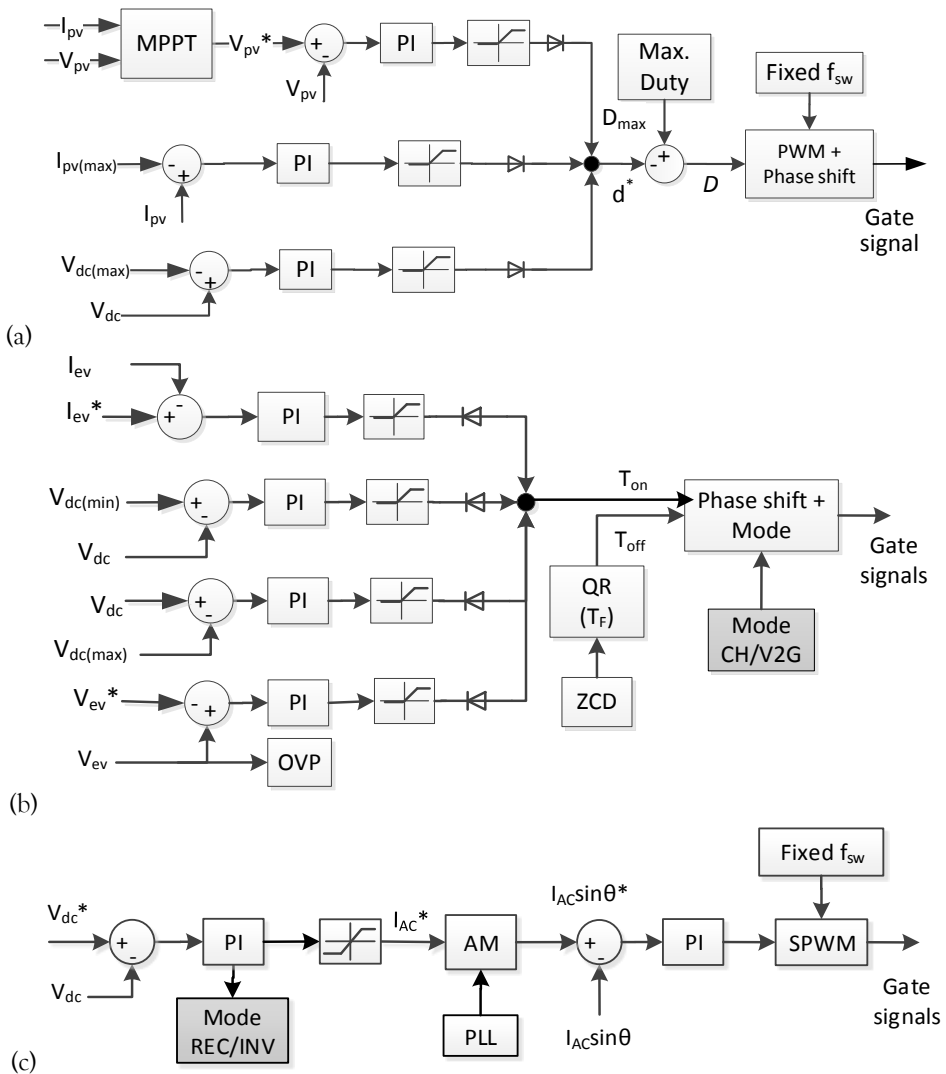


Fig. 5.12. Schematic of the closed loop control: (a) PV converter, (b) EV charger and (c) Grid inverter

converters (Fig. 5.12). The primary purpose of the control for the PV IBC, EV IBFC and grid inverter are MPPT, control of EV charging and power balance, respectively. The inverter uses the DC-link voltage to perform the power balance, and the PV and EV converters implement power curtailment if the DC-link voltage is out of bounds.

5.6.1. PV converter

The IBC's control has three control loops working in parallel to control the duty cycle D as in Fig. 5.12 (a):

$$D = D_{max} - d^* \quad (33)$$

The diode in the block diagram indicates that only one of the three parallel loops will be active at any point in time. The control output d^* is the maximum value as dictated by all the three loops (indicated by the three diodes connected in such a way that the N-cathode side is common). The maximum duty cycle $D_{max}=62.5\%$. The first loop is for MPPT, that uses a microcontroller to continuously adjust the duty cycle by perturb-and-observe method based on the PV array voltage, V_{pv} and the PV array current, I_{pv} [17]. The second and third loop are used to limit duty cycle if the PV current is more than $I_{pv(max)}=32A$ or if DC-link voltage is beyond $V_{dc(max)}=810V$.

5.6.2. DC/DC bidirectional EV charger

The IBFC control for the EV charging has four control loops acting in parallel, as seen in Fig. 5.12 (b). The diode in the block diagram indicates that only one of the four parallel loops will be active at any point in time. The control output T_{on} is the lowest value as dictated by all the four loops (indicated by the four diodes connected in such a way that the P-anode side is common).

The first loop controls the MOSFET on-time, T_{on} based on the current reference, I_{EV}^* . The next two loops are used for curtailment of charging and V2G power if the minimum ($V_{dc(min)}=700V$) and maximum ($V_{dc(max)}=810V$) DC-link voltage are reached, respectively. The last loop is used to limit the on-time when the maximum battery voltage V_{ev}^* is reached. The MOSFET off-time, T_{off} is determined by the zero-current detection (ZCD) and QR valley detection circuit. The phase shift block is responsible for maintaining the 90° phase shift between the four interleaved modules. Depending on charge or V2G mode, the gate signals are provided to the appropriate MOSFETs on the primary or secondary side of the flyback converter.

5.6.3. DC/AC Grid inverter

The DC/AC inverter is responsible for maintaining the DC-link voltage at $V_{dc}^*=750V$ by controlling the grid current, $I_{AC} \sin\theta$ that is either drawn (Rectifier mode, REC) or fed to the grid (inverter mode, INV). A phase locked loop (PLL) is used to estimate the voltage phase and maintain a high power factor, as shown in Fig. 5.12 (b). There are two PI loops, the outer loop controls the DC-link voltage, while the fast inner loop is used to control the current, I_{AC} .

The control design as described above is simple as it only requires an external voltage V_{ev}^* and current set point for the EV, I_{ev}^* . DC-link voltage is effectively used to

indirectly communicate and control the power flow in the converter. If the inverter is disconnected suddenly, then the DC-link voltage will increase or decrease till it reaches $V_{dc(min)}$ or $V_{dc(max)}$. Then, both the PV and EV converters move to power curtailment mode and ensure safety.

5.7. Experimental setup & verification

5.7.1. Modular prototype of EV-PV converter

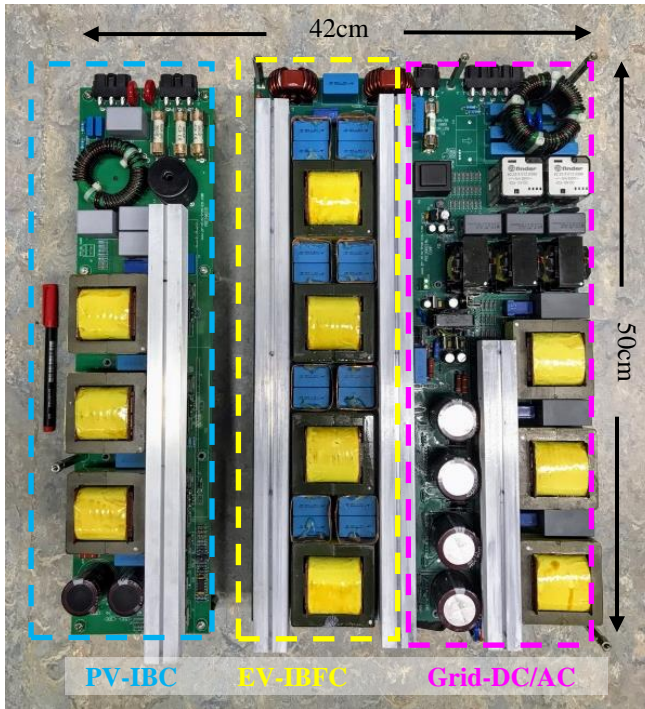


Fig. 5.13 - Experimental prototype of 10kW three-port EV-PV converter

Fig. 5.13 shows the prototype of the developed EV-PV converter with the PV IBC, EV IBFC and the grid inverter. In order to provide flexibility to the user and to increase the commercial viability of the EV-PV charger, the converter is modularly built as two power modules. The first power module consists of the PV IBC and its controller built on two PCBs, respectively. The second power module consists of the IBFC and the three-phase inverter on one PCB and their controllers on a second PCB. The two PCB are connected by connecting the common DC-link and the communication port of the two controllers. The DC-link is, hence, externally accessible and provides the possibility to connect to other EV charger power modules, PV power modules and future DC-grids. The complete EV-PV converter is 50x42x12cm with the control PCB placed at the back-side of power PCB on both the power modules. Based on cabinet dimensions, the power density of the PV converter,

EV+Grid converter and the complete EV-PV converter are 1380W/l, 555W/l and 396W/l, respectively.

The controllers in the two power modules are designed to enable two levels of modular operation. First, the power module with the IBFC and the inverter can operate with and without the power module of the PV IBC. Therefore, the charger can be used either as a solar-powered EV charger or as a bidirectional EV charger without solar as the case may be. Secondly, several bidirectional EV charger modules can be operated in parallel by giving them a common current setpoint, I_{ev}^* . By doing so, the charging power can be scaled up from 10kW to reach up to 100kW. Hence, the developed charger can be used for both Level 2 medium power charging and Level 3 fast charging.

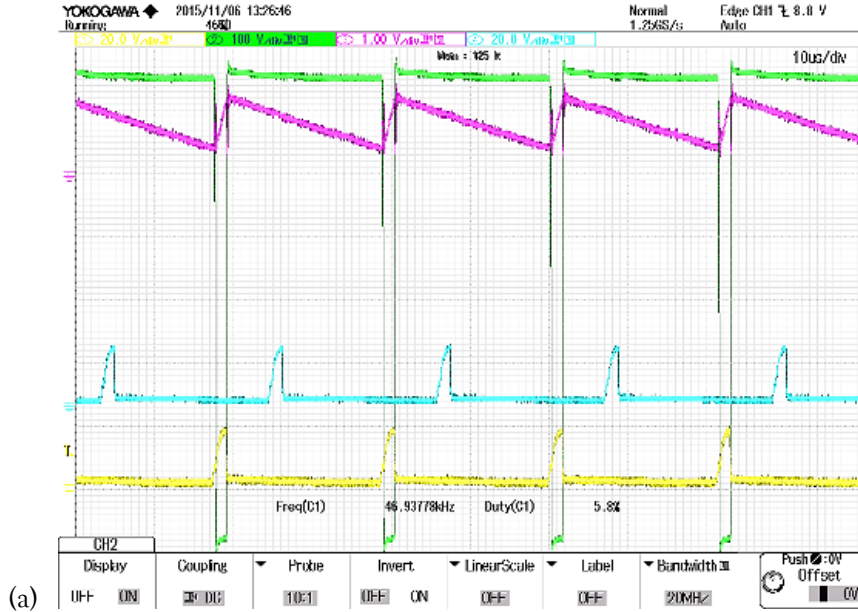
In order to make the solar EV charger commercially usable, the prototype is designed to be compatible with the following standards: EN60950 for safety, EN55011 (class A) for Emission (Industrial), EN61000-4-2 to EN61000-4-6, EN61000-4-11 for Immunity (Industrial), 2004/108/EC directive for Electromagnetic compatibility (EMC) and IEC62116 for grid connectivity. PRE was responsible designing the EMC filters and controllers of the converter so as to meet the above standards. Further, PRE was responsible for designing the control circuitry for the startup, AC synchronization, protection and shutdown of the converter. These aspects are outside the scope of this thesis.

5.7.2. Experimental waveforms

Fig. 5.14(a) shows the operating waveforms of the PV IBC for continuous conduction mode (CCM) and Fig. 5.14(b) shows the waveforms for discontinuous conduction mode (DCM), where a PV emulator is used as input. The figure shows the waveforms for the phase shifted gate voltage V_{GS} , Inductor current I_L and the MOSFET drain-source voltage V_{ds} . During CCM, the inductor current $I_{L(l)}$ rises when the gate voltage $V_{GS(l)}$ is ON and then begins to fall once the gate is OFF, as seen in Fig. 5.14(a). In DCM, the inductor current $I_{L(l)}$ goes to zero before the end of the switching cycle, causing the drain-source voltage $V_{ds(l)}$ to oscillate as it goes from $V_{ds(on)}$ to V_{PV} , in Fig. 5.14(b).

Fig. 5.15 shows the MOSFET drain-source $V_{ds(1)}$, and the gate-source voltage $V_{gs(1)}$ for one of the four interleaved stages of the EV IBFC for charge mode. The quasi-resonant operation can be clearly seen in Fig. 5.15(a) where the switch is turned on exactly when the quasi-resonant valley is detected. At lower powers, the maximum frequency setting of 350 kHz ensures that valley skipping occurs, as shown in Fig. 5.15(b). The quasi-resonant time period was measured to be $T_F=1.52\mu s$, close to the estimated value of $T_F=1.596\mu s$.

Finally, Fig. 5.16 shows the waveforms of the AC current fed to the grid in V2G mode by the DC-AC inverter. The waveforms are obtained at the full power of $P_{ev}=10kW$ at $V_{ev}=402V$. The corresponding total harmonic distortion measurements, (THD) in the grid current is 2.95% at full load, at 0.987 power factor.



$V_{ds}(1)$ $I_L(1)$ $V_{gs}(3)$ $V_{gs}(1)$

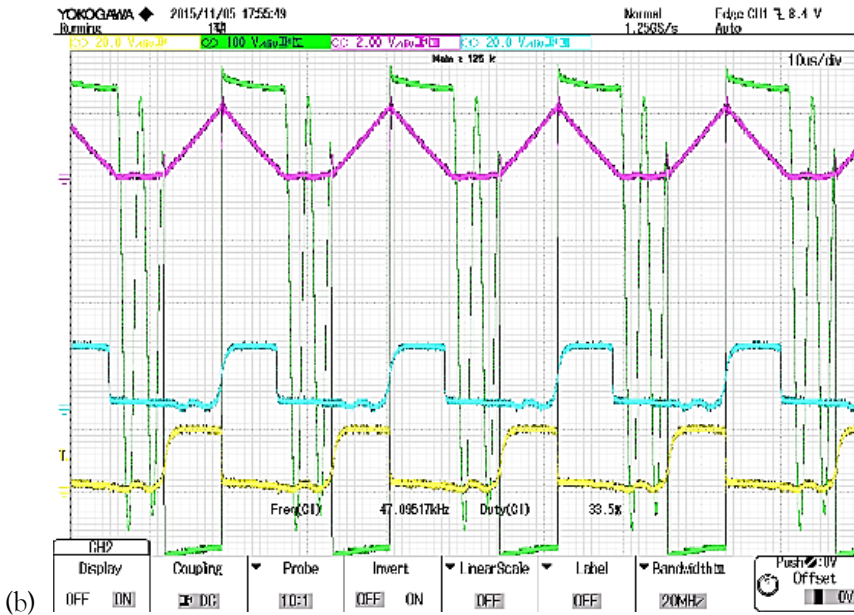


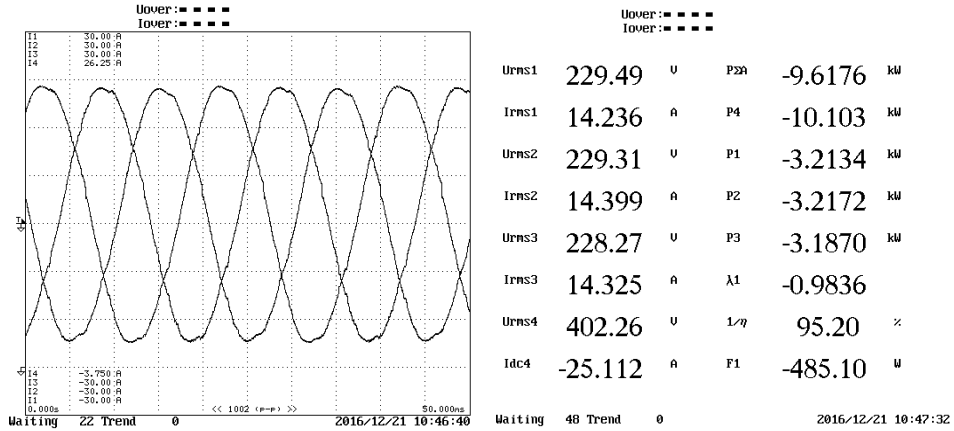
Fig. 5.14. (a) Waveforms for the PV IBC for the phase shifted gate voltage V_{GS} , Inductor current I_L and MOSFET drain-source voltage V_{ds} for (a) CCM mode ($V_{PV}=700$ V, $I_{PV}=10$ A); (b) DCM mode ($V_{PV}=400$ V, $I_{PV}=10.75$ A)



$V_{ds(1)}$ $V_{gs(1)}$



Fig. 5.15. Drain-source voltage V_{ds} and gate voltage V_{gs} for one phase of the IBFC for CH mode: (a) Quasi-resonant operation LVS for $V_{ev}=250V$, $I_{ev}=5A$ (b) Valley skipping and DCM operation at low powers for $V_{ev}=100V$, $I_{ev}=1A$



		Uover: ■ ■ ■ ■	PLL Src: U1				
		Iover: ■ ■ ■ ■					
		***** I 1 List *****	***** I 1 List *****				
		Or.	I[A]	Hdf [%]	Or.	I[A]	Hdf [%]
PLL	U1		14.230	-----	dc	1.293	9.13
Freq	50.011 Hz	1	14.165	100.00	2	0.092	0.65
		3	0.311	2.19	4	0.041	0.29
U1	229.57 V	5	0.067	0.47	6	0.036	0.25
I1	14.230 A	7	0.190	1.34	8	0.022	0.16
P1	-3.2117kW	9	0.029	0.21	10	0.020	0.14
S1	3.2523kVA	11	0.021	0.15	12	0.020	0.14
Q1	-0.5118kvar	13	0.083	0.59	14	0.019	0.13
λ1	-0.9875	15	0.031	0.22	16	0.012	0.09
φ1	189.05 °	17	0.058	0.41	18	0.006	0.04
Uthd1	2.05 %	19	0.025	0.17	20	0.018	0.13
Ithd1	2.95 %	21	0.004	0.03	22	0.022	0.16
Pthd1	0.01 %	23	0.010	0.07	24	0.024	0.17
Uthf1	0.55 %	25	0.020	0.14	26	0.020	0.14
Ithf1	1.43 %	27	0.007	0.05	28	0.012	0.08
Utif1	18.74	29	0.014	0.10	30	0.009	0.06
Itif1	62.11	31	0.021	0.15	32	0.013	0.09
hvf1	0.81 %	33	0.014	0.10	34	0.025	0.17
hcf1	1.48 %	35	0.002	0.01	36	0.015	0.10
F1	229.51 V	37	0.027	0.19	38	0.013	0.09
F2	-----	39	0.011	0.08	40	0.013	0.09
F3	-----	41	0.017	0.12	42	0.005	0.03
F4	-----	43	0.003	0.02	44	0.007	0.05
φU1-U2	119.62 °	45	0.013	0.09	46	0.006	0.04

Waiting 12 Trend 0 2016/12/21 10:45:48

Fig. 5.16. Waveforms of the AC current fed to grid in V2G mode for $P_{cr}=10kW$, $V_{cr}=402V$ and the corresponding power and THD measurements

5.7.3. Efficiency of converter

Fig. 5.17 shows the measured efficiency of the converter for different power flows: EV→PV, PV→Grid, Grid→EV when $V_{ev}=400V$. The peak efficiencies were 95.2%, 96.4% and 95.4%, respectively. The efficiency of EV→Grid was nearly the same as Grid→EV. The power converter has a 16W no-load power consumption when the mains relay and auxiliary power supplies are ON, and the switches are not switching. Once the switches are activated for switching ('enable' state), the no-load power consumption increases to 40W. This excludes the power consumed by the 9 fans on the two power modules.

During operation at the nominal power of 10kW with an ambient temperature of 25°C, the internal temperature of the converter cabinet was generally found to be 40°C. The heatsinks were at 60°C and semiconductor case temperature was typically 75°C. This can correspond to a junction temperature in the range of 95-105°C. More importantly, the electrolytic capacitors on the DC-link were measured to be at a temperature of 45-50°C. At this temperature, the capacitors can last for around 10 years with continuous operation, before the electrolyte would dry out. Since the EV chargers would not be used all the time (most probably), the expected lifetime of the capacitor would be higher by a factor of 1.5-3 depending on usage.

Fig. 5.17 compares the measured and estimated of the converter, and they are found to be in close to each other. The difference between the measured and estimated efficiencies is attributed to the following reasons:

- The loss estimation was made with an assumption of a fixed junction of 75°C. In practice, the junction temperature continuously varies and directly influences the conduction and switching losses of the semiconductor devices.

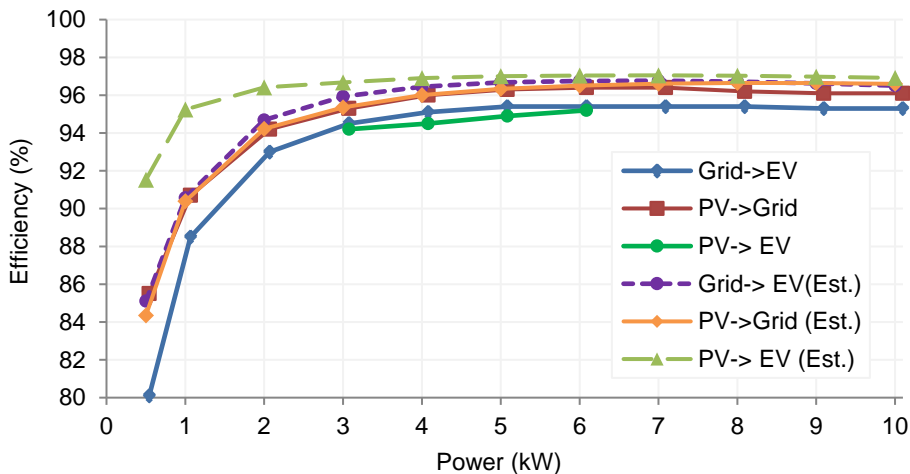


Fig. 5.17. Measured and estimated efficiency of converter for power flow paths: EV→PV, PV→Grid, Grid→EV

- The loss model for estimating the core losses did not consider the DC bias in the inductor current [31] and impact of temperature variation.
- The loss model linearly extrapolated several values from the datasheet to account for differences between operating conditions and datasheet measurements for device voltage, current, gate resistance, junction temperature. These dependencies are not strictly linear but assumed to be such due to limited information in datasheets. For example, the turn-on gate resistance used is much higher than the nominal values provided by the manufacturer and this loss dependency is not strictly linear. This is especially true for SiC where the losses increase drastically with gate resistance and it becomes an important factor in CCM where turn-on losses are significant.
- The current sharing between the three interleaved SiC switches in the PV IBC was not found to be equal when operated in CCM, showing differences of up to 5°C on switch case temperature. The main reasons for this are the soft saturation of the powdered iron core inductor (which causes the actual operation inductance to be slightly different in each leg), PCB layout, thermal conduction of heatsink and offsets in the duty cycle between the three legs.
- When the PV IBC operates in discontinuous conduction mode (DCM), only a part of the switch turn-on energy is lost, and the rest is sent back to the source depending on the parasitic drain-source capacitance. The loss model assumes that all energy is lost in the switch during the turn-on process. Similarly, during switch turn-off in the IBFC, the losses are not zero as all the turn-off energy does not go to the QR capacitor.
- In case of IBFC, the switching frequency as estimated as estimated by (27) is not very accurate at low powers. This is because the commutation time of the diode and switch is neglected and this becomes significant when the switching frequency increases at low powers. Secondly, the quasi-resonant time period T_F is assumed to be a constant. In reality, T_F is dependent on the output capacitance of the diode and MOSFET which are themselves voltage dependent. In the model, the capacitance at 400V drain-source voltage is used and the commutation time is neglected.
- Finally, the loss models do not consider the power consumed by the cooling fans. This is because the fans are designed to draw power proportional to the heat sink feature, and this is in turn dependent on the operating power and voltage, and the environment.

5.7.4. Comparison with conventional design

The developed three port converter is compared to a conventional solar EV charger that uses a 10kW solar inverter [18] and 10kW unidirectional EV charger [19]. [18], [19] have the specifications as listed in Table 5.1. , but uses the AC grid to exchange power from the PV to EV, instead of DC. This is the same as system architecture 1 described in Chapter 2. [18] uses a three-phase resonant topology, while [19] uses an

IBC with a three-phase inverter, similar to what is developed here. Moreover, it is interesting to note that the two converters are based on silicon IGBT technology and ferrite cores.

Fig. 5.18 shows the efficiency of the developed converter compared to that of the conventional converters based on AC power exchange between EV and PV. Firstly, it can be seen that for the power conversion for Grid→EV and PV→EV, the developed converter has a much higher peak and a higher partial load efficiency than the resonant topology, as seen in Fig. 5.17. The high partial load efficiency makes it suitable for smart charging of EVs where the EV charging power is continuously varied [20]. Secondly, the efficiency for PV→Grid of the developed converter is similar to that of conventional design with relatively small differences.

Fig. 5.19 shows the size comparison of the 10kW PV inverter, EV charger and the bidirectional EV-PV charger. The power density of the developed charger (396W/l) is three times that of the two converters combined (134W/l) as clearly seen in Fig. 5.19, while still providing all the functionalities. In addition, the developed charger is bidirectional and capable of V2G while the conventional design is not.

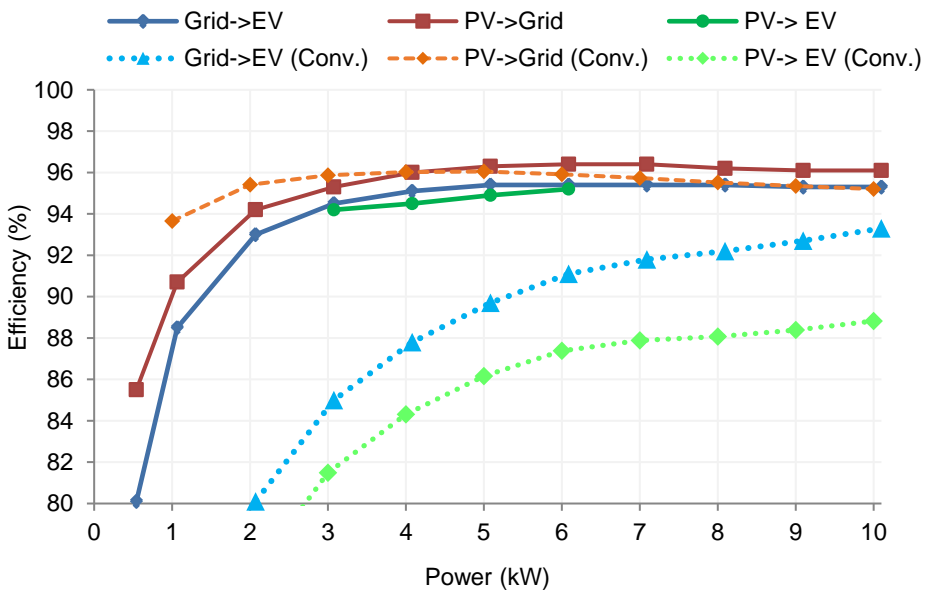


Fig. 5.18. Measured efficiency of the developed converter compared to that of the conventional design based on AC power exchange between EV and PV; for power flow paths: EV→PV, PV→Grid, Grid→EV

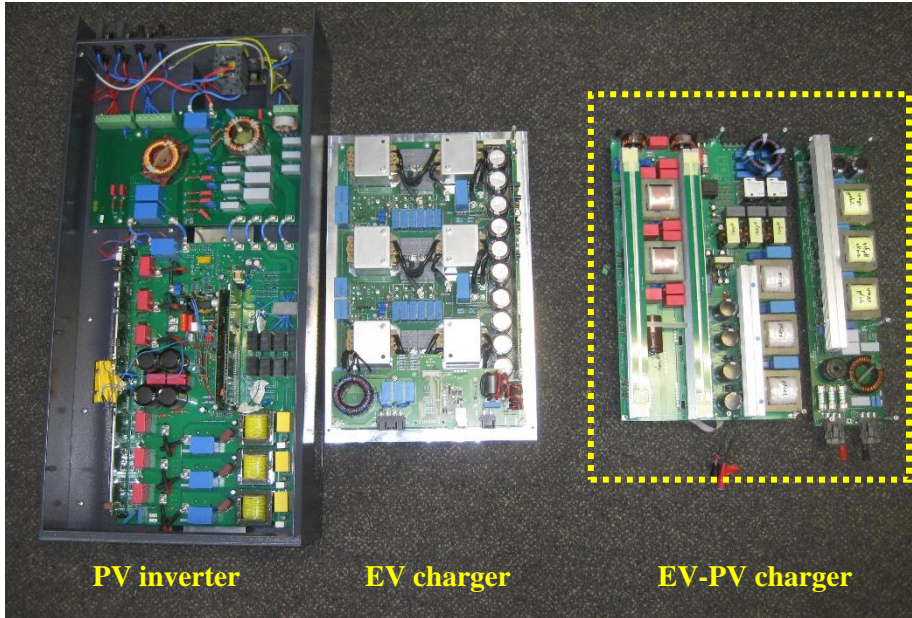


Fig. 5.19. The relative size of a conventional 10kW solar inverter [18] (left) and a 10kW unidirectional EV charger [19] (middle) based on silicon IGBTs and ferrite cores compared to the developed 10kW solar powered bidirectional EV charger (right). The developed charger has a 3x power density compared to the combined power density of the solar inverter and EV charger.

5.8. Testing with a Nissan Leaf - Charging and V2G

Fig. 5.20(a) shows the testing of the converter to charge and discharge a V2G enabled Nissan Leaf EV using an outdoor cabinet. A CHAdeMO charge controller (developed by Last Mile Solutions) that implements the CAN communication with the EV was used to provide the voltage V_{ev}^* and current set points I_{ev}^* to the power converter. Fig. 5.20(b) shows the 390V EV battery being successfully discharged (V2G) and then charged with a current and power of 24A, 9.36kW respectively. Due to the absence of PV panels at the test location, there was no PV power input.

5.9. Datasheet of EV-PV charger

Appendix D has the datasheet and brochure of the developed 10kW solar powered bidirectional EV charger. It also provides the physical design and pictures of the EV-PV charging station based on the MSc thesis project of M. Leendertse, which was done in collaboration with the Industrial Design faculty of TU Delft. The charging station design is done considering aesthetics, ergonomics, user comfort and safety.

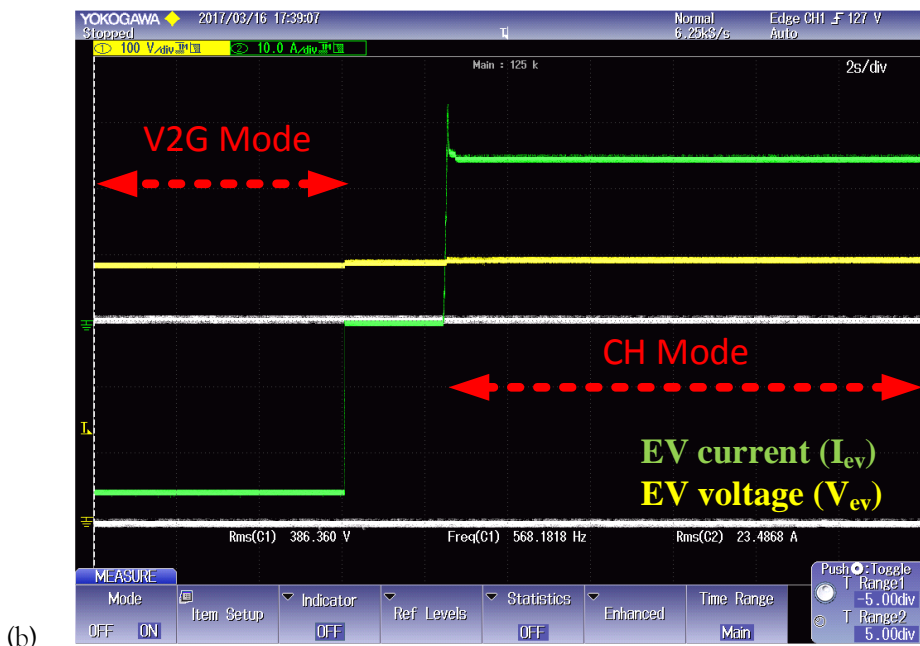


Fig. 5.20. (a) Test setup of EV-PV charger with a CHAdEMO charge controller connected to a V2G enabled Nissan Leaf EV (b) Scope showing the Nissan Leaf during V2G and CH operation using the developed power converter with the battery voltage V_{ev} in yellow and charging/discharging current I_{ev} in green.

5.10. Conclusions

This chapter presents the development of a 10kW, three-port, bidirectional converter for direct DC charging of EV from PV. The developed converter is compatible with CCS and CHAdeMO EV charging standard and can operate with a PV array of wide voltage and power range. Interleaving of converters, Silicon carbide (SiC) devices and powdered alloy core inductors are extensively used to increase the switching frequency, while keeping the converter losses within limits. This has helped to increase the power density by a factor of three when compared to conventional designs based on silicon IGBTs and ferrites, and AC power exchange between EV and PV.

The converter is modularly designed with three sub-converters connected on a 750V central DC-link: interleaved boost converter for PV, three-phase inverter for AC grid and interleaved flyback converter for EV. While the flyback is traditionally considered suitable only for low powers, this chapter shows how the use of SiC devices in a QR mode flyback converter can achieve high efficiency even at high powers. Three closed loop controls were developed and tested for the three sub-converter which enables four power flows: PV→EV, EV→grid, grid→EV and PV→grid.

A 10kW prototype was built and tested and exhibits a peak efficiency of 96.4%. The developed prototype has a much higher peak efficiency and higher partial load efficiency than currently existing solutions. The charge and V2G operation at 10kW were tested with a Nissan Leaf EV with a CHAdeMO charge controller.

5.11. References

- [1] “Standard IEC 61851 - Electric vehicle conductive charging system - Part 1, 21, 23, 24,” pp. 1–287, 1–47, 1–159, 1–63, 2014.
- [2] CHAdeMO Association, “Technical specifications of quick charger for the electric vehicle,” *CHAdeMO Protoc. Rev. 1.1*, 2010.
- [3] C. E. Weitzel, J. W. Palmour, C. H. Carter, K. Moore, K. K. Nordquist, S. Allen, C. Thero, and M. Bhatnagar, “Silicon carbide high-power devices,” *IEEE Trans. Electron Devices*, vol. 43, no. 10, pp. 1732–1741, 1996.
- [4] G. R. Chandra Mouli, J. H. Schijffelen, P. Bauer, and M. Zeman, “Design and Comparison of a 10kW Interleaved Boost Converter for PV Application Using Si and SiC Devices,” *IEEE J. Emerg. Sel. Top. Power Electron.*, vol. 5, no. 2, pp. 610–623, Jun. 2017.
- [5] “Technical Bulletin - MAGNETICS Kool M μ E-Cores,” 2005.
- [6] “Technical Bulletin - MAGNETICS Kool M μ , A Magnetic Material for Power Chokes,” 2005.
- [7] O. Hegazy, J. Van Mierlo, and P. Lataire, “Analysis, Modeling, and Implementation of a Multidevice Interleaved DC/DC Converter for Fuel Cell Hybrid Electric Vehicles,” *IEEE Trans. Power Electron.*, vol. 27, no. 11, pp. 4445–4458, Nov. 2012.
- [8] J. Reinert, A. Brockmeyer, and R. W. A. De Doncker, “Calculation of losses in ferro- and ferrimagnetic materials based on the modified Steinmetz equation,” *IEEE Trans. Ind. Appl.*, vol. 37, no. 4, pp. 1055–1061, 2001.

-
- [9] MAGNETICS, "Powder Core Catalog," 2015.
- [10] A. M. A. Hava, R. J. R. Kerkman, and T. A. T. Lipo, "Simple analytical and graphical methods for carrier-based PWM-VSI drives," *IEEE Trans. Power Electron.*, vol. 14, no. 1, pp. 49–61, 1999.
- [11] B. Singh, B. N. Singh, A. Chandra, K. Al-Haddad, A. Pandey, and D. P. Kothari, "A Review of Three-Phase Improved Power Quality AC–DC Converters," *IEEE Trans. Ind. Electron.*, vol. 51, no. 3, pp. 641–660, Jun. 2004.
- [12] M. P. Kazmierkowski and L. Malesani, "Current control techniques for three-phase voltage-source PWM converters: a survey," *IEEE Trans. Ind. Electron.*, vol. 45, no. 5, pp. 691–703, 1998.
- [13] M. Liserre, F. Blaabjerg, and S. Hansen, "Design and control of an LCL-filter-based three-phase active rectifier," *IEEE Trans. Ind. Appl.*, vol. 41, no. 5, pp. 1281–1291, 2005.
- [14] K. Jalili and S. Bernet, "Design of LCL filters of active-front-end two-level voltage-source converters," *IEEE Trans. Ind. Electron.*, vol. 56, no. 5, pp. 1674–1689, 2009.
- [15] Epcos, "Epcos Core and accessories - E 65/32/27; Ferrites and accessories - SIFERRIT material N87," Epcos, 2015.
- [16] C. R. Sullivan, "Computationally efficient winding loss calculation with multiple windings, arbitrary waveforms, and two-dimensional or three-dimensional field geometry," *IEEE Trans. Power Electron.*, vol. 16, no. 1, pp. 142–150, 2001.
- [17] M. A. G. de Brito, L. Galotto, L. P. Sampaio, G. de A. e Melo, and C. A. Canesin, "Evaluation of the Main MPPT Techniques for Photovoltaic Applications," *IEEE Trans. Ind. Electron.*, vol. 60, no. 3, pp. 1156–1167, Mar. 2013.
- [18] STECAGRID, "Datasheet - STECAGRID 10,000+ 3ph Solar Inverter."
- [19] PRE, "Datsheet EVC500V30A - 10kW EV Charger Module - Power Research Electronics B.V," 2017.
- [20] D. van der Meer, G. R. Chandra Mouli, G. Morales-Espana, L. Ramirez Elizondo, and P. Bauer, "Energy Management System with PV Power Forecast to Optimally Charge EVs at the Workplace," *IEEE Trans. Ind. Informatics*, vol. 14, no. 1, pp. 311–320, 2018.

6

Energy management system for smart charging of EVs

6. Energy management system for smart charging of EVs

This chapter is based on:

D. van der Meer, G. R. Chandra Mouli, G. Morales-Espana, L. Ramirez Elizondo, and P. Bauer, "Energy Management System with PV Power Forecast to Optimally Charge EVs at the Workplace," IEEE Trans. Ind. Informatics, vol. 14, no. 1, pp. 311–320, 2018

G.R. Chandra Mouli, M. Kefayati, R. Baldick, P. Bauer, "Integrated PV Charging of EV Fleet Based on Energy Prices, V2G and Offer of Reserves,"IEEE Trans. Smart Grids, 2017, pp.1-13

Summary

The design of the EV-PV system and power converter was delved into in chapters 3-5. The power converter can enable direct DC charging of EV from PV and V2G, but it does not have any intelligence of its own. The goal of chapter 6 is to develop smart EV charging algorithms to reduce the cost of charging EVs based on the solar forecast, EV user preferences, offer of ancillary services, use of vehicle-to-grid (V2G), multiplexing of EVs and charging based on energy prices. A smart charging algorithm based on Mixed Integer Linear Programming (MILP) is proposed that controls the charging of an EV fleet based on the above applications. It is applied to two scenarios namely, Netherlands and Texas, USA to quantify its benefits and net cost reduction.

Outline

Section 6.2 explains the differences between uncontrolled charging and smart charging. 6.3 reviews the existing algorithms that have been proposed for smart charging of EVs based on PV generation, energy prices and offer of ancillary services and use of vehicle-to-grid (V2G) technology. The scientific gaps in using these algorithms for the proposed EV-PV charging system are identified. 6.4 elucidates the layout and parameters of the energy management system (EMS) and receding horizon implementation. The MILP formation and the corresponding parameters, constraints and objective function are elaborated in section 6.5. Section 6.6 and 6.7 describes the two scenarios for the Netherlands and Texas, respectively. The simulation parameters and numerical results quantifying the benefits of the algorithm are shown. The last section 6.8, delves into the implementation aspects of the algorithm: scalability, adaptability, benefit sharing and market feedback.

6.1. Nomenclature

- t, v, c - Optimization indices for time, electric vehicle (EV), and charger respectively
- $x_v^{e(ar)}$ - 'Average rate' charging power of v^{th} EV (kW)
- t_{dly} - Time delay for randomly delayed charging (h)
- C^{ev} - Charging costs for entire EV fleet (\$)
- S^{PV} - Revenue from sales of PV power (\$)
- S^{as} - Revenue from sales of ancillary services (\$)
- $C^{ar}, C^{rnd}, C^{imm}, C^{opt}$ - Net costs for average rate, randomly delayed, immediate and optimized charging from PV (\$)

6.1.1. Optimization input parameters

Electric vehicle parameters (index v)

- T_v^a, T_v^d - Arrival and departure time of EV respectively (h)
- B_v^a - Energy in the battery of the v^{th} EV upon arrival T_v^a (kWh)
- B_v^d - Energy in the battery of the v^{th} EV at departure T_v^d (kWh)
- d_v - Charging energy demand of v^{th} EV (kWh)
- C_v^p - Penalty for not meeting energy demand d_v by departure time T_v^d of v^{th} EV (\$/kWh)
- C^{V2X} - Battery degradation penalty paid to the EV user for participating in V2G services (\$/kWh)
- B_v^{min}, B_v^{max} - Minimum and maximum possible energy in the battery of the v^{th} EV (kWh) respectively
- x_v^{ub}, x_v^{lb} - Maximum charging and discharging i.e. vehicle to grid (V2X) power of v^{th} EV (kW) respectively
- $\eta_v^{ch}, \eta_v^{v2x}$ - Efficiency of charging and discharging of the battery of v^{th} EV (kW) respectively

EV-PV power converter parameters (index c)

- p_c^{conv} - Rated power of the DC/AC inverter (kW)
- p_c^{EVr} - Rated power of each EV charger in c^{th} EV-PV power converter (kW)
- p_c^{PVr} - Rated power of photovoltaic array (PV) connected to c^{th} charger (kW_p)
- η_c^{conv} - Rated efficiency of c^{th} EV-PV charger (%)
- K_c^{PV} - PV scaling factor that takes into account the losses due to orientation and shading with respect to a 1kW optimally oriented PV array at car park
- N_c^{conn} - Maximum number of EVs that can be connected to the c^{th} EV-PV power converter
- N_c^{ch} - Maximum number of EVs that can be simultaneously charged from c^{th} EV-PV converter
- $K_{v,c}$ - Binary variable indicating connection of v^{th} EV with c^{th} charger (1,0; Connected=1)

PV forecast, car park and ISO parameters (index t)

- ΔT - Time step for the model predictive control (h)
 V - Number of EV in the car park at time t
 C - Number of EV-PV chargers in the car park
 $P_t^{PV(fc)}$ - Power generation forecast of $1kW_p$ PV array installed at the workplace or car park (kW)
 C^{PV} - Cost of obtaining PV energy (\$/kWh)
 $y^{PV(fc)}$ - Maximum uncertainty in solar forecast data (%)
 $p_t^{e(buy)}, p_t^{e(sell)}$ - Market clearing price for buying and selling electricity from the grid respectively (\$/kWh)
 $p_t^{r(up)}, p_t^{r(dn)}$ - Market clearing price for offering reserve capacity for up and down regulation respectively (\$/kW)
 P_t^{DN+}, P_t^{DN-} - Distribution network capacity for drawing and feeding power to car park respectively (kW)

6.1.2. Optimization variables

All variables listed below are positive

- $B_{t,v}$ - SOC of v^{th} EV battery at time t (kWh)
 $P_{t,c}^{PV}$ - Power generated by PV connected to the c^{th} charger at time t (kW)
 $a_{t,v}^c$ - Binary variable that determines if the v^{th} EV is active i.e. charging/discharging at a finite power or idle at time t (1,0; Active =1)
 $a_{t,v}^{ch.v2x}$ - Binary variable that determines if the v^{th} EV is in charge or V2G mode at time t (1,0; Charge =1)
 $a_{t,c}^{d-f}$ - Binary variable that determines if the c^{th} charger is drawing or feeding power to the car park at time t (1,0; Draw =1)
 $x_{t,v}^{r(up)}, x_{t,v}^{r(dn)}$ - Reserve power capacity offered to grid for up and down regulation by v^{th} EV at time t (kW)
 $x_{t,v}^{e+}, x_{t,v}^{e-}$ - Charging and discharging power of v^{th} EV at time t respectively (kW)
 $P_{t,c}^{draw}, P_{t,c}^{feed}$ - Power drawn and fed to car park by c^{th} EV-PV charger at time t respectively (kW)
 $P_t^{g(imp)}, P_t^{g(exp)}$ - Power imported and exported to grid by the EV car park at time t respectively (kW)

6.2. Introduction

The EV-PV charger in its current form will be able to charge the EV from solar energy, but it will not have any intelligence of its own. For example, if it is known from the solar forecast that it will be a sunny afternoon and energy prices are low in the morning, it will be beneficial to charge the EV from the grid in the morning and from the solar in the afternoon. In order to realize such control, smart charging algorithms will be required in the EV-PV charging system.

6.2.1. Immediate, average rate and randomly delayed charging

Today, when an EV arrives at the workplace and is connected to the electric vehicle supply equipment (EVSE), the EV starts charging essentially immediately at the nominal maximum EVSE power rating, P_c^{EVr} . The charging continues at approximately constant power until the battery is nearly full¹. This is referred to as immediate charging (IMM) or uncontrolled charging [1]. This is the simplest form of charging requiring no information from the user or communication infrastructure and results in the lowest charging time. However, IMM typically results in a huge demand on the grid based on the EVSE, as shown in Fig. 6.1.

At the same time, the long parking times of EVs at workplace offers the flexibility in scheduling the charging in terms of both charging power and duration. This means that EVs can be charged at a much lower power than the EVSE nominal rating if the EV user arrival time, T_v^a , departure time, T_v^d and required energy demand, d_v are known. One approach is the ‘‘Average Rate’’ (AR) charging policy [1], where the charging power $x_v^{e(ar)}$ is the minimum of the EVSE capacity, P_c^{EVr} , and the ratio of the energy demand divided by the parking time of the EV¹:

$$x_v^{e(ar)} = \text{Min.} \left\{ \frac{d_v}{T_v^d - T_v^a}, P_c^{EVr} \right\} \quad \forall t \in \{T_v^a, T_v^d\} \quad (1)$$

The advantage of the AR policy is that the charging of the fleet is spread throughout the day instead of being concentrated around the arrival time (typically early morning), as seen in Fig. 6.1. Combining the ideas of AR and IMM is Randomly

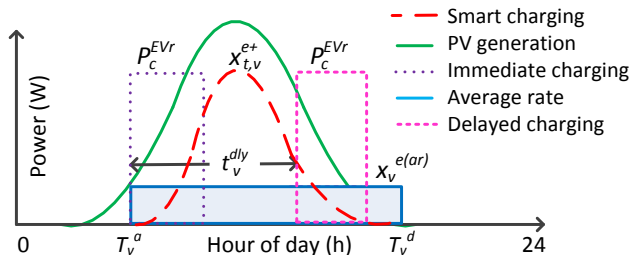


Fig. 6.1. Immediate, average rate, randomly delayed and smart charging of EV

¹ The analysis does not consider the duration in the constant-voltage (CV) charging mode, which occurs typically when EV battery is above 80% SOC and the maximum charging power is limited [36].

Delayed Charging (RND): a type of charging where the start of the charging is delayed by a random time duration t_v^{dly} such that the EV reaches its desired SOC by the departure time [2], [3]:

$$t_v^{dly} = \text{Random} \left[0, (T_v^d - T_v^a) - \frac{d_v}{P_c^{EVr}} \right] \quad (2)$$

Just like IMM, the charging power is fixed and equals the rated power of the EVSE, P_c^{EVr} . With a fleet of EV, the net charging profile of RND is similar to AR in the sense that the charging of different EV is spread-out in time throughout the day, instead of being concentrated at the arrival time. At the same time, however, IMM, RND and AR strategies are not completely ‘smart’ as the consumption has no correlation to the variation of local renewable generation, distribution network capacity constraints and/or energy prices.

6.2.2. Smart charging

The optimal way to charge EVs is hence to schedule the charging by taking into consideration the EV user preferences, local renewable generation, distribution network and energy prices from the market. Fig. 6.1 shows an example of smart charging where the EV charging follows the PV generation. Further, EVs can have an extremely fast ramp up and ramp down rate. CHAdeMO and Combo EV charging standards for DC charging stipulate response time of 200ms for power changes [4]. This makes EVs ideal candidates for providing ancillary services in the form of regulation services to the grid [5]–[8].

Following the formulation in [6], [9], an Energy Services Company (ESCO) company acts as an intermediary between the wholesale market operated by the Independent System Operator (ISO) and the EV end-users. The ESCo operates at the workplace where employees drive to the office with an EV, and the building has overhead PV installation or a solar carport. The motive of the ESCo is to schedule the charging of the EV and feeding of PV power to the grid in such a way that EV charging costs are lowered, regulation services are offered to the ISO, and at the same time, the income from PV is increased. ESCo achieves this motive by using an Energy Management System (EMS) to schedule the EV based charging on a multitude of inputs:

1. Information from the EV user about EV type, arrival and departure times, the state of charge (SOC) of EV battery and energy demand.
2. Settlement point prices for buying and selling electricity from the grid at time t ($p_t^{e(buy)}$, $p_t^{e(sell)}$).
3. Clearing prices for capacity for offering reserves to the ISO for up and down regulation. ($p_t^{r(up)}$, $p_t^{r(dn)}$).
4. Distribution network limits for drawing and feeding power between the EV car park and the grid (P_t^{DN+} , P_t^{DN-}). These values can be adjusted to implement demand side management (DSM).
5. Solar forecast information to help reduce the uncertainties due to variability in PV generation on diurnal and seasonal basis ($P_t^{PV(fc)}$).

6.3. Literature review and overview of contributions

Several earlier works have formulated the optimization problem to charge EV based on renewable generation, energy prices, and offering of ancillary services.

Fuzzy logic is used to optimize the EV charging based on PV generation forecast, energy prices in [10] and V2G frequency regulation, grid energy exchange in [11]. The disadvantage is that the use of fuzzy logic without optimization techniques does not guarantee that the obtained solution is optimal.

In [6], [9], linear programming (LP) is used to find the optimal EV strategy for charging and offering reserves based on market prices. In [12], LP is used to reduce the cost of charging EV from PV based on time of use tariffs and PV forecasting. Cost reduction of 6% and 15.2% compared to the base case are obtained for simulation for 12 EV powered from a 50kW PV system. The LP formulation in [13] and heuristic methods used in [14] aim to achieve the two goals: increasing the PV self-consumption in a micro-grid by charging of EVs and reducing the dependency on the grid. However, there is no consideration for time of use tariffs without which there is no incentive to achieve the two goals.

In [15], LP is used for planning the EV charging based on renewable power forecasting, spinning reserve, and EV user requirements in a micro-grid. A two-layered optimization is used for EV charging based on variable energy prices which results in increased number of EVs charged and up to 18% increased revenues [16]. While realistic vehicular mobility pattern is used, there is, however, no consideration for V2G, regulation or local generation. A MILP formulation in [17], [18] is used for EV charging based on PV, EV user, energy prices and without the offer of regulation services. 10%-171% reduction in net cost is obtained in [17] based on the proposed method.

Stochastic programming (SP) is used in [19] to plan EV charging and offer regulation services based on day-ahead and intraday market prices. For a case study with 50 EV, cost reduction of 1% to 15% was achieved. Two-stage SP is proposed in [20] for workplace charging of EV based on PV, V2G and dynamic energy prices resulting in 7.2% and 6.9% average cost reduction.

With respect to ancillary services, a dynamic control of EVs in [21], robust optimization in [22] and SP based on Markov decision problem in [23] is used to provide frequency regulation services while considering the EV user requirements and regulation prices.

Earlier works have considered the different applications of smart charging as separate optimization problems or as a combination of two or three applications. The disadvantage is that each application gives a different optimized EV charging profile and all these profiles cannot be implemented on the same EV at the same time! The best approach is to combine them into one formulation which will then yield a single optimized EV charging profile. The second disadvantage is that the above formulations do not consider the characteristics of the EV charging hardware. This is

vital as the hardware is more expensive than the smart charging controller and its algorithms.

The main contributions of the work reported below include:

- Proposing an integrated model that captures charging of EV from PV, use of dynamic grid prices, implementation of V2G for grid support, using EV to offer ancillary services, and considering distribution network capacity constraints as a single mixed integer linear programming (MILP) formulation. The chapter demonstrates that the integrated formulation results in large cost savings, which is much higher than what has been achieved earlier. This is due to the addition of benefits from each application, such that the net benefit is economically attractive. With the prior approaches, the economic benefits were too small to warrant mass adoption of smart charging
- The chapter proposes the use of an integrated EV-PV converter for the combined optimization of EV charging and PV generation. This provides higher efficiency due to the direct current (DC) power exchange between EV and PV; leads to a lower capital cost of the power converter as it needs only a single DC/AC inverter to the grid; and removes the necessity for communication between EV charger and PV inverter as they are now integrated.
- The integrated scheduling of EV and PV makes PV an economically controllable commodity with respect to feeding power to the grid, which would not be possible otherwise. Depending on grid energy prices, PV energy can be diverted either to the EV or to the grid or curtailed.
- The chapter shows that the benefit of V2G from energy sales can be far outweighed by the increased up-regulation that can be offered by a bidirectional EV charger when battery degradation costs are included in the optimization.
- With a large number of EV parked at the workplace with long parking times, multiplexing a few EVSEs to a larger number of EVs is a cost-effective strategy [24]-[26]. The scheduling of the multiplexing is formulated in the MILP to reduce charging infrastructure cost.

6.4. Preliminaries and Inputs

6.4.1. Layout of the EMS

The schematic of the EV-PV charger and the EMS used by the ESCo to optimize the EV charging is shown in Fig. 6.2.

1. EV and user input

Each EV arrives at the car park with a battery of energy content B_v^a at time T_v^a and is parked at one of the several EV-PV chargers. The EV owners provide the information to the EMS about their expected departure time T_v^d and charging energy demand d_v . This means that the departure energy content of the vehicle B_v^d is:

$$B_v^d = B_v^a + d_v \quad (3)$$

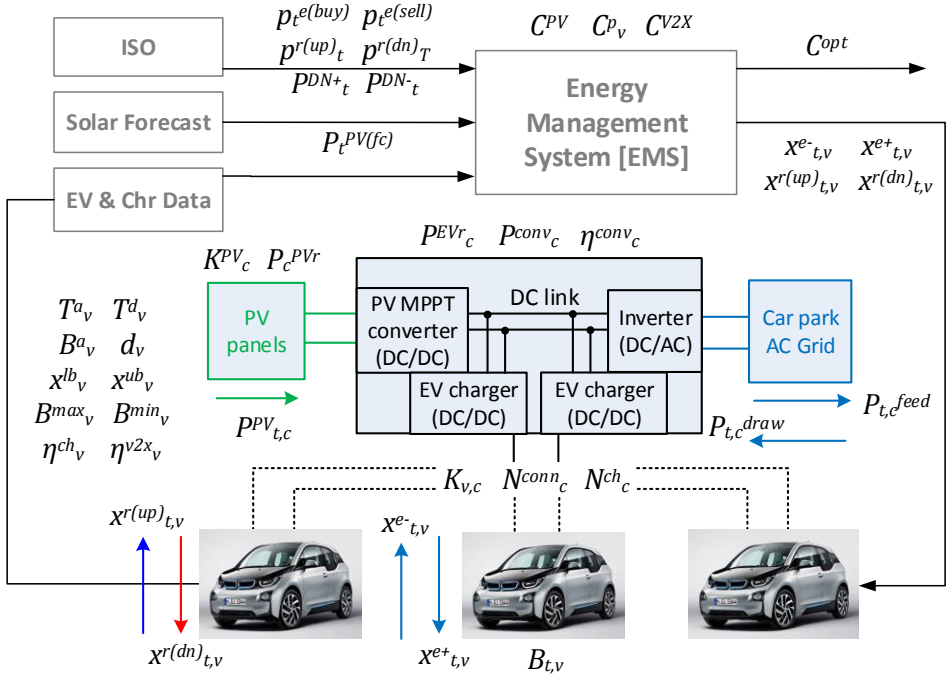


Fig. 6.2. Schematic of the Energy Management System for the solar powered EV parking lot consisting of several EV-PV chargers as shown above.

If the required SOC is not reached by the departure time, the EV owner will be compensated by the ESCo at the rate of C^p_v \$/kWh. The users can enter the maximum and minimum allowed energy of the EV battery (B_v^{min} , B_v^{max}) and the maximum charging and discharging power (x_v^{ub} , x_v^{lb}) respectively. By setting x_v^{lb} to a non-zero value, the users can choose to participate in V2G services. The efficiency of the EV battery for charging and discharging (η_v^{ch} , η_v^{2x}) is either obtained from the EV or stored in a database within the EMS for different EV models.

2. EV-PV charger

The ‘EV-PV charger’ as the term is used here means an integrated power converter that consists of three ports to connect to the EVs, PV, and the AC grid, as shown in Fig. 6.2 [24], [27], [28]. Each EV-PV charger is connected to a PV array of rated power P_c^{PVr} via a maximum power point tracking (MPPT) DC/DC converter [29]. The output of the DC/DC PV converter is connected to an internal DC-link. The DC-link is connected to the grid via a DC/AC inverter of rated power P_c^{conv} , such that $P_c^{PVr} \leq P_c^{conv}$. There are N_c^{ch} number of isolated DC/DC converters for EV charging that are connected to the DC-link and each have a rated power P_c^{EVr} . All power exchanges between any of the three ports namely PV, EV, and grid are via the DC-link.

This integrated converter provides several benefits compared to using separate converters for PV and EV connected over the 50Hz AC grid. First, direct interconnection of the PV and EV over a DC-link is more efficient than an AC interconnection [30], [31]. Second, the integrated converter requires one common inverter to the AC grid instead of separate inverters for PV and EV. This reduces the component count and size of the converter [24]. Third, by making the isolated DC/DC converter for the EV bidirectional, the EV can now offer V2G services via the integrated converter.

Due to the long parking times of EVs at the workplace, it is economical to use a single EVSE that can be multiplexed to several EVs, with the possibility to charge the EVs simultaneously or sequentially as shown in Fig. 6.2 [24]–[26]. Therefore, N_c^{conn} EVs can be connected to each EV-PV charger via DC isolators. The binary variable $K_{v,c} = 1$ indicates the physical connection of v^{th} EV with c^{th} charger and a zero value indicates otherwise.

Each EV-PV charger has N_c^{ch} number of isolated DC/DC converters, where $N_c^{ch} \leq N_c^{conn}$. As per the EV charging standards [32], each EV must be connected to separate power converter and isolated from all power sources. This means that N_c^{ch} of the total N_c^{conn} EVs connected to each EV-PV charger can be simultaneously charged or discharged. In the simple case where $N_c^{ch} = 1$, $N_c^{conn}=2$ and $P_c^{conv} = P_c^{EVR}$, two EVs are connected to one EV-PV charger and one of the two can (dis)charge at any time up to a power of P_c^{conv} . The binary variable $a_{t,v}^c$ indicates which of the N_c^{conn} EVs connected to an EV-PV charger is actively (dis)charging at time t .

$$\sum_{v=1}^{v=V} K_{v,c} \leq N_c^{conn} \quad \forall c \quad (4)$$

$$\sum_{v=1}^{v=V} K_{v,c} a_{t,v}^c \leq N_c^{ch} \quad \forall c \quad (5)$$

Each EV-PV charger feeds $P_{t,c}^{feed}$ or draws $P_{t,c}^{draw}$ power from the EV car park as determined by the EMS. Different EV-PV chargers can exchange power within the car park and these are ‘intra-park’ power exchanges. In the event, that there is no EV connected to an EV-PV charger, it merely acts like a solar inverter and feeds the power to the car park in AC. A neighboring EV-PV charger, for example, can then use this AC power to charge the car. When the net ‘intra-park’ energy exchanges are non-zero, the EV park imports or exports power with the external grid referred to as $P_t^{g(imp)}$, $P_t^{g(exp)}$ respectively.

6.4.2. Trading energy and reserves in the energy market

The ESCo uses the EMS to control the solar powered EV car park for energy trading with the grid. Since $P_t^{g(imp)}$, $P_t^{g(exp)}$ are small relative to the power traded in the market, the ESCo is a price taker and does not influence the market clearing prices. It uses the settlement point prices for trading power in the market and reserve capacity prices for offering up and down regulation services. Markets like the Electric Reliability Council of Texas (ERCOT) provide different prices for offering capacity reserves for up and down regulation (asymmetric, $p_t^{r(up)} \neq p_t^{r(dn)}$). However, other US markets such as PJM trade up and down regulation as a single product (symmetric). In

order to make the EMS flexible and work with both types of markets, it is designed to take different inputs for $p_t^{r(up)}$ and $p_t^{r(dn)}$ and allow for a requirement that up and down regulation quantities could be equal.

The amount of reserves offered by the EV depends on whether the user enables V2G option or not, i.e., if $x_v^{lb}=0$ or not. When an EV is connected to a bidirectional charger and $x_v^{lb} \neq 0$, even an idle EV that is not charging can offer up and down regulation up to x_v^{lb} and x_v^{ub} respectively. With a unidirectional charger, an idle EV that is not charging can only offer down regulation up to x_v^{ub} .

Power generated by PV panels can be ramped down by moving out of the maximum power point of the PV array. This can be achieved by controlling the DC/DC converter in the EV-PV charger that is connected to the PV array. This PV power curtailment can also be offered for down-regulation services.

6.4.3. Receding horizon model predictive control

There are two sources of variability in the EV-PV system. The first is the diurnal and seasonal variation in PV generation due to changes in weather. The EMS uses solar forecast information as an input to predict the PV variation. Any solar forecast data source can be used for the given MILP formulation. For example, the online short-term solar power forecasting [33], the autoregressive integrated moving average (ARIMA) models [34] or any of the methods listed in [35]. $P_t^{PV(fc)}$ is power generation forecast for an optimally orientated $1kW_p$ PV array at the car park location with a maximum uncertainty in forecast of y_{PV}^{fc} . It is vital to recognize that all forecasting methods will have forecasting errors in terms of temporal and spatial resolution. The second variability is the variation in the arrival and departure patterns of the EV user and the EV parameters like charging powers limits, efficiency of the battery and SOC.

The EMS is implemented as a receding horizon model predictive control with a time step ΔT to manage these two variations. The horizon for the model is from 00:00AM to 23:59 PM at midnight. This means that at every time step, the EMS can utilize updated forecast information and input parameters, perform the optimization and plan the EV charging for the rest of the day. Hence, the receding horizon implementation helps in minimizing forecasting errors and model inaccuracies at every time step.

6.5. MILP formulation

This section describes the objective function and constraints for the MILP formulation of the EMS. It is important to note that all optimization variables considered are positive.

6.5.1. Acceptance criteria

When an EV arrives at the EV car park, it is connected to one of the C numbers of EV-PV chargers. As mentioned earlier, each EV-PV charger can have up to N_c^{conn} number of EV connected to it. The user links to the EMS and the EMS instructs the

user on which EV-PV charger he/she must connect to, based on two ‘acceptance criteria’. The first criteria is that the energy demand d_v and parking time, $(T_v^d - T_v^a)$ of all the EVs connected to one EV-PV charger must be within the power limits of the charger, (6). The second criteria is that the arrival energy content of the vehicle must be above the minimum limit as set by the user, (7). This is to ensure that constraint (21) is satisfied.

$$\sum_{v=1}^V \sum_{c=1}^C K_{v,c} \frac{d_v}{T_v^d - T_v^a} \leq \text{Min.} \{N_c^{ch} P_c^{EVr}, P_c^{conv}\} \quad \forall v, c \quad (6)$$

$$B_v^{min} \leq B_v^a \quad \forall v \quad (7)$$

6.5.2. Constraints: EV and user inputs

As indicated in Fig. 6.3, the EMS controls the charging power $x_{t,v}^{e+}$ and discharging power $x_{t,v}^{e-}$, up and down regulation reserve capacity $x_{t,v}^{r(up)}$, $x_{t,v}^{r(dn)}$ of each EV and the power extracted from the PV system $P_{t,c}^{PV}$ of each charger at time t . Equations (8) and (9) are used to set the charging power of the EV to zero before the arrival ($t < T_v^a$) and after the departure of the EV ($t \geq T_v^d$).

The binary variable $a_{t,v}^c$ indicates if the EV is connected to the isolated DC/DC converter for charging/discharging and can offer regulation services or not. Since an EV cannot simultaneously charge and discharge, a second binary variable $a_{t,v}^{ch-v2x}$ is used to ensure that only one of the two variables $x_{t,v}^{e-}$, $x_{t,v}^{e+}$ has a non-zero value for a given t . $a_{t,v}^{ch-v2x}$ is set to 1 for charging and to 0 for V2G. $x_{t,v}^{e-}$, $x_{t,v}^{e+}$ have to be within the power limits of the power converter P_c^{EVr} and the charging and discharging power limits x_v^{ub} , x_v^{lb} as set by the EV, respectively, as shown in equations (10)-(15).

The maximum charging and discharging powers are also dependent on the SOC of the EV battery as shown in (16) and (17). For example, fast charging of EV battery cannot be done beyond 80% SOC of the battery [36]. Here, it is assumed that the maximum charging power linearly reduces from x_v^{ub} to zero when the battery is charged beyond 80% SOC till 100% ($S_{ch}=0.8$). Similarly the maximum discharging power reduces linearly from x_v^{lb} to zero when the battery is discharged below 10% SOC till 0% ($S_{v2x}=0.1$). Even though the exact dependence of battery power on the SOC is non-linear, this is not considered here as it is beyond the scope of the chapter and would prevent us from casting the problem into an MILP formulation.

$$x_{t,v}^{e-}, x_{t,v}^{e+}, x_{t,v}^{r(up)}, x_{t,v}^{r(dn)}, a_{t,v}^c = 0 \quad \forall t < T_v^a \quad (8)$$

$$x_{t,v}^{e-}, x_{t,v}^{e+}, x_{t,v}^{r(up)}, x_{t,v}^{r(dn)}, a_{t,v}^c = 0 \quad \forall t \geq T_v^d \quad (9)$$

$$x_{t,v}^{e+} \leq x_v^{ub} (a_{t,v}^c) \quad \forall t, v \quad (10)$$

$$x_{t,v}^{e+} \leq x_v^{ub} (a_{t,v}^{ch-v2x}) \quad \forall t, v \quad (11)$$

$$x_{t,v}^{e-} \leq -x_v^{lb} (a_{t,v}^c) \quad \forall t, v \quad (12)$$

$$x_{t,v}^{e-} \leq -x_v^{lb} (1 - a_{t,v}^{ch-v2x}) \quad \forall t, v \quad (13)$$

$$x_{t,v}^{e-}, x_{t,v}^{e+} \leq P_c^{EVr} \quad \forall K_{v,c}=1 \quad (14)$$

$$a_{t,v}^c, a_{t,v}^{ch-v2x}, a_{t,c}^{d,f} \in \{0,1\} \quad \forall t, c, v \quad (15)$$

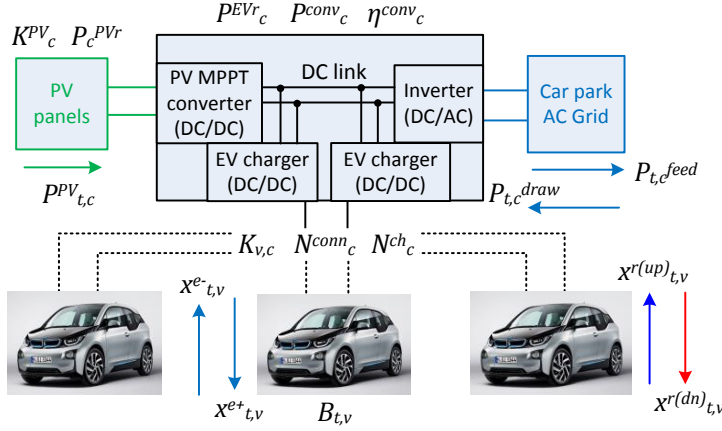


Fig. 6.3. The EV-PV charger with solar inputs and connection to AC grid is shown. The charger can be multiplexed to several EVs, N_c^{ch} of the total N_c^{conn} EV connected to each EV-PV charger can be simultaneously charged or discharged, where $N_c^{ch} \leq N_c^{conn}$.

$$x_{t,v}^{e+} \leq \frac{-x_v^{ub}}{(1 - S_{ch})} \left(\frac{B_{t,v}}{B_v^{max}} - 1 \right) \quad \forall t, v \quad (16)$$

$$x_{t,v}^{e-} \leq \frac{-x_v^{lb}}{S_{v2x}} \left(\frac{B_{t,v}}{B_v^{max}} \right) \quad \forall t, v \quad (17)$$

Equations (18)-(23) are used to set the initial SOC of the EV battery and estimate the SOC of the battery $B_{t,v}$ based on the charging and discharging efficiency (η_v^{ch} , η_v^{v2x}) and power ($x_{t,v}^{e+}$, $x_{t,v}^{e-}$) respectively. At every time step of the receding horizon, the current time and battery energy of all EVs are updated into the parameters B_v^a and T_v^a . The EMS restricts the SOC to be within the limits B_v^{min} , B_v^{max} as set by the EV and/or user. It is assumed that the net energy delivered/absorbed by the EV over one time period due to offer of reserves is zero [6], [9]. Hence, $x_{t,v}^{r(up)}$, $x_{t,v}^{r(dn)}$ do not appear in (23) for SOC estimation.

$$B_{t,v} = 0 \quad \forall t < T_v^a \quad (18)$$

$$B_{t,v} = B_v^a \quad \forall t = T_v^a \quad (19)$$

$$B_{t,v} \leq d_v + B_v^a \quad \forall t = T_v^d \quad (20)$$

$$B_{t,v} \geq B_v^{min} \quad \forall t \geq T_v^a \quad (21)$$

$$B_{t,v} \leq B_v^{max} \quad \forall t \geq T_v^a \quad (22)$$

$$B_{t+1,v} = B_{t,v} + \Delta T \left(x_{t,v}^{e+} \eta_v^{ch} - \frac{x_{t,v}^{e-}}{\eta_v^{v2x}} \right) \quad \forall t, v \quad (23)$$

6.5.3. Constraints: EV-PV charger and car park

Under normal operation, the EMS extracts maximum power from the PV array using MPPT as shown in right side of equation (24). The PV power is dependent on the scaling factor K_c^{PV} which scales the installation characteristics (e.g. azimuth, tilt, module parameters) of the PV array connected to the charger c with respect to the

1kWp reference array used for the forecast data $P_t^{PV(fc)}$. The EMS implements PV curtailment if it is uneconomical to draw PV power or if there are distribution network constraints for feeding to the grid. This means that the actual PV power extracted $P_{t,c}^{PV}$ can be lower than the MPPT power of the array, as shown in (24).

The DC-link is used for power exchanges between the three ports of the converter and (25) is the power balance equation for the EV-PV converter. It is assumed that each of the power converters within the EV-PV charger operates with an efficiency η_c^{conv} . Power levels $P_{t,c}^{draw}$, $P_{t,c}^{feed}$ are limited by the power limit of the inverter port P_c^{conv} . The binary variable $a_{t,c}^{d,f}$ is used to ensure that only one of the two variables has a non-zero value for a given t as shown in (26)-(27).

$$P_{t,c}^{PV} \leq K_c^{PV} P_c^{PVr} P_t^{PV(fc)} \quad \forall t, c \quad (24)$$

$$\left\{ P_{t,c}^{PV} + P_{t,c}^{draw} + \sum_{v=1}^{v=V} (K_{v,c} x_{t,v}^{e-}) \right\} \eta_c^{conv} \quad \forall t, c, v \quad (25)$$

$$= \left\{ P_{t,c}^{feed} + \sum_{v=1}^{v=V} (K_{v,c} x_{t,v}^{e+}) \right\} / \eta_c^{conv}$$

$$P_{t,c}^{draw} \leq P_c^{conv} (a_{t,c}^{d,f}) \quad \forall t, c \quad (26)$$

$$P_{t,c}^{feed} \leq P_c^{conv} (1 - a_{t,c}^{d,f}) \quad \forall t, c \quad (27)$$

The intra-car park power exchanges between different EV-PV chargers are related to the power exchanged with the external grid $P_t^{g(imp)}, P_t^{g(exp)}$ using (28). Both $P_t^{g(imp)}, P_t^{g(exp)}$ will not have finite values at the same time because of the way the objective function is formulated and because $p_t^{e(buy)} \geq p_t^{e(sell)}$ at all times. $P_t^{g(imp)}, P_t^{g(exp)}$ should be within the distribution network capacity P_t^{DN+}, P_t^{DN-} as shown in (29)-(30). P_t^{DN+}, P_t^{DN-} are used as a thermal proxy for all potential limitations in the distribution network including voltage limits, line limits and transformer capacity. The values can come from the distribution system operator (DSO), ISO or EScO based on loading and voltage in the network and can be set at every time step in the receding horizon implementation.

$$\sum_{c=1}^{c=C} (P_{t,c}^{draw} - P_{t,c}^{feed}) = P_t^{g(imp)} - P_t^{g(exp)} \quad \forall t \quad (28)$$

$$P_t^{g(imp)} \leq P_t^{DN+} \quad \forall t \quad (29)$$

$$P_t^{g(exp)} \leq P_t^{DN-} \quad \forall t \quad (30)$$

Finally, the up and down regulation offered $x_{t,v}^{r(up)}, x_{t,v}^{r(dn)}$ should be within the power limitations of the EV (x_v^{ub}, x_v^{lb}) and the EV charger port P_c^{EVr} as shown in Fig. 6.4. From the EV-PV charger perspective, the regulation power offered must be within the power rating of the inverter port P_c^{conv} , the power exchanged with the grid $P_{t,c}^{draw}, P_{t,c}^{feed}$ and the SOC of the EV battery (like (16), (17)). This is summarized in equations (31)-(36). While asymmetric reserve offers are assumed here ($x_{t,v}^{r(up)} \neq x_{t,v}^{r(dn)}$), symmetric reserves can be achieved by including $x_{t,v}^{r(up)} = x_{t,v}^{r(dn)}$ to the constraints.

$$\sum_{v=1}^{v=V} K_{v,c} x_{t,v}^{r(up)} + P_{t,c}^{feed} \leq P_c^{conv} \quad \forall t, c, v \quad (31)$$

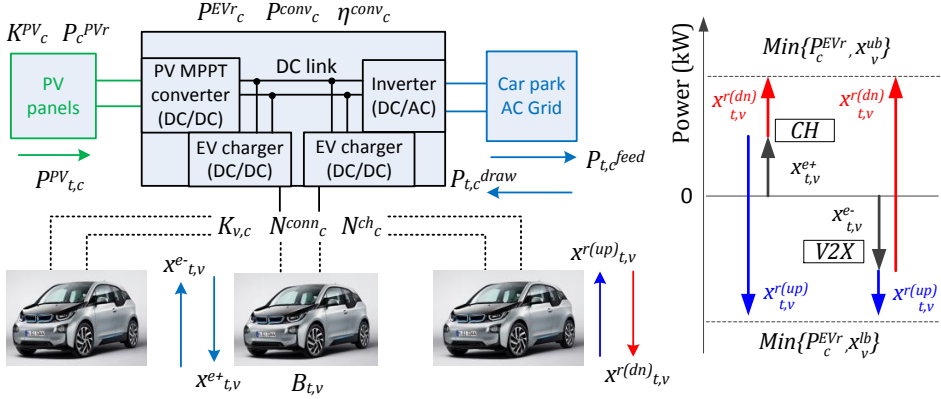


Fig. 6.4. Offer of reserve power capacity $x_{t,v}^{r(up)}$, $x_{t,v}^{r(dn)}$ for up and down regulation during charging (CH) and discharging (V2G) of EV

$$\sum_{v=1}^{v=V} K_{v,c} x_{t,v}^{r(dn)} + p_{t,c}^{draw} \leq p_c^{conv} \quad \forall t, c, v \quad (32)$$

$$x_{t,v}^{e-} + x_{t,v}^{r(up)} \leq p_c^{EVr}(a_{t,v}^c) \quad \forall K_{v,c}=1 \quad (33)$$

$$(x_{t,v}^{e-} - x_{t,v}^{e+}) + x_{t,v}^{r(up)} \leq (-x_v^{lb}) \quad \forall t, v \quad (34)$$

$$x_{t,v}^{e+} + x_{t,v}^{r(dn)} \leq p_c^{EVr}(a_{t,v}^c) \quad \forall K_{v,c}=1 \quad (35)$$

$$(x_{t,v}^{e+} - x_{t,v}^{e-}) + x_{t,v}^{r(dn)} \leq x_v^{ub} \quad \forall t, v \quad (36)$$

$$(x_{t,v}^{e+} - x_{t,v}^{e-}) + x_{t,v}^{r(dn)} \leq \frac{-x_v^{ub}}{(1 - S_{ch})} \left(\frac{B_{t,v}}{B_v^{max}} - 1 \right) \quad \forall t, v \quad (37)$$

$$(x_{t,v}^{e-} - x_{t,v}^{e+}) + x_{t,v}^{r(up)} \leq \frac{-x_v^{lb}}{S_{v2x}} \left(\frac{B_{t,v}}{B_v^{max}} \right) \quad \forall t, v \quad (38)$$

6.5.4. Objective function

$$\text{Min. } C^{opt} = \left(B_v^a + d_v - B_{T_v}^d \right) C_v^p \quad (39)$$

$$+ \Delta T \sum_{t=1}^T \left(p_t^{g(imp)} p_t^{e(buy)} - p_t^{g(exp)} p_t^{e(sell)} \right)$$

$$- \Delta T (1 - y_{PV}^{fc}) (\eta_c^{conv})^2 \sum_{t=1}^T \sum_{c=1}^C \sum_{v=1}^V K_{v,c} \{ x_{t,v}^{r(up)} p_t^{r(up)} + x_{t,v}^{r(dn)} p_t^{r(dn)} \}$$

$$+ \Delta T \sum_{t=1}^T \sum_{v=1}^V x_{t,v}^{e-} C^{V2X} + \Delta T \sum_{t=1}^T \sum_{c=1}^C P_c^{PVr} P_t^{PV(fc)} C^{PV}$$

The objective function is to minimize the total costs C^{opt} of EV charging, feeding PV power and offering reserves. The formulation is such that the C^{opt} can be positive or negative. It has five components, namely:

- The penalty to be paid to the user if the energy demand d_v is not met by the departure time T_v^d . C_v^p is EV user specific and the penalty can be different for each user based on EV battery size, tariff policy and customer 'loyalty' program.
- The cost of buying and selling energy from the grid based on the settlement point prices $p_t^{e(buy)}, p_t^{e(sell)}$. The market dynamics will ensure that $p_t^{e(buy)} \geq p_t^{e(sell)}$
- Income S^{as} obtained from offering reserve capacity $x_{t,v}^{r(up)}, x_{t,v}^{r(dn)}$ to the ISO. $(\eta_c^{conv})^2$ indicates the energy losses in the two step conversion between the EV and grid port of the EV-PV charger. Since the reserves offered to the grid have to be guaranteed and the uncertainty in the PV forecast is y_{PV}^{fc} , only a fraction $(1 - y_{PV}^{fc})$ of the available reserves are guaranteed and sold to the ISO.
- EV battery capacity degrades due to the additional cycles caused by the V2G operation, and EV user is compensated for this loss. Typical value of $C^{V2G} = 4.2\text{¢/kWh}$ based on analysis in [37], [38]. The possible battery degradation due to variable power smart charging is not considered here, as several studies have shown that its effect is insignificant [39]-[41].
- PV power that is used to charge the EV need not always be free of cost. If the PV is installed by a third-party, it can be obtained at a pre-determined contractual cost of C^{PV} .

6.5.5. Simulation

Simulations are performed to test the validity of the proposed MILP formulation and to quantify the reduction in costs of EV charging from PV with respect to IMM, AR, and RND. Two scenarios, one for the Netherlands and the second for Texas, USA are done to estimate the economic benefits of the proposed formulation. The main difference in the two scenarios is the climatic conditions and the fact that offering of reserves in the day ahead or real-time markets is not possible in the Netherlands.

6.6. Simulation study: Netherlands

The Netherlands like most countries in Europe, decouples the day-ahead and intra-day wholesale energy markets, and the ancillary services market. Hence, the simulation for the Netherlands will not have EVs offering the sale of up and down regulation reserves. So $x_{t,v}^{r(up)} = x_{t,v}^{r(dn)} = 0$

6.6.1. Simulation parameters

Energy prices for $p_t^{e(buy)}$ are obtained from the Amsterdam Power Exchange (APX), with a data resolution of 1hr. The wholesale energy prices from APX are scaled such that the average consumer electricity price over the day is 0.23€/kWh, thus reflecting the current retail energy prices in the Netherlands. Since separate values for $p_t^{e(sell)}$ was not available, it is assumed that $p_t^{e(sell)} = 0.9 * p_t^{e(buy)}$. Since retail prices are used, the $p_t^{e(sell)}$ can also be referred to as the feed-in tariff (FIT) as well.

Table 6.1. EV and EV-PV Charger Data

v	T_v^a	T_v^d	B_v^a	B_v^d	B_v^{max}	Chr conn.
	(h)		(kWh)			
1	7.31	18.19	29.7	70.2	85	1
2	8.37	19.23	13.8	21.9	30	1
3	7.54	17.17	10.6	17.4	22	1
4	8.50	15.09	10.8	21.3	85	1
5	7.50	16.45	37.5	64.5	60	2
6	9.02	18.59	10.3	23.3	24	2

For the PV generation forecast $P_t^{PV(fc)}$, the forecast is made based on the PV system output estimated for Netherlands in chapter 3. Seasonal autoregressive integrated moving average (SARIMA) models are built in MATLAB and the parameters are tuned for the Netherlands. Reference [17], [34] can provide details of the modelling approach and the tuned parameters. It is assumed that the PV installation is owned by the workplace and hence $C^{PV}=0$.

Workplace charging tends to be used merely to extend the range of the EV, with an average energy transfer of 8.53 kWh and standard deviation of 6.49 kWh [42]. Realistic initial and final energy content need to be selected for the case studies, which is often done by using a probability function, e.g., uniform [14], [43] or lognormal [44]. This thesis uses a uniform distribution between $0.3 \cdot B_v^{max}$ and $0.5 \cdot B_v^{max}$ for initial energy content, B_v^a . The required energy stored in the battery upon departure lies between $0.6 \cdot B_v^{max}$ and $0.8 \cdot B_v^{max}$. Consequently, maximum and minimum energy demand of a single EV will be $(0.8 - 0.3) \cdot 90 \text{ kWh} = 45 \text{ kWh}$ and $(0.6 - 0.5) \cdot 22 \text{ kWh} = 2.2 \text{ kWh}$, respectively.

Yearly, the Dutch mobility survey (MON) shows recursive behaviour in driving patterns of commuters with clear peaks at 8 a.m. and 6 p.m. for morning and evening commute, respectively [45]. Furthermore, these peaks show normal behaviour with approximately one-hour standard deviation [10]. The EV arrival and departure times and energy requirements are listed in Table 6.1 for 6 EVs. The average energy demand amounts to 17.65 kWh.

The EV data imitates the capacity of two Tesla Model S (90kWh), one Renault Zoe (22kWh) and three Nissan Leaf (30kWh). For all the EVs, $B_v^{min}=0.3 \cdot B_v^{max}$, $x_v^{ub}=50\text{kWh}$, $x_v^{lb}=43\text{kWh}$ for Leaf, $x_v^{lb}=(-10\text{kWh})$, $\eta_v^{ch}=\eta_v^{v2x}=0.96$, $C_v^p=5\text{€}/\text{kWh}$, $C^{V2X}=0.038\text{€}/\text{kWh}$. There are 2 EV-PV chargers and Table 6.1 shows the connections of the 6 EVs to the 2 chargers in 'Chr conn.'. 10kW_p PV is connected to both chargers 1,2. Chargers 1,2 have four and two EVs connected to them, respectively. $N_c^{ch}=1$ for all chargers, which means that only one of the EVs can be charged at a time for chargers 1,2.

The following parameters are used: $P_c^{EVr}=P_c^{conv}=10\text{kW}$, $P_t^{DN+}=P_t^{DN-}=20\text{kW}$. η_c^{conv} is provided three values depending on the which of the three sub-converters is

concerned: $\eta_c^{conv}=0.94$ for isolated DC/DC EV charger, $\eta_c^{conv}=0.98$ for DC/DC PV converter and $\eta_c^{conv}=0.98$ for DC/AC grid converter [46], [47]. $\Delta T=15\text{min}$ for all simulation.

6.6.2. Simulation platform

For this simulation, the MILP is modelled in the General Algebraic Modeling System (GAMS) and solved using the CPLEX solver, version 12.6.

6.6.3. Simulation results

Two cases are studied in the simulation: EV 1-4 connected to one EV-PV charger with 10kW PV and EV 1-6 connected to two EV-PV chargers with 10kW PV each. A summer day is chosen for the analysis where the 10kW PV system generates 72.72 kWh over the day. In both cases the optimized charging is compared with respect to IMM to estimate the reduction in net costs:

$$C_{\%imm}^{opt} = 100(C^{imm} - C^{opt})/C^{imm} \quad (40)$$

Further, a second criterion is used for comparison:

- The net energy exchanged with the grid over the day, E^{grid}

$$E^{grid} = \sum_{t=0000h}^{t=2359h} (P_t^{g(imp)} + P_t^{g(exp)}) \quad (41)$$

- The PV self-consumption, which is the ratio of the PV energy used for EV charging compared to the total PV generation

1. One charging point with 4 EVs and 10kW PV

Fig. 6.5 present the results of the uncontrolled charging policy and the optimal charging strategy for one charging point with 4 EVs. There are at least three points of interest. First, in case of uncontrolled charging, the power drawn from the grid (shown as 'Grid' in the figure) and tariff levels have a peak during the morning and decrease thereafter. Evidently, this is opposite of what can be considered optimal. In addition, PV power is fed into the grid while $p_t^{e(sell)}$ is at its minimum around 1500h, consequently reducing revenue. Second, Fig. 6.5(c) shows that the EMS shifts demand away from the peak in the morning tariff, while feeding generated PV power to the grid. Additionally, the surplus of PV power in the morning is immediately fed into the grid at high grid prices, thereby increasing the PV revenues until 900h. Therefore, it can be concluded that the EMS actively performs demand side management (DSM) by peak shaving and load shifting.

Third, the EMS proves that V2G does not lead to optimality all the time. There is essentially one possibility for V2G, which is during the second peak of $p_t^{e(sell)}$ around 1700h. However, due to the limited time period in which the purchase tariff is low, it is not feasible to charge an EV beyond its energy requirement, so as to sell it later.

Table 6.2 presents the numerical results of the uncontrolled and optimal charging strategies. PV self-consumption, i.e., the fraction of generated PV power consumed by the EVs, has been increased from 73.65% to 82.41%. Additionally, energy exchange with the grid, E^{grid} , was reduced by 31.66%. Furthermore, total net cost has been reduced by 118.44%, thus turning cost a into profit. Finally, if the results are

Table 6.2. EV Charging costs, PV self-consumption, total energy exchanged with grid and net cost reduction for case one and two

Charging policy	PV self-consumption (%)	E^{grid} (kWh)	C^{opt}, C^{imm} (€)	Cost reduction $C_{\%imm}^{opt}$ (%)
IMM - 4 EVs	73.65	39.61	2.181	118.44
OPT - 4 EVs	82.41	27.07	-0.4022	
IMM - 6 EVs	58.04	94.24	-1.468	427.45%
OPT - 6 EVs	66.32	75.20	-7.743	

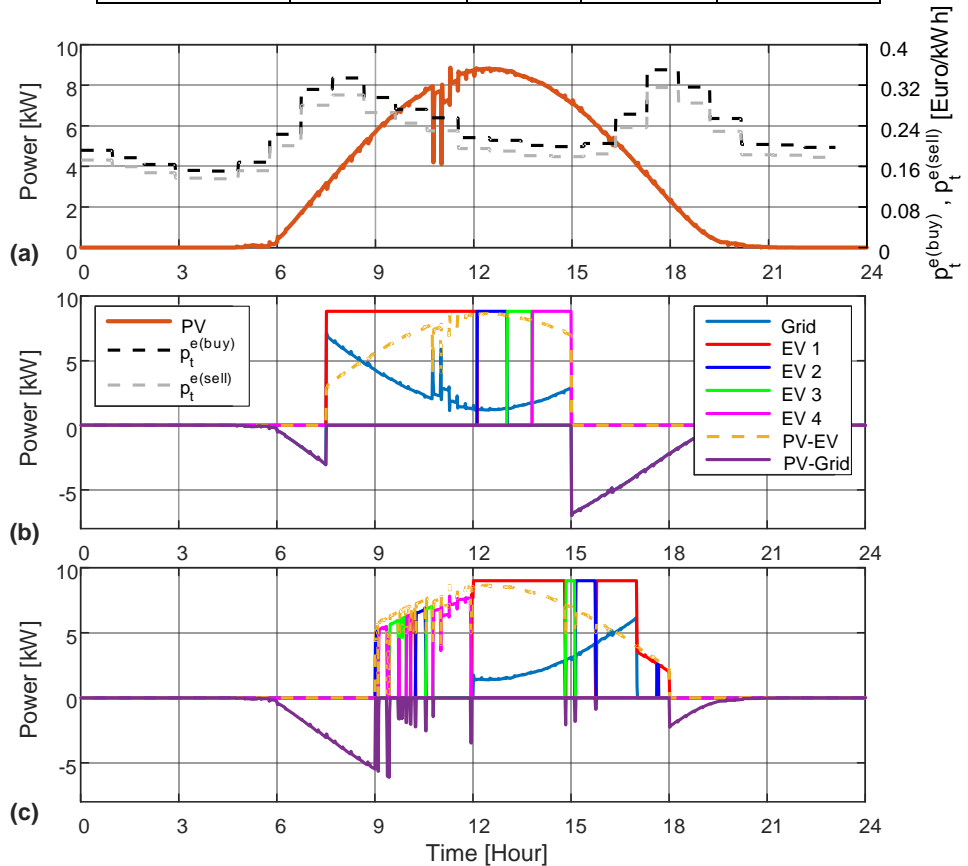


Fig. 6.5. (a) PV generation, energy prices, (b) Uncontrolled EV charging (IMM) and (c) Optimized EV charging of 4 EVs from a single EV-PV charger with 10kW PV

extended to 10 fully occupied charging points i.e., 40 EVs, the net cost will come down from 21.81€ to -4.022€.

2. Two charging point with 6 EVs and 20kW PV

The case study with two chargers will investigate the effect of collaboration when a second charging point is introduced that is occupied for 50%, which is a likely scenario during, e.g., vacation periods. As a consequence, there will likely be a surplus of PV power. Since the EMS is formulated such that it allows collaboration as long as that is optimal, it can be assessed whether or not the overproducing charging point in terms of PV power can complement the fully occupied charging point.

Fig. 6.6 presents the power allocation during the uncontrolled charging policy (IMM) and optimal charging strategy, respectively. In both cases, we can see similar patterns as in the previous section. In case of IMM as shown in Fig. 6.6(b), power

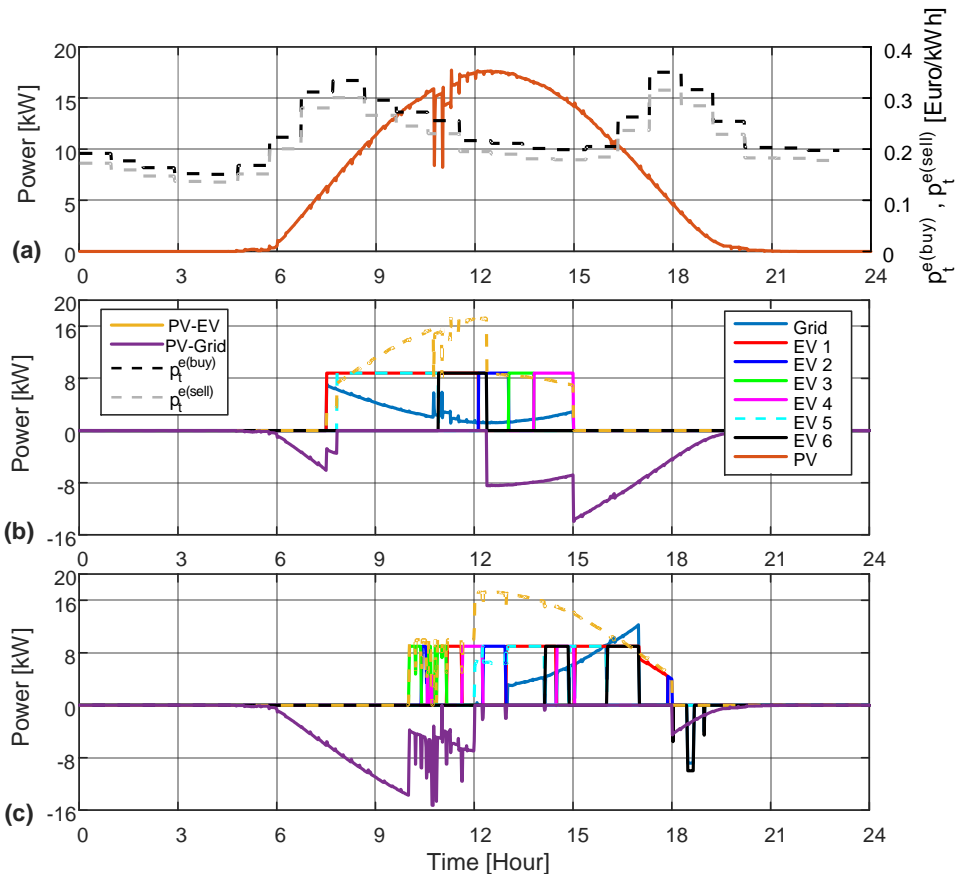


Fig. 6.6. (a) PV generation, energy prices, (b) Uncontrolled EV charging (IMM) and (c) Optimized EV charging of 6 EVs from two EV-PV charger with 10kW PV connected to each charger

withdrawal from the grid occurs during peak price, and power is fed into the grid when $p_t^{e(sell)}$ is significantly lower. In contrast, the EMS shows that the optimal charging strategy is to shift demand away from peak price period while feeding PV power into the grid during this peak, as seen in Fig. 6.6(c).

Furthermore, the EMS makes EV 6 participate in V2G during the evening peak due to the high FIT. The EMS stores energy in EV 6, which is connected to the semi-occupied charging point, so as to feed it back into the grid during peak FIT. This is accompanied by additional charging/discharging losses. However, this is more profitable than feeding PV power directly into the grid during the afternoon, even when taking battery degradation into account. Moreover, Fig. 6.6(c) shows that there are instances in time that there is a collaboration between the charging points when solar power from one charging station is used EVs connected to the other station.

Table 6.2 presents the numerical results, where the PV self-consumption increased from 58.04% to 66.32%, whereas energy exchange with the grid was reduced by 20.20% due to the proposed strategy. Furthermore, profit has increased by 427.45%. This notable result is mainly due to the ability to shift demand away from the peak in purchase tariff and cooperation between the charging points.

6.7. Simulation study: Texas

In case of Texas, the energy generation and the regulation services are integrated in the day-ahead market. Hence, currently generators, and in the future, EVs can offer energy and regulations services to the grid through the same market platform.

6.7.1. Simulation parameters

For the Texas case, Settlement point prices (SPP) and prices for reserve capacity (REGUP, REGDN) are obtained from the ERCOT day-ahead market (DAM) for Austin, Texas for 2014 for load zone LZ_AEN, as shown in Fig. 6.7. These are wholesale energy prices with a data resolution of 1hr. Since separate values for $p_t^{e(sell)}$ was not available, it is assumed that $p_t^{e(sell)}=0.98*p_t^{e(buy)}$.

For 2014, the largest values observed for $p_t^{e(buy)}$, $p_t^{r(up)}$, $p_t^{r(dn)}$ were 136.47¢/kWh, 499.9¢/kWh and 31¢/kWh respectively while the average values were 3.9¢/kWh, 1.25¢/kWh, 0.973¢/kWh. It can be clearly seen than energy prices are normally much higher than regulation prices, but there are several instances where it is otherwise.

The PV generation data is obtained from the Pecan Street Project database for a house in the Mueller neighbourhood with an 11.1 kW PV system [48]. The data resolution is 1min. The power output is scaled down for a 1kW system for use as $P_t^{PV(fc)}$ with $y^{PV(fc)}=10\%$. It is assumed that the PV installation at the car park is owned by the workplace and hence $C^{PV}=0$.

The EV arrival and departure times and battery energy requirements are listed in Table 6.3 for 6 EVs. The EV data imitates the capacity of a Tesla Model S, BMW i3 and a Nissan Leaf. For all the EVs, $B_v^{min}=5\text{kWh}$, $x_v^{ub}=50\text{kWh}$, $x_v^{lb}=-10\text{kWh}$, $\eta_v^{ch} =$

$\eta_v^{2x}=0.95$, $Cpv=1\$/kWh$, $C^{V2X}=4.2\text{¢}/kWh$. The penalty Cpv is approximately 25 times the average wholesale ERCOT electricity price of $3.9\text{¢}/kWh$.

There are 4 EV-PV chargers, and Table 6.3 shows the connections of the 6 EVs to the 4 chargers in ‘Chr conn.’. $10kW_p$ PV is connected to each of chargers 1,2,4, and no PV is connected to charger 3. Chargers 1,4 have two EV connected to them. $N_c^{ch}=1$ for all chargers, which means that only one of the two EVs can be charged at a time for chargers 1,4. The following parameters are used: $\eta_c^{conv}=0.96$, $P_c^{EVr}=P_c^{conv}=10$ kW, $P_t^{DN+} = P_t^{DN-}=40$ kW. $\Delta T=15$ min for all simulation.

6.7.2. Simulation platform

The EMS engine is implemented in C# leveraging Microsoft Solver Foundation for algebraic modelling in Optimization Modeling Language (OML). MS SQL Server database is used to warehouse system inputs, namely the EV, charger, network and market data as well as the decision outputs that are sent to the EV-PV chargers in the field. The MILP formulation is solved using branch-and-bound (B&B) algorithm using ‘LPsolve’ open source solver. One of the main advantages of the B&B algorithm is that, given enough computation time, it guarantees global optimality despite the non-convex nature of the problem. The EV-PV chargers will be interfaced with the output database to implement the optimal power profiles.

Table 6.3. EV and EV-PV Charger Data

v	T_v^a	T_v^d	D	B_v^a	B_v^{max}	Chr conn.	$\frac{P_c^{EVr}}{P_c^{conv}}$
	(h)						(kWh)
1	9.00	17.00	40	20	85	1	10
2	8.30	16.30	30	20	60	1	10
3	9.30	17.30	10	5	24	2	10
4	9.00	17.00	40	20	85	3	10
5	8.30	16.30	30	20	60	4	10
6	9.30	17.30	10	5	24	4	10

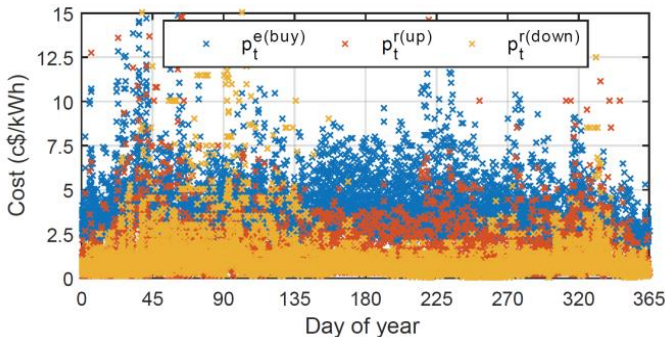


Fig. 6.7. Settlement point and regulation prices from ERCOT for 2014. Values greater than $15\text{c}/kWh$ are not shown to maintain scale.

6.7.3. Simulation results

1. Average rate, randomly delayed and immediate charging

The net costs of EV charging and PV sales for average rate C^{ar} , randomly delayed C^{rnd} and immediate charging C^{imm} are estimated using (1), (2), (42).

$$C^{ar}, C^{rnd}, C^{imm} = C^{ev} - S^{PV} = \Delta T \sum_{t=1}^T \sum_{v=1}^{v=V} (\eta_c^{conv})^2 x_{t,v}^{e+} p_t^{e(buy)} - \Delta T \sum_{t=1}^T \sum_{c=1}^C (\eta_c^{conv})^2 P_c^{PVr} P_c^{PV(fc)} (p_t^{e(sell)} - C^{PV}) \quad (42)$$

where C^{ev} is the EV charging costs and S^{PV} the revenues from PV sales. For AR, $x_{t,v}^{e+} = x_v^{e(ar)}$ and for IMM and RND, $x_{t,v}^{e+} = P_c^{EVr}$. With AR, RND and IMM, there is no provision to provide V2G, regulation services or multiplexing of chargers due to the absence of communication with an EMS. The peak power for the car park would be 60kW for IMM, 20kW for AR charging and between 20kW to 60kW for RND charging for 6 EVs based on (1).

Fig. 6.8 and Table 6.4 shows the net costs C^{ar} , C^{imm} , C^{rnd} estimated for 2014 with the corresponding mean and standard deviation (SD). Four vital observations can be made. First, there is a large variation in net costs, ranging between {1.35\$, 24.17\$} and {-19.58\$, 40.43\$} for AR and IMM respectively. This is mainly due to the varying energy prices in ERCOT. The costs went negative for IMM on certain days indicating that the ESCo got paid by the ISO. It must be remembered that PV sales S^{PV} for both strategies is the same as shown in Table 6.4.

Second, IMM charging was found to be better than AR in summer and vice versa in winter, with IMM charging net costs being cheaper than AR for 233 days. Third, the average net cost per day for 2014 for AR and IMM was found to be 3.79\$ and 2.90\$, with IMM being cheaper than AR by 31.7%. This is because EVs are charged in the morning for IMM when ERCOT prices are generally lower when compared to prices in the afternoon. Thus, for the given scenario it is found that IMM is better than AR. Fourth, the charging cost for randomly delayed charging is nearly the same as AR charging. This is because the process of randomly delaying the charging of individual EVs makes the net EV charging profile extended over the day, similar to AR charging.

2. Optimized net costs

Using the MILP formulation for the optimized charging (OPT) described in section III, the net costs C^{opt} are determined for each day of 2014 based on (39) and shown in Fig. 6.8 and Table 6.4. The benefits of the MILP optimization can be clearly seen in the figure, where the optimized net costs are much lower than IMM and AR. C^{opt} range is {-42.91\$, 11.56\$}, which is much lower than IMM and AR. Due to the large penalty $C_p^p = 1\$/kWh$, EVs were always charged up to the required departure SOC by the departure time.

EV charging costs C^{ev} (not net cost!) are estimated separately for AR, IMM and OPT and shown in Table 6.4. It can be seen that mean value of C^{ev} is not that

different between IMM and OPT. The reason is that the objective function is not optimized to reduce EV charging costs alone but increase the sale of PV power and reserves as well.

The percentage reduction in net costs $C_{\%}^{imm}$, $C_{\%}^{EV-PV}$ is estimated based on AR net costs C^{ar} using (43)-(44) and shown in Fig. 6.9 for each day. C^{ar} was chosen as a reference as the costs do not have values close to zero or go negative.

$$C_{\%}^{imm} = 100(C^{ar} - C^{imm})/C^{ar} \tag{43}$$

$$C_{\%}^{opt} = 100(C^{ar} - C^{opt})/C^{ar} \tag{44}$$

As can be seen, the proposed optimized charging results in a cost reduction $C_{\%}^{opt}$ in the range of 32% to 65%, with a mean of 159% with respect to AR charging. A reduction of >100% should be interpreted as meaning that the net cost is negative. That is, the EV car park receives money for the EV charging, sale of PV and reserves rather than having to pay overall. This goes to show the big potential of the integrated EV-PV-V2G-regulation approach.

Table 6.4. EV Charging costs, PV sales and Net Costs - Mean, SD (\$)

[Mean, SD]	AR	RND	IMM	OPT
S^{PV}	4.41, 2.81	4.41, 2.81	4.41, 2.81	-
C^{ev}	8.21, 3.21	8.17, 3.13	7.32, 3.87	7.30, 1.92
C^{ar}, C^{imm}, C^{opt}	3.79, 2.13	3.75, 2.07	2.90, 4.20	-1.53, 3.92
$C_{\%}^{imm}, C_{\%}^{opt}(\%)$			31.72, 61.26	158.63, 87.88

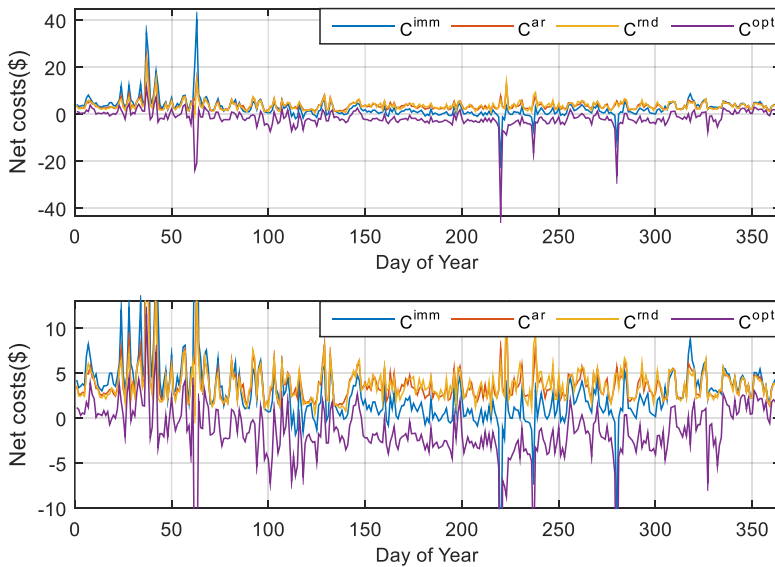


Fig. 6.8. Cost of charging the EV fleet by average rate, immediate and the proposed optimized charging strategy (top); zoomed view (bottom)

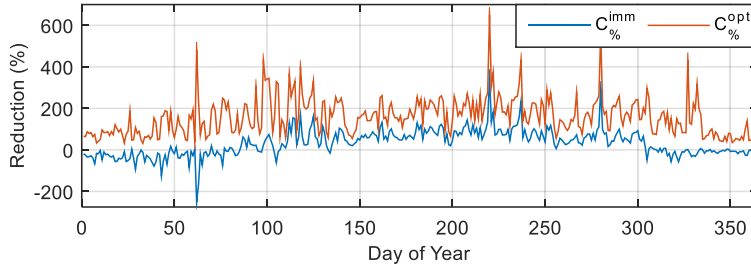


Fig. 6.9. Percentage reduction in the net cost for the proposed charging strategy and immediate charging with respect to average rate charging

MILP solve times were in the range of 11.2-17.3s with a relative MILP gap of 0.015%. The mean solve-time was 13.05s with a standard deviation of 1.09s. A Windows PC with Intel Xeon 2.4Ghz CPU and 12GB RAM was employed.

6.7.4. Case studies

Six case studies are performed in order to evaluate the net reduction in cost if only one or few of the smart charging applications are considered. Table 6.5 shows the six cases considered based on: the possibility for bidirectional charging ($x_v^{lb}=0$ or not); if the EMS is provided input data for PV forecast ($y^{PV(fc)}=0$ or not) and if the objective function optimizes based on the energy/regulation prices or not. For the cases that do not optimize based on the energy/regulation prices, the energy prices part (in red) and/or the regulation prices part (in blue) is removed in the objective function, (39). For all the cases, the distribution network constraints, the EV user requirements and multiplexing of EVs are employed. Five sample days are considered and the percentage reduction in net costs with respect to AVG is estimated for all six cases, similar to Eqn. (44) as shown in Table 6.6. The average cost reduction for the five days considered is shown in the last row of the table.

From Table 6.6, it can be clearly seen that as more smart charging applications are included in the optimization, the net costs reduces drastically. For example, the cost reduction goes from 9.29% for case 2 to 317.83% for OPT, for day 332. In particular, the cost reduction for case 3 is always more than that for case 2 or case 1, while the cost reduction for case 4 is always more than case 2.

Case 6 and OPT differ on whether V2G is possible or not and this results in $(256.7-171.43)=85.2\%$ reduction in net costs on an average for the given days, as seen in Table 6.6. Interestingly, it was found that no V2G energy was fed on the five days except for day 220 with EV3 delivering 7.42kWh. This means that the cost reduction was mainly due to the increased up-regulation power $x_{t,v}^{r(up)}$ that was sold to the ISO on all five days. This goes to show that the main benefit of V2G is not always in energy sales but in increased regulation services offered as well.

Table 6.5. Case studies considering different smart charging applications

Case	Bidirectional V2G	Energy prices	Regulation services	PV forecast
IMM/AVG	No	No	No	No
Case 1	No	No	Yes	No
Case 2	No	Yes	No	No
Case 3	No	Yes	Yes	No
Case 4	No	Yes	No	Yes
Case 5	Yes	No	Yes	Yes
Case 6	No	Yes	Yes	Yes
OPT	Yes	Yes	Yes	Yes

Table 6.6. Reduction in net costs (%) with respect to AVG for different cases estimated for various days (column 'Day') of the year.

Day	Case 1	Case 2	Case 3	Case 4	Case 5	Case 6	OPT
33	13.60	6.42	20.76	7.62	11.49	22.26	31.62
83	38.83	12.81	57.71	19.75	30.90	65.81	96.73
153	74.95	38.51	99.14	53.80	45.10	112.84	186.47
220	239.96	205.76	355.53	244.61	451.93	376.11	650.83
332	243.91	9.29	255.63	19.56	256.58	280.15	317.83
Avg.	122.25	54.56	157.76	69.07	159.20	171.43	256.70

To reiterate this point, the annual V2G energy fed to the grid for OPT was estimated and found to be 42.2 kWh. This is 0.072% of the total annual demand of the EVs of $365 \times 80 = 58,400$ kWh. Combined V2G sales over the year were 13.14\$ or 3.6c/day, without considering the battery degradation penalty of 1.77\$. V2G occurred only on 7 days of the 365 days and 3 EVs out of 6 participated, largely discouraged by the battery degradation penalty, C^{V2G} .

6.7.5. Inferences

The large cost reduction is a hence result of aggregating the multi-aspect PV, EV, energy market problem into a single MILP formulation. This results in the sale of PV and V2G power when prices are high, buying of EV charging power when prices are low and continuous sale of regulation services. The current MILP formulation is such that IMM or AR will be a special case of optimized charging as dictated by the PV forecast and market prices. Second, the sharing of a single charger to charge several EVs results in a reduction of charging infrastructure cost. While these costs have not been included in the estimate, they can be up to 15,000\$ for 10kW chargers with $N_c^{conn}=4$.

Third, if battery degradation and energy efficiency losses are considered, the energy prices in the day-ahead market for the cases considered were not drastically different over the day to warrant V2G. The main benefit of using a bidirectional charger was the increased revenues from up-regulation services. Fourth, as with any forecasting

and modelling, there will be small but finite errors in the PV forecasting and inaccuracies in the modelling of the EV and charger. For example, the solar forecast will have errors in the temporal domain over the day and in the spatial domain over different locations. The impact of the modelling and forecasting error is that it will lead to reduced revenues than what is estimated. It is also why only a fraction $(1 - y_{PV}^{fc})$ of the available reserves are guaranteed and sold to the ISO. The receding horizon approach that responds to changes in model parameters, including solar PV forecast, is hence used to reduce the impact of these errors. The impact of the errors can be further reduced with smaller time steps than 15min.

6.8. Implementation aspects

In this section, the practical aspects of implementing this optimization are analyzed.

1. Adaptability

It must be kept in mind that even though wholesale DAM prices and small EV fleet have been used in this simulation, the formulation is generic to be used with large EV fleet, real-time market (RTM) and retail electricity prices as well. The parameters listed in the nomenclature section can be adapted for different markets, PV, EV types and to different smart charging scenarios as highlighted by the six case studies done for Austin.

2. Capital cost and sharing of benefits

The capital cost of building the proposed EV-PV integrated charging facility will be cheaper than a non-integrated system due to four reasons:

- The integrated bidirectional EV-PV charger costs the same as the sum of the cost of buying a similarly rated solar inverter and unidirectional EV charger [28]. The benefit of integration is the bidirectional operation of EV at no additional cost, a smaller converter as it needs only one DC/AC inverter to the AC grid and no communication hardware needed between the EV and PV system.
- The multiplexing system will allow the connection of a single charger to several EVs. This will drastically reduce the EV charging infrastructure cost by a factor proportional to how many cars are multiplexed to one charger.
- The use of rolling horizon implementation as opposed to stochastic optimization to handle forecasting errors and uncertainties simplifies the formulation and reduces the computational complexity; hence less powerful and cheaper hardware can be used.
- The integrated scheduling of EV-PV-V2G-regulation reduces the net costs on an average by 158%, and this could provide a revenue stream to recover the capital cost.

The EV-PV car park has several players involved namely the owner of PV and parking area, the ESCo, the ISO EV user and in a general scenario, the charge-point operator (CPO), e-mobility service provider (eMSP) and the DSO. The capital

investment of the EV-PV charging facility and the benefit of the net cost reduction will ultimately have to be shared amongst all these parties. This will be dependent on the contractual business agreement between the parties.

3. Scalability

Similar to any MILP problem, the problem size will grow exponentially with the number of EV. At the same time, different parking locations are decoupled by their EV, PV and distribution constraints and hence the model dimension is naturally limited to the size of a single parking lot, about 5 to 1000 EVs. Thus, the MILP's dimensionality is limited to problem sizes that are tractable by the current technology and therefore fairly scalable. Further, the receding horizon implementation makes the problem more scalable in terms of computational complexity when compared to stochastic optimization.

Stochastic optimization is an alternative to the receding horizon approach. But it was not considered here for two reasons. First, the given problem has a lot of stochastic variables, making it computationally intensive and hence less scalable. This is especially a problem as the number of EV grows to above 50 in a parking lot. The MILP formulation with receding horizon approach makes it computationally easier. Second, stochastic optimization requires the generation of probabilistic data for all inputs and creating different scenarios for PV, EV, and market. Due to limited EV penetration, there is insufficient data now on EV and EV user patterns creating lots of dimensions of uncertainty. If such limited data is used as input, it is difficult to get reliable and useful results.

4. Interaction with de-regulated energy markets

With up to 1000 EVs and 10kW EV charger, the total car park is handling 10MW power at maximum, considering no multiplexing. This is small in relation to the power scales in the energy market. Hence, no perturbations will be observed on the market prices and no feedback on prices would be required for this system. At the same time, the net car park power can be occasionally lower than the minimum bid required by ISOs to participate in regulation services (for example, 0.1MW for PJM, 0.1MW for ERCOT and typically 1MW in other ISOs) It is expected that ISOs around the world would lower the minimum bid requirements in the future to allow EVs to participate in ancillary services.

6.9. Conclusions

EV charging from PV can be controlled to achieve several motives - to take advantage of the time of use tariffs, provide ancillary services or follow the PV production. However, the common approach is that each of these applications is solved as separate optimization problems which lead to several EV charging profiles. This is impractical, as a single EV cannot be controlled at the same time with different charging profiles. Further, the economic benefits of this approach are too small to warrant mass adoption of smart charging. Hence it is vital to make a single problem

formulation that bundles several applications together so that one optimal EV charging profile with cumulated benefits is obtained.

In this chapter, an MILP formulation has been proposed for charging of an EV fleet from PV that has several application built into one - charging of EV from PV, using time of use tariffs to sell PV power and charge EV from the grid, implementation of V2G for grid support, using EV to offer ancillary services in the form of reserves and considering distribution network capacity constraints. The formulation was developed considering a three-port converter topology, which allows the bidirectional charging of EV from PV on DC with a connection to AC grid for power balance. The scheduling of the connection of a single EVSE to several EVs has been included in the formulation. This provides the ability to share the EVSE amongst many EVs resulting in substantial reduction in the cost of EV infrastructure. The MILP optimization has been implemented as a receding horizon model predictive control and operates with a fixed time period.

Using 2014 data from Pecan Street Project and ERCOT market, simulations were performed for an EV fleet of six connected to four chargers. The formulation of five applications into one resulted in large reductions in the net costs in the range of 32% to 651% with respect to average rate charging. The net costs were far lower than those for immediate and randomly delayed charging, highlighting the benefits of the proposed smart charging algorithm. Using six case studies, it has been shown that when several smart charging applications are combined together, it results in huge cost savings. Further, for the scenario simulated, it was observed that a large portion of the V2G revenues came from increased regulation services offered rather than from V2G energy sales due to the battery degradation penalty.

In a second scenario, simulations were performed for the Netherlands using data from KNMI and scaled APX energy prices, where ancillary services market are not bundled with the wholesale electricity markets. In case of one charging point with 4 EVs, total cost was reduced by 118.44%, whereas profit was increased by 427.45% when two charging points with 6 EVs were considered. In addition, it was found that energy sales through vehicle-to-grid (V2G) are currently not economically viable due to battery degradation costs, except in case of a significant surplus of PV power production.

The MILP formulation is generic, scalable and can be adapted to different energy and ancillary markets, EV types, PV array installations and EVSE.

6.10. References

- [1] M. Kefayati and R. Baldick, "Harnessing demand flexibility to match renewable production using localized policies," in *2012 50th Annual Allerton Conference on Communication, Control, and Computing (Allerton)*, 2012, pp. 1105–1109.
- [2] A. D. Hilshey, P. D. H. Hines, P. Rezaei, and J. R. Dowds, "Estimating the Impact of Electric Vehicle Smart Charging on Distribution Transformer Aging," *IEEE Trans. Smart Grid*, vol. 4, no. 2, pp. 905–913, Jun. 2013.
- [3] Q. Gong, S. Midlam-Mohler, V. Marano, and G. Rizzoni, "Study of PEV Charging on Residential Distribution Transformer Life," *IEEE Trans. Smart Grid*, vol. 3, no. 1, pp.

- 404–412, Mar. 2012.
- [4] G. R. C. Mouli, J. Kaptein, P. Bauer, and M. Zeman, “Implementation of dynamic charging and V2G using Chademo and CCS/Combo DC charging standard,” in *2016 IEEE Transportation Electrification Conference and Expo (ITEC)*, 2016, pp. 1–6.
 - [5] M. Caramanis and J. M. Foster, “Management of electric vehicle charging to mitigate renewable generation intermittency and distribution network congestion,” in *Proceedings of the 48th IEEE Conference on Decision and Control (CDC) held jointly with 2009 28th Chinese Control Conference*, 2009, pp. 4717–4722.
 - [6] M. Kefayati and C. Caramanis, “Efficient Energy Delivery Management for PHEVs,” in *2010 First IEEE International Conference on Smart Grid Communications*, 2010, pp. 525–530.
 - [7] W. Kempton and J. Tomić, “Vehicle-to-grid power implementation: From stabilizing the grid to supporting large-scale renewable energy,” *J. Power Sources*, vol. 144, no. 1, pp. 280–294, 2005.
 - [8] H. Lund and W. Kempton, “Integration of renewable energy into the transport and electricity sectors through V2G,” *Energy Policy*, vol. 36, no. 9, pp. 3578–3587, 2008.
 - [9] M. Kefayati and R. Baldick, “Energy Delivery Transaction Pricing for flexible electrical loads,” in *2011 IEEE International Conference on Smart Grid Communications (SmartGridComm)*, 2011, pp. 363–368.
 - [10] T. Ma and O. A. Mohammed, “Optimal Charging of Plug-in Electric Vehicles for a Car-Park Infrastructure,” *IEEE Trans. Ind. Appl.*, vol. 50, no. 4, pp. 2323–2330, Jul. 2014.
 - [11] T. Ma and O. Mohammed, “Economic analysis of real-time large scale PEVs network power flow control algorithm with the consideration of V2G services,” in *2013 IEEE Industry Applications Society Annual Meeting*, 2013, pp. 1–8.
 - [12] Y.-M. Wi, J.-U. Lee, and S.-K. Joo, “Electric vehicle charging method for smart homes/buildings with a photovoltaic system,” *IEEE Trans. Consum. Electron.*, vol. 59, no. 2, pp. 323–328, May 2013.
 - [13] M. van der Kam and W. van Sark, “Smart charging of electric vehicles with photovoltaic power and vehicle-to-grid technology in a microgrid; a case study,” *Appl. Energy*, vol. 152, pp. 20–30, Aug. 2015.
 - [14] N. Liu, Q. Chen, J. Liu, X. Lu, P. Li, J. Lei, and J. Zhang, “A Heuristic Operation Strategy for Commercial Building Microgrids Containing EVs and PV System,” *IEEE Trans. Ind. Electron.*, vol. 62, no. 4, pp. 2560–2570, Apr. 2015.
 - [15] M. Honarmand, A. Zakariazadeh, and S. Jadid, “Integrated scheduling of renewable generation and electric vehicles parking lot in a smart microgrid,” *Energy Convers. Manag.*, vol. 86, pp. 745–755, 2014.
 - [16] M. S. Kuran, A. Carneiro Viana, L. Iannone, D. Kofman, G. Mermoud, and J. P. Vasseur, “A Smart Parking Lot Management System for Scheduling the Recharging of Electric Vehicles,” *IEEE Trans. Smart Grid*, vol. 6, no. 6, pp. 2942–2953, Nov. 2015.
 - [17] D. van der Meer, G. R. Chandra Mouli, G. Morales-Espana, L. Ramirez Elizondo, and P. Bauer, “Energy Management System with PV Power Forecast to Optimally Charge EVs at the Workplace,” *IEEE Trans. Ind. Informatics*, vol. 14, no. 1, pp. 311–320, 2018.
 - [18] L. Yao, Z. Damiran, and W. H. Lim, “Optimal Charging and Discharging Scheduling for Electric Vehicles in a Parking Station with Photovoltaic System and Energy Storage System,” *Energies*, vol. 10, pp. 1–20, Apr. 2017.
 - [19] P. Sanchez-Martin, S. Lumbreras, and A. Alberdi-Alen, “Stochastic Programming Applied to EV Charging Points for Energy and Reserve Service Markets,” *IEEE Trans. Power Syst.*, vol. 31, no. 1, pp. 198–205, Jan. 2016.
 - [20] D. Wu, H. Zeng, C. Lu, and B. Boulet, “Two-Stage Energy Management for Office

- Buildings With Workplace EV Charging and Renewable Energy,” *IEEE Trans. Transp. Electrification*, vol. 3, no. 1, pp. 225–237, Mar. 2017.
- [21] H. N. T. Nguyen, C. Zhang, and J. Zhang, “Dynamic Demand Control of Electric Vehicles to Support Power Grid With High Penetration Level of Renewable Energy,” *IEEE Trans. Transp. Electrification*, vol. 2, no. 1, pp. 66–75, Mar. 2016.
- [22] E. Yao, V. W. S. Wong, and R. Schober, “Robust Frequency Regulation Capacity Scheduling Algorithm for Electric Vehicles,” *IEEE Trans. Smart Grid*, pp. 1–14, 2016.
- [23] J. Donadee and M. D. Ilic, “Stochastic Optimization of Grid to Vehicle Frequency Regulation Capacity Bids,” *IEEE Trans. Smart Grid*, vol. 5, no. 2, pp. 1061–1069, Mar. 2014.
- [24] G. R. Chandra Mouli, P. Bauer, and M. Zeman, “Comparison of system architecture and converter topology for a solar powered electric vehicle charging station,” in *2015 9th International Conference on Power Electronics and ECCE Asia (ICPE-ECCE Asia)*, 2015, pp. 1908–1915.
- [25] H. Zhang, Z. Hu, Z. Xu, and Y. Song, “Optimal Planning of PEV Charging Station With Single Output Multiple Cables Charging Spots,” *IEEE Trans. Smart Grid*, pp. 1–10, 2016.
- [26] C. Chung, P. Chu, and R. Gadh, “Design of smart charging infrastructure hardware and firmware design of the various current multiplexing charging system,” *7th Glob. Conf. Power Control Optim.*, pp. 1–14, 2013.
- [27] G. R. Chandra Mouli, P. Bauer, and M. Zeman, “System design for a solar powered electric vehicle charging station for workplaces,” *Appl. Energy*, vol. 168, pp. 434–443, Apr. 2016.
- [28] PRE-TUD, “Datasheet V2G500V30A - 10kW Bidirectional Solar EV Charger Module - Power Research Electronics B.V, Delft University of Technology,” 2017.
- [29] G. R. Chandra Mouli, J. H. J. H. Schijffelen, P. Bauer, and M. Zeman, “Design and comparison of a 10-kW interleaved boost converter for PV application using Si and SiC devices,” *IEEE J. Emerg. Sel. Top. Power Electron.*, vol. 5, no. 2, pp. 610–623, 2017.
- [30] C. Hamilton, G. Gamboa, J. Elmes, R. Kerley, A. Arias, M. Pepper, J. Shen, and I. Batarseh, “System architecture of a modular direct-DC PV charging station for plug-in electric vehicles,” in *IECON 2010 - 36th Annual Conference on IEEE Industrial Electronics Society*, 2010, pp. 2516–2520.
- [31] G. Carli and S. S. Williamson, “Technical Considerations on Power Conversion for Electric and Plug-in Hybrid Electric Vehicle Battery Charging in Photovoltaic Installations,” *IEEE Trans. Power Electron.*, vol. 28, no. 12, pp. 5784–5792, Dec. 2013.
- [32] “Standard IEC 62196 - Plugs, socket-outlets, vehicle connectors and vehicle inlets - Conductive charging of electric vehicles - Part 1, 2, 3,” pp. 1–176, 1–122, 1–71, 2014.
- [33] P. Bacher, H. Madsen, and H. A. Nielsen, “Online short-term solar power forecasting,” *Sol. Energy*, vol. 83, no. 10, pp. 1772–1783, Oct. 2009.
- [34] G. E. P. Box, G. M. Jenkins, G. C. Reinsel, and G. M. Ljung, *Time series analysis: forecasting and control*. John Wiley & Sons, 2013.
- [35] M. Diagne, M. David, P. Lauret, J. Boland, and N. Schmutz, “Review of solar irradiance forecasting methods and a proposition for small-scale insular grids,” *Renew. Sustain. Energy Rev.*, vol. 27, pp. 65–76, Nov. 2013.
- [36] Y. Cao, S. Tang, C. Li, P. Zhang, Y. Tan, Z. Zhang, and J. Li, “An Optimized EV Charging Model Considering TOU Price and SOC Curve,” *IEEE Trans. Smart Grid*, vol. 3, no. 1, pp. 388–393, Mar. 2012.
- [37] M. A. Ortega-Vazquez, “Optimal scheduling of electric vehicle charging and vehicle-to-grid services at household level including battery degradation and price uncertainty,” *IET*

- Gener. Transm. Distrib.*, vol. 8, no. 6, pp. 1007–1016, Jun. 2014.
- [38] S. B. Peterson, J. Apt, and J. F. Whitacre, “Lithium-ion battery cell degradation resulting from realistic vehicle and vehicle-to-grid utilization,” *J. Power Sources*, vol. 195, no. 8, pp. 2385–2392, 2010.
- [39] B. Lunz, Z. Yan, J. B. Gerschler, and D. U. Sauer, “Influence of plug-in hybrid electric vehicle charging strategies on charging and battery degradation costs,” *Energy Policy*, vol. 46, pp. 511–519, Jul. 2012.
- [40] L. De Vroey, R. Jahn, N. Omar, and J. Van Mierlo, “Impact of smart charging on the ev battery ageing-discussion from a 3 years real life experience,” in *EVS28 International Electric Vehicle Symposium and Exhibition*, 2015, pp. 1–8.
- [41] D. Wang, J. Coignard, T. Zeng, C. Zhang, and S. Saxena, “Quantifying electric vehicle battery degradation from driving vs. vehicle-to-grid services,” *J. Power Sources*, vol. 332, pp. 193–203, Nov. 2016.
- [42] I. S. Bayram, V. Zamani, R. Hanna, and J. Kleissl, “On the evaluation of plug-in electric vehicle data of a campus charging network,” in *IEEE International Energy Conference, ENERGYCON*, 2016, pp. 1–6.
- [43] L. Jian, Y. Zheng, X. Xiao, and C. C. Chan, “Optimal scheduling for vehicle-to-grid operation with stochastic connection of plug-in electric vehicles to smart grid,” *Appl. Energy*, vol. 146, pp. 150–161, 2015.
- [44] W. Su and M.-Y. Chow, “Investigating a large-scale PHEV/PEV parking deck in a smart grid environment,” in *2011 North American Power Symposium*, 2011, pp. 1–6.
- [45] J. Harikumar, G. Vereczki, C. Farkas, and P. Bauer, “Comparison of quick charge technologies for electric vehicle introduction in Netherlands,” in *IECON Proceedings (Industrial Electronics Conference)*, 2012, pp. 2907–2913.
- [46] ABB Electric Vehicle Charging Infrastructure, “Datasheet - ABB Terra 51 fast charging station,” 2016.
- [47] SMA, “Datasheet - SUNNY ISLAND 6.0H / 8.0H,” 2015.
- [48] Pecan Street, “Dataport - Pecan Street Inc.,” 2016.

7

Implementation of Smart charging and V2G

7. Implementation of Smart charging and V2G

This chapter is based on:

G. R. Chandra Mouli, J. Kaptein, P. Bauer, and M. Zeman, "Implementation of dynamic charging and V2G using CHAdeMO and CCS/Combo DC charging standard," in 2016 IEEE Transportation Electrification Conference and Expo (ITEC), 2016, pp. 1–6.

Summary

In Chapter 6, smart charging algorithms for the EV-PV system were proposed that can reduce the cost of EV charging by controlling the charging power of the EV. In order to implement these algorithms in practice, it is vital to understand the EV charging standards, their communication protocol and to build a testbed to control the (dis)charging power of commercially available EVs. This chapter compares the DC charging standards in their implementation of smart charging and vehicle to grid (V2G) and brings out its influence on the charging system design, response time, and flexibility in charging from renewable sources and buffer capacity that is required. Experimental results of smart charging using CHAdeMO and CCS/COMBO are presented for different compatible EV that shows their fundamental differences.

Outline

Section 7.2 explains how smart charging is implemented in AC chargers currently and why V2G is currently not possible on AC chargers. In section 7.3, the implementation of smart charging and V2G using CHAdeMO charging standard is described. In section 7.4, the implementation of smart charging and V2G using CCS/Combo charging standard is elucidated highlighting the vital differences with CHAdeMO. Section 7.5 presents the experimental results of implementing smart charging and V2G using a commercially available CHAdeMO and Combo electric car respectively. Based on the experimental results, recommendations are provided for automobile manufacturers and for members of standardization working groups.

7.1. Introduction

Smart charging provides several benefits such as reduced cost of charging, lower peak demand on the grid, delayed infrastructure upgrade, the increased penetration of renewables and lower destination system losses. As seen in chapter 6, the use of smart charging in an EV-PV system provides a drastic reduction in net costs. The key to implementing smart charging is the communication and control protocols between the charger/EVSE and the EV. This chapter investigates the implementation of smart charging and V2G for AC charging, ChAdeMO and CCS/COMBO. The basics of different AC and DC EV charging systems can be seen in chapter 2.

7.2. Smart Charging and V2G on AC

Communication between EV and the charger for AC charging is done using a control pilot (CP) and proximity pilot (PP). The proximity pilot keeps track of the physical connection between the charger and EV and control pilot communicates the maximum ampacity of the charger cable.

7.2.1. Smart charging via AC charging

To implement AC smart charging:

- The control pilot has a PWM signal that can be adjusted to modify the maximum charging current that is available from the charger, as shown in Fig. 7.1(a) as the 'variable set point.'
- Based on the PWM signal on CP, the EV decides the charging current based on the status of the battery such as the state of charge (SOC) and temperature. The charging current request is hence set by the EV, which is the MASTER and the current requested by the EV can be less than or equal to the maximum charger current.
- The charger is the SLAVE and supplies the current requested by the EV. If the

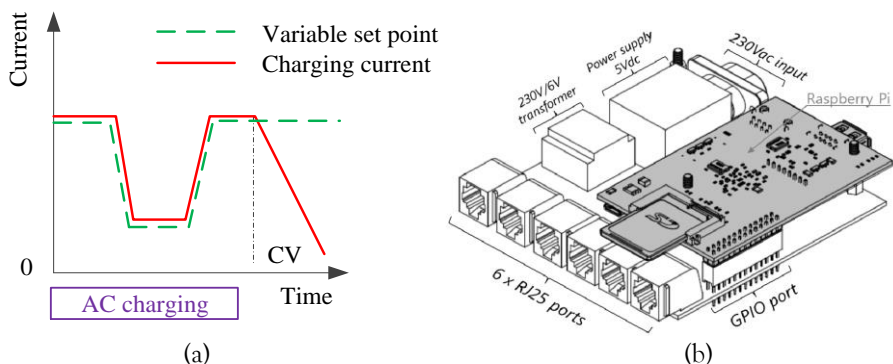


Fig. 7.1. (a) Smart charging using AC charging via Type 1 or Type 2 plug. (b) 3D rendering of the Smart Charging Controller for AC charging [1]. The device collects measurements from current transformers and controls the charging power

EV battery SOC or temperature is too high, the battery management system of the EV will draw a current lower than the setpoint. For example in Fig. 7.1(a), the EV SOC is too high in the 'CV' region, and the battery goes into constant voltage charging and draws a current that is lower than the setpoint. Thus by controlling the PWM on the CP, smart charging can be implemented.

For example, the *Smart Charging Controller* developed by Cohere [1] shown in Fig. 7.1(b), used this technique to dynamically charge the EV based on the local PV generation and local residential consumption.

7.2.2. V2G via AC charging

Since EV owners may not be willing to make a separate investment for a DC charger at home, V2G via onboard AC chargers has an enormous potential for the future. Secondly, the V2G power levels of 10kW are of the same order of the power levels of onboard chargers [2].

However, implementation of V2G using AC chargers is currently not possible due to two reasons:

1. EVs currently in the market are not equipped with bidirectional onboard chargers that support EV discharging.
2. Communication protocol for AC charging via CP, PP has no provision for initiating V2G. In the V2G mode, the charger acts like the MASTER and requests the EV for discharging a required amount of current. However, in current AC charging protocol, the EV is the MASTER, and such a V2G request cannot be enabled.

To overcome the two barriers, EV manufacturers should look into the possibility of installing bidirectional chargers onboard EV. If communication on the CP, PP for AC charging can be integrated to include PLC as with CCS (will be discussed later in the chapter), the opportunity for V2G via AC chargers can be realized.

7.3. Smart Charging via CHAdeMO

CHAdeMO v1.0 charging control mechanism is similar to the AC charging for type 1 and type 2. The car is the MASTER and decides the required charger current and sends a current request command every 200ms. The charger is the SLAVE and supplies the requested current. The charging protocol is shown in Fig. 7.2(a) and is as follows:

- The EV and charger make a handshake to:
 - Share information on the EV like model, battery voltage and SOC
 - Set the upper charging current limit based on the maximum charging power of the EV and the charger.
- EV continuously makes a current set point every 200ms based on the battery like SOC, temperature, etc.

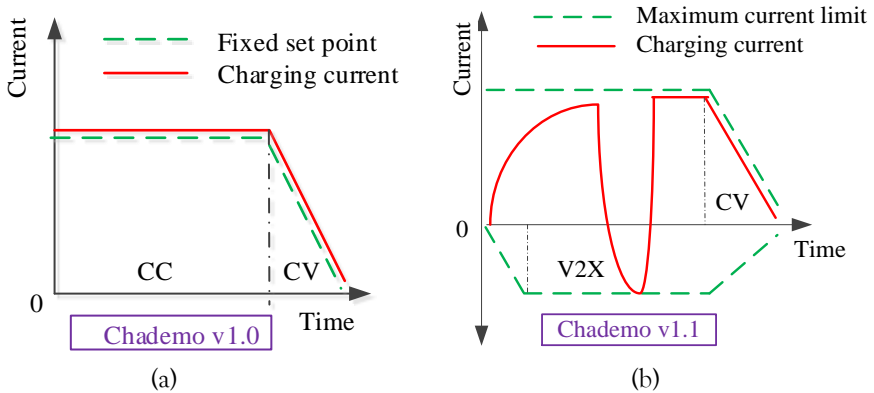


Fig. 7.2. (a) Conventional charging using CHAdeMO v1.0; (b) Smart charging using CHAdeMO v1.1

- The charger has to supply the requested current, with a current resolution of 2.5A. So the charging current supplied by the charger can vary from the set point of the EV by up to 2.5A
- The maximum current set point of charger and EV set at handshake remains constant throughout for CHAdeMO v1.0. There is no mechanism for the charger to request a change of maximum limit. So essentially, smart charging is not possible. This is unlike AC charging where the upper set point of the charger current can be set continuously with PWM on the CP. Secondly, CHAdeMO v1.0 does not have the facility for V2G. This is due to two reasons. Firstly, the v1.0 necessitates the presence of a diode at the charger output which will only allow charging and V2G.

Secondly, the communication protocol does not have a facility to make the charger the MASTER, to set the charging current and direction. This is implemented in CHAdeMO v1.1 V2G, shown in Fig. 7.2(b) where the output diode is not required:

- The EV and charger make a handshake to share information on the EV battery. The maximum charging and discharging current is set based on the power ratings of the EV and the charger.
- Once charging begins, EV continuously sets the maximum current for charging and discharging every 200ms, as shown in Fig. 7.2(b) based on the battery characteristics like SOC, temperature, etc. When the maximum discharge current is zero, it means that V2G is not possible.
- The charger can provide any charging current between the upper and lower bounds with a resolution of 2.5A. This essentially means that a varying PV power can be translated into a varying EV charging current as long as it is within the upper and lower bounds. In Fig. 7.2(b), it can be seen that at the start of the graph, the SOC is low and the maximum discharge current (negative limit) is small. The discharge current limit increases as SOC increases with charging. At the left of the graph, the battery is nearly full, and the maximum charging current limit is slowly reduced by the EV to prevent overcharging the EV batteries.

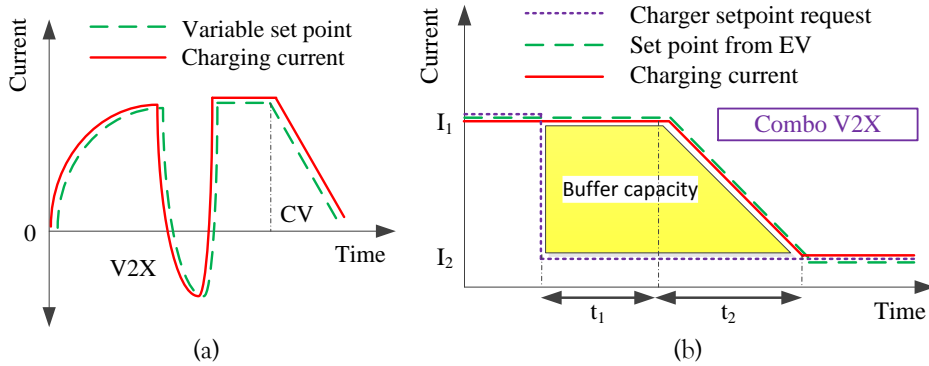


Fig. 7.3. (a) Smart charging and V2G using CCS/COMBO; (b) Time delays in the execution of smart charging and the required buffer capacity

Hence, CHAdeMO v1.1 facilitates smart charging with high flexibility. A smart energy management system can decide on the optimal charging profile of the EV based on user preferences, energy prices or renewable generation and it can be implemented via smart charging.

7.4. Smart Charging via CCS/COMBO

CCS/COMBO facilitates smart charging and V2G by using PLC communication over the CP, PP using ISO 15118. This allows high-level communication, overcoming the limitations of only using PWM for communication in AC charging. The implementation of V2G and smart charging for CCS varies from CHAdeMO and is shown in Fig. 7.3(a):

- The EV and charger make a handshake to share information EV and set the maximum charging current limit based on the power rating of the EV and the charger.
- Once charging begins, EV and charger continuously negotiate and set a charging/discharging current set point based on the battery characteristics like SOC, temperature, etc. For V2G or smart charging, the charger can make a request for change of current and EV has to accept this request. The communication is based on ISO 15118.
- If the request is accepted, EV changes the current setpoint and the charger has to charge/discharge the EV based on the negotiated set point as shown in Fig. 7.3(a). The current resolution is 2.5A.

Smart charging with CCS is hence not as flexible as in CHAdeMO. If the EV charging current has to change from I_1 to I_2 due to a sudden change of renewable generation or energy prices, the EV charger will need to send a request for a new set point as shown in Fig. 7.3(b). It takes time t_1 for the car to respond to the new request and it changes the set point from I_1 to I_2 over the time t_2 . For the period $(t_1 + t_2)$, a buffer capacity E_{buff} is required to store the energy from the renewable source or the grid based on the EV battery voltage V_{ev}

$$E_{buffer} = V_{ev}(I_1 - I_2) \left(t_1 + \frac{t_2}{2} \right) \quad (1)$$

This buffer capacity is not necessary with CHAdeMO. t_1 and t_2 are mainly dependent on the manufacturer of the EV, SOC of the battery and the current set points I_1 , I_2 . As per the CCS standard, the EV can take up $t_1=60s$ to respond to the request for a new current setpoint from the charger. This is very long time considering the fact that many V2G or smart charging applications like providing ancillary services or changing the charging power in correspondence to renewable generation would require the EV to respond within few seconds ($\leq 2s$ or less). Secondly, the CCS standard is silent on the time limit t_2 that can be taken by the EV to change the current setpoint from I_1 to I_2 . t_2 can be as high as 10s or more, as shown in the next section. Both of these are serious drawbacks from the point of view of smart charging as it makes the EV susceptible to be slow in response. While manufacturers can design their EV to respond much quicker, the fact that a 60s response time for t_1 and no upper limit for t_2 makes the COMBO implementation slow in theory and requiring a large buffer capacity E_{buffer} .

7.5. Experimental Verification

7.5.1. Smart charging and V2G using CHAdeMO

An experimental setup was built to implement the smart charging of EV and V2G. The schematic of the setup is shown in Fig. 7.4(a) where a bidirectional charger is used with a CHAdeMO compatible EV. CAN bus communication is used between the EV and charge protocol interface that implements the CHAdeMO v1.1 protocol. A standard ABB EV charger was used for charging the EV and a commercially available solar inverter was used for discharging EV for V2G. In the experiment, the charging protocol for CHAdeMO v1.1 was implemented for smart charging and V2G by changing the EV from charging mode to discharging mode and back, as seen in the waveforms in Fig. 7.4(b).

Using the AC/DC rectifier module, the EV is first charged at -4A current (sign convention: negative current denotes charging and a positive current is discharging). Using the main controller, the current is then varied by the charger at 20A/s slope to +4A current for V2G operation. The solar inverter module draws DC current from the EV and supplies it back to the grid as seen by the green waveform. Due to lack of CAN bus communication with inverter module, the AC/DC rectifier module continue to supply 4A, so inverter draws 4A each from the EV and from the charger module, totalling 8A. Such a mechanism can hence be used in relation to a smart charging system that varies the charging to match the renewable generation or grid energy prices.

7.5.2. Smart charging and V2G using CCS/Combo

An experimental setup using an ABB 50kW Terra 53C CCS charger as shown in Fig. 7.5 was used to test smart charging on two CCS compatible EV. The charge protocol interface in the EV charger is used to send PLC signals to the EV to control

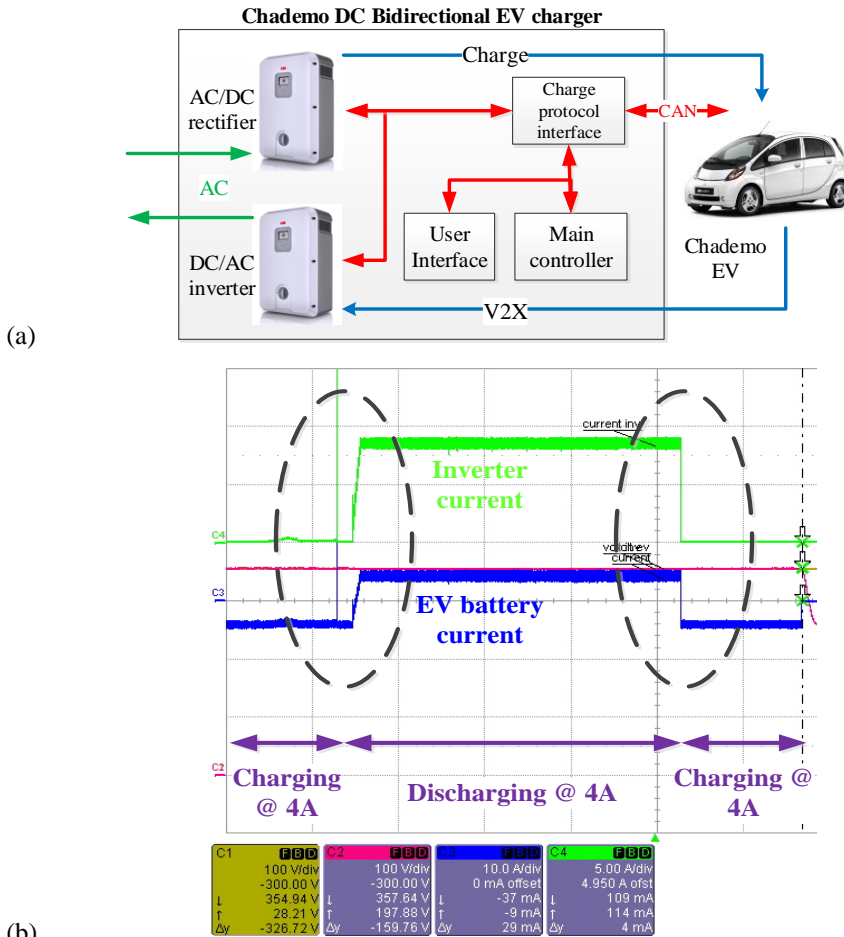


Fig. 7.4. (a) Experimental setup for smart charging and V2G using CHAdeMO v1.1; (b) Experimental waveforms showing the EV current going from negative (CH) to positive (V2G) showing change operating mode and current direction

the charging current. The main controller was used to send charging current commands I_{ref} every 100ms to the EV as shown in Fig. 7.6. The EV continuously sends a current request command I_{set} every 100ms, and the EV charger then supplies the requested current I_{set} via the CCS charger plug. When there is a change in the charger current command I_{ref} , EV has to respond within $(t_1 + t_2)$ as discussed in the previous section.

Smart charging was implemented on two different CCS compatible EV and tested for comparing their performance. Fig. 7.6 shows the smart charging of both the EVs with varying EV charging current indicated by I_{set} . Fig. 7.6(a) shows the measurement of charger current reference I_{ref} requested by the charger every 100ms over PLC and the corresponding EV current request I_{set} as a function of time for EV 1. It can be

seen that the EV responds immediately by changing the setpoint I_{set} with $t_1 = 100\text{ms}$. However, to change the setpoint I_{set} from I_1 to I_2 , the EV takes a long time t_2 depending on how big is the difference between I_1 and I_2 . For example, when the setpoint I_{ref} is increased from 25A to 70A at $t = 135.6\text{s}$, the EV responded by changing the setpoint I_{set} in approximately $t_2 = 10\text{s}$.

On the other hand, when the setpoint I_{ref} is decreased, the EV response is relatively faster, and t_2 is in the order of 0.2s depending on I_1 , I_2 . Thus, the EV

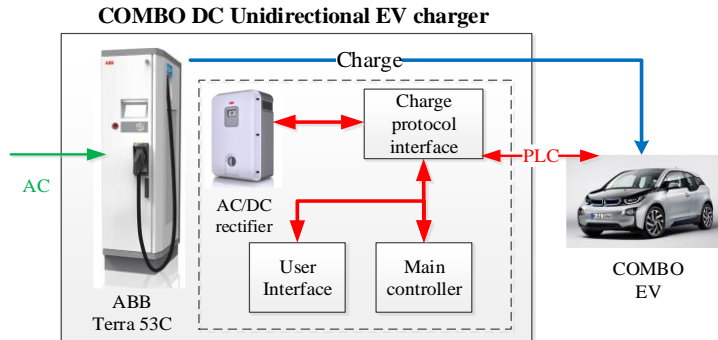


Fig. 7.5. Experimental setup for smart charging using CCS using a 50kW ABB Terra 53C charger. CCS uses PLC communication on CP between charger and EV

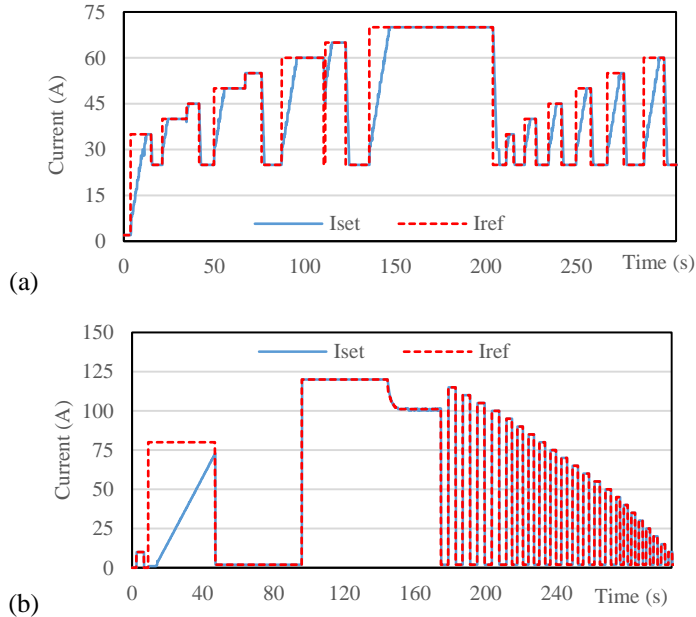


Fig. 7.6. Measurement of charger current reference I_{ref} sent every 100ms over PLC and corresponding EV current request I_{set} for CCS compatible EV of (a) Manufacturer 1; (b) Manufacturer 2

responds quickly when the setpoint is reduced while the response is much slower when the setpoint is increased. While the response times of 100ms is within the stipulated 60s limit as per CCS, the total time ($t_1 + t_2$) is very long when a fast response to the order of <2s is required for smart charging and V2G applications.

In contrast, the behaviour of EV 2 was found to be quite in contrast. In Fig. 7.6(b), it can be seen that when the charging session is to begin, a current setpoint of 10A is used to test the EV-charger connection and protection mechanism before initiating the charging. Then a charger current reference of $I_{ref}=80A$ is sent. The EV responds over a time of ($t_1 + t_2$)=38s when I_{set} increases from 0A to 70A. Interestingly, this relatively slow response occurs only during startup. After that, when the current setpoint from charger I_{ref} was changed, the EV responded within $t_2=100ms$, as shown in Fig. 7.6(b). The time taken was irrespective of the difference between I_1, I_2 and whether the charger setpoint I_{ref} was increasing or decreasing.

Rapid smart charging with fast change of current reference from the charger could hence be tested and implemented as shown in Fig. 7.6(b) for $t=180s$ to $280s$. The current reference I_{ref} was changed every 5s and the EV responded within 100ms. This was much lower than the response time of first CCS EV that was tested. Such an EV with fast response time of the order of 100ms would hence be excellent for use in smart charging and V2G applications. The experimental tests go to show the smart charging can be implemented using a CCS/COMBO electric car and how the performance of the charging varies from EV to EV.

7.6. Conclusions

Smart charging and V2G correspond to the method of charging EV with variable charging power and supplying energy back to the grid, respectively. The two technologies have a tremendous potential for the future to match the EV charging with local renewable energy production, providing grid support and ancillary services and optimizing the cost of charging EV. In this chapter, the implementation of smart charging and V2G using AC charging (SAE J1772, Mennekes) and DC charging via CCS/COMBO and CHAdeMO is analyzed in detail. It has been shown that AC charging can offer smart charging via PWM on control pilot while V2G is not currently possible due to the absence of onboard bidirectional EV chargers.

CHAdeMO v1.1 offers maximum flexibility for smart charging and V2G. The EV only sets the maximum currents for charging and discharging and the charger has maximum control to vary the charging current and direction within these limits. On the other hand, CCS provides for negotiated smart charging where the EV charger can send current commands every 100ms and EV is required to respond within a time frame of ($t_1 + t_2$) seconds. The CCS standard currently allows the EV to take up to $t_1=60s$ to respond to the charger current request. The standard is silent on the upper limit for the response time t_2 . The ($t_1 + t_2$) response time as stipulated by the standard is slow considering that any real-world smart charging and V2G application would require the EV to respond fast within milliseconds or few seconds. Hence, it would be

advisable if CCS sets an upper limit for t_2 would reduce the response time to the order of $(t_1 + t_2) = 1-2s$ in the future.

Experimental results of smart charging have been presented that prove the fundamental differences between using CHAdeMO and COMBO for different compatible EV. A CHAdeMO compatible EV was moved from charging to V2G state using the CHAdeMO v1.1 protocol. Smart charging was implemented on two different CCS compatible EVs, and the two EVs exhibited very different response time.

7.7. References

- [1] B. V. E. Bakolas, P. Bauer, and D. Prins, "Testing of Smart Charging Controller for dynamic charging from solar panels," in *2014 IEEE Transportation Electrification Conference and Expo (ITEC)*, 2014, pp. 1–4.
- [2] CHAdeMO Association, "Technical specifications of quick charger for the electric vehicle," *CHAdeMO Protoc. Rev. 1.1*, 2010.

Conclusions

8. Conclusions

Charging electric vehicles from solar energy would result in a truly sustainable form of transportation for the future. In this thesis, the power converter, charging algorithm and system-level design for a solar powered electric vehicle charging system has been developed. The system design for the Netherlands has shown that a 10kW_p PV system can deliver on an average 30kWh energy per day, sufficient to charge a Nissan Leaf EV to drive approx. 55,000km/year.

A 10kW power converter has been built that can directly charge electric vehicles from photovoltaic panels on direct current (DC). The charger is bidirectional and can implement V2G, where the EV can feed power back to the grid. The closed-loop control of the converter can realize four power flows: PV→EV, EV→Grid, Grid→EV and PV→Grid. The modular design of the converter and its control allows it to be easily scaled up to higher powers of the order of 100kW. The charger can hence use the EV battery as a storage for the PV, negating the need for additional storage. The charger has a much higher peak and partial-load efficiency, three times higher power density and lower cost than existing solutions based on AC exchange of power between EV and PV. The charger is compatible with the CHAdeMO, CCS charging standard and the grid and EMI regulation for commercial usage. Successfully tests have been carried out with a commercial EV by charging it from PV panels and feeding power back to the grid via V2G.

New smart algorithms developed in the thesis can control the EV charging based on PV forecast, energy prices, V2G, regulation services and distribution network constraints. These algorithms have the potential to reduce the net costs by up to 427% in the Netherlands and up to 651% in Texas, USA when compared to average rate charging. The smart charging allows the multiplexing of a single charger to several EVs thus enabling sharing and a significant reduction in charging infrastructure cost.

8.1. Contributions

The main contributions of the thesis are:

- System level design of a solar-powered EV charging station for workplaces considering the interrelation between EV charging requirements, PV generation, local storage and working days per week.
- Developing a 10kW bidirectional power converter for charging of EV from PV and grid, that is compatible with CHAdeMO and CCS/COMBO DC charging standard.
- Demonstrating the use of interleaving, SiC devices and powdered alloy core inductors to achieve high power density, high efficiency, modularity and lower cost in high power converters.
- Determining the optimal topology for a high power solar power electric vehicle charger based on power density, efficiency, controllability and component count.
- Design of closed-loop control for EV-PV charger that can realize four power flows: PV→EV, EV→Grid, Grid→EV and PV→Grid

- Mathematical models for estimation of inductance variation and non-linear currents in powdered alloy inductors.
- Implementing smart charging of EVs based on the concept of multiplexing that allows the sharing of the EV charger with multiple EVs, thereby by drastically reducing the cost of the charging infrastructure
- Development of smart charging algorithms to reduce the net cost of EV charging based on the solar forecast, EV user preferences, electricity prices, and offer of regulation services.
- Implementation and comparison of smart charging and V2G using CHAdeMO and CCS/COMBO compatible EVs

8.2. Conclusions

The key findings that answer the research questions of the thesis are mentioned in this section. The conclusions are categorized into three: System design, power converter and charging algorithms

System design

Advantages and drawbacks of the existing system for charging EVs from PV:

Even though EV and PV are DC by nature, existing EV-PV system often use the AC grid as an interface for exchanging power. This leads to additional conversion steps and associated losses. Two inverters, one each in the EV charger and PV inverter are required, increasing the cost and size of the power converters. At the same time, this architecture is simple and can be realized easily with off-the-shelf components. Isolation and ripple requirements of the EV DC/DC converter are neglected by most research works making the design more theoretical and less practical.

System architecture for the grid-connected EV-PV charging system:

Architecture 3 which uses a three-port converter that connects to the EV, PV and grid using a DC-link provides several advantages over the other architecture - direct use of DC power of PV for EV charging, the ease of control and higher power density that is achieved due to the utilization of an integrated converter and the usage of the existing AC grid for connection of multiple EV-PV chargers. 10kW is chosen as the nominal power rating based on V2G power requirements, modularity and low power requirements at workplaces due to long parking times of cars

Meeting the EV charging requirements at a workplace in the Netherlands with a 10kW PV system:

With a daily commuting distance of 50km/day, 10kWh/day charging energy is required by a Nissan Leaf (121km range as per EPA driving cycle) assuming 95% charging efficiency. On the other hand, the annual yield of a 10kW PV system in the Netherlands is 10,890kWh or approx. 30kWh/day (facing south, 28° tilt). 30kWh/day thus corresponds to the commuting energy needs of three Leafs. At the same time, the average daily PV generation exhibits a difference of five times between

summer and winter. This necessitates a grid connection for the EV-PV charger to supply power in winter and to absorb the excess PV power in summer.

Use of a solar tracking system for increasing the winter energy yield:

Using a 1-axis and 2-axis solar tracker increases the yield by 13.3% and 17.3%, respectively. But, this gain is concentrated in summer. The average gain in yield in the winter months of November to February due to a 2-axis tracker is 1.9kWh/day while in summer the gain is as high as 11.6kWh/day for the month of July. Solar tracking was thus found to be ineffective in increasing the winter yield, which is the bottleneck of the system.

Use of a local storage help to match the PV supply with the EV charging demand:

Different EV charging profiles were evaluated in combination with the PV to estimate the grid dependence because of mismatch between EV demand and PV supply. It was proved that a local battery storage does not eliminate the grid dependence of the EV-PV charger in the Netherlands, especially due to seasonal variations in insolation. However small-sized storage in the order of 10kWh helped in mitigating the day-day solar variations and reduced the grid energy exchange by 25%. The storage remains empty in winter for 7days/week load and gets periodically full on weekends for 5days/week load.

Influence of employees at the workplace for 5 days or 7 days a week on the system design:

In case of employees charging 5 days per week, the excess PV power has to be fed to the grid on the weekends. This increases the net energy exchange with the grid for all charging profiles. On the other hand, the net energy exchange with grid reduces significantly when a local storage is used for 5 days/week EV load. This is due to the PV charging of the local storage on weekends in winter and supplying of the EV load on Monday.

Multiplexing a single charger to several EVs for sharing of the charging infrastructure:

Multiplexing multiple EVs to a single EV-PV charger provides for sharing of the charging infrastructure and hence drastically brings down its cost. It provides flexibility to the user that they don't have to connect and disconnect their EVs due to limited charging points at the workplace. Multiplexing can be achieved by using DC disconnectors or several isolated DC/DC converters on the central DC-link to realize a modular design.

EV-PV power converter

Influenced of the EV and PV regulation standards on the power converter design:

The EV charging standards require the EV to be isolated from all power sources, including the grid and PV. However, the European standards do not need the PV to be isolated from the grid as long as the ground-leakage currents are within limits. Secondly, there are strict requirements for the EV current ripple as it influences the battery life. Similarly, the PV current ripple directly influences the efficiency of the MPPT operation and hence must be very small. In order to satisfy the requirements,

an isolated converter topology is required for the EV operating at a very high switching frequency to limit the current ripple. Alternately, an interleaved topology at a much lower switching frequency can be used.

Power converter topology for high efficiency and bidirectional power flow:

The solar EV charger is built using three converters connected to a central DC-link, one converter for each of the EV, PV and grid ports. For the PV port, a three-phase interleaved boost converter was the best topology mainly driven by its high efficiency, easy control and low component count compared to the CIIBC and TLBC. For the EV port, the four-phase interleaved bidirectional flyback converter in quasi-resonant mode was superior to the DAB due to its high power density, high partial load efficiency and low current ripple. For the grid port, the two-level converter with sinusoidal PWM was better than the three-level topologies due to lower component count and simpler control while still maintaining a comparable efficiency.

High efficiency and high power density converter using SiC devices and powder alloy cores:

>900V SiC MOSFETs with fast switching speeds can be used in high power converters that were earlier dominated by >600V IGBT with low switching speeds and high switching losses. Secondly, SiC Schottky diodes perform better than Si diodes due to nearly zero reverse recovery losses, even at blocking voltages of up to 1700V. Hence, SiC devices can operate at much higher frequencies with lower losses, thereby reducing the size and losses of passive components. Thirdly, a new generation of powdered alloy core inductors are now available with lower core losses and higher saturation flux density. They can, hence, replace ferrites in applications that require high power density by using smaller core with the possible trade-off of increased core losses.

Modular closed-loop converter control to implement four power flows: PV → EV, EV → Grid, Grid → EV, PV → Grid:

In order to scale up the 10kW EV-PV charger to higher power and to realize four different power flows, the control is organized as three independent closed-loop for each of the converters. The grid inverter control is responsible for maintaining the DC-link voltage at its nominal value by either feeding or drawing power from the grid. The PV control is responsible for the MPPT operation and for power curtailment in the event that the DC-link voltage is too high. The EV control regulates the EV (dis)charging power and implements power curtailment if the DC-link voltage is too high or too low for V2G and CH operation, respectively. By such a design, the control works suitably when more converters are modularly connected in parallel to scale up the power.

Modeling the variation of inductance and non-linear currents in powdered alloy inductors:

Powdered iron core inductors are an excellent choice for use in high power density converters due to their high saturation flux density. As a result of soft saturation, the inductance varies as a function of the inductor current resulting in non-linear

inductor currents. A mathematical model of this non-linear behaviour and its simplification based on the middle-current method were developed.

Smart charging algorithms

Review of existing smart charging algorithms and scope for improvement:

There are several applications for smart charging like charging from renewables, reducing charging costs or delaying distribution network upgrade. The focus of existing research in this domain is to find better and efficient algorithms for each of these applications considering them as separate optimization problems. The disadvantage of this method is two-fold. First, this approach is impractical, as a single EV cannot be controlled at the same time with different charging profiles catering to different applications. Second, the economic benefits of for a single smart charging application is too small to warrant mass adoption of smart charging. Hence, it is vital to make a single problem formulation that bundles several applications together, so that one optimal EV charging profile with cumulated benefits is obtained.

Formulating EV smart charging algorithm based on the solar forecast, energy prices, multiplexing, ancillary services, EV user and V2G:

A mixed integer linear programming formulation has been proposed for charging of an EV fleet from PV that has several applications integrated into one - charging of EV from PV, using time of use tariffs to sell PV power and charge EV from the grid, implementation of V2G for grid support, using EV to offer ancillary services in the form of reserves and considering distribution network capacity constraints. The objective is to reduce the cost of EV charging and increase the sales of PV generation and offer of regulation services. The scheduling of the multiplexing of a single EVSE to several EV has been included that helps in drastically reducing the cost of the charging infrastructure by sharing a single EV charger amongst several EVs.

The MILP optimization has been implemented as a receding horizon model predictive control and operates with a fixed time period. The formulation is generic, scalable and can be adapted to different energy and ancillary markets, EV types, PV array installations and EVSE.

Reduction in the net cost of EV charging from PV using charging algorithms that combine solar forecast, energy prices, regulation services and V2G:

For the Texas scenario, 2014 data from Pecan Street Project and ERCOT market were used considering 6 EVs connected to 4 EV-PV chargers. The proposed algorithm resulted in substantial reductions in the net costs in the range of 32% to 651%, with an average reduction of 158.6% with respect to average rate charging. The net costs were far lower than those for immediate and randomly delayed charging, highlighting the benefits of the proposed smart charging algorithm.

In the case of the Netherlands, simulations were performed using data from KNMI and scaled APX energy prices, where ancillary services market are not bundled with the wholesale electricity markets. In case of one charging point with 4 EVs, total cost was reduced by 118.44% with respect to uncontrolled charging. On the other hand,

the cost reduction was 427.45% when two charging points with 6 EVs were considered.

Differences in the implementation of smart charging and V2G between CHAdeMO and CCS/COMBO DC charging standard and which is more suitable:

CHAdeMO v1.1 offers maximum flexibility for smart charging and V2G. The EV only sets the maximum current for charging and discharging, and the charger has full control on the charging current and direction. On the other hand, CCS provides for negotiated smart charging where the EV charger sends current commands every 200ms and EV is required to respond within $t_1 + t_2$, with $t_1 < 60s$ and no limit for t_2 . The $(t_1 + t_2)$ response time is slow considering that smart charging application would require response milliseconds. Hence, it would be advisable if CCS sets the limit for $(t_1 + t_2) < 1s$ in the future.

8.3. Future work

Solar charging of EVs is in its nascent stage, and mass adoption of the technology is expected when EVs are widely used globally. As an extension of this thesis, several tasks for future work are possible and listed below.

Scaling up and scaling down the rated power of the EV-PV charger

The 10kW nominal rating of the developed charger may not fit the requirements of all EV charging applications. For example, fast charging applications on the highway or slow residential charging. Hence, a scaled down 6kW version of the EV-PV charger is currently under development at PRE B.V. which uses a single phase grid connection. Second, for fast charging applications, high power version of the 10kW system are being made by connecting several 10kW units in parallel. The first prototype for 20kW has been built at PRE by connecting two modules in parallel. Charging powers of up to 100kW or more can be realized by the parallel operation of modules.

Implementing multiplexing of EV chargers

The multiplexing concept where EV charger is shared amongst several EVs is a useful technique for any form of public charging. It would be interesting to implement multiplexing using the EV-PV charger and also with conventional EV chargers. Building and operating a multiplexer using minimal communication, high reliability and low cost can be an interesting topic of research. Several patents on this subject exist already and would be an excellent starting point.

Designing the EV-PV charger to work from future DC grids and trolley grids

The DC-link of the EV-PV converter is rated for 750V and is close to the voltage of trolley grids for buses and trams and that expected for future DC distribution grids. The control of the EV and PV converter can be modified to work directly with a DC grid without interaction with the currently existing inverter part. Further, the ability of the switches to operate under conditions of fast varying DC grid voltage must be investigated and solutions must be developed to handle extreme circumstances.

CCS/COMBO compatible EV-PV charger

The current version of the EV-PV charger works with a CHAdeMO charge controller that is compatible with Japanese and Korean EVs. Charging and V2G was tested using a Nissan Leaf EV. In the next step, the aim is to use a CCS/Combo charge controller with the EV-PV charger and implement charging and V2G on CCS compatible German and American EVs.

Smart charging using stochastic optimization

The smart charging algorithm developed in this thesis uses a MILP formulation with receding horizon implementation. The next step would be the use of stochastic optimization framework, where EV parking times, electricity demand from the BEVs, energy prices are considered to be uncertain. Furthermore, as the output of any PV system is inherently uncertain, probabilistic PV power forecasting can be considered. By incorporating these uncertainties, the optimal charging strategy under highly variable circumstances can be found.

Testing smart charging using EV-PV charger

The thesis resulted in the development of 10kW solar-powered EV charger and development of the corresponding smart charging algorithms. However, the smart charging algorithms have not been implemented using the EV-PV charger in practice. The reason is the necessary ICT framework to bring together EV users, energy markets, solar forecast data, charger point operators (CPO), distribution system operators (DSO) does not currently exist. If the smart charging algorithms are then implemented on the ICT framework, then a true multi-application EV smart charging system can be realized.

Economics of solar charging of EV

For future work on the economics of solar charging of EVs, it is recommended to include factors relating to maintenance costs, insurance, depreciation, the rate of interest and that provide the Total Cost of Ownership (TCO) of gasoline car and EV. This can be expanded to a well-to-wheel lifecycle assessment from the perspective emissions and energy efficiency of EVs and fossil fuel powered cars. Further, a sensitivity analysis is required to investigate the impact of the variation of parameters such as electricity energy mix, fuel economy, tax benefits, and prices of batteries, solar PV system and energy prices. The assessment of the economic impact including that of smart charging can be made from the perspective of different stakeholders such as EV user, TSO, or DSO. For example, from the perspective of a DSO, the reduced costs of network expansion and increased renewable energy production and usage would be interesting. While for an EV user, lower charging cost would be a priority.

A-D

Appendix

Appendix A: GHG of gasoline, HEV, PHEV and PEV

The well-to-wheel greenhouse gas emissions (GHG) of gasoline, hybrid electric vehicle (HEV), plug-in hybrid electric vehicle (PHEV) and plug-in battery electric vehicle (PEV) is estimated based on data from the Alternative Fuels Data Center, US Department of Energy (<https://www.afdc.energy.gov>). The assumptions underlying the model are listed below:

Parameter	Value	Source
Kilogram of CO ₂ e per gallon of gasoline	10.66	Full fuel cycle (well to wheels) greenhouse gas emissions (GHG) factors derived from GREET 2015. Results are in CO ₂ equivalents. (www.greet.es.anl.gov)
National average GHG from electricity (kg/kWh)	0.5488	Energy Information Administration, Electricity Net Generation, Open Data, API (www.eia.gov/opendata/qb.cfm?category=1)
State-wise average GHG from electricity (kg/kWh)	0- 2.27	
Conventional vehicle miles per gallon (mpg)	24.3	Corporate Average Fuel Economy (CAFÉ) Standard
HEV mpg	44.4	Sales-weighted average of 2016 model year vehicles with sales in 2015: 2015 sales from "U.S. HEV Sales by Model" 2015 sales from "U.S. PHEV Sales by Model" 2015 sales from "U.S. PEV Sales by Model" (https://www.afdc.energy.gov/data/vehicles.html); MPGs from 2016 Fuel Economy Guide (https://www.fueleconomy.gov/feg/)
PHEV mpg	37.9	
PHEV: Energy required per mile (kWh/miles)	0.367	
PHEV All-electric range (miles)	33	Estimate based on the industry standard, SAE J2841 (www.avt.inel.gov/pdf/EVProj/EVProjectUtilityFactorVolt.pdf)
EV: Energy required per mile (kWh/miles)	0.32	
PHEV annual miles driven on electricity (%)	55%	Transportation Energy Data Book #34, , Table 8.1 (www.cta.ornl.gov/data/download34.shtml); Total vehicle miles travelled divided by vehicles in operation, 2013
Average annual vehicle miles driven (miles)	11,824	

Appendix B: Economic and CO₂ Emission Benefits of Solar Charging of EVs

This appendix is based on:

G. R. Chandra Mouli, M. Leendertse, V. Prasanth, P. Bauer, S. Silvester, S. van de Geer, and M. Zeman, "Economic and CO₂ Emission Benefits of a Solar Powered Electric Vehicle Charging Station for Workplaces in the Netherlands," in *2016 IEEE Transportation Electrification Conference and Expo (ITEC), 2016*, pp. 1–7

B.1. Introduction

The success of any new technology is determined by its economic prospects. In chapter 6, the economic benefits of smart charging were reviewed, and it was shown how smart charging of EV from PV could lead to a substantial cost reduction. Even without smart charging, solar charging of EV is cheaper than charging EV from the grid. Further, the use EVs as against gasoline/diesel cars leads to significant reduction in fuel costs and reduction in CO₂ emissions when compared to fossil fuel powered vehicles. This appendix makes a simple economic evaluation for the use of gasoline/diesel cars in the Netherlands when compared to EVs and evaluate the benefits of solar charging of EVs as against charging from the grid.

B.2. Gasoline Vs. electric vehicles

B.2.1. Fuel costs and taxes

The annual kilometres driven by a car in the Netherlands on an average is 20,000km (for cars >1500Kg weight which is typical for EV) [1]. This corresponds to a daily distance of 55km/day. With approximately 260 working days a year, 14,300km are driven on days going to the workplace. A major component of this is daily commuting to work which comprises 45km/day or ~80% of the daily distance driven [2].

The cost of using a gasoline car for daily commuting to the workplace on workdays is summarized in Table B.1. The yearly cost of fuel amounts to €2,013/year on average. The price of gasoline is taken as 1.69€/L, and the vehicle is assumed to drive 100km with 8.33L of fuel. With respect to CO₂ emissions, the average emission of new cars sold in the Netherlands is 119g/km, 109g/km and 107g/km for 2011, 2012 and 2013 respectively [3]. For 14,300 km of commuting distance a year, this results in CO₂ emissions of 1.8 tons/year as shown in Table B.2. In reality, the emissions are much higher considering two factors. Firstly, there is a mix of new and old cars on the road, with the older cars having much higher levels of emissions. Secondly, the cars normally have higher emission during usage when compared to emission values

Table B.1. Cost of Gasoline vehicle, Grid charged and Solar charged electric vehicle

	Fuel car	Grid charged	Solar charged	Solar carport
Annual distance (km)	14,300	14,300	14,300	14,300
Fuel price (€/l or €/kWh)	1.69	0.23	0.10	0.28
Fuel per 100 km (l or kWh)	8.33	15	15	15
Fuel/year (l or kWh)	1,191	2,145	2,145	2,145
Fuel costs/ year	€ 2,013	€ 493	€ 215	€ 601
Saving/year for 1 car	€ 0	€ 1,520	€ 1,798	€ 1,412
Savings for 10 years for 4 cars	€ 0	€ 60,800	€ 71,920	€ 56,480
Extra Investment for 4 EV	€ 0	€ 40,000	€ 40,000	€ 40,000
Total benefit 10 years, 4 cars	€ 0	€ 20,800	€ 31,920	€ 16,480

obtained during testing [4]. If a typical car (not new) is considered, then the emissions are 163 g/km for petrol cars and 156g/km diesel cars [5].

The annual costs of using the gasoline car in Table B.2 excludes the annual motor taxes and vehicle tax paid during vehicle purchase, which are fully based on CO₂ emissions of the car as per Dutch regulations [6]. For example, the owner of a 1500kg gasoline car in South Holland has to pay €912 annual motor taxes (*Motorrijtuigenbelasting*) as shown in Table B.2. From 2016, this tax is zero if you own an EV and is reduced by 50% if the CO₂ emissions of the vehicle are less than 50g/km. In the same way, the vehicle tax paid during the purchase of a car (*bpm* tax) is directly proportional to the CO₂ emissions of the car as shown in Fig. B.1. For example, the taxes to be paid when buying a car with 109g/km emission is €2884, while for a car with 180g/km emission, the taxes are €15,997. In case of an EV, the taxes are zero. For a diesel car, an additional fuel surcharge corresponding to an emission of 86€ per 1g/km of CO₂ emissions applies when the emission is over 67g/km. These aggressive emission based vehicle taxes have made the Netherlands the leading country in Europe with respect to lowest average CO₂ emissions of newly sold cars [3].

On the other hand, an EV costs an average €10,000 more than the corresponding gasoline vehicle in the Dutch market with respect to size and comfort. But the costs of charging the EV are much lesser than using gasoline. For example, the NEDC driving range of the Tesla Model-S (85kWh) and Nissan Leaf (24kWh 2013) is 500km and 200km respectively. This corresponds to a fuel use of 12kWh and 17kWh for the Leaf and Model-S respectively for driving 100km.

With 0.23€/kWh electricity price in the Netherlands and fuel use of 15kWh for 100km, it corresponds to €493 fuel cost per year for driving 14,300km as shown in Table B.1. As mentioned earlier, the EV owner gets an additional financial benefit via zero annual vehicle taxes compared to gasoline cars, which is close to 1000€ giving a net benefit of ~€2500/year in operational costs.

B.2.2. CO₂ emissions

While most people assume that the CO₂ emissions of an EV are zero, this is not the case in reality. This is because electricity production by itself results in CO₂ emissions. This is particularly the case in the Netherlands where large amounts of fossil fuels like natural gas are used in power production. This results in a net CO₂ emission of 470g/kWh as per 2012 estimates [7]. If the energy use of EV is taken to be 15kWh for 100km, this results in a net CO₂ emission of 70.5g/km. This is similar to the estimate of 35-77g/km calculated in [8]. So, if the gasoline and EV vehicle usage are compared, the benefits of using EVs:

1. An annual saving of € 1,520 just based on fuel costs
2. CO₂ emissions are reduced on an average by 38.5g/km based on fuel usage. This results in annual CO₂ emission reduction of 551kg/car/year for the distance of 14,300km and 770kg/car/year for the total 20,000km driven per year.
3. Tax benefits in the form of zero vehicle taxes for EVs

Considering four EV used over a period of ten years, the net benefit is €60,800. without considering maintenance cost and tax benefits as shown in Table B.1 (It will be explained later why four EV are taken as reference). In the Dutch market, an EV typically costs €10,000 more than the corresponding gasoline vehicle. If this cost is considered, the net benefit for four cars is €20,800 as shown in Table B.1. If tax benefits are considered, the gain will be an additional $(2844+912)*10=11,964€$ per car and 47,856€ for four cars. This shows the lifetime economic and environmental

Table B.2. CO₂ emissions and taxes when using Gasoline vehicle, Grid and Solar charged EV

	Gasoline car	Grid charged	Solar charged	Solar carport
Motor Taxes/year	€ 912	€ 0	€ 0	€ 0
Vehicle purchase tax	€ 2884	€ 0	€ 0	€ 0
Tax benefit (PV, EV)	No	MIA/KIA/EIA		
CO ₂ emission (g/km)	109	70.5	0	0
CO ₂ emission for 14,300 km (kg/yr)	1559	1008	0	0
CO ₂ emission for 20,000 km (kg/yr)	2180	1410	0	0

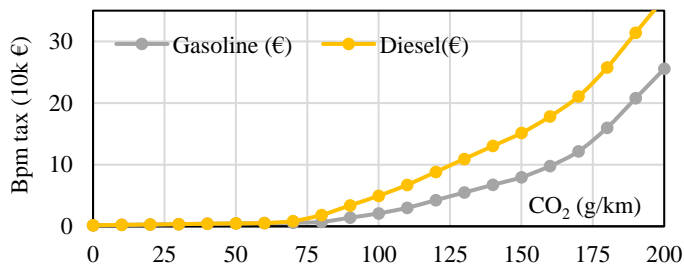


Fig. B.1. Dutch Bpm purchase tax of EV as based on rated CO₂ g/km emissions of the car with an additional surcharge for diesel cars.

benefits of using an EV over gasoline vehicles in the Netherlands. With increased driving range, improved charging infrastructure and lower cost of EV, these advantages are only bound to increase.

At the same time, one must keep in mind the charging infrastructure for EVs is not built yet and hence there is a range anxiety with the use of EVs due to limited battery size and range. Secondly, the tax benefits and subsidies given to EVs will eventually be removed once the ownership of EVs reaches a tipping point. Finally, the procurement of materials for batteries and the recycling of EVs batteries will play a key economic and environmental role in the future.

B.3. Solar generation in working hours

The main benefit of solar charging of EV is it results in zero CO₂ emission unlike gasoline vehicles or EV charged from the grid. At the same, a second and more compelling advantage is that the cost of PV electricity is less than half of that of conventional electricity from the grid in the case of a country like the Netherlands.

The PV generation data for the Netherlands, estimated in Chapter 3, is used here

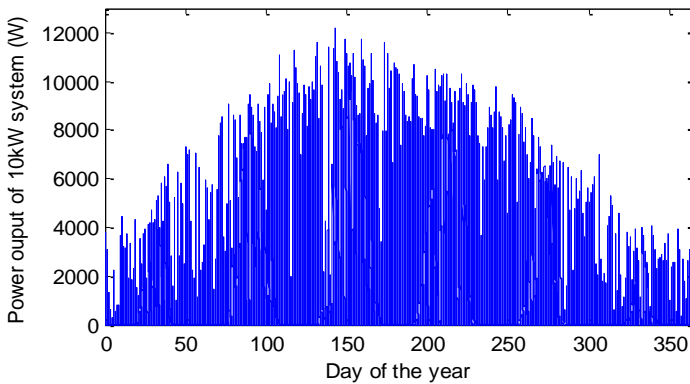


Fig. B.2. Power output of 10kW PV system for 2013 (South facing, 28° tilt)

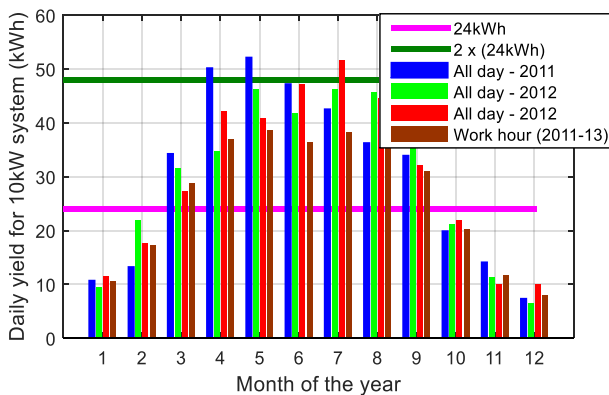


Fig. B.3. Average daily yield of 10kW PV system for different months for 2011-2013

Table B.3. Annual energy yield of 10kW PV system with 28° tilt

	2011	2012	2013	Avg.
Annual yield of PV, E_y (kWh) [A]	11039	10753	10876	10890
Annual yield in working hours, $E_{y(wh)}$ (kWh) [B]	9682	9469	9541	9564
Annual yield in working hours on weekdays, $E_{y(wh)}^{wk}$ (kWh) [C]	6915	6763	6815	6831
% of energy [B/A*100] (%)	87.7	88.0	87.7	87.8
% of energy [C/A*100] (%)	62.6	62.8	62.6	62.7

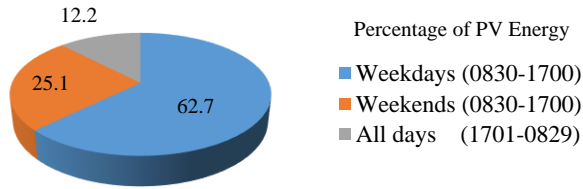


Fig. B.4. Pie chart showing the percentage of annual PV energy production during working and non-working hours (830h-1700h) on weekdays and weekends

for the economic analysis. A 10kW_p PV system orientated at an optimal orientation of azimuth $A_m=0^\circ$ (i.e., facing south) and tilt angle $\theta_m=28^\circ$ is considered. It can be concluded that this optimal orientation results in maximum energy yield over the year.

Fig. B.3 and Fig. B.3 are repeated here from Chapter 3. Fig. B.3 shows the power output of the 10kW PV array with 1 min data resolution, showing the seasonal variation in power output from January to December. Fig. B.3 shows the average daily energy yield of the system for different months. The annual energy yield (E_y) for 2011-2013 period is indicated in Table B.3 and the average is $E_y=10,890\text{kWh}/\text{year}$. It must be remembered that the calculations above have not considered shading due to nearby buildings/trees and installation in non-optimal orientations [9], [10]. The yield would then be appropriately lower based on the location characteristics.

For EV charging from PV, what is vital is the daily PV energy yield during working hours. Here the working hours is considered as the period between 0830hr to 1700hr. Using the model developed, the estimated annual energy yield in the working hours is $E_{y(wh)}=9564\text{kWh}/\text{year}$, which corresponds to 87.8% of the total energy yield of the year as seen in Table B.3. This goes to show the huge potential of charging the EV from PV. However, a small part of this energy cannot be used for EV charging, if the EVs are available at workplace only on weekdays and not on weekends.

Then, the energy available for charging EV from PV during work hours on weekdays is $E_{y(wh)}^{wk}=6831\text{kWh}/\text{year}$ which is 62.7% of annual yield as shown in Fig. B.4. The percentage would be slightly different if the working hours considered are different, for example working hours are 09:00- 18:00. This variability is not considered here as it changes based on factors like company, location or weather.

B.4. Charging EV from Rooftop PV or PV carport

B.4.1. PV system cost

Based on the metrological conditions in the Netherlands, it was shown in Chapter 3 that a 13kW PV array could be connected to a 10kW inverter resulting in only 3% energy loss in the year. Therefore, a higher peak power PV array can be connected to smaller power rated inverter with minimal losses due to non-MPPT operation [11]. Using a 13kW PV system connected to a 10kW EV-PV charger, 13449 kWh/year is produced in the working hours assuming 5% system losses, as shown in Table B.4. The corresponding revenues generated from PV energy is 3093€/year based on the retail residential electricity price of 0.23€/kWh when net metering is considered.

To install the solar panels for charging the EVs, two options exist: installing the PV on the rooftop or as a solar carport. The most cost-efficient solution is to place the panels on a roof of the office/factory building as it only requires low-cost racks for mounting. On the other hand, the cost of construction of a carport is much higher than a rooftop installation. Solar carports have the advantage that it has proximity to the EV making the transmission losses lower, it provides shade for the car and creates a ‘green’ image for the workplace. But they also have the disadvantage that the carport suffers from shading losses owing to the shading from nearby objects such as trees, buildings and lampposts.

In terms of cost, PV panels are sold in the Dutch market at 0.75-1 €/W_p, inverters for 0.15-0.25€/W_p and rooftop mounting kits for 30€/panel [12], [13]. Based on these costs, the cost of a 13kW PV system is 19,700€ as shown in Table B.4 considering the worst case price of 1€/W_p for PV and 0.25€/W_p for the inverter. In comparison, the cost of a solar carport like Orion, Upsolar or Schletter is priced between 2500€-5000€/kW for the physical construction based on the type of structure and material used [13], [14]. For the solar carport developed in [15], the estimated cost of

Table B.4. Annual revenue from Energy of 13kW PV (5% losses)

	Energy (kWh)	Revenue (€)
Full year	13449	3093
Working hours	11812	2717
Weekdays working hours	8436	1940

Table B.5. Cost of 13kW PV Rooftop system & Carport

	Unit cost (€)	Quantity	Cost (€)	Cost (€)
330W PV module	330	40	13,200	13,200
10kW PV inverter	2,500	1	2,500	2,500
Replacement inverter	2,500	1	2,500	2,500
Module mounting	30	50	1,500	0
Solar carport 13kW	39,000	1	0	39,000
Total Cost			19,700	57,200

construction was in the range of 2300€-3250€/kW. For this section, a mid-value of 3000€/kW is used for the calculations in Table B.5 for the cost of the solar carport. A 13kW solar carport will hence cost 57,200€, nearly three times as expensive as the rooftop installation.

B.4.2. PV electricity cost

Based on Table B.4 and Table B.5, the cost of the energy generated from PV can be estimated assuming a 15 year lifetime for the PV system. In general, PV panels have a warranted life of 20-25 years with a gradual reduction in performance. Fifteen years is chosen here as a conservative average during which period the decrease in PV performance is neglected. In the 15 years, an inverter would need to be replaced considering its lower lifetime with respect to the panels and this cost has been included in the lifetime costs. This corresponds to an electricity price C_{PV} over the 15 year period of 0.097€/kWh and 0.283€/kWh for the rooftop PV and solar carport respectively, as shown in Table B.6. Further, these costs are reducing as well.

B.4.3. Solar charging of EV

With 8436 kWh of PV energy available per year on weekdays during office hours, the number of times a Nissan Leaf (24kWh battery) and Tesla Model-S (85kWh battery) can be fully charged, and the total distance that can be driven on solar energy is shown in Table B.6. Thus, solar charging at the workplace can provide annual charging capability for 70,300 km for a Nissan Leaf and 49,625km for a Model-S. This is a substantial number considering that the average amount of kilometres driven by a car on workdays is 14,300km as mentioned earlier. So the energy produced by a 13kW PV system is sufficient to match the driving needs of five small EV like Leaf and three large EV like Tesla Model S for travel requirements on working days. This explains why four EV were chosen for comparison with gasoline vehicles in Table B.1. The number will remain the same if the working days are considered to be 7 days/week where the additional PV production in the weekend will match the

Table B.6. Cost of Electricity from 13kW Solar Rooftop and Carport

	Cost of System (€)	Energy (kWh/year)	Electricity Cost (€/kWh)
Rooftop PV	19,700	13,448	0.097
Solar carport	57,200	13,448	0.28
Grid	-	-	0.23

Table B.7. Number of EV that can be charged by 13kW PV @ workplace considering charging during working hours on weekdays

Energy	EV	kWh/100km	Full charges per year	Distance (km/year)	Cars/year
PV Energy 8436 kWh	Leaf	12	351 of 24kWh	70,300	4.91
	Model S	17	99 of 85kWh	49,625	3.46
Grid Capacity 22100 kWh	Leaf	12	920 of 24kWh	184,000	12.87
	Model S	17	260 of 85kWh	130,000	9.09

corresponding EV demand.

If only the capacity of the EV charger of 10kW is considered then, $10\text{kW} \cdot (8.5\text{h} \cdot 260\text{days}) = 22,100\text{kWh}$ of energy can be delivered by the system over the year. 8,436 kWh or 38% of this energy will be from solar energy. The number of times each of the cars can be fully charged, and total distance that can be driven using the full 10kW capacity is shown in Table B.6 exhibiting the possibility to charge nine to thirteen EVs every day. It must be kept in mind that the PV production has a seasonal dependence, so the same amount of ‘solar’ miles is not spread evenly throughout the year but can only be realized over an annual basis.

To compare the economics of grid charging and solar charging, the electricity price from solar is 0.097€/kWh which is less than half of the grid price of 0.23€/kWh. This difference in electricity price leads to a reduction in fuel costs per year by more than half, from €493 to €215 as seen in Table B.1. However, the larger benefit of solar charging is that the CO₂ emissions are completely zero as the electricity is itself produced from a renewable source. The emissions reduce from 109g/km and 70.5g/km for gasoline and grid charged EV to 0g/km for solar-charged EV. Further, the energy from a solar carport is 0.05€/kWh more than the grid prices which could be very attractive where the application derives benefits from the car shade and aesthetic appeal. The dual benefit of lower fuel cost and emission make EV charging from PV to be both economical and environmentally beneficial compared to grid charging. Further, the installation of PV and use of EV can provide additional tax and governmental benefits in the form of *Milieu-investeringsaftrek*(MIA), *Energie-investeringsaftrek*(EIA) and *Kleinschaligheids-investeringsaftrek* (KIA) in the Netherlands.

B.5. Impact of Feed-In Tariffs

There has been a renewed push towards motivating users to increase their self-consumption of PV power. This is due to problems in the grid due to large-scale PV generation in the form of overvoltage, overloading of lines and reverse flow [16]. Secondly, wholesale energy prices (0.02-0.04€/kWh) are much lower than the retail prices (0.23€/kWh) which has caused grid operators to reduce feed-in tariffs for PV to a value much lower than retail prices [17], [18]. Fig. B.5 shows the revenues from PV generation which are obtained for different feed-in tariffs ranging from 0-0.40€/kWh. The revenues of the show a big variation ranging from 0 - 5380€/year based on the feed-in tariff. The effect of local load consumption of the workplace on the PV revenues is not considered here so as to consider the PV charging station as an independently metered entity.

With the introduction of EV charging for 7days/week during work hours, 11,812kWh or 87.8% of PV electricity can be annually diverted for EV charging which would have otherwise been purchased from the grid for 2717€ at 0.23€/kWh. With an indirect revenue of 2717€ for the PV from EV charging, only the remaining PV energy is fed back to the grid (12.2%) resulting in improved PV revenues when the feed-in tariff is <0.23€/kWh as seen in Fig. B.5. If EV charging is done only on weekdays during work hours, 8436kWh or 62.7% of PV electricity can be annually

used for EV charging which values to €1940 as shown in Table B.4. Due to lower self-consumption, the revenues are lower than the 7day/week but much higher than having a PV system with no EV charging integrated.

It can thus be seen that by charging EV from PV, the PV self-consumption is increased preventing the economic losses due to the lower feed-in tariff. Secondly, demand charges at the workplace can be avoided if there is no seasonal variation in PV generation and part of the EV charging power is consistently supplied by PV.

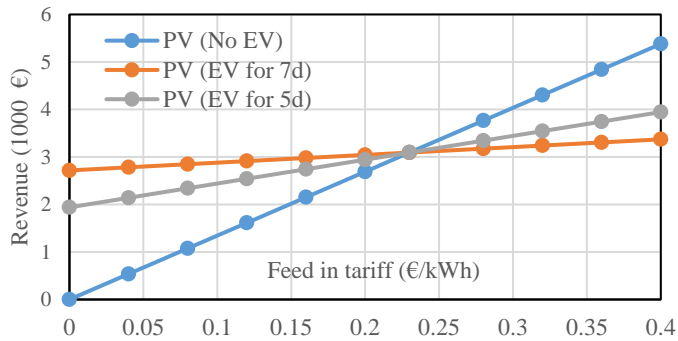


Fig. B.5. Annual PV revenues as a function of feed-in tariffs with/without EV charging for a 13kW PV system in the Netherlands, assuming no local load consumption

B.6. Assumptions and limitations of the model

It must be noted that the results obtained in this economic analysis are directly dependent on the assumptions made for EVs, gasoline cars and PV system like cost, fuel economy, emissions, energy mix, energy prices and current tax law. The variability in these values has not been considered in this study and can be expanded using a sensitivity analysis. Further, the factors relating to maintenance costs, insurance, depreciation, the rate of interest and downtime costs that provide the Total Cost of Ownership (TCO) of gasoline car and EV have not been included in this study as well. The maintenance costs of EV are generally much lower than that of fossil fuel vehicles due to a lower number of moving parts and the absence of a combustion engine and liquid fuel.

B.7. Conclusions

The economic benefits and CO₂ emission reduction of a solar-powered EV charging station for the Netherlands have been analyzed. Driving an electric vehicle instead of a gasoline car to work every day results in an annual saving of €1,520 just based on fuel costs and CO₂ emissions are reduced on an average by 38.5g/km. based on the current electricity energy mix in the Netherlands, this results in an annual CO₂ emission reduction of 770kg/car/year for a distance of 20,000km. Further, the purchase tax and annual car taxes are zero for an electric as against tax €2844 and €912 respectively for a gasoline car of 1.5ton weight and 109g/km of CO₂ emissions.

While EVs are cleaner than a gasoline car, their usage still results in 70.5g/km of CO₂ on average because the Dutch energy mix for power production is primarily based on fossil fuels with 470g/kWh of CO₂ emission.

A truly sustainable way of driving is hence to charge an EV using solar energy. This results in zero CO₂ emission. The electricity price from PV is 10c/kWh, which is less than half of the current grid price of 23c/kWh. Using a 13kW PV, 13448 kWh/year is produced during the working hours. This can provide annual charging capability for 70,300km for Nissan Leaf and 49,620km for a Tesla Model-S. EV charging promotes the self-consumption of PV, and this results in increased PV revenues when feed-in tariffs are lower than retail electricity price. Thus the dual benefit of lower fuel cost and emission make EV charging from PV to be both economical and environmentally beneficial.

B.8. References

- [1] "Traffic Performance of personal cars - ownership, fuel, weight, age," *Cent. Bur. Stat. - Netherlands*, 2012.
- [2] J. Harikumar, G. Vereczki, C. Farkas, and P. Bauer, "Comparison of quick charge technologies for electric vehicle introduction in Netherlands," in *IECON Proceedings (Industrial Electronics Conference)*, 2012, pp. 2907–2913.
- [3] "CO₂ emissions per vehicle kilometer from new passenger cars 1998-2013," *Cent. Bur. Stat. - Netherlands, Den Haag; Planbur. voor Leefomgeving, Den Haag; Wageningen UR, Wageningen*, 2014.
- [4] N. E. Ligterink and A. R. A. Eijk, "Update analysis of real-world fuel consumption of business passenger cars based on Travelcard Nederland fuelpass data," 2014.
- [5] O. P. R. van Vliet, T. Kruitthof, W. C. Turkenburg, and A. P. C. Faaij, "Techno-economic comparison of series hybrid, plug-in hybrid, fuel cell and regular cars," *J. Power Sources*, vol. 195, no. 19, pp. 6570–6585, 2010.
- [6] "Belasting - Motorrijtuigenbelasting en Bpm," *De Belastingdienst, Netherlands*, 2015.
- [7] "Efficiencies and CO₂ emissions from electricity production in the Netherlands, 2012 update," *Cent. Bur. Stat. - Netherlands*, 2014.
- [8] O. Van Vliet, A. S. Brouwer, T. Kuramochi, M. Van Den Broek, and A. Faaij, "Energy use, cost and CO₂ emissions of electric cars," *J. Power Sources*, vol. 196, no. 4, pp. 2298–2310, 2011.
- [9] O. Isabella, G. G. Nair, A. Tozzi, J. H. Castro Barreto, G. R. Chandra Mouli, F. Lantsheer, S. van Berkel, and M. Zeman, "Comprehensive modelling and sizing of PV systems from location to load," *MRS Proc.*, vol. 1771, pp. 1–7, Apr. 2015.
- [10] V. V. Ashok, C. Onwudinanti, G. R. Chandra Mouli, and P. Bauer, "Matching PV Array Output With Residential and Office Load by Optimization of Array Orientation," in *PowerTech (POWERTECH), 2015 IEEE Eindhoven*, 2015, pp. 1–6.
- [11] B. Burger and R. R  ther, "Inverter sizing of grid-connected photovoltaic systems in the light of local solar resource distribution characteristics and temperature," *Sol. Energy*, vol. 80, no. 1, pp. 32–45, 2006.
- [12] "Solar MetDeZon," www.zonnepanelen.nl, 2015.
- [13] "Energy Limburg," www.energylimburg.nl, 2015.
- [14] "Commercial Solar Carports Systems," www.solarelectricsupply.com, 2015.
- [15] M. Leendertse, "MSc thesis - Solar powered charging station for electric cars- conductive

- and wireless inductive,” Delft University of Technology, 2015.
- [16] G. R. Chandra Mouli, P. Bauer, T. Wijekoon, A. Panosyan, and E.-M. Barthlein, “Design of a Power-Electronic-Assisted OLTC for Grid Voltage Regulation,” *IEEE Trans. Power Deliv.*, vol. 30, no. 3, pp. 1086–1095, Jun. 2015.
- [17] R. Cherrington, V. Goodship, A. Longfield, and K. Kirwan, “The feed-in tariff in the UK: A case study focus on domestic photovoltaic systems,” *Renew. Energy*, vol. 50, pp. 421–426, Feb. 2013.
- [18] T. Couture and Y. Gagnon, “An analysis of feed-in tariff remuneration models: Implications for renewable energy investment,” *Energy Policy*, vol. 38, no. 2, pp. 955–965, Feb. 2010.

Appendix C: Estimation of ripple and inductance of powdered alloy core inductors

This appendix is based on:

G. R. Chandra Mouli, J. Schijffelen, P. Bauer, and M. Zeman, "Estimation of ripple and inductance roll off when using powdered iron core inductors," in *Proc. Power Convers. Intell. Motion (PCIM) Eur.*, May 2016, pp. 1–8

C.1. Introduction

Inductors are widely used in DC/DC converters as an energy storage element and as a filter. The inductance L can be related to the number of turns of the copper wire N , core material and the dimensions of the core by

$$L = \left(\frac{\mu_0 \mu_r A_c}{l_e} \right) N^2 = A_L N^2 \quad \text{where} \quad A_L = \left(\frac{\mu_0 \mu_r A_c}{l_e} \right) \quad (1)$$

where $\mu_0 = 4\pi \times 10^{-7}$, μ_r - relative permeability of the material, A_c - core area, l_e - magnetic path length, A_L is permeance of the material.

When a DC voltage V_L is applied across the inductor, the current through the inductor i_L linearly increases/decreases based on the sign of the voltage where $i_{L(0)}$ is the inductor current at time $t=0$, Δi_L is the current ripple in time Δt :

$$V_L = L \frac{di_L}{dt} \quad (2)$$

$$\Delta i_L = i_L(t) - i_{L(0)} = \frac{V_L}{L} \Delta t$$

When inductors are designed using ferrite cores, the core exhibits a practically constant permeability and permeance in the operating region. This is because it has a fixed air gap and the reluctance of the core is primarily characterized by this air gap, as seen in Fig. C.1(a). This means that the inductance does not vary with the magnetic field strength generated by the inductor coils in the operating region. When the core is close to saturation, then there is a rapid change in inductance from its initial value to zero as shown in Fig. C.1(c) [19], when μ_r reduces from its initial value to zero.

C.1.1. Inductors with variable permeability

Powdered iron cores come under the category of distributed air gap cores. They have small air gaps distributed evenly throughout the cores, as seen in Fig. C.1(b). There are a number of powder iron cores that are commercially available – for example Kool M μ ®, MPP, High Flux, XFlux®, AmoFlux® cores from magnetics or powder cores from Micrometals. These cores differ from ferrite cores in a number of ways.

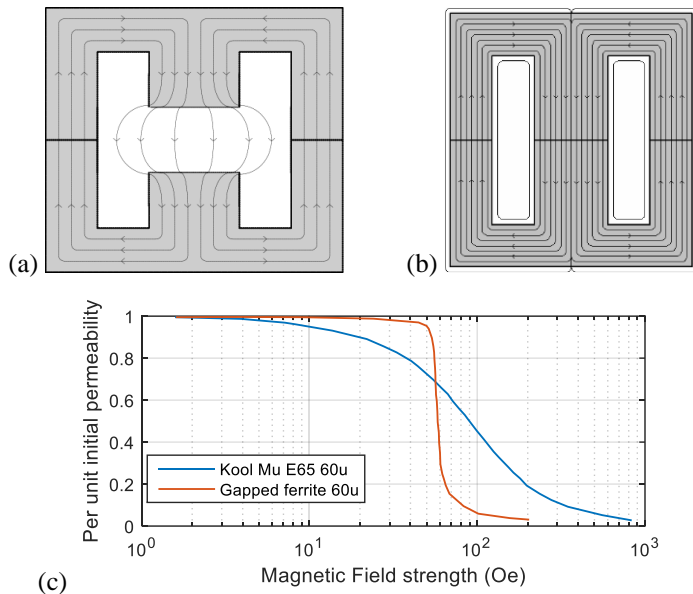


Fig. C.1. Path of flux lines through a (a) gapped ferrite core and (b) a powdered iron core. (c) Variation of permeability of core as a function of magnetic field strength for a KoolM μ powdered iron core and gapped ferrite core, both of which have an initial permeability of $\mu_r=60$ (bottom) [19]

1. The permeability of the core is dependent only on the core material. Powdered iron core thus have a 'fixed' distributed air gap. This is unlike ferrites where the air gap and number of turns can be varied for the same inductance to give the least inductor losses.
2. The powdered iron cores have a higher saturation flux density B_{sat} which can be more than twice as that of ferrite cores [20]. 60μ KoolM μ , Epcos N87 ferrite cores have a B_{sat} of 1000mT and 490mT respectively [21]. This means that fewer parallel core sets would be required to build high current inductor in high power density converters [22]–[24].
3. With the increase in magnetic field strength, the small pieces of powdered iron gradually saturate one after the other starting with the smallest piece of iron. The process is called soft saturation [25]. This results in the permeability of the core to slowly reduce with increase in inductor current [26], as seen in Fig. C.1(c) and Fig. C.2.
4. There is no fringing flux in the air gap, unlike ferrite cores as seen in Fig. C.1(a). This eliminates additional copper losses in the winding at high frequencies.
5. Powdered iron cores have much higher core losses when compared to ferrites, by a factor of ten to fifty times depending on the manufacturer and operating currents [20].

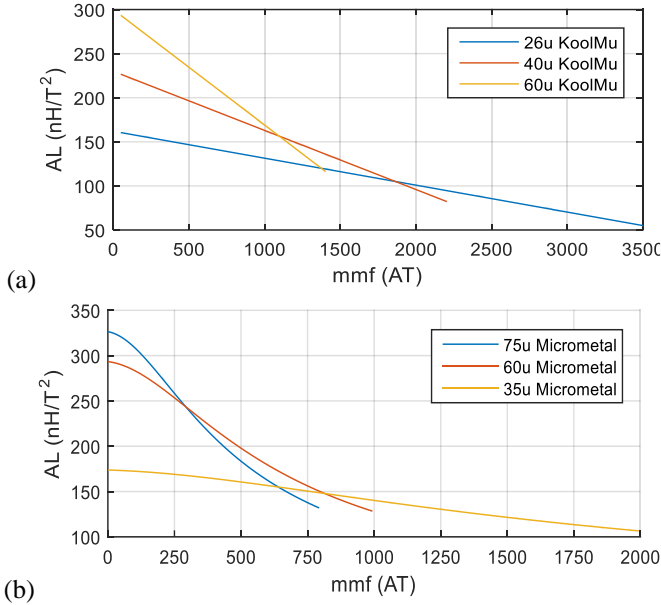


Fig. C.2. Permeance AL of three core of different permeability as a function of the ampere-turns for (a) KoolM μ E65 and (b) Micrometal E-255. The permeance and inductance of the core reduce linearly with increase in current through the inductor.

C.1.2. Mathematical formulation for variable permeance

Due to the soft saturation, the permeance of the core depends on the magnetic field strength. With the increase in the ampere-turns, the permeance reduces gradually. While this dependency is largely non-linear, the variation can be linearized in the operating region of the inductor, as shown in Fig. C.2 for a KoolM μ E65 core of permeability 26 μ , 40 μ , 60 μ and a Micrometal core of permeability 35 μ , 60 μ and 75 μ . The inductance variation can be expressed by (3), where A_{L0} is the permeance at zero ampere-turns and M_L is the slope of the permeance (or permeability) variation as a function of ampere-turns. As a result, the inductance L linearly varies with inductor current i_L given by (4) where L_0 is the inductance at zero current and K_L is the slope of inductance reduction with current. K_L and M_L can hence be related by N^3 :

$$A_L = A_{L0} - M_L(Ni_L) \quad (3)$$

$$L = L_0 - K_L i_L \quad (4)$$

$$K_L = N^3 M_L \quad (5)$$

It is common that manufacturers provide information regarding the variation of permeance with ampere-turns as shown in Fig. C.2. Since the inductance continuously varies with current, it has two important effects.

1. The slope of the current varies with time, and this causes non-linear currents through the inductor, unlike what is found in ferrites.

2. Secondly, the reduction in inductance necessitates the oversizing of inductance so that there is sufficient inductance L_{min} at the maximum inductor current [26].

C.2. Ripple and inductance roll-off for variable permeability cores

For DC/DC converters especially boost, buck, buck-boost and flyback converters, two modes of operation are possible - continuous conduction mode (CCM) and discontinuous conduction mode (DCM). In both modes, there is a current ripple ΔI_L through the inductor and in case of CCM, there is a continuous average DC current through the inductor $I_{L(avg)}$. Fig. C.3 shows the inductor current waveforms for a boost converter where D is the duty cycle [27].

$$\text{In CCM,} \quad I_{L(max)} = I_{L(avg)} + \Delta I_L/2 \quad (6)$$

$$I_{L(min)} = I_{L(avg)} - \Delta I_L/2 \quad (7)$$

$$\text{In DCM,} \quad I_{L(min)} = 0; \quad I_{L(max)} = \Delta I_L \quad (8)$$

The current ripple ΔI_L is dependent on the inductance as shown in (2). However, when using powdered iron cores, the inductance is itself is dependent on the current through it. This interdependency makes it difficult to directly calculate the either the inductance or the ripple, as in (2). This also means that the determination of the inductor cores losses will be inaccurate as the core losses depend on the ripple estimation [20] and the corresponding peak-peak variation in flux density ΔB , as given by the Steinmetz equation

$$P_{core} = A f_{sw}^a B_{pk}^b V_e \quad (9)$$

$$B_{pk} = \frac{\Delta B}{2} = \mu_0 \mu_r \frac{\Delta H}{2} = \frac{\mu_0 \mu_r}{2} \left(\frac{N \Delta I_L}{l_e} \right) \quad (10)$$

where V_e is volume of core, A,a,b are the Steinmetz parameters, f_{sw} is the switching frequency and $B_{pk} = \Delta B/2$. (Even though the Steinmetz equation is applicable for sinusoidal inductor currents, in the above situation it is being approximated for DC application). In order to manage the interdependency between inductance and inductor current when using cores with variable permeability and to determine both the parameters, four approaches can be made:

1. Considering no inductance variation

This case is similar to the case of ferrites. Without considering inductance reduction due to ampere-turn, the inductance will be the estimated by setting $K=0$ in (4). The inductance will be the highest at $L=L_0$, and the estimated ripple will be the lowest, as shown in (11) and (12). This method will lead to under-sizing of the inductor with respect to the actual design requirements and underestimation of the inductor ripple and core losses.

$$L = L_0, \quad K_L = 0 \quad (11)$$

$$\Delta I_L = \frac{V_L}{L_0} \Delta t \quad (12)$$

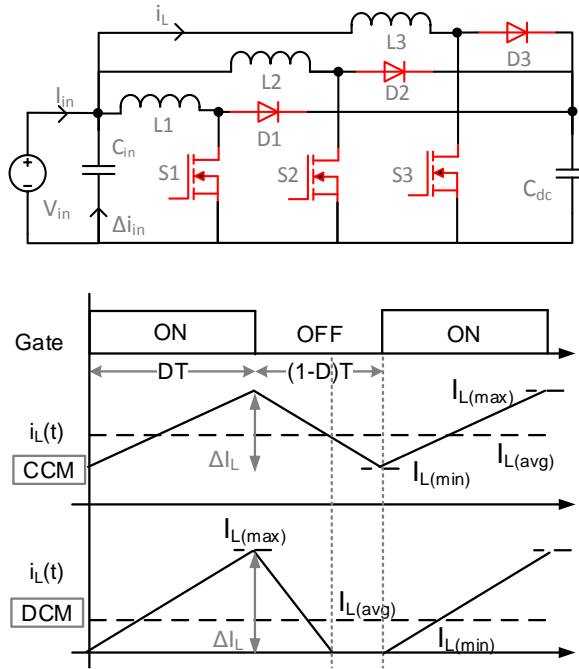


Fig. C.3. The topology of interleaved boost converter used for experimental verification (top). Inductor current with ripple for a boost converter operating in CCM and DCM modes (bottom)

2. Using peak current $I_{L(max)}$ to determine the inductance

In this method, the peak inductor current is used to determine the operational inductance. Using (12), the inductor ripple is estimated assuming no inductance variation. Then using equations (6),(7),(8) and based on the mode of operation, the maximum inductor current $I_{L(max)}$ can be determined. The operational inductance and actual ripple can be estimated as:

$$L_{min} = L_0 - K_L I_{L(max)} \quad (13)$$

$$L_{max} = L_0 - K_L I_{L(min)} \quad (14)$$

$$\Delta i_L = \frac{V_L}{L_{min}} \Delta t = \frac{V_L}{L_0 - K_L I_{L(max)}} \Delta t \quad (15)$$

Estimating the ripple based on $I_{L(max)}$ will give the lowest possible value of inductance and overestimation of the ripple and the core losses. In practice, the measured ripple will be lower than that estimated by (15) but higher than that estimated by (12). This is because, as the current increases from $I_{L(min)}$ to $I_{L(max)}$, the inductance will reduce from L_{max} to L_{min} . Estimating the ripple based on $I_{L(max)}$ will hence lead to over-sizing the required size of passive filters and overestimating the core losses.

3. Using middle current $I_{L(mid)}$ to determine the inductance

Based on the above argument, a simple way to consider the inductance variation is to use the inductor middle current, $I_{L(mid)}$. Using (12), the inductor ripple is estimated assuming no inductance variation. Then using equations (6),(7),(8) and based on the mode of operation, the middle inductor current $I_{L(mid)}$ can be determined by (16):

$$\begin{aligned} \text{For CCM,} \quad & I_{L(mid)} = (I_{L(max)} + I_{L(min)})/2 \\ & I_{L(mid)} = I_{L(avg)} \end{aligned} \quad (16)$$

$$\begin{aligned} \text{For DCM,} \quad & I_{L(mid)} = \Delta I_L / 2 \\ & L = L_0 - K_L I_{L(mid)} \end{aligned} \quad (17)$$

$$\Delta i_L = \frac{V_L}{L_{mid}} \Delta t = \frac{V_L}{L_0 - K_L I_{L(mid)}} \Delta t \quad (18)$$

The operational value of inductance averaged over a time period and the corresponding inductor ripple can be estimated by (17) and (18) respectively. The accuracy of this method is largely dependent on the mode of operation. In CCM with a small ripple Δi_L in relation to the average current, the approximation can be made that $\Delta i_L / I_{L(avg)} \approx 0$. In such a situation, the inductance is largely determined by the DC bias due to the $I_{L(avg)}$. The inductance and ripple can be estimated based on (17) and (18) with high accuracy. However in DCM or BCM, this approximation will never hold true as $\Delta i_L / I_{L(mid)}$ will differ by a factor of two. In such a situation we need to mathematically solve the ripple, inductance dependence as shown in next section.

4. Differential equation for determination of non-linear inductor current

To get an accurate estimation of inductance and ripple when using variable permeability cores, it is essential to mathematically derive the inductance-current dependence. A time-dependent variation of inductance can be written based on (4) as

$$L(t) = L_0 - K_L i_L(t) \quad (19)$$

$$V_L = L(t) \frac{di_L(t)}{dt} = (L_0 - K_L i_L(t)) \frac{di_L(t)}{dt} \quad (20)$$

The inductor current $i_L(t)$ as a function of time can be expressed as a first order non-linear ordinary differential equation shown above. The solution to this differential equation is

$$V_L t = \left(L_0 i_L(t) - \frac{K_L i_L(t)^2}{2} \right) + C_1 \quad (21)$$

Using the initial condition that at $t=0$, $i_L = i_{L(0)}$

$$C_1 = - \left(L_0 i_{L(0)} - \frac{K_L i_{L(0)}^2}{2} \right) \quad (22)$$

Using (22) in (21),

$$\frac{K_L i_L(t)^2}{2} - L_0 i_L(t) + \left(V_L t + L_0 i_{L(0)} - \frac{K_L i_{L(0)}^2}{2} \right) = 0 \quad (23)$$

$$i_L(t) = \frac{L_0}{K_L} - \sqrt{\frac{L_0^2}{K_L^2} - \frac{2}{K_L} \left(V_L t + L_0 i_{L(0)} - \frac{K_L i_{L(0)}^2}{2} \right)} \quad (24)$$

(23) is a quadratic equation in $i_{L(t)}$ and it has two roots. When V_L is positive, current through the inductor increases. So of the two solutions, the negative solution is correct and is shown in (24). The above equation can hence be used to determine the non-linear current through an inductor with variable permeability. The equation is applicable not only to powdered iron cores but to all cores that exhibit a linear variation in permeability with DC bias.

C.3. Ripple and inductance estimation for boost converter

Using a boost converter as an example, the derived mathematical model is applied to both CCM and DCM mode of operation. For DCM, $i_{L(0)} = 0$ as seen in Fig. C.3 and (24) can be written as (25) where $t=DT$ is the ON time of the switch when inductor current increases. Based on this, the ripple $\Delta i_{L(DCM)}$ and the average inductance $L_{avg(DCM)}$ over a time Δt in DCM can be expressed as in equation (26) and (27) respectively:

$$i_L(t) = \frac{L_0}{K_L} - \sqrt{\frac{L_0^2}{K_L^2} - \frac{2V_L t}{K_L}} \quad (25)$$

$$\Delta i_{L(DCM)} = i_{L(max)} = \frac{L_0}{K_L} - \sqrt{\frac{L_0^2}{K_L^2} - \frac{2V_L(DT)}{K_L}} \quad (26)$$

$$L_{avg(DCM)} = \frac{V_L \Delta t}{\Delta i_L} = V_L \Delta t / \left(\frac{L_0}{K_L} - \sqrt{\frac{L_0^2}{K_L^2} - \frac{2V_L \Delta t}{K_L}} \right) \quad (27)$$

For CCM, with $i_{L(0)} = i_{L(min)}$ the switch is ON till $t=DT$ as seen in Fig. C.3. The ripple in CCM $\Delta i_{L(CCM)}$ and average inductance $L_{avg(CCM)}$ over a time Δt can be expressed as:

$$i_L(t) = \frac{L_0}{K_L} - \sqrt{\frac{L_0^2}{K_L^2} - \frac{2}{K_L} \left(V_L t + L_0 i_{L(min)} - \frac{K_L i_{L(min)}^2}{2} \right)} \quad (28)$$

$$\Delta i_{L(CCM)} = i_{L(max)} - i_{L(min)} = \left\{ \frac{L_0}{K_L} - \sqrt{\frac{L_0^2}{K_L^2} - \frac{2}{K_L} \left(V_L(DT) + L_0 i_{L(min)} - \frac{K_L i_{L(min)}^2}{2} \right)} \right\} - i_{L(min)} \quad (29)$$

$$L_{avg(CCM)} = \frac{V_L \Delta t}{\left(\frac{L_0}{K_L} - \sqrt{\frac{L_0^2}{K_L^2} - \frac{2}{K_L} \left(V_L(\Delta t) + L_0 i_{L(min)} - \frac{K_L i_{L(min)}^2}{2} \right)} - i_{L(min)} \right)} \quad (30)$$

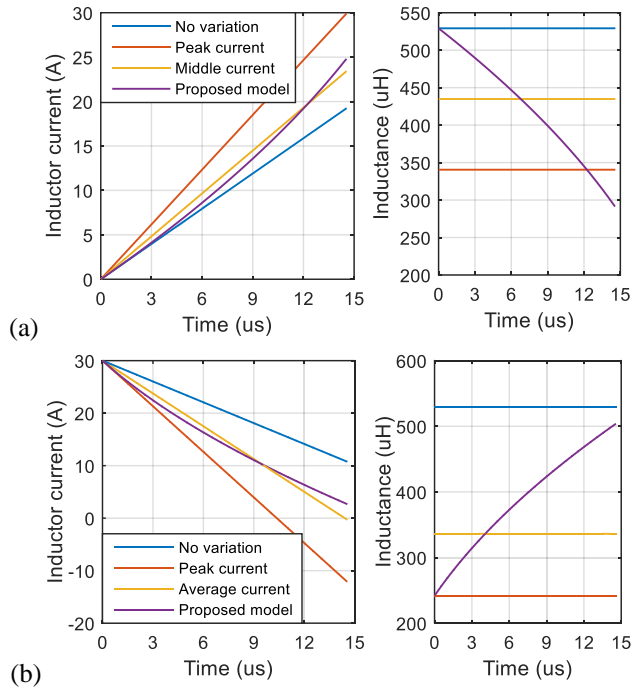


Fig. C.4. Inductor current and inductance estimated by four methods for $L_0=529.2\mu H$ using 60μ KoolM μ core with (a) $V_L=700V$, $\Delta t=15 \mu s$, $i_{L0}=0$ and (b) $V_L= -700V$, $\Delta t=15\mu s$, $i_{L0}=30A$

From a practical design perspective, since $L_{avg(CCM)}$ and $L_{avg(DCM)}$ will be lower than L_0 , it is important to increase the number of turns of the inductor so as to compensate for the loss of inductance and increase of ripple magnitude.

C.3.1. Simulation of four models using KoolM μ inductor in a boost converter

The above four methods to determine the inductor ripple and inductance are applied to an E65 KoolM μ powdered iron core inductor. Using a bobbin of $N=42$ turns, three inductors are built with KoolM μ core of permeability 60μ , 40μ and 26μ . Table C. shows the core permeability, permeance A_{L0} , permeance variation slope M_L and calculated inductance at zero current L_0 . With $V_L = \pm 700V$ and $\Delta t = 15 \mu s$, the inductor current and inductance as estimated by the four methods using MATLAB are shown in Fig. C.4 for 60μ core and $i_{L(0)}=0$ and $30A$ respectively. The following observations can be made:

- The first two methods assume a constant inductance as a function of time and do not accurately estimate the inductor current. At $t=15\mu s$, the current estimated by the first and second methods show a difference of $> 10A$, as seen in Fig. C.4.
- The third method based on the middle current is very good in approximately estimating the inductor current even though it assumes a fixed average inductance. At $t=15\mu s$, the estimated current deviates from that shown by the fourth method by about $1A$.

- The fourth method based on the partial differential equation shows a varying inductance as a function of time and estimates a non-linear current. Method 1 and 2 have an error of up to 20% compared to 4. Experimental verification presented in the next section proves that this method is most accurate.

C.3.2. Experimental verification using KoolM μ core in boost converter

To verify the proposed model for estimating the ripple, a 10kW three leg interleaved boost converter with powdered iron core inductors and MOSFETs is used [24], as shown in Fig. C.3 and Fig. C.5. It has a switching frequency of $f_{sw}=47\text{kHz}$ and an input voltage range of 350V-700V. It is operated at a fixed output voltage of $V_{out}=750\text{V}$. The maximum current through the inductors L1, L2, L3 is $I_{L(ave)}=10\text{A}$, and it occurs when the input is $P_{in}=10\text{kW}$, $V_{in}=350\text{V}$, $I_{in}=30\text{A}$ and the input current I_{in} is shared between the three legs. Table C. shows the actual and percentage inductance $L_{@10A}$ at 10A. It can be seen that the operational inductance is reduced by 8% to 18% depending on the core permeability.

Experimental measurements of the inductor ripple from the boost converter using the 26 μ core with $L_0=284\mu\text{H}$ are shown in Table C.2 and Fig. C.6. The measurements are compared with estimation of inductor ripple from the four proposed methods in the table. An error of up to 5% is obtained if method 1 and 2 are used for ripple estimation. Method 3 and 4 are close to experimental measurements with less than 0.05% error, showing a ten times reduction in error. The estimates from Method 3 and 4 are very close in value in this case, that it can be concluded that method 3 is an excellent choice for simplified calculations. In situations where a high level of accuracy is required in ripple and current estimation, method 4 can be implemented.

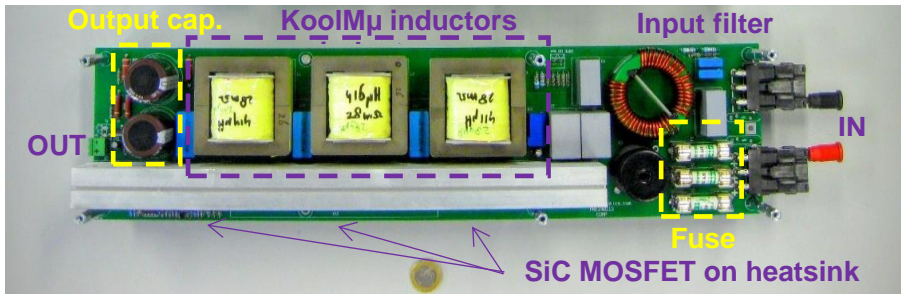


Fig. C.5. Practical setup of interleaved boost converter with three KoolM μ 26 μ E65 cores

Table C.1. KoolM μ core inductors with their corresponding permeance and inductance

μ_r	A_{L0} (nH)	M_L (nH/A)	N	K_L (nH/A)	L_0 (μH)	$L @ 10\text{A}$ (μH)	$L @ 10\text{A}$ (%)
60 μ	300	181/1400	42	9.58	529	433.21	81.89
40 μ	230	143/2200	42	4.82	405	356.84	88.11
26 μ	162	106/3500	42	2.24	285	262.56	92.13

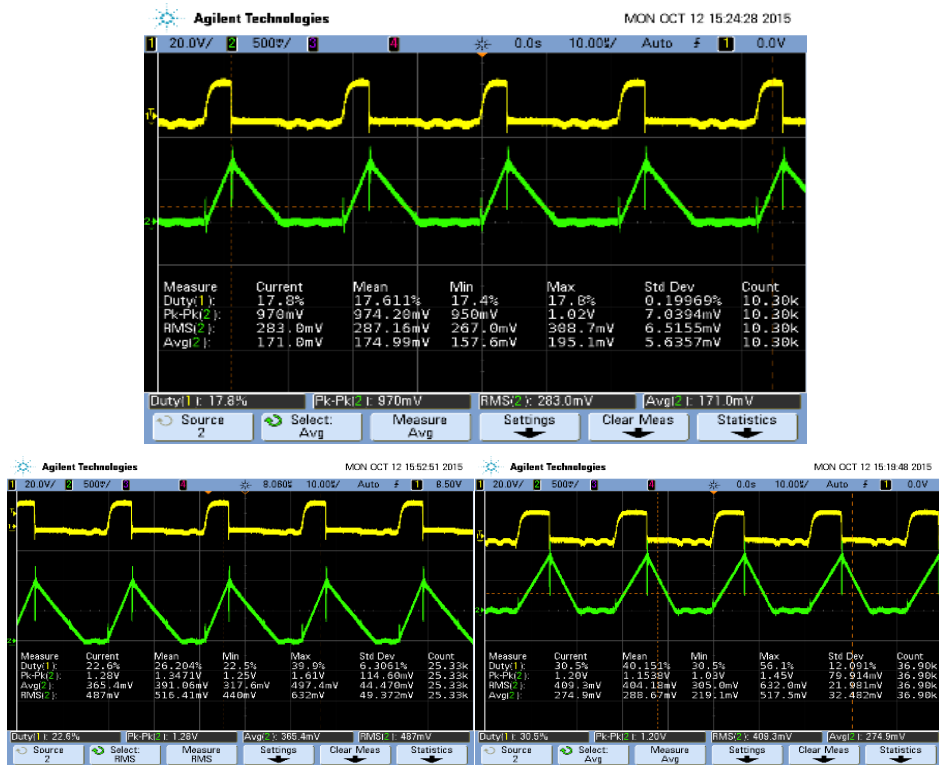


Fig. C.6. Gate voltage of the MOSFET and current waveforms of the KoolM μ inductor measured using current probe: (top) $V_{in}=350V$, $I_{L(avg)}=8A$; (bottom-left) $V_{in}=500V$, $I_{in}=5.5A$; (bottom-right) $V_{in}=500V$, $I_{in}=11A$

Table C.2. Estimated and measured value of inductor ripple using 26 μ KoolM μ

$V_L(V)$	$I_{L(avg)}(A)$	Duty (%)	Mode	$V_{out}(V)$	Inductor ripple (A) measured and estimated using proposed method				
					1	2	3	4	Meas.
350	2.67	30.5	DCM	750	7.94	8.47	8.20	8.21	8.16
400	4.67	38.5	DCM	750	11.46	12.6	12.00	12.03	12.0
500	3.67	22.6	DCM	750	8.41	9.00	8.70	8.71	8.75
500	1.83	17.8	DCM	750	6.62	6.99	6.80	6.80	6.81
600	3.07	15.2	DCM	750	6.79	7.17	6.97	6.98	6.97

C.4. Conclusion

Powdered iron core inductors are an excellent choice for use in high power density converters due to their high saturation flux density. The core exhibits a gradual saturation and reduction of inductance with increasing ampere-turns, unlike ferrites that abruptly reduce to zero inductance near the saturation region. As a result of soft saturation, the inductance varies as a function of inductor current resulting in non-

linear currents. This appendix provides a mathematical derivation of this non-linear behaviour for both continuous and discontinuous mode of converter operation. The non-linear model is compared with three other simplified approaches, of which the middle-current method gives the closest results. Experimental verification using KoolM μ powdered iron core in a boost converter have proven the accuracy of the proposed model.

C.5. References

- [19] “Technical Bulletin - MAGNETICS Kool M μ E-Cores,” 2005.
- [20] M. S. Rylko, K. J. Hartnett, J. G. Hayes, and M. G. Egan, “Magnetic Material Selection for High Power High Frequency Inductors in DC-DC Converters,” in *2009 Twenty-Fourth Annual IEEE Applied Power Electronics Conference and Exposition*, 2009, pp. 2043–2049.
- [21] Epcos, “Epcos Ferrites and accessories - SIFERRIT material N87,” Epcos, 2015.
- [22] G. R. Chandra Mouli, P. Bauer, and M. Zeman, “Comparison of system architecture and converter topology for a solar powered electric vehicle charging station,” in *2015 9th International Conference on Power Electronics and ECCE Asia (ICPE-ECCE Asia)*, 2015, pp. 1908–1915.
- [23] G. R. Chandra Mouli, P. Bauer, and M. Zeman, “System design for a solar powered electric vehicle charging station for workplaces,” *Appl. Energy*, vol. 168, pp. 434–443, Apr. 2016.
- [24] G. R. Chandra Mouli, J. H. Schijffelen, P. Bauer, and M. Zeman, “Design and Comparison of a 10kW Interleaved Boost Converter for PV Application Using Si and SiC Devices,” *IEEE J. Emerg. Sel. Top. Power Electron.*, vol. 5, no. 2, pp. 610–623, Jun. 2017.
- [25] Bong-Gi You, Jong-Soo Kim, Byoung-kuk Lee, Gwang-Bo Choi, Dong-Wook Yoo, B.-G. You, J.-S. Kim, B. Lee, G.-B. Choi, and D.-W. Yoo, “Optimization of powder core inductors of buck-boost converters for Hybrid Electric Vehicles,” in *2009 IEEE Vehicle Power and Propulsion Conference*, 2009, pp. 730–735.
- [26] J. D. Pollock, W. Lundquist, and C. R. Sullivan, “Predicting inductance roll-off with dc excitations,” in *2011 IEEE Energy Conversion Congress and Exposition*, 2011, pp. 2139–2145.
- [27] N. Mohan, T. M. Undeland, and W. P. Robbins, *Power Electronics: Converters, Applications, and Design*. John Wiley & Sons, 2007.

Appendix D: Datasheet and brochure of 10kW EV-PV charger

EV-PV charger is commercially sold by PRE (www.pr-electronics.nl)

D.1. Specifications: 10kW Bidirectional EV Charger



Product: **10kW V2G EV Charger Module**
 Document: **Datasheet (Preliminary, 2017)**

Revision 2.3 – release version
 Page 1/2

10kW Bidirectional Charger Module

Based on years of experience PRE has developed a standard 10kW bidirectional Power Concept for EV chargers with 3 phase AC Input. The charger has active PFC and is based on the latest techniques of HF power electronics based on SiC semiconductors and quasi-resonant technology which results in high efficiency and excellent overall performance. The Power Module can be configured as 'bidirectional' or 'Charger only' operation. Output Voltage and Current can be controlled and monitored by a CAN bus Interface.



Features

- Bidirectional (V2G) operation
- CAN/BMS Control Interface
- Combo/CCS & CHAdeMO compatible
- Optional Solar Input with MPP-Tracker
- Parallel operation for EV Fast Chargers

Applications

- EV (Fast) Chargers
- V2G Home Chargers
- Smart-Grid and Peak-Shaving
- Power Supply / DC Load



Key Specifications

Model	EVC500V30A (Charger only)	V2G500V30A (Bidirectional)		
Output (Battery)	Voltage Range	50 – 500Vdc	50 – 500Vdc	
	Current Range	0 .. 30A (0 .. 28A with internal fuse)	-30 .. +30A (-28 .. +28A with internal fuse)	
	Rated Power (5)	10.000W	10.000W	
	Voltage Ripple + Noise (2)	500mVp-p		
	Voltage & Current Tolerance (3)	<1%		
	Line / Load Regulation	<2%		
	Current Ripple	<1Arms @ Rated Power (measured on a resistive Load)		
	Hold up Time	10mSec.		
	Input (Mains)	AC Voltage & Current Range (5)	400Vac +/-10%, 0-16Aac, 47-63Hz (11kVA max.) 3L + N + PE	
		Power Factor (Control)	>0,99 @ 400Vac & Rated Power (-0.8 .. +0.8 Reactive Power Control)	
Total Harmonic Current		<3% @ 400Vac & Rated Power		
Efficiency		>95% @ 400Vac & Rated Power		
Stand-by consumption		<1W @ Mains Relay Off / 15W @ Mains Relay On (Stand-by)		
Inrush Current (typ.)		50A Cold Start @ 400Vac		
Leakage Current		<3.5mA @ 400Vac		
Protection		Input UVP & OVP	Voltage & Frequency Window, Phase error, DC Injection (external fuse)	
	Output OVP & OCP	550V (30A 600Vdc Fuse)		
	Over Temperature	80°C at main Heatsink. Output Power derating at Tamb. >50 °C		
Control	Control	CAN bus with hardware Interlock (Charge Enable) (CANopen protocol / 500kbps)		
	Auxiliary supply (Input)	9V – 32V 100mA max.		
General	Protection Class (Isolation)	Class 1 (4kV In-Output/2kV PE-input, PE-Output/4kV CAN/Interface)		
	Cooling	Fan cooled.		
	IP protection class	IP20		
	Working (Storage) Temp. & Humi.	-20 .. 50°C (-20 .. 70°C) / 20 .. 90% Non Condensing		
	Dimension & Weight	Approx. 500x300x110mm / 15kg (excl. fans)		
	Lifetime (MTBF)	>100.000 hours @ 25 °C (Designed to meet <0.1% / Year)		
Safety & EMC(4)	Safety (LVD)	low-voltage directive 2006/95/EC (EN60950)		
	EMC	EMC directive 2004/108/EC		
	Grid connectivity	IEC62116 (EU), C83/2, G59/3 (UK), DIN V VDE V 0126-1-1, VDE-AR-N-4105 (D)		



1. All parameters NOT specially mentioned are measured at 400VAC input, rated load and 20°C ambient temperature.
 2. Ripple & noise are measured at 20MHz bandwidth by using a standard probe.
 3. Tolerance : includes set up tolerance, line regulation and load regulation.
 4. The Charger Module is considered a component which will be installed into a final equipment. The final equipment must be re-confirmed that it still meets EMC directives.
 5. Derating may be needed under low input voltage and higher ambient temperature. Please check the derating curve for more details.
 6. © Copyright, All rights reserved. Specifications are subjected to change without notice.

D.2. Specifications: Add-on solar module



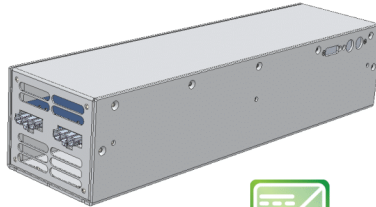
Product: 10kW V2G EV Charger Module
 Document: Datasheet (Preliminary, 2017)

Revision 2.3 – release version
 Page 2/2

10kWp Solar Input Module

Features

- Up to 10kWp PV systems.
- Triple 10A Input. (1 dynamic MPPT)
- 99% Efficiency.
- Direct PV to EV DC Charging.
- PV Fuses & Surge protection inside.
 (Only external DC Isolation switch needed)

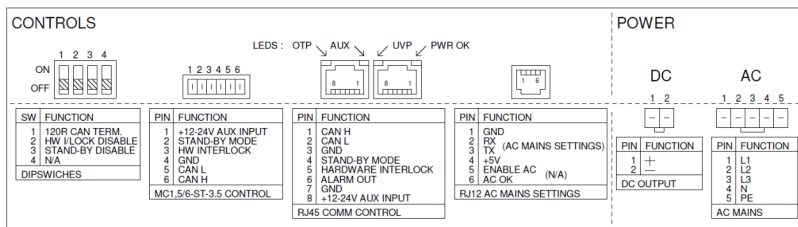


Key Specifications

Model	PV750V30A	
Input (Solar)	Voltage Range (Vstart – Voc max)	275 – 750Vdc
	MPPT Voltage Range	300 – 650Vdc
	Power Range	3 – 10kWp (72 Cells 10 – 18 Solar panels in series per Input.)
	Number of MPP Trackers	1x Dynamic MPPT
	Number of Inputs	3x 10A max.
	Efficiency (max.)	99% (System efficiency : PV – Grid : 97% / PV – EV : 96%)
Output (DC Bus)	Voltage	700 – 760Vdc
	Current Range	0 – 14A
Protection	Input OCP	3x 12A / 1000V Midget Fuse
	Output OVP	800V
	Over Temperature	80°C at main Heatsink. Output Power derating at Tamb. >50 °C
	Isolation Monitor Device	Disconnect @ <800kΩ (in combination with V2G Charger Module)
General	Protection Class (Isolation)	Class 1 ⚡ Transformer less design
	Cooling	Fan cooled.
	IP protection class	IP20
	Working (Storage) Temp. & Humi.	-20 .. 50°C (-20 .. 70°C) / 20 .. 90% Non Condensing
	Dimension & Weight	Approx. 500x140x110mm / 5kg (excl. fans)
	Lifetime (MTBF)	>100.000 hours @ 25 °C (Designed to meet <0.1% / Year)
Safety & EMC(4)	Safety (LVD)	low-voltage directive 2006/95/EC (EN60950)
	EMC	EMC directive 2004/108/EC
	Solar connectivity	IEC 61727:2004, IEC 62109-2:2011

1. All parameters NOT specially mentioned are measured at nominal input, rated load and 20°C ambient temperature.
2. Ripple & noise are measured at 20MHz bandwidth by using a standard probe.
3. Tolerance : includes set up tolerance, line regulation and load regulation.
4. The Charger Module is considered a component which will be installed into a final equipment. The final equipment must be re-confirmed that it still meets EMC directives.
5. Derating may be needed under low input voltage and higher ambient temperature. Please check the derating curve for more details.
6. © Copyright. All rights reserved. Specifications are subjected to change without notice.

Connections



AC Connector : Molex Mini-Fit Sr 5 Way Housing: 42816-0512 / Crimp Terminal : 42815-0012 (12-10 AWG/4-6mm²)
 DC Connector : Molex Mini-Fit Sr 2 Way Housing: 42816-0212 / Crimp Terminal : 42815-0012 (12-10 AWG/4-6mm²)
 Solar Connector : Molex Mini-Fit Sr 3 Way Housing: 42816-0312 / Crimp Terminal : 42815-0012 (12-10 AWG/4-6mm²)
 Control Interface : RJ45 Ethernet cable or Phoenix Contact MC1.5/6-ST-3,5 connector. (RJ12 connector for factory settings only)

D.3. Brochure of EV-PV charger

Solar EV Charging Station

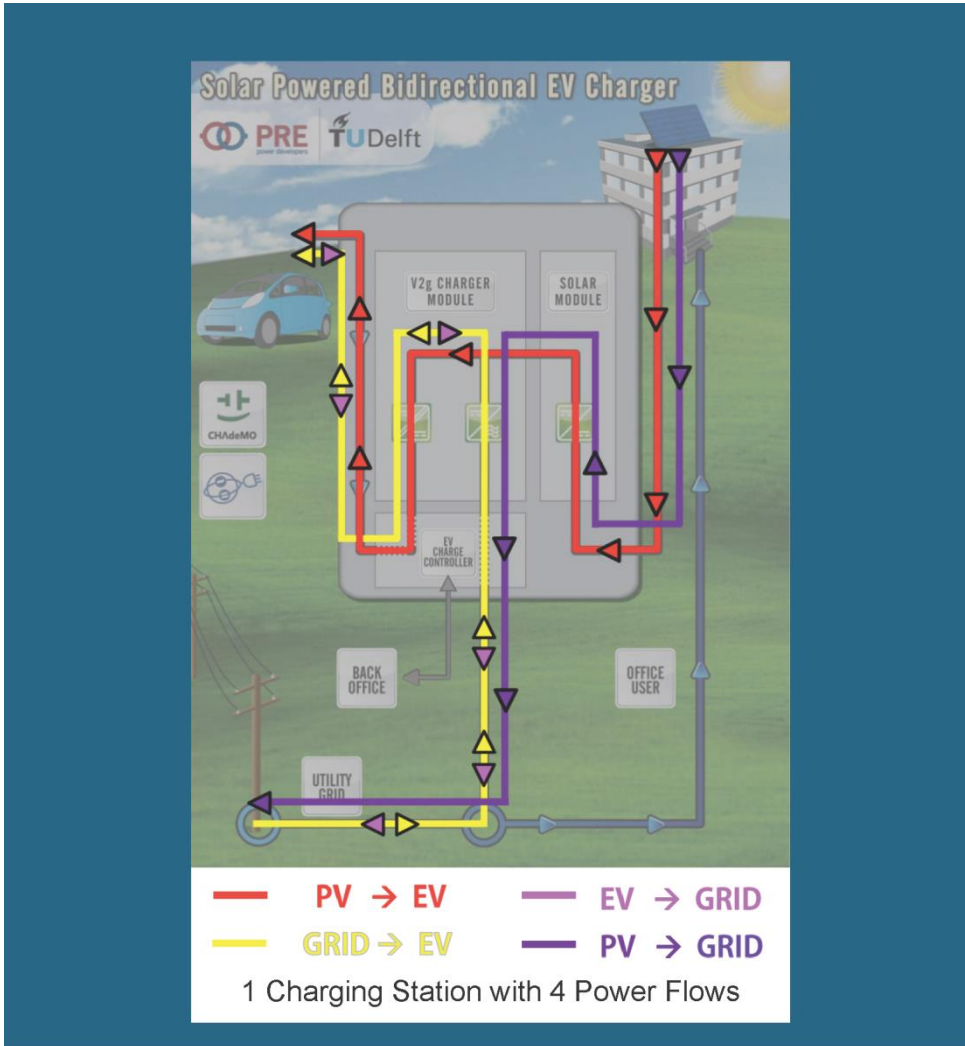


- Direct DC charging of electric vehicle (EV) from PV solar
- Bidirectional, Vehicle-to-grid (V2G) supported
- Smart charging based on EV user, energy prices, PV forecast
- CHAdeMO and CCS/COMBO standard compatible
- High efficiency (>96%) and high power density
- 10kW modular design for fast charging and multiplexing

Would you like to know more about
the solar EV charging station?

Visit bit.ly/EVPV-TUD





TU Delft Gautham Ram, Pavol Bauer, Miro Zeman

PRE Menno Kardolus, Jos Schijffelen

Contact P.Bauer@tudelft.nl

Funded by TKI URBAN ENERGY
Topsector Energie

TU Delft ABB

PRE TEXAS
The University of Texas at Austin

last mile solutions

TU Delft

Faculty of Electrical Engineering, Mathematics and Computer Science

D.4. Concept for future EV-PV charging station

The M.Sc. thesis of Mark Leendertse - *Solar powered charging station for electric cars - conductive and wireless inductive* was a collaboration between the DCE&S group, TU Delft and Industrial Design Faculty, TU Delft to create a concept for a futuristic EV charging station for workplaces that is powered by solar energy. The project was supervised by: G.R. Chandra Mouli, V. Prasanth, S. Silvester, S. van de Geer and P. Bauer. The following are images and video from the thesis:

Video concept of EV-PV charging station:
To view, scan QR code





A short history of Electric Vehicles

Date	Event
1830	Joseph Henry introduced the first DC-powered motor
1830-35	Several inventors in Hungary, the Netherlands and the U.S. build their first prototypes of small-scale electric cars
1832	Robert Anderson develops the first crude electric vehicle in Britain using non-rechargeable batteries
1834	The first (rail) EV was studied and suggested in 1834 by Thomas Davenport in the U.S (who submitted a patent “Improvement in propelling machinery by magnetism and electromagnetism”)
1859	French physicist Gaston Planté invents the rechargeable lead-acid storage battery. It was later improved by Camille Faure in 1881
1874	With the advent of the lead-acid battery, David Salomons successfully built a rechargeable battery-powered EV
1884	English inventor Thomas Parker builds the first practical production electric car in London
1889-91	William Morrison from Iowa creates the first successful electric automobile in the U.S, an electrified wagon for 6 passengers with top speed of 14mph
1899-12	The Baker Electric, the first production electric car is produced by Baker Motor Vehicle Company. Electric cars gain popularity as they are quiet, easy to drive and have no emissions. By 1900, electric vehicles account for around a third of all road vehicles in the U.S
1901	Ferdinand Porsche creates the Lohner-Porsche Mixte the world's first hybrid electric car, powered by a battery and a gas engine
1908-12	Ford introduces the Model-T, and it delivers a blow to electric vehicles due to the high driving range and affordability. With the invention of the automobile starter motor by Ketter in 1911, the need for operating a hand -crank to start the ICE vehicle was gone

1920-35	Decline in electric vehicles and complete takeover by gasoline vehicles owing to cheaper cars and low price of oil
1968-73	Gas prices soar creating renewed interest in the development and use of electric vehicles amongst several auto manufacturers. Governments enact legislation recommending the use of electric vehicles as a means of reducing air pollution. EV Prototypes developed in the period were limited by low range and top speed.
1971	NASA's Lunar rover drives on the moon and runs on electricity
1969-72	BMW debuted its first electric car concept, BMW 1602E at the 1972 Summer Olympics with a lead-acid battery and using a 32kW motor.
1974-77	U.S company Sebring-Vanguard launches its CitiCar, an electric vehicle with a 50-mile range, 30mph top speed and using the lead-acid battery. The Zele, a small electric car is produced by the Italian company Zagato. The vehicle could reach 45 mph and had a range of 60 miles. The Enfield 8000 built by Enfield Automotive uses lead-acid batteries and has a top speed of 48 mph and range of about 40 miles
1994	The REVA Electric Car Company is formed in India to make EVs exclusively. The first car REVAi was launched in 2001 with 50-mile range
1996	GM releases the EV1, an EV with 80-mile range using lead-acid batteries. It uses a custom wireless charging system.
1997	Toyota introduces the first mass-produced hybrid, Prius in Japan, which used a Nickel Metal-Hydride battery. It would eventually go on to become the best-selling hybrid in the world.
1997-00	Research to improve electric vehicles and batteries takes steam amongst several auto manufacturers and research institutions. Several EVs such as Honda's EV Plus, Ford's Ranger pickup EV, Nissan's Altra EV, Chevy's S-10 EV, and Toyota's RAV4 EV are produced by big car manufacturers
2006	Silicon Valley startup Tesla unveils the Tesla Roadster which was the first EV with >200-mile range using a 53kWh battery. The car came 3 years after Tesla was founded in 2003 and sales began in 2008.

2008	BYD releases the F3DM, the world's first mass-produced plug-in hybrid compact sedan in China with 16kWh battery pack. The Th!nk City electric car from Norway and Mitsubishi i-MiEV are introduced with up to a 100-mile range. GM releases the Chevy Volt, a plug-in hybrid electric vehicle which will eventually become the best-selling PHEV in the world. Public sales of the i-MiEV began in 2009 while that of the F3DM and Volt in 2010.
2010	Nissan begins the sale of the LEAF, an all-electric car with 100-mile range using a 24kWh battery. The Leaf which will go on to become the most sold EV of all time.
2012	After being unveiled in 2009, Tesla began sales of the Model S EV with 85kWh lithium-ion battery and EPA range of 265 miles. In the same year, Tesla unveils the Model X, an electric SUV/crossover with similar performance to the Model S.
2011-13	Massive drop in the prices of EV batteries leads to several EVs being launched commercially.
2014	Numerous 100% electric and plug-in hybrid electric vehicles are on the market from BMW, BYD, Cadillac, Chevy, Citroën, Fiat, Ford, Honda, Kia, Mercedes-Benz, Mia, Mitsubishi, Nissan, Opel, Peugeot, Peugeot, Porsche, Renault, Smart, Tesla, Toyota, Via, Volvo, Volkswagen, Wheego.
2016	GM launches Chevy Bolt, the world's first sub 40,000\$ EV with a range greater than 200 miles. Tesla announces its affordable Tesla Model III with range of about 200 miles and a base price of about \$35,000
2017	Global electric vehicle sales reaches 1.2 million of which 66% are pure electrics and rest are plug-in hybrids. China is the biggest global market for electric cars. China, India, Germany, France, Britain, Norway, and Netherlands make commitments to eliminate sales of new fossil fuel cars by 2040 or earlier.

List of Publications

List of Publications (Related to this thesis)

Journal publications

1. G. R. Chandra Mouli, P. Bauer, and M. Zeman, "System design for a solar powered electric vehicle charging station for workplaces," *Appl. Energy*, vol. 168, pp. 434-443, 2016
2. G. R. Chandra Mouli, J. Schijffelen, P. Bauer, and M. Zeman, "Design and Comparison of a 10kW Interleaved Boost Converter for PV Application Using Si and SiC Devices," *IEEE J. Emerg. Sel. Top. Power Electron.*, vol. 5, issue 2, pp. 610-623, 2016
3. D. van der Meer, G. R. Chandra Mouli, G. Morales-Espana, L. Ramirez Elizondo, and P. Bauer, "Energy Management System with PV Power Forecast to Optimally Charge EVs at the Workplace," *IEEE Transactions on Industrial Informatics*, vol. 14, issue 1, pp. 311-320, 2018
4. G. R. Chandra Mouli, R. Baldick, M.Kefayati, and P. Bauer, "Integrated PV Charging of EV Fleet Based on Dynamic Prices, V2G and Offer of Reserves", *IEEE Transactions on Smart Grids*, 2017, pp. 1-13

Journal publications (Under review at the time of thesis publication)

1. G. R. Chandra Mouli, J. Schijffelen, M.v.d Heuvel, M.Kardolus, P. Bauer, and M. Zeman, "A 10kW Solar-Powered Bidirectional EV Charger Compatible with Chademo and COMBO", *IEEE Transactions on Power Electronics*, under review
2. A. Bassa, G. R. Chandra Mouli and P. Bauer, "Evaluation of Topologies for a Solar Powered Bidirectional Electric Vehicle Charger", *IET power electronics*, under review

Conference publications

1. G. R. Chandra Mouli, P. Bauer, and M. Zeman, "Comparison of system architecture and converter topology for a solar powered electric vehicle charging station," in 2015 9th International Conference on Power Electronics and ECCE Asia (ICPE-ECCE Asia), 2015, pp. 1908-1915
2. G. R. Chandra Mouli, J. Kaptein, P. Bauer, and M. Zeman, "Implementation of dynamic charging and V2G using Chademo and CCS/Combo DC charging standard," in 2016 IEEE Transportation Electrification Conference and Expo (ITEC), 2016, pp. 1-6
3. G. R. Chandra Mouli, M. Leendertse, V. Prasanth, P. Bauer, S. Silvester, S. van de Geer, and M. Zeman, "Economic and CO₂ Emission Benefits of a Solar Powered Electric Vehicle Charging Station for Workplaces in the Netherlands," in 2016 IEEE Transportation Electrification Conference and Expo (ITEC), 2016, pp. 1-7
4. G. R. Chandra Mouli, J. Schijffelen, P. Bauer, and M. Zeman, "Estimation of ripple and inductance roll off when using powdered iron core inductors," in *Power Conversion and Intelligent Motion(PCIM) Europe 2016*, pp. 1-8
5. G.R. Chandra Mouli, D. van der Meer, P. Bauer, M. Zeman, J. Schijffelen, M. van den Heuvel and M. Kardolus, "Charging Electric Vehicles from Solar Energy: Integrated Converter and Charging Algorithms", *Energy Open symposium*, 2017

Presentations & Poster

1. G.R. Chandra Mouli, P. Huijbrechts, M. Kardolus, P. Bauer, M. Zeman, “EV supported PV smart grid”, World of Energy solutions conference, 2015.
2. G.R. Chandra Mouli, V. Prasanth, J.A. Ferreira, P. Bauer, M. Zeman, “Charging of EV from PV and Contactless Power”, Energy Informatics & Management (EIM) conference, 2016
3. G.R. Chandra Mouli, J. Schijffelen, M. van den Heuvel, D. van der Meer, P. Bauer, M. Zeman, M. Kardolus, D. van der Meer, R. Baldick, M.Kefayati “Solar powered bidirectional EV charger with V2G”, Symposium on Applied Research on Charging Infrastructure (ARCHI), 2018

Recognition received

1. *Best poster award*. G.R. Chandra Mouli, V. Prasanth, J.A. Ferreira, P. Bauer, M. Zeman, “Charging of EV from PV and Contactless Power”, Energy Informatics & Management (EIM) conference, 2016
2. *Web of science ‘highly cited paper’* placed it in the top 1% of the academic field of Engineering. G. R. Chandra Mouli, P. Bauer, and M. Zeman, “System design for a solar powered electric vehicle charging station for workplaces,” Appl. Energy, vol. 168, pp. 434–443, 2016.
3. ‘Apple Prize’ for G.R. Chandra Mouli for outstanding research in the Department of Electrical Sustainable Energy, TU Delft, 2016
4. Solar powered bidirectional EV charger featured on the Dutch national television NPO1, in their prime time series ‘Breakthrough’ (Doorbraak) as part of the show Een Vandaag in July 2017
5. TU Delft, PRE, LMS were one of three finalists for the *emove360° award 2017 in the category of Energy Storage* for the developed Solar powered bidirectional EV charger with V2G
6. Solar powered bidirectional EV charger showcased in the annual TU Delft research exhibition *Dig-it*, the largest scientific expo in the Netherlands, held on 6-8 June 2017

List of Publications (Collaborative projects)

Journal publications

1. G. R. Chandra Mouli, P. Bauer, T. Wijekoon, A. Panosyan, and E.-M. Barthlein, “Design of a Power-Electronic-Assisted OLTC for Grid Voltage Regulation,” IEEE Trans. Power Deliv., vol. 30, no. 3, pp. 1086–1095, Jun. 2015.
2. P. Venugopal, A. Shekhar, E. Visser, N. Scheele, G. R. Chandra Mouli, P. Bauer, and S. Silvester, “Roadway to self-healing highways with integrated wireless electric vehicle charging and sustainable energy harvesting technologies,” Appl. Energy, vol. 212, pp. 1226–1239, Feb. 2018.

Conference publications

1. G.R. Chandra Mouli, V. Prasanth, P. Bauer and E. M. Bärthlein, "Comparative analysis of on-load tap changing (OLTC) transformer topologies," 16th International Power Electronics and Motion Control Conference and Exposition, Antalya, pp. 918-923, 2014
2. O. Isabella, G. G. Nair, A. Tozzi, J. H. Castro Barreto, G. R. Chandra Mouli, F. Lantsheer, S. van Berkel, and M. Zeman, "Comprehensive modelling and sizing of PV systems from location to load," MRS Proc., vol. 1771, pp. 1-7, Apr. 2015.
3. L. Mackay, T. G. Hailu, G. R. Chandra Mouli, L. Ramirez-Elizondo, J. A. Ferreira, and P. Bauer, "From DC Nano- and Microgrids Towards the Universal DC Distribution System - A Plea to Think Further Into the Future," IEEE Power & Energy Society General Meeting, 2015, pp. 1-5.
4. E. Marafante, L. Mackay, T. G. Hailu, G. R. Chandra Mouli, L. Ramirez-Elizondo, and P. Bauer, "PV architectures for DC microgrids using buck or boost exclusive microconverters," IEEE PowerTech, pp. 1-6, 2015.
5. V. V. Ashok, C. Onwudinanti, G. R. Chandra Mouli, and P. Bauer, "Matching PV Array Output With Residential and Office Load by Optimization of Array Orientation," IEEE PowerTech, pp. 1-6, 2015.
6. J. Sridhar, G. R. Chandra Mouli, P. Bauer and E. Raaijen "Analysis of load shedding strategies for battery management in PV-based rural off-grids," IEEE PowerTech, pp. 1-6, 2015.
7. I. Sulaeman, V. Vega-Garita, G. R. Chandra Mouli, N. Narayan, L. Ramirez-Elizondo, and P. Bauer, "Comparison of PV-battery architectures for residential applications," IEEE Int. Energy Conf., pp. 1-7, 2016.
8. V. Vega-Garita, L. Ramirez-Elizondo, G. R. Chandra Mouli, and P. Bauer, "Review of residential PV-storage architectures," IEEE Int. Energy Conf., pp. 1-6, 2016.
9. V. V. Vijay Vasan Ashok, G. R. Chandra Mouli, J. van der Burgt, S. P. Vera, M. Huibers, L. Ramirez Elizondo, and P. Bauer, "Using dedicated EV charging areas to resolve grid violations caused by renewable energy generation," IEEE Transportation Electrification Conference and Expo (ITEC), pp. 1-6, 2016.
10. V. Prasanth, N. Scheele, E. Visser, A. Shekhar, G. R. Chandra Mouli, P. Bauer, and S. Silvestser, "Green energy based inductive Self-Healing highways of the future," IEEE Transportation Electrification Conference and Expo (ITEC), pp. 1-6, 2016.
11. G. R. Chandra Mouli, P. Venugopal, and P. Bauer, "Future of electric vehicle charging," International Symposium on Power Electronics (Ee), pp. 1-7, 2017

Presentations/Poster

1. G.R. Chandra Mouli, M. Kontos, S. Mao, W. Wang, J. Popovic, F. Pansier, P. Bauer, "Inside the box and out of the box - About innovations in power converters and what it means to system integrators", World of Technology and Science expo, 2016
2. G.R. Chandra Mouli, P. van Duijssen, G. Nair, T. Velzeboer, Y. Zhao, O. Isabella, S. Silvester, P. Bauer, M. Zeman, "Solar e-bike charging station", Vermogenselectronica, 2016

Acknowledgements

My PhD research would not have been possible without the contributions of several people. I would like to express my sincere gratitude and appreciation to everyone who has contributed to the successful completion of this work.

I am deeply grateful to Professor Pavol Bauer, with whom I have been associated with since my master thesis in 2012. First of all, I thank him for the giving me the opportunity to work on this wonderful project. He has motivated and inspired my research and was constantly supportive of my endeavours. In spite of his busy schedule, he made sure he was available for a discussion when required. Under his supervision, I not only built my research skills but learnt a lot of inter-personal skills as well. I especially appreciate the innumerable opportunities he created so that I can give lectures, presentations, conference talks, and write research proposals.

I like to thank my promoter Miro Zeman for his guidance during the thesis. He played an important role in supporting and encouraging the demo at the dig-it exhibition and for the building of the solar e-bike charging station. He brought his vital experience in PV systems to the system design aspects of the project. I thank him, and Professor Bauer for offering a postdoctoral research position in the department and I look forward to our future collaboration.

I thank Power Research Electronics, Breda and especially to Jos Schijffelen, Menno Kardolus and Mike van den Heuvel for their active involvement in the project. Without the prior experience of PRE in building EV chargers and PV converters, the development of the EV-PV charger would have been infeasible. During the many visits to their Breda office, they made me feel like one of them. We gave joint presentations at the WOS 2015, PCIM 2016, Digit 2017 and at emove360 2017. I particularly targeted Jos with a lot of Why's and How's and he was kind to always answer my questions patiently. I gained so many practical insights into the project due to his association. Similarly, I thank ABB EV charging infrastructure, Rijswijk and particularly to Johan Kaptein for collaborating in the project and helping me understand the EV charging standards. I also like to acknowledge Last Mile Solutions for providing the CHAdeMO charge controllers that were used for testing the charger with commercial electric cars.

I thank Professor Ross Baldick for his guidance during my three-month tenure as a visiting scholar at the University of Texas at Austin. I closely worked in that period with Mahdi Kefayati who helped to learn about ancillary service markets and its potential via EVs. I would like to acknowledge Paul Voskuilen from Alliander for facilitating this exchange. Many thanks to Decebel and Elena Mocanu from TU Eindhoven who provided great company and made my stay at Austin enjoyable.

I thank my doctoral examination committee consisting of Prof.dr. E. Lomonova, Prof.dr.ir. J. van Mierlo, Prof.dr. B. Nahid-Mobarakeh, Prof.dr.ir. A.H.M. Smets and Prof.ir. P.T.M. Vaessen for taking out their precious time to read my draft thesis and

be part of the defense ceremony. I got valuable feedback from them which greatly helped improve the thesis and I am thankful for the same.

My personal interest in the field of electrical engineering was triggered by the wonderful teachers I have had during my studies. In particular, I would like to thank Henk Polinder, Jelena Popovic, Peter Morshuis, Frans Pansier, Pavol Bauer, Miro Zeman, Arno Smets and Bram Ferreira from TU Delft and K. Sundareswaran, M.P. Selvan, N. Gounden, M. Venkata Kirthiga and P. Raja from NIT Trichy, for triggering my curiosity in Electrical Engineering. Frans especially took out time on several occasions to explain practical concepts in power electronics and magnetic design. I thoroughly enjoyed those discussions. Professor Sundareswaran played an important role in encouraging me to pursue a PhD and motivate me to work in the field of power electronics. Further, I want to acknowledge my three excellent science teachers in high school namely, Srividya mam, Vasanthi mam and Shyamala mam.

I would like to thank Harrie Olsthoorn, Joris Koeners, Bart Roodenburg, Chris Swanink and Ad Winkels for all their help in the practical work. Harrie was patient in explaining things and helping you get a grip on things in the lab. Ad and my PhD colleagues Pavel and Aditya played a key role in ensuring the success of the demo that was done in the dig-it exhibition. Sincere thanks go to Sharmila Rattansingh and Ellen Schwencke-Karlas for their support at all levels in so many different things. I fondly recollect all the times Sharmila sent wishes for Indian festivals and brought sweets to the office. Peter, his wife Linda and Nils did a great job in translating my summary to Dutch; thank you for the help.

Sincere thanks go to the Dutch Government who have supported me twice in my education. My PhD project was funded by Topsector TKI Switch2Smart grids grant (currently TKI Urban Energy). My M.Sc studies were funded by the Huygens scholarship program via the Nuffic. I am extremely grateful for it. Several anonymous reviewers gave excellent feedback and helped in improving my manuscripts. I thank them for their time spent in the reviewing process.

My DCE&S and EPP colleagues ensured that I had a memorable and enjoyable time at the university. Thank you Aditya, Aniel, Anoop, Carlos, Dong, Emile, Faisal, German, Gu, Ilija, Ivan, Jianing, Johan, Laurens, Lucia, Martin, Minos, Mladen, Na, Nils, Nishant, Pavel, Peter, Prasanth, Rick, Rodrigo, Seyedmahdi, Silvio, Soumya, Tim, Todor, Tsegay, Udai, Victor, Wenbo, Xuezhou and Yeh. It helps a lot to share tips, results, experiences, frustrations, jokes and a lot of coffee.

I especially would like to thank Prasanth for being a mentor and friend since the days I was in India and was planning to come to Delft for my masters. Our friendship has transcended over both personal and professional lines in the last 7 years. My cheerful and not so cheerful days at my office LB 03.680 were made enjoyable thanks to Johan, Ivan, Tim, Victor, Nishant and Na. It was wonderful to share the office with you all. I had a great time travelling with Todor and Milena during the PEMC conference in Turkey, with Prasanth in Korea for ECCE Asia, with Soumya in ITEC USA and with Aditya at Energyopen. Thank you Malden, Ilija and Todor for the organizing the trip to Serbia and to Pavel for the trip to Slovakia. I am grateful to

Sharita and Lonneke for helping with the press release and communication for the EV-PV project, the e-bike station project and for the een-vandaag shoot.

I had the opportunity of working together with several master students during the course of my PhD: Jeyakrishna, Vijay, Dozie, Jagannath, Jessica, Yunpeng, Gireesh, Tim, Mark, Natalia, Dennis (2), Iman, Yunhe, Gerry, Albert, Alvaro, Isabelle, Novy, Wenrui. I would like to thank them for the interesting discussions and the knowledge I gained from the collaboration. Part of the results from the master thesis of Albert, Dennis and Mark have been used in this thesis, and I thank them for the support. In the e-bike station project, I worked with Peter and Olindo, and I would like to acknowledge them for their guidance.

On the personal front, no words can express the gratitude I have for my wife, Kamakshi. I have lost track of the number of days I have been 'late finishing off work', 'busy with a deadline', 'full this Sunday' or 'tired because of work'. She has been a pillar of reassurance, willpower and inspiration. She always had an ear for my university updates, paper stories, lab happenings and mis-happenings. She pushed me hard when I was wavering and she supported me when I was exhausted. I thank her for proofreading my papers, her honest feedback on my presentations and managing it alone when I was in the US. She has been my biggest motivator and critic. Thank you so much for everything.

I would like to thank my *Amma* and *Appa* for their love throughout my life. I had a wonderful childhood, excellent schooling, constant words of encouragement and was instilled with important life values. I thank my sister Manasa for her continuous love, support and company all of the time. All of this would not have been possible without you all. Thank you so much for it.

The unconditional love of my grandparents Pattu Patti, Mani thatha and Lalitha patti; and my Ramesh Mama are invaluable. Thank you mama for all that you have done over the years. I fondly recollect the visit of my aunt Indu to Delft and Frankfurt and the nice time we had together. I miss my late grandparents, Ananada patti and Chundu thatha and dedicate this thesis to them. I thank my parents-in-law Jagdish and Kavita and my brother-in-law Kunal for all their love and for caring for me like their own son and brother, respectively.

My personal life in the Netherlands would not have been memorable without the presence of several people. I would like to thank Adi, Abhinav, Abiram, Akshey, Amrit, Anjana, Ankit, Anand, Bharadwaj, Bedhashritha, Chidambaresan, Diinesh, Davide, Ganesh mama, Harish, Jeyakrishna, Jaikishen, KKHS, Koen, Karthik, Lakshmi, Manimaran, Megha, Nandini, Nirupa, Natalia, Prasanth, Ranjini, Rajesh, Saish, Sriram & Sriram, Supraja, Seshan(ji), Shyam, Syam, Sebastian, Sindhu, Sowmiya, Sneha, Sathya mami, Sadhna, Sayee, Saashwath, Saurabh, Vijay, Vasu, Viknesan and Yaseer. I had so many pleasurable evenings with all of them, celebrated Indian festivals together, enjoyed delicious India food, celebrated each other's birthdays, played cricket and simply had a great time together. I am probably not in touch with a few of you right now, but I will never forget the good times we have had.

It was a once in a lifetime experience visiting Davide and his family for the Christmas of 2017. HK, Rahul, Bharathwaj gave me great company during my three-month stay in Austin; thank you so much guys. I had a great and unforgettable experience living in the home of Mr. & Mrs. Van Hulst and their son Harold during the first year of my PhD. They continue to treat Kamakshi and I like their own kith and kin, and there is always a warm smile when I knock on their door. It was a pleasure to meet Ritwik, Rashmi, Ramesh mama, Sriram and Gaurav during their visit to the Netherlands. I wish your stay was longer. It was great working with Ankit, Beda, Koen and Davide on the NRG battle, TU Delft teamwork prize and subsequently on the TedxDelftAward and ClimateKIC Launchpad.

Finally, I thank the Almighty for everything I have been bestowed in this life. The completion of this thesis would not have been possible without your blessings.

எல்லாப் புகழும் இறைவனுக்கே!

Curriculum Vitae



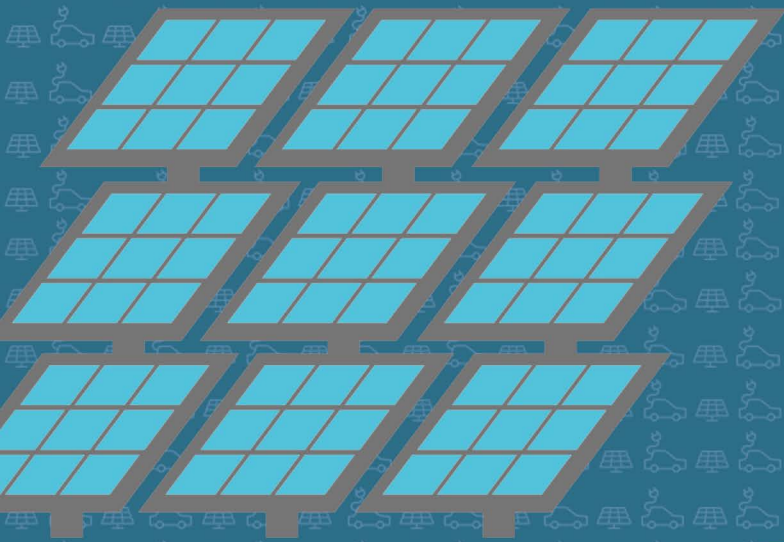
Gautham Ram Chandra Mouli was born on 6 March 1990 in Chennai, India. He received his bachelor degree in Electrical and Electronics Engineering (*Gold medal*) from the National Institute of Technology Trichy, India in 2011 and his M.Sc. degree (*cum laude*) in Electrical Power Engineering from the Delft University of Technology, The Netherlands in 2013. He worked in collaboration with GE Global Research Munich for his internship and master thesis from Aug. 2010 to July 2013 on power electronic based voltage regulators and on-load tap changers.

Since October 2013, he is a PhD researcher on the ‘Electric vehicle supported PV smart grid’ project at TU Delft. For his PhD, he co-developed a smart charger for electric vehicles that is powered by solar panels, in association with PRE, Breda. In the same period, he was a visiting scholar at the University of Texas at Austin as part of the smart city collective initiative. From October 2017, he is working as a researcher at the Delft University of Technology on several projects related to electric mobility.

LinkedIn profile: www.linkedin.com/in/cgauthamram/

Email: G.R.Chandramouli@tudelft.nl (or) c.gautham.ram@gmail.com

**“Sustainable electric transport
requires sustainable electricity”**




TU Delft

ISBN 9789461869012



9 789461 869012